UCGE Reports
Number 20189

Department of Geomatics Engineering

Earth Synthesis: Determining Earth's Structure from Geopotential Fields

(URL: http://www.geomatics.ucalgary.ca/links/GradTheses.html)

by

Dean Allen Provins

January 2004

UNIVERSITY OF CALGARY

Earth Synthesis: Determining Earth's Structure from Geopotential Fields

by

Dean Allen Provins

A THESIS

SUBMITTED TO THE FACULTY OF GRADUATE STUDIES

IN PARTIAL FULFILMENT OF THE REQUIREMENTS FOR THE

DEGREE OF DOCTOR OF PHILOSOPHY

DEPARTMENT OF GEOMATICS ENGINEERING

CALGARY, ALBERTA

December, 2003

ABSTRACT

The intent of this research was to make a contribution to the synthetic Earth project. To that end, this dissertation describes three attempts to determine the mantle density distribution that results in the Earth's geopotential field. Each has advantages and limitations, as will be described in the sequel. To begin, a description of the Earth models that are in current use is given, and with those descriptions, some of the work that has been done in the synthetic Earth project is outlined. This is followed by the background needed for the chapters which describe experimental results.

A wavelet approach for anomalous body identification and depth estimation was the first attempted. The technique employed is one which is suitable for mineral exploration. It was expected also to be useful for crust and mantle analysis, but this was found not to be the case. Analysis of simple bodies was found to be straightforward, but complex anomaly assemblages rendered the technique unusable.

An examination of the geopotential spectrum revealed a power law characteristic that related the spectrum to depth. By making simplifying assumptions with regard to source configuration, and accepting that not all causative bodies might be recognized, it proved possible to classify a geopotential field into several layers. Two of the deepest were used in an inversion strategy to characterize individual causative bodies, and subsequently to replicate the measured field. While the correlation of the measured to synthesized field appeared quite good, the discrepancies between the two were larger than was deemed acceptable.

By taking an alternative approach based on Green's equivalence layer, the same depth

layers interpreted in the previous analysis were inverted as continuous shells of arbitrary thickness. The estimated density contrast variation, and consequently anomalous mass variation, was seen to be within the range predicted or used by other researchers. That there was a direct connection between the measured geopotential field and the density contrast as a function of interpreted depth and shell thickness is considered to be a strong argument for validating this approach, which may be used as more modern spectra are developed.

Acknowledgements

I acknowledge the patience of my wife who found it necessary to 'put me through school one more time'. I also acknowledge the suggestions of my supervisor, the availability of his mathematical expertise, and access to his extensive library.

It is also important to acknowledge the valuable contribution of the Open Source movement, the Free Software Foundation and specifically, Linus Torvalds. Without the development of the Linux kernel and the extensive library of compilers, debuggers and the myriad of other tools that have been contributed by countless individuals, this research exercise would not have been as productive as it has been. The development of the thousands of lines of code that went into various stages of this study was done almost entirely with freely available tools and libraries, the only exception being the temporary use of the University's MACI cluster and its proprietary compiler and libraries. Furthermore, this document was created by the GNU Troff (Groff) typesetting system using a customized set of 'ms' macros. In acknowledgement of this contribution, it is the intent of the writer to make the more important codes that were developed freely available to the community at large.

Table of Contents

List of Tables

List of Figures

1 Introduction

Like the Preliminary Reference Earth Model (**PREM**) of [Dziewonski and Anderson 1981], which has been used in geophysical studies, a synthetic model of the Earth's gravity field would be an invaluable asset for numerical research. Such was the thinking of the International Association of Geodesy (**IAG**) when special study group 3.177 was created in 1996[1]. The IAG felt that such a model would be very useful for computational experimentation. A synthetic Earth model could be used to look at the problems associated with approximations used in geodetic studies. It could allow one to study how errors are propagated through various numerical processes. It could allow researchers around the world to experiment with common, well understood and well characterized datasets. By addressing the practical aspects of producing a synthetic gravity model, it could also allow one to capture the essence of crust or mantle geology through the appropriate choice of a model. Thus the result would be a model representing not only the observed gravity and its derivatives, but also present a possible picture of that geology.

Some of the suggested objectives of the synthetic Earth project were related to global geology: the density and mass structure of anomalous bodies in the mantle and crust. [Featherstone 1999a] mentions the desirability of realistic fields, possibly based on point masses which might be fixed, freely positioned or in some manner adaptable to specific needs. Furthermore, some form of numerical density structure was deemed most desirable. These areas were of most interest in the research to be described, and they have been of interest to other researchers as well.

Over recent decades, considerable work has been done by various researchers, at times independently of this IAG initiative. Work to date ranges from an early model created by [Moritz 1968a] and [Moritz 1968b] to high order models (up to degree and order 1800) which were constructed by G. Wenzel prior to his recent death. These (see [Wenzel 1998b] and [Wenzel 1998a] for details) were based on 5' by 5' world-wide datasets of mean free air gravity anomalies.

Other workers have experimented with synthetic models using point masses, suitably distributed so as to replicate the observed field. A review article covering such approaches is contained in [Vermeer 1995]. Forward modelling which employs geologically-controlled structures, suggested from geophysical (often seismic) experiment has been used in the past for mineral exploration. Such procedures often employ analytic models (point

[1] http://www.cage.curtin.edu.au/~will/iagssg3177.html

masses, lines, ribbons and the like) for which gravitational attraction can be computed. Example studies include that of [Lehmann 1993] who used an iterative technique ascribed to [Barthelmes 1986] for modelling the field in the Gulf of Bothnia, and [Martelet et al. 2001] who investigated deeper structures, principally that of the Himalayas, reaching from about 7 km to about 20 km depth. Studying gravity anomalies as a means of interpreting Earth structure has been going for many years however; it is not a new phenomenon. See for example [Dobrin 1960] and the references therein. A very readable discussion may be found in [Blakely 1995].

In another recent paper [Papp et al. 1996], the authors constructed a three-dimensional volume element model of the upper crust and mantle to study sediment compaction in north western Hungary. In part the model was derived from deep seismic sounding and gravity inversion. It was successfully used to reconstruct geoid undulations of short wavelengths in the Pannonian Basin, and these were favourably compared to the existing quasi-geoid solution (to about the 10 cm level in RMS).

[Pail 1999] has constructed a synthetic global gravity model based on the equivalent source principle. As such, he has employed lateral density variations at the surface of the upper mantle which were parameterized by recent tomographic models. These mantle density variations have been superimposed on PREM and have been augmented by an isostaticly compensated crustal layer. Owing to its parameterization, the upper limit of resolution is said to be low; nevertheless it has been used for satellite gravity gradiometry simulations.

Recently [Featherstone 1999b] developed two gravimetric models of the geoid over a portion of Australia. These were constructed from modified forms of Stokes' formula. The justification for doing this, as opposed to experimenting with observed gravity data, was that a consistent, or well-known set of gravity anomalies and undulations were thus available. These in turn could be used for experimental purposes as the error in numerical computation would be self evident. As it turned out, Featherstone was able to establish that the modified Stokes' operator was superior to the commonly used remove-restore approach for geoid computation in his geographic area.

[Allasia 2001] examined the interpolation of gravitational potential on scattered data. [Claessens et al. 2001] experimented with the free positioning of point masses as the authors attempted to model the region around the city of Perth in Western Australia.

[Haagmans 1999] built topographic and Earth potential models to a high degree for comparison with current and existing models. Another interesting approach was taken in [Vajda and Vaníček 1999] where the properties of a point mass anomaly when processed by a truncated Stokes' function, were studied. The examination of "dimple" events occurring in the derivatives of the truncated geoid allowed the researchers to estimate the depth of the point mass independently of its mass.

Many other researchers have also been active. See for example the bibliography in [Featherstone 2002], the report in [Featherstone et al. 2001] and the recent paper by [Kuhn and Featherstone 2002a] which is an attempt to construct a forward gravity field model. This paper discusses the generation of a synthetic Earth gravity model based on surface topography and bathymetry, and a 2° by 2° crustal model of densities that extends into the upper mantle. It was successful in a partial match with **EGM96**[2] for higher degrees, but lacked the deeper mantle mass anomalies to permit a match for the lower degrees. One other related paper by [Kuhn and Featherstone 2002b] discusses the spatial resolution needs for crustal mass distributions for forward gravity model generation. An extended Meissl scheme for forward gravity field modelling is developed. They found that currently available digital elevation models were sufficient to find the effect on the geoid height caused by topographic masses with an omission error less than 1 cm. The effect of deeper data on geoidal heights, given spatial data resolved to about 20 km (where available) could be derived with omission errors of less than 1 mm. These two papers will be seen to complement the research to be described in the sequel.

In a very recent paper, [Kuhn 2003] describes experiments with determining the geoid using isostatic models augmented by information derived from geological maps for SW Germany. He tried both constant and variable density cases for both planar and spherical isostatic models and concluded that the difference in the geoid height could reach 1 dm with different density assumptions, a value that he pointed out was too high for precise geoid determination.

1.1 Modelling the Earth

Earth models have been developed since at least the early 1980's when [Dziewonski and Anderson 1981] published their paper describing a preliminary Earth reference model, or **PREM** as it has become known. It is a radially symmetric Earth model described by key

[2] EGM96 is a publicly-available geopotential model computed by Goddard Space Flight Centre (GSFC), the National Imagery and Mapping Agency (NIMA) and Ohio State University (OSU) from JGM-3 (Joint Gravity Model 3) and terrestrial/altimetric 30' x 30' anomalies [Lemoine et al. 1998].

geophysical parameters, including shear and compressional velocity, as well as the density which is of interest in this research. That attribute is illustrated graphically in **Figure 1-1**.

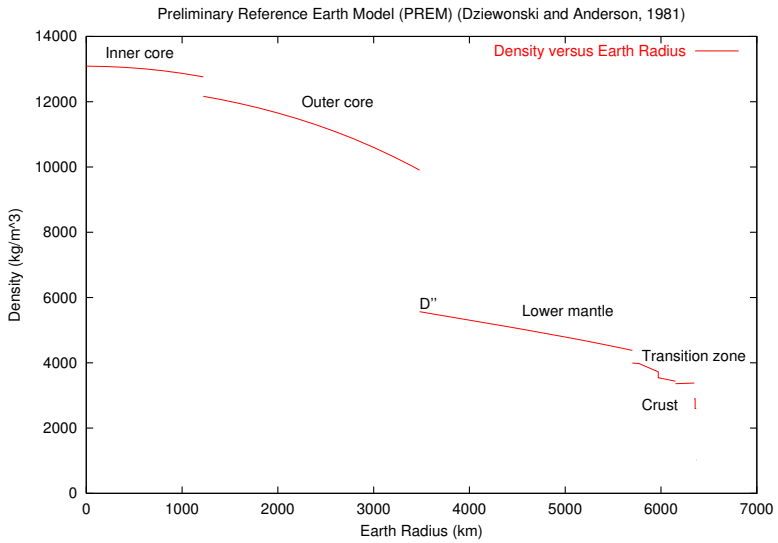

Figure 1-1: *Dziewonski and Anderson's 1981 Preliminary Earth Reference Model. Shown are density versus Earth radius values.*

The Earth however is not radially symmetric as the shape of the geoid so aptly indicates. An exaggerated (for display purposes only) version of a low order geoid is illustrated in **Figure 1-2**. For reference, continental and island coastlines have been 'floated' above the geoid. Divergence from a sphere is particularly apparent in the lower portion of the image. Geodesy is the theory of the size and shape of the Earth and the variations seen in the figure indicate a non-uniform density for the interior, and hence the presence of structures beneath the surface [Garland 1965].

It is with this thought in mind that from the PREM model has emerged a new Earth reference model (**REM**) for which one objective is that it will also accurately reflect the geoid. It is the intention of seismological researchers that this model encapsulate more geophysical parameters than the seismic constraints of PREM.

Recent research appears to have been focussed on the crust. See for example, the latest updates to the **REM subgroup 5** page[3] which may be referenced from the Whole Earth

[3] http://mahi.ucsd.edu/Gabi/rem.dir/crust/rem.crust.html#3smac

,

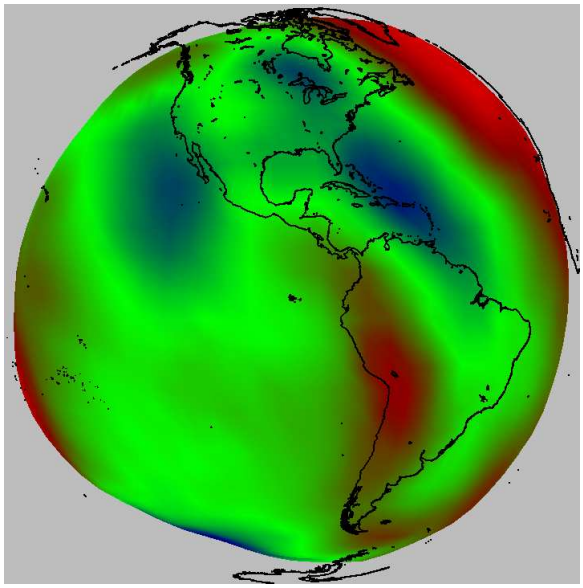

Figure 1-2: *This is an exaggerated image of a low order geoid with coastlines shown 'floating' above for reference. Divergence from a sphere is readily apparent.*

Geophysics page[4]. From all appearances, there has been little work done on density estimation for the mantle since the primary focus has been seismic analysis [Laske, Dziewonski, and Masters 2003]. The next section describes the efforts to develop a new model.

1.1.1 Reference Earth Model REM

Currently the development of a new Reference Earth Model (**REM**) is underway[5]. The objective is to produce a replacement for the PREM which is now over 20 years old [Laske, Dziewonski, and Masters 2003]. The subgroups include the following:

1 Modes and surface waves

2 Travel times and source locations

3 Regional waveforms

4 Global waveforms

[4] http://mahi.ucsd.edu/index.html

[5] http://mahi.ucsd.edu/Gabi/rem.dir/rem.home.html

5 Crust, lithosphere, age and topography

6 Mineral physics

7 Geodynamics

8 Geochemistry

Of these, the closest to our research interest might be the fifth which deals with the crust[6] and lithosphere[7], both of which are defined in [Whitten and Brooks 1979].

The crustal model currently available is named **CRUST 2.0** and its density structure[8] has been specified using newly available constraint data from field and laboratory studies. In areas without field measurements, statistical estimates have been made based on similarities in crustal age and tectonic settings with better known areas. A cross section of the crust for different geological settings is available[9]. Note that the model gives only an estimate of the upper mantle density. Over the Earth, 341 crustal profiles describe the variations in the 16,200 2° by 2° cells, and from these the mantle density immediately beneath the crust was found to have mean and variance 3.17±0.43 gm/cc.

There are other recent crustal models such as **3SMAC** [Nataf and Ricard 1996] which is a model of the crust and upper mantle with a focus on tomographic observables (P and S wave velocity). Another is **RUM**, a model of seismic structure of the upper mantle. It too is a seismic model generated through tomographic inversion and provides modelled P and S wave speed or travel times. The last is the **Global Digital Sediment Map** which is a 1° by 1° model developed in the late 1990's [Laske and Masters 1997]. Its use is aimed at providing more accurate crustal corrections for mantle tomographic studies. Information available in the model includes P and S wave velocities, plus density divided into 3 depth zones: 2 km, 5 km and the remainder, depending on crustal depth.

These recent models are of little use in this research on mantle inhomogeneity. Some work at the Berkeley Seismological Laboratory is more relevant, however. An online paper available[10] is that of [Rousset and Romanowicz 2002]. This is a discussion of the

[6] The crust is that part of the Earth lying above the **Mohorovičić discontinuity** which has an average depth of about 35 km, and which separates the crust from the mantle, a zone of substantially greater density composed primarily of olivine.

[7] The lithosphere is that part of the crust containing the outer, rigid **sial**, (composed of silica and aluminum). It also includes the upper part of the less rigid **sima**, (composed of silica and magnesium).

[8] CRUST 2.0 also provides shear and compressional velocities [Bassin et al. 2000].

[9] http://mahi.ucsd.edu/Gabi/crust/crust.keys.gif

[10] http://www.seismo.berkeley.edu/seismo/annual_report/ar01_02/node1.html

use of the Neighbourhood Algorithm [Sambridge 1999a; Sambridge 1999b] to estimate mantle density (and velocity) variability. This technique uses forward modelling to sample the parameter space preferentially where the fit is better and then exploits the result to obtain quantitative information. The result was good for shear wave estimation, but less so for compressional wave estimates. The density estimates were oscillatory.

A related paper, available at the same site is [Kuo and Romanowicz 2001]. It examines the question of resolving the three dimensional structure of the mantle by using synthetic data to support the hypothesis that low density structures in the lower mantle were correlated with low velocities. This is in sharp contrast with the work of [Ishii and Tromp 1999] who concluded from their studies that exactly the opposite was the norm, that is that low velocities were associated with high density regions. Kuo's conclusion in part, was that current methods and datasets were insufficient to establish density variations in the Earth. Their work supported the conclusions of others [Resovsky and Ritzwoller 1999] that it is not possible to correlate or de-correlate density variations in terms of seismic velocity as a function of depth.

A recent paper on the South African uplift has been related to mantle density structure [Gurnis et al. 2000]. It is a discussion of how a positively buoyant structure within the mid to lower mantle is related to the uplift observed in southern Africa. They use **dynamic topography**[11] and uplift rate to constrain mantle density and thus model the lower to mid mantle (2500 $\leftrightarrow$ 1500 km in depth) density as being 0.2% less dense in that area.

An online abstract [Hipkin 2000] suggests that unless deep causative bodies have sufficient magnitude, shallower bodies will always swamp their surface expression. Hipkin notes that most anomalies observed in **EGM96** are from the lithosphere (wavelengths less than about 500 km), with several exceptions: first the wavelength range of 3000 $\leftrightarrow$ 1300 km is indicative of bodies near 1300 km depth; and secondly, a zone of density anomalies near 230 km is also visible, making density variations at the 670 km boundary invisible. These findings are similar to those found in this research, although the 230 km depth is not in agreement with the present work, as that depth was found to be about 320 km. Hipkin's work was aimed more at estimating mantle viscosity from estimated density variations.

[11] That topography which is maintained by dynamic processes. For example, the elevation of a boundary surface due to upward or downward flow induced by density anomalies in the mantle.

His comments concerning the lithosphere dominating the measured field are supported by earlier researchers, such as [Cook 1963] who noted that higher order harmonics could not originate at great depth, while the low orders might. These he speculated resulted from undulations in the boundary between the solid mantle and the fluid core.

Except for Hipkin's oral presentation, it seems that little published work is available on the subject of mantle density calculation, to the specific degree that this writer's research has been aimed. Clearly, the subject of mantle density is an open question that will be researched and explored for many years to come. The most direct method available for geophysical analysis remains the seismic method, with subsequent Earth characteristic modelling based largely on tomography. Expressions relating density to shear and compressional velocity, providing the elastic constants for bulk modulus and rigidity are known, allow subsequent estimates of density to be made [Stacey 1969].

A check on the interests of well-known Canadian researchers would also suggest that mantle density is not the focus of current deep Earth model research. Workers such as Bruce Buffett[12] at the University of British Columbia, and Gary Jarvis[13] at York are interested more in geodynamics, with specific emphasis on core/mantle interactions, mantle convection, thermal evolution and numerical modelling of temperature and velocity fields. A wider cross section of interests can be reviewed with the organization known as **SEDI**, an acronym for the Study of the Earth's Deep Interior[14], which is an umbrella group, or union committee of the International Association of Geodesy and Geophysics (**IUGG**). Its reason for existence is to "*amalgamate all sources of data and all points of view to generate the most coherent and consistent picture of the workings of the Earth's deep interior*". Its focus is on the past and present thermal, dynamic and chemical states of the deep Earth, and what effect these may have at the surface.

A review of SEDI's recent publications indicates little specific reference to density or mass anomaly estimation. References to density are generally in the context of the core or the core/mantle boundary, with the exception of a report of some work in 1996 of mantle tomography. This showed mantle convection, and slab structures passing through the transition zone into the lower mantle. Some of the structures were draped along the 670 km level, and also apparent were slab-like structures at the 1300 km level. This model was attributed to R. van der Hilst (Massachusetts Institute of Technology) in

[12] http://www.eos.ubc.ca/public/people/faculty/buffett.html

[13] http://www.eas.yorku.ca/eas/faculty/jarvis.html

[14] http://www.sedigroup.org/

collaboration with S. Widiyantoro (Australian National U.) and E.R. Engdahl (USGS, Denver).

Gravity field analysis is much less direct than seismic analysis, although in some mineral exploration areas it remains very useful, judging by the recent wavelet analysis work discussed elsewhere in this document. For Earth characterization and its application to the synthetic Earth project, it is ambiguous at best, although spectral analysis with traditional inversion techniques can be quite enlightening. Much further research is warranted. The research described herein is an attempt to contribute to that knowledge base.

1.2 Research Objectives and Contributions

The **primary objective** of this research was to contribute to the synthetic Earth project by making reasonable estimates of deep Earth mass anomalies' magnitude and depth. These estimates were to be judged as acceptable on the basis of their plausibility and the degree to which the measured geopotential field matched that generated by the estimated bodies. The source of all analysis was to be the expansion of a publicly-available geopotential field, such as **EGM96** or other recent coefficient sets.

The **subordinate objective** was the development of various tools and techniques to facilitate achieving the primary goal: the simulation of the Earth's geopotential field. These included procedures for handling geopotential field synthesis, expansion, filtering, normalization, synthetic field generation and other procedures required in this research; methods to perform wavelet analysis on both global and local fields insofar as required for their numerical analysis and subsequent interpretation; the facility to analyze fields for recognizable anomalies and to perform mass estimates for those anomalies; and finally, developing a method to permit the assessment of lateral variations of identified and interpreted anomalies.

To the extent that the measured potential or the gravity field can be used for estimating deeply buried mass anomalies, this research exercise was successful.

Selected **contributions** of this research to the synthetic Earth project, and potentially to the overall knowledge of the Earth's interior follow:

- Using a simple model, a method to make use of the geopotential field to estimate the depth to anomalous bodies has been identified and exploited.

- A model of possible mass anomalies numbering several hundred in total has been constructed. These range in depth from 300 to 1100 km and have mass sizes in the order of 10^{22} grams. The mass model is reasonably well correlated to the low order coefficients of the EGM96 and the CHAMP geopotential models (to degree 27). This model of mantle mass anomalies generates a plausible field using point masses as suggested in [Featherstone 1999a], although discrepancies make it less than ideal.
- A method to estimate the lateral variability of the aforementioned model has been identified, coded and used for the evaluation of the mid to upper mantle. Based on a direct link to the measured and interpreted geopotential field, this method permits a continuously variable density contrast (or anomalous mass) analysis at arbitrary mantle depths. In this research, the depths employed were specified by the interpretation of the measured field. The resulting analysis compares favourably with portions of the mass model, and also with aspects of other researchers' work. Because of the manner in which it was computed, the model has the property of reproducing the measured field.
- An evaluation of the wavelet techniques described in the context of exploration geophysics was performed. To the extent that simple features were available, this was found to be an acceptable method of depth assessment for deep-seated mass anomalies. For complex surface expressions, it was demonstrated to be lacking and in need of additional knowledge of the subsurface to be effective. Thus, unlike the three previous contributions, this work demonstrated an unsatisfactory method for the depth analysis of mantle structure.
- Various codes for spherical harmonic expansion, synthesis, filtering, normalization and display were developed in the context of an analysis suite suitable for reliable interaction with and the interpretation of published geopotential or other coefficient sets. Other tools developed were for wavelet analysis, synthesis and expansion employing orthogonal wavelets. Procedures to use continuous wavelets for processing global gravity or geopotential fields were also created.

1.3 Dissertation Organization

Chapter 2 provides necessary background on spherical harmonics. It provides an overview of the subject, and how they are calculated and normalized. To the extent that derivatives and integrals are required, the subject is covered, as is a discussion on sampling and spectral resolution. There is a brief review of the approaches used to expand

functions, or to synthesize them, with a focus on the technique used in this research. There are some comments on other codes of interest and idiosyncrasies of which users must be aware. Finally, some specific mathematical development required for the experimentation described in later chapters is provided.

Chapter 3 covers the subject of wavelets, a relatively new field that has seen considerable interest and application in many scientific areas. The continuous and its discretized cousin are discussed, and the orthogonal transform that provides for a multiresolution analysis is also covered. The relationship of wavelets to potential fields, and their application for global gravity field analysis completes the chapter.

Chapter 4 is one of two that applies the techniques described in the previous material to global potential field analysis. In this chapter, the wavelet technique is exploited to ascertain its applicability for deep Earth characterization. For simple models this proves to be useful, but it will be seen that for the complexity of the real geopotential field, the technique leaves much to be desired.

Chapter 5 is the second that applies the techniques of previous chapters to global potential field analysis. In this chapter, a review of some of the work of other researchers is provided. Standard inversion procedures are used in synthetic studies. Problems associated with resolution are identified and an alternative is proposed. This permits defining some error limits for the inversion process. A means to identify mass anomalies is described and used to locate likely bodies. Using the spectrum with simplifying assumptions, depth estimates are made from the surface expression presumed due to underlying mass anomalies. These are inverted to give mass estimates, and from them, a match with the published field is produced. Further numerical work attempts to characterize the shape of the anomalies with good success. A technique using an interpretation of a geopotential spectrum allows plausible inversions of the measured field to be performed, and this is demonstrated for several depths. This allows a continuously variable density contrast to be estimated.

A summary of the work, a detailed list of contributions and several recommendations for future work are provided in the closing chapter.

2 Spherical Harmonics

This chapter discusses spherical harmonics to the degree necessary[15] to understand the basic theory and how they may be profitably employed in unravelling the mysteries of the Earth's interior. Readers wishing a much more extensive background are referred to the classic [Hobson 1931] and the equally instructive monograph [MacRobert 1967]. These two works cover the subject very well, although some areas relevant to the derivatives and integrals of Legendre polynomials are better described elsewhere, as will be seen.

2.1 A Brief Introduction

It is the solution to Laplace's homogeneous equation in space, expressed in spherical coordinates, that result in what are known as spherical harmonics. The simplest harmonic function is that described by the inverse distance between two points: (x, y, z) and (ξ, η, ζ), as per

$$\frac{1}{l} = \frac{1}{\sqrt{(x-\xi)^2 + (y-\eta)^2 + (z-\zeta)^2}} \tag{2-1}$$

where this and other functions (expressed here as U, and as V in the sequel when referring to gravitational potential) are said to be harmonic if they satisfy Laplace's equation,

$$\Delta U = 0 \tag{2-2}$$

which is the common abbreviation for $\nabla^2 U = 0$.

As indicated in [Heiskanen and Moritz 1966], a well known example of such a function is that indicated by the exterior potential of a homogeneous sphere,

$$V = \frac{GM}{l} \tag{2-3}$$

with G being the gravitational constant, M and the sphere's mass, and l the distance from the centre of the sphere to the measurement point. In the general case, this would be expressed as

$$V_P = k \iiint_v \frac{\rho_Q}{l_{PQ}}\, dv \tag{2-4}$$

which indicates that the potential measured at P results from the integration of all density elements within volume v at points Q (i.e. $\rho_Q dv$) separated from point P by distance l_{PQ}.

[15] No pun intended.

As an aside, note that this equation is illustrative of the fundamental problem at hand, that of estimating Earth structure from measurements of the exterior potential. Unfortunately, the problem is complicated by the fact that any harmonic function exterior to a surface S, is uniquely determined by its values on S. See, for example [Butkov 1968], for a detailed explanation of Stokes' theorem, of which this is a particular instance. As [Heiskanen and Moritz 1966] thus point out, it is not possible to determine a unique solution by the inversion of the Earth's potential; nevertheless, a study principally employing spherical harmonics was pursued to gain insight into that structure.

Continuing with the discussion of spherical harmonics, by following the development in [Heiskanen and Moritz 1966], one finds that the conversion from Cartesian coordinates in (x, y, z) to the orthogonal spherical coordinates in (r, θ, λ) affords a solution to Laplace's equation for an arbitrary harmonic function U in both **surface** and **solid spherical harmonics**. That equation is expressed as,

$$\Delta U = \frac{1}{r^2}\frac{\partial}{\partial r}\left(r^2\frac{\partial U}{\partial r}\right) + \frac{1}{r^2\sin\theta}\frac{\partial}{\partial\theta}\left(\sin\theta\frac{\partial U}{\partial\theta}\right) + \frac{1}{r^2\sin^2\theta}\frac{\partial^2 U}{\partial\lambda^2} \tag{2-5}$$

Separation of variables into r and (θ, λ) is the usual first step.

$$\begin{aligned} U &= U(r, \theta, \lambda) \\ &= f(r)Y_n(\theta, \lambda) \end{aligned} \tag{2-6}$$

where $Y_n(\theta, \lambda) = g(\theta)h(\lambda)$. The radial solutions $f(r) = r^n$ or $f(r) = r^{-(n+1)}$, are called **solid spherical harmonics** and are expressed as either (or both in the case of a sum),

$$U = \sum_{n=0}^{\infty}\begin{Bmatrix} r^n \\ r^{-(n+1)} \end{Bmatrix} Y_n(\theta, \lambda) \tag{2-7}$$

The $Y_n(\theta, \lambda)$ are known as the **surface spherical harmonics**, with $r = 1$ on the unit sphere. After separating the other two variables, the following expressions for the surface spherical harmonics result from the solution to the two-variable differential equation[16],

$$Y_n(\theta, \lambda) = P_{nm}(\cos\theta)\begin{Bmatrix} \cos m\lambda \\ \sin m\lambda \end{Bmatrix} \qquad m = 0, 1, \cdots, n \tag{2-8}$$

The two solutions for $h(\lambda)$ are $\cos m\lambda$ and $\sin m\lambda$. The solution for $g(\theta)$ are the $P_{nm}(\cos\theta)$, which are known as **Legendre functions**. Because of the linearity of these equations, any linear combinations are also solutions, such as

[16] The $Y_n(\theta, \lambda)$ are defined in [Heiskanen and Moritz 1966] on page 21, equations 1-48 and 1-53.

$$\begin{aligned} Y_n(\theta,\lambda) &= \sum_{m=0}^{n}\Big[a_{nm}P_{nm}(\cos\theta)\cos m\lambda + b_{nm}P_{nm}(\cos\theta)\sin m\lambda\Big] \\ &= \sum_{m=0}^{n}\Big[a_{nm}R_{nm}(\theta,\lambda) + b_{nm}S_{nm}(\theta,\lambda)\Big] \end{aligned} \tag{2-9}$$

with $R_{nm}(\theta,\lambda) = P_{nm}(\cos\theta)\cos m\lambda$ and $S_{nm}(\theta,\lambda) = P_{nm}(\cos\theta)\sin m\lambda$.

The surface harmonics can be used to expand any arbitrary function on a surface, by appropriate choice of coefficients a_{nm} and b_{nm}. It should be noted that the terms $R_{nm}(\theta,\lambda)$ and $S_{nm}(\theta,\lambda)$ are individually and collectively mutually orthogonal for non equal values of degree (n) and/or order (m). Furthermore, their square over a sphere has the value,

$$\iint_{\sigma}(R_{nm}(\theta,\lambda))^2 d\sigma = \iint_{\sigma}(S_{nm}(\theta,\lambda))^2 d\sigma = \frac{(2^{\delta_{m0}})2\pi}{2n+1}\,\frac{(n+m)!}{(n-m)!} \tag{2-10}$$

Note the delta function in equation equation 2-10. It indicates that for $m = 0$, an additional factor of 2 appears in the result. A similar expression appears in later equations.

For functions respectively inside or outside a normalizing sphere of radius R, potential is given by

$$\begin{aligned} U_{inside}(r,\theta,\lambda) &= \sum_{n=0}^{\infty}\left(\frac{r}{R}\right)^n Y_n(\theta,\lambda) \\ U_{outside}(r,\theta,\lambda) &= \sum_{n=0}^{\infty}\left(\frac{R}{r}\right)^{n+1} Y_n(\theta,\lambda) \end{aligned} \tag{2-11}$$

The general expression for a Legendre function is expressed in either the form for a **Legendre polynomial** as

$$P_n(t) = \frac{1}{2^n n!}\,\frac{d^n}{dt^n}\,(t^2-1)^n \tag{2-12}$$

where $t = \cos\theta$,[17] or in the modified form for a **associated Legendre function** as

$$\begin{aligned} P_{nm}(t) &= (1-t^2)^{m/2}\,\frac{d^m P_n(t)}{dt^m} \\ &= \frac{1}{2^n n!}\,(1-t^2)^{m/2}\,\frac{d^{n+m}(t^2-1)^n}{dt^{n+m}} \end{aligned} \tag{2-13}$$

[17] Here, θ is the colatitude, or 90 minus geographic latitude. Note that some authors use geographic coordinates, and for them $t = \sin\theta$, with appropriate modifications to Rodrigues formulae.

both of which are known as **Rodrigues formula** [Butkov 1968].

In general, $P_{nm}(t)$ is the same as $(-1)^m P_n^m(t)$, as indicated by [Hobson 1931, p. 90] and[18]

$$P_n^m(t) = (-1)^m (1-t^2)^{m/2} \frac{d^m P_n(t)}{dt^m} \tag{2-14}$$

where $(1-t^2)^{m/2}$ has its positive value when m is odd.

Note that 'm' is a positive integer quantity for geodetic use, having the range $m = 0, 1, \cdots, n$ where n is the degree.

2.2 Legendre Function Calculations

The polynomial functions (i.e. $m = 0$) are easily derived from a recursive formula, given the first two expressions for the polynomials[19]. That formula is

$$P_n(t) = -\frac{n-1}{n} P_{n-2}(t) + \frac{2n-1}{n} t P_{n-1}(t) \tag{2-15}$$

and the first few expressions are

$$\begin{aligned} P_0(t) &= 1 \\ P_1(t) &= t \\ P_2(t) &= 1.5t^2 - 0.5 \\ P_3(t) &= 2.5t^3 - 1.5t \end{aligned} \tag{2-16}$$

by which the recursive formula is seen to be correct. Note that when n is even, $P_n(t)$ is also even, as shown by [MacRobert 1967] in,

$$P_n(-t) = (-1)^n P_n(t) \tag{2-17}$$

To calculate the associated functions, Rodrigues formula may be used, and this results in expressions such as (to $n = m = 2$, with $t = \cos\theta$ and $u = \sin\theta$),

$$\begin{aligned} &P_{00}(t) = 1 \\ &P_{10}(t) = t \qquad\qquad P_{11}(t) = u \\ &P_{20}(t) = 1.5t^2 - 0.5 \quad P_{21}(t) = 3ut \quad P_{22}(t) = 3u^2 \end{aligned} \tag{2-18}$$

Many recursion relations exist for the associated Legendre functions, several of which follow. For the case of $n > 0$ and $m \le n, m \ne 0$, the following relation from [Sideris 1997] attributed to [Singh 1981] obviously holds

[18] MacRobert indicates that this function is called **Ferrer's function**

[19] Orthogonal functions generally satisfy three term recursions. See for example [Szegö 1939].

$$P_{nm}(t) = (2n-1)(1-t^2)^{\frac{1}{2}} P_{n-1\ m-1}(t) + P_{n-2\ m}(t) \tag{2-19}$$

As does this from [Blais 1995], also attributed to [Singh 1981]

$$\begin{aligned} P_{nm}(t) &= \frac{2n-1}{n-m}\, tP_{n-1\ m}(t) - \frac{n+m-1}{n-m}\, P_{n-2\ m}(t) && n-2 \geq m \\ &= \frac{2(m-1)t}{(1-t^2)^{\frac{1}{2}}}\, P_{n\ m-1}(t) - (n-m+2)(n+m-1)P_{n\ m-2}(t) && m \geq 2 \end{aligned} \tag{2-20}$$

given the initial values for $P_0(t)$, $P_1(t)$, $P_{11}(t)$ and $P_{21}(t)$ above.

An alternative expression from [MacRobert 1967, page 115, example (i)] and also in [Hobson 1931, page 107, equation 40], indicates the following recursive relationship for constant n,

$$P_{n\ m+2}(t) = (n-m)(n+m+1)P_{nm}(t) - \frac{2(m+1)t}{\sqrt{t^2-1}}\, P_{n\ m+1}(t) \tag{2-21}$$

The expression as indicated is complex, and is intended for the case where t is not real, and is less than one. However, if the signs of the coefficients are reversed and the signs under the radical are also reversed, an expression appropriate for real, non-negative t results. This is similar to Hobson's equation 41, with the signs of the coefficients as shown here,

$$P_{n\ m+2}(t) = \frac{2(m+1)t}{\sqrt{1-t^2}}\, P_{n\ m+1}(t) - (n-m)(n+m+1)P_{nm}(t) \tag{2-22}$$

Note that this expression is identical to that in equation 2-20, except that the order m has been incremented by two. Sometimes such alternative expressions are more convenient to use. For example, from [Hobson 1931, page 108, equation 42] there are two relations with constant m, where the only difference is the increment to the degree n,

$$P_{n+1\ m}(t) = \frac{1}{(n-m+1)}\Big[(2n+1)tP_{nm}(t) - (n+m)P_{n-1\ m}(t)\Big] \tag{2-23}$$

$$P_{n+2\ m}(t) = \frac{1}{(n-m+2)}\Big[(2n+3)tP_{n+1\ m}(t) - (n+m+1)P_{nm}(t)\Big] \tag{2-24}$$

The associated Legendre functions where $n = m$ may also be computed recursively. Observe the sequence calculated from the definition in equation 2-13.

$$\begin{aligned}
P_{11}(\cos\theta) &= \sin\theta \\
P_{22}(\cos\theta) &= 3\sin^2\theta \\
P_{33}(\cos\theta) &= 15\sin^3\theta \\
P_{44}(\cos\theta) &= 105\sin^4\theta \\
P_{55}(\cos\theta) &= 945\sin^5\theta \\
P_{nn}(\cos\theta) &= (2n-1)(2n-3)\cdots 1\sin^n\theta
\end{aligned} \tag{2-25}$$

This reduces to

$$P_{nn}(\cos\theta) = (2n-1)\sin\theta P_{n-1\ n-1}(\cos\theta) \tag{2-26}$$

A related recursion relation exists for the $P_{n+1\ n}(t)$ term. Derived in a similar manner, the first few terms and the general relation are,

$$\begin{aligned}
P_{10}(\cos\theta) &= \cos\theta \\
P_{21}(\cos\theta) &= 3\cos\theta\sin\theta \\
P_{32}(\cos\theta) &= 15\cos\theta\sin^2\theta \\
P_{43}(\cos\theta) &= 105\cos\theta\sin^3\theta \\
P_{54}(\cos\theta) &= 945\cos\theta\sin^4\theta \\
P_{n+1\ n}(\cos\theta) &= (2n+1)(2n-1)(2n-3)\cdots 1\cos\theta\sin^n\theta
\end{aligned} \tag{2-27}$$

This reduces to

$$P_{n+1\ n}(\cos\theta) = (2n+1)\sin\theta P_{n\ n-1}(\cos\theta) \tag{2-28}$$

Many other recursions exist, including those employed by Swarztrauber in his **Spherepack** routines, to be described in the sequel [Swarztrauber 1993]. In this article he provides several additional recursion relations, including the following four point relation:

$$\begin{aligned}
(n+m)(n+m-1)P_{n-1}^{m-1}(t) - (n-m+1)(n-m+2)P_{n+1}^{m-1}(t) \\
+P_{n-1}^{m+1}(t) - P_{n+1}^{m+1}(t) = 0
\end{aligned} \tag{2-29}$$

These show that all $P_n^{2m}(t)$ can be expressed as a linear combination of the $P_n^0(t)$ and that all $P_n^{2m+1}(t)$ can be expressed as a linear combination of the $P_n^1(t)$. Furthermore, as there is no functional dependence on θ, the derivatives are easily calculated from this recursion as well.

The recurrence relation is initialized by pre-computing $P_n^0(t)$ and $P_n^1(t)$. It is also possible to compute $P_n^m(t)$ for $n = m$ and $m = n-1$ by setting $P_n^m(t) = 0$ when $n < m$.

It is worthwhile to note that not all P_n^m need to be calculated as certain symmetries may be exploited. One in particular is $P_n^m(\cos(\pi-\theta)) = (-1)^{n+m} P_n^m(\cos\theta)$, which implies that only one hemisphere needs to be determined [Oh et al. 1999] and also [Adams and Swarztrauber 1997].

In [Heiskanen and Moritz 1966] there is the suggestion that the following formula might also be used to calculate values for the associated functions, but as one will see later, numerical problems occur rapidly,

$$P_{nm}(t) = \frac{(1-t^2)^{m/2}}{2^n} \sum_{k=0}^{\lfloor (n-m)/2 \rfloor} (-k)^k \frac{(2n-2k)!}{k!(n-k)!(n-m-2k)!} t^{n-m-2k} \tag{2-30}$$

Earlier it was noted that an arbitrary functions on a surface could be expanded in surface spherical harmonics by a suitable choice of coefficients. These are computed in much the same way that the coefficients of a Fourier expansion are determined [Heiskanen and Moritz 1966],

$$\begin{aligned} a_{nm} &= \frac{2n+1}{(2^{\delta_{m0}})2\pi} \frac{(n-m)!}{(n+m)!} \iint_\sigma f(\theta,\lambda) R_{nm}(\theta,\lambda) d\sigma \\ b_{nm} &= \frac{2n+1}{(2^{\delta_{m0}})2\pi} \frac{(n-m)!}{(n+m)!} \iint_\sigma f(\theta,\lambda) S_{nm}(\theta,\lambda) d\sigma \end{aligned} \tag{2-31}$$

where $n = 0, 1, 2, \cdots \infty$ and $m = 0, 1, 2, \cdots n$.

Lastly, note that the values of the surface harmonics can take on a wide range of values, and that **normalized Legendre functions** are generally employed. These are expressed as

$$\begin{aligned} \bar{R}_{nm}(\theta,\lambda) &= \sqrt{2^{1-\delta_{m0}}(2n+1)\frac{(n-m)!}{(n+m)!}} R_{nm}(\theta,\lambda) \\ \bar{S}_{nm}(\theta,\lambda) &= \sqrt{2^{1-\delta_{m0}}(2n+1)\frac{(n-m)!}{(n+m)!}} S_{nm}(\theta,\lambda) \end{aligned} \tag{2-32}$$

with the **unnormalized functions** $R_{nm}(\theta,\lambda)$ and $S_{nm}(\theta,\lambda)$ defined in equation 2-9. Using these expressions, an expansion of an arbitrary function takes the form (the usual geodetic formulation),

$$f(\theta,\lambda) = \sum_{n=0}^{\infty} \sum_{m=0}^{n} \left[\bar{a}_{nm} \bar{R}_{nm}(\theta,\lambda) + \bar{b}_{nm} \bar{S}_{nm}(\theta,\lambda) \right] \tag{2-33}$$

with the coefficients being determined via

$$\bar{a}_{nm} = \frac{1}{4\pi} \iint_{\sigma} f(\theta, \lambda) \bar{R}_{nm}(\theta, \lambda) d\sigma$$
$$\bar{b}_{nm} = \frac{1}{4\pi} \iint_{\sigma} f(\theta, \lambda) \bar{S}_{nm}(\theta, \lambda) d\sigma \qquad (2\text{-}34)$$

The standard way of computing the coefficients is via quadrature formulae. These indicate that for some grid (σ_i) and integration weights ($w(\sigma_i)$), the difference between the quadrature (i.e. summation formula) of a set of discrete values $f(\sigma_i)$ of a continuous function $f(\sigma)$ and the analytic integral approaches zero. Mathematically, this is stated as [Yakowitz and Szidarovszky 1989],

$$0 \approx \sum_{i=1}^{N} w(\sigma_i) f(\sigma_i) - \int_{\sigma} f(\sigma) d\sigma \qquad (2\text{-}35)$$

On the parallels, the grid points are defined at the zeros of the cosine and sine basis functions used in the Fourier transform. On the meridians, the points are defined at the zeros of the Legendre polynomials[20]. This ensures that the contribution of each grid point is counted only once, in a manner similar to that of integrating when using Lagrange polynomial functions as a basis.

It should be noted that the normalization factors used in geodetic work (see equation 2-32) are not the only factors in common usage. In geomagnetic studies, the **Schmidt functions** are commonly used [Blakely 1995, page 113].

$$\begin{aligned} \bar{P}_{nm}(\cos\theta) &= P_{nm}(\cos\theta) && \text{if } m = 0 \\ &= \sqrt{2\frac{(n-m)!}{(n+m)!}} P_{nm}(\cos\theta) && \text{if } m > 0 \end{aligned} \qquad (2\text{-}36)$$

2.3 Normalized Recursion Relations

As might be expected, recursions for the normalized functions also exist. In this section is the development of the recursion relation used in this research, and elsewhere (citations follow).

The Legendre functions along the diagonal (i.e. $n = m$) enjoy a simple relationship. This is seen by comparing two adjacent expressions: $\bar{R}_{n-1\ n-1}(t)$ and $\bar{R}_{nn}(t)$ as follows.

[20] Other authors use the nodes of the Chebyshev polynomials [Driscoll and Healy 1994, page 218].

$$\bar{R}_{n-1\ n-1}(t) = \sqrt{\frac{2(2(n-1)+1)((n-1)-(n-1))!}{((n-1)+(n-1))!}}\, R_{n-1\ n-1}(t) \tag{2-37}$$

and

$$\bar{R}_{nn}(t) = \sqrt{\frac{2(2n+1)(n-n)!}{(n+n)!}}\, R_{nn}(t) \tag{2-38}$$

Their ratio is then after simplification,

$$\bar{R}_{nn}(t) = \sqrt{\frac{2n+1}{2n}}\, \bar{R}_{n-1\ n-1}(t)\, \frac{R_{nn}(t)}{(2n-1)R_{n-1\ n-1}(t)} \tag{2-39}$$

But earlier it was learned from equation 2-26 that there existed a relation between the diagonal elements. Using this, it is seen that

$$\bar{R}_{nn}(t) = \sqrt{\frac{2n+1}{2n}}\, \sin\theta \bar{R}_{n-1\ n-1}(t) \tag{2-40}$$

The elements immediately below the diagonal enjoy a similar relationship with the diagonal elements. Consider $\bar{R}_{n+1\ n}(t)$ and $\bar{R}_{nn}(t)$ as follows.

$$\bar{R}_{n+1\ n}(t) = \sqrt{\frac{2(2n+3)1!}{(2n+1)!}}\, R_{n+1\ n}(t) \tag{2-41}$$

and

$$\bar{R}_{nn}(t) = \sqrt{\frac{2(2n+1)0!}{(2n)!}}\, R_{nn}(t) \tag{2-42}$$

Their ratio then yields,

$$\bar{R}_{n+1\ n}(t) = \sqrt{\frac{2(2n+3)1!}{(2n+1)!}\,\frac{(2n)!}{2(2n+1)0!}}\, \frac{R_{n+1\ n}(t)}{R_{nn}(t)}\, \bar{R}_{nn}(t) \tag{2-43}$$

But combining equation 2-26 and equation 2-28 it is found that

$$P_{n+1\ n}(t) = (2n+1)\cos\theta P_{nn}(t) \tag{2-44}$$

which means that

$$\begin{aligned} \frac{R_{n+1\ n}(t)}{R_{nn}(t)} &= \frac{\cos(n\lambda)P_{n+1\ n}(t)}{\cos(n\lambda)P_{nn}(t)} \\ &= (2n+1)\cos\theta \end{aligned} \tag{2-45}$$

which simplifies equation 2-43 to

$$\begin{aligned} \bar{R}_{n+1\ n}(t) &= \frac{\sqrt{2n+3}}{2n+1}(2n+1)\cos\theta\bar{R}_{nn}(t) \\ &= \sqrt{2n+3}\cos\theta\bar{R}_{nn}(t) \end{aligned} \tag{2-46}$$

Using the recursion relation cited in equation 2-15, one can develop a similar relation for the normalized polynomials. Recall that

$$\begin{aligned} \bar{R}_n(t) &= \sqrt{2n+1}P_n(t) \\ \bar{R}_{n-1}(t) &= \sqrt{2(n-1)+1}P_{n-1}(t) \\ \bar{R}_{n-2}(t) &= \sqrt{2(n-2)+1}P_{n-2}(t) \end{aligned} \tag{2-47}$$

then a substitution into equation 2-15 yields,

$$\bar{R}_n(t) = \frac{\sqrt{2n+1}\sqrt{2n-1}}{n}t\bar{R}_{n-1}(t) - \frac{\sqrt{2n+1}(n-1)}{n\sqrt{2n-3}}\bar{R}_{n-2}(t) \tag{2-48}$$

This can be generalized for $n \neq m$ to

$$\begin{aligned} \bar{R}_{nm}(t) = \sqrt{\frac{(2n+1)(2n-1)}{(n-m)(n+m)}}t\bar{R}_{n-1\ m}(t) - \\ \sqrt{\frac{(2n+1)(n+m-1)(n-m-1)}{(2n-3)(n+m)(n-m)}}\bar{R}_{n-2\ m}(t) \end{aligned} \tag{2-49}$$

and confirmed by substitution. It is the recursion in equation 2-49 that is used in [Rapp 1982] and in subsequent work when it was extended to higher degree and order. It was this recursion coded in C and extended for derivatives, that was used in the course of this research.

As far as accuracy of the recursion relations is concerned, [Wenzel 1998b] notes that the well known relation

$$\sum_{m=0}^{n}\bar{P}_{nm}^2 = 2n+1 \tag{2-50}$$

can be used. He explored numerical accuracy with a FORTRAN compiler and found that accuracies of $10^{-13}\cdots10^{-11}$ was achievable for the fully normalized functions up to degree 1800 for polar distances to 180° with 15 digits of precision. Recently, [Holmes and Featherstone 2002a] and [Holmes and Featherstone 2002b] discussed numerical procedures for extending the recursions of Legendre functions to degree and order 2700.

Relative error similar to that experienced by Wenzel was obtained.

In a group effort, Blais and colleagues recently examined the inaccuracy of pre-computing the normalization factor independently of the Legendre function, and then using their product when synthesizing a model composed of unit coefficients to represent a model on the sphere. It was found that after a low degree and order (between 32 and 64) unacceptable error began to creep into the process. By using a code similar to that described in this section, numerical imprecision problems were not observed to at least degree 1024 [Blais 2003]. The experiments used the commercial program known as **Mathematica**, a code with extended precision capabilities.

2.4 Derivatives and Integrals

Upon occasion, either or both the derivatives or integrals of Legendre polynomials or the associated functions will be required. During the course of this research, both were needed at different times, and this section summarizes the results of exploring this area.

As the derivatives of the Legendre polynomials are straightforward to compute, they will not be repeated here. Instead, only the derivatives for the associated functions are given. From equation 2-40, one can deduce the derivative of $\bar{R}_{nn}(t)$ with respect to colatitude directly, as

$$\frac{d\bar{R}_{nn}(t)}{d\theta} = \sqrt{\frac{2n+1}{2n}}\left(\sin\theta\,\frac{d\bar{R}_{n-1\ n-1}(t)}{d\theta} + \cos\theta\bar{R}_{n-1\ n-1}(t)\right) \qquad (2\text{-}51)$$

It was this latter form that was suggested in [Colombo 1981] and used in [Rapp 1982]. For a given m, the values are determined to a given n, leaving[21],

$$\frac{d\bar{P}_{nm}(\cos\theta)}{d\theta} = \frac{1}{\sin\theta}\left(n\bar{P}_{nm}(\cos\theta)\cos\theta - \left(\frac{2n-1}{(n^2-m^2)(2n+1)}\right)^{\frac{1}{2}}\bar{P}_{n-1\ m}(\cos\theta)\right) \qquad (2\text{-}52)$$

The start value is

$$\frac{d\bar{P}_{00}(\cos\theta)}{d\theta} = 0 \qquad (2\text{-}53)$$

An alternative formulation from [Swarztrauber 1993] is the derivative of the unnormalized function,

[21] Switching from $\bar{R}_{nm}(\cos\theta)$ to $\bar{P}_{nm}(\cos\theta)$ is acceptable as the former is simply the latter multiplied by either $\cos m\lambda$ (or $\sin m\lambda$ in the case of $\bar{S}_{nm}(\cos\theta)$). See equation 2-9 and equation 2-32.

$$\frac{dP_{nm}(\cos\theta)}{d\theta} = \frac{1}{2}\left(P_{n\ m+1}(\cos\theta) - (n+m)(n-m+1)P_{n\ m-1}(\cos\theta)\right) \qquad (2\text{-}54)$$

The derivatives of the normalized Legendre functions with respect to λ are quite straightforward, and require no repeating here.

With respect to integrals, only integration with respect to $t = \cos\theta$ was an issue for this research. For integrals of the polynomials, examination of equation 2-15 suggests

$$\int P_n(t)d(t) = \frac{P_{n+1}(t) - P_{n-1}(t)}{2n+1} \qquad (2\text{-}55)$$

This is very easily evaluated; however, the integration of the associated functions is not at all obvious. Various authors have attempted evaluation procedures. For example, [Young 1970] and [Christodoulidis and Katsambalos 1977] are both referenced in [Paul 1978] as having either instability problems near the poles (Young) or computational time and accuracy problems (Christodoulidis). Paul on the other hand developed an accurate recurrence of the following expression,

$$\int_{t_1}^{t_2} P_{nm}(t)dt \qquad (2\text{-}56)$$

which will not be repeated here; merely note that to at least degree 100, for functions integrated over any arbitrary interval within 90°, the errors detected never exceeded 10^{-23} in magnitude.

Other authors extended Paul's work. These include [Gerstl 1980] who examined the domain of stability in order to recommend which of either forward or reverse recursion should be employed to compute the integral in equation 2-56.

Straightforward numerical integration of equation 2-56 is also possible, but tedious and in need of an extended arithmetic code as it is fraught with numerical considerations. The principal problem is the magnitude of the numbers with which a user must deal.

The basic formula, as cited in equation 2-30, can be broken down into two parts:

$$T_{nmk} = \frac{(-1)^k(2n-2k)!}{2^n k!(n-k)!(n-m-2k)!} \qquad (2\text{-}57)$$

which is independent of $\cos\theta$ (i.e. cosine of the colatitude), and

$$\int_{\cos\theta_1}^{\cos\theta_2} (1-\cos^2\theta)^{m/2}\cos^{n-m-2k}\theta\, d(\cos\theta) = \int_{\mu_1}^{\mu_2}(1-\mu^2)^{m/2}\mu^{n-m-2k}\,d\mu = \int_{\theta_1}^{\theta_2}(1-\cos^2\theta)^{m/2}\cos^{n-m-2k}\theta(-\sin\theta)d\theta \tag{2-58}$$

to show two equivalent formulations of the integral. Summing the products of T_{nmk} with the respective integrations provides a final result. Unfortunately, the T_{nmk} can become extremely large. The normalization factor,

$$\sqrt{\frac{2(2n+1)(n-m)!}{(n+m)!}} \tag{2-59}$$

provides a correction for these values, which can easily yield values in excess of 700 digits. For example, 360!, in the denominator of T_{nmk} is 767 digits in length. The largest term in the normalization factor for the same degree and order is 1747 characters. Clearly, special care is required to handle numbers of such magnitude.

Normally, the values of the $\bar{P}_{nm}$ are determined recursively, and as normalization is included, the values remain moderate in size. Since the experiment was to attempt direct computation however, it was imperative to employ an extended precision code.

One effective tool is an arbitrary precision arithmetic machine. This device, of which **GNU bc**[22] is an example of a command line, interpreted and programmable language, allows arithmetic operations to virtually any desired degree of precision. Several C and C++ tool sets are also available. One such library is **GNU MP**[23], a multiple precision arithmetic library [Granlund 2002].

Initial codes were written in **GNU bc** to calculate the integrals of lower order P_{nm} terms. As the scale parameter was set only to 100 digits of precision, this limited the applicability to degree and order 35. Other codes with caller-specified scale parameters were later developed with GNU MP. This library was the easiest to modify for the requirement at hand. Other libraries that are available include [Arndt 1997] and [Tommila 1999].

As a matter of interest, several tables of integrals had to be consulted to obtain expressions which could be successfully evaluated numerically, including [Gröbner and

[22] http://www.gnu.org/software/bc/bc.html

[23] http://www.gnu.org/directory/gnump.html

Hofreiter 1961; Selby 1964] and [Beyer 1991]. There were typographical errors in each, which might be excusable in the first reference which appeared to be hand-written, but not so for the latter. The same errors were faithfully copied from edition to edition.

2.5 Sampling and Spectral Resolution

How many data points are needed in each direction for a successful analysis? For the meridians, it is some $N = N_{\max} + 1$, where $N_{\max}$ is the maximum degree included in the data, as described by the N data samples $0 \le n \le N - 1$. For the parallels, it is $2N - 1 = 2N_{\max} + 1$, as described by the $2N$ data samples $0 \le m \le 2N - 1$ [Colombo 1981]. This corresponds to $N_{\max}$ frequencies resolvable along each latitude for an equiangular grid: $\Delta\lambda = \Delta\theta = \pi/N$. It has also been shown that for band limited functions on a spherical surface, inversion is possible with N samples in both directions (i.e. non-equiangular), as outlined in [Driscoll and Healy 1994] and described here in the sequel.

Using a fast Fourier transform along the parallels will yield N frequencies from $2N$ data points. The DC ($f = 0$ radians per unit length) and Nyquist ($f_{Ny} = N/2$ radians per unit length) are even functions, and the intermediate frequencies are complex, making the number of coefficients resulting from the transform equal to the number of data points input to the transform. Since the maximum order equals the maximum degree, then for $N_{\max}$ as the maximum degree, one expects $2 * N_{\max} + 2$ points along each latitude. This indicates needing $(2 * N_{\max} + 2) * (N_{\max} + 1) = 2N^2$ data points in agreement with Colombo.

Note also that for some degree N, there are $2N + 1$ coefficients resulting from an analysis, for a total of $(N_{\max} + 1)^2$ for a complete analysis to degree $N_{\max}$. These correspond to $2N$ values for orders not equal to zero, and the zero order value. Since the zero order value is the DC component and has no imaginary value, the extra value must result from the addition of an imaginary value at the Nyquist frequency.

From another perspective, a recent thesis by [Kampes 1998] discusses the minimum amount of data required for an expansion to degree $N_{\max}$. He notes that for $m = 0$, the maximum number of unknowns are apparent (i.e. from $n = 0$ to $N_{\max}$, totalling $N_{\max} + 1$). Thus, for a solution to the equation (where $m = 0$, meaning there is no λ dependence)

$$f(\theta) = \sum_{n=0}^{N_{\max}} P_{n0}(\cos\theta) C_{n0} \tag{2-60}$$

one requires a minimum of $N_{\max} + 1$ observations[24]. The dependence on λ, for the m component, is a minimum of $2N_{\max}$ observations. This corresponds to the $N_{\max} + 1$ even components (for $m = 0$, $0 \le n \le N_{\max}$) and $N_{\max} - 1$ odd components ($1 \le m \le N_{\max}$ on each parallel because $\sin m\theta$ is zero for $m = 0$ and $m = f_{Nyquist}$). All components along the parallels then total $2N_{\max}$.

According to Kampes then, it takes $N_{\max} + 1$ parallels and $2N_{\max}$ meridians to compute a spectrum to maximum degree $N_{\max}$. This corresponds to $2N_{\max}^2 + 2N_{\max}$ data points, which is typical of analysis programs like Spherepack which include the poles in its calculations. For example, a 5° equiangular grid, including the poles would have 37 parallels and 72 meridians for a maximum degree (and order) of 36 from 2664 data samples. By contrast, Colombo's equiangular centre point grid requires $2 * 37^2 = 2738$ samples.

Why then, if for maximum degree $N_{\max}$, are there only $(N_{\max} + 1)^2$ coefficients, when one started with $2N_{\max}(N_{\max} + 1)$ data points (Kampes, Spherepack), or $(2 * N_{\max} + 2) * (N_{\max} + 1)$ data points (Colombo), and can one invert? Certainly for a Fourier transform on the plane, there are exactly as many coefficients as there are data points, but not so in the sphere. The answer appears to lie in how the coefficients are computed and what they represent. For example, the zero degree coefficient, which is real and even is just the mean or DC value. There is also a "DC" value for degree 1, order 0. For this degree there is only one fundamental frequency to be computed, the Nyquist, which is also even, but for which an imaginary component is computed. Degree 2 has a "DC" value, a Nyquist value (with an imaginary component) and a fundamental contributing 2 coefficients, and so on.

The Fourier transform estimates the magnitude of representative coefficients along the parallels. These are the averages of the inner products of sinusoids at each frequency of interest over the interval [Blais 1988]. This operation requires $2N_{\max}$ values per parallel at the maximum degree. Once computed, the average of the inner product of the associated Legendre functions and the previously computed Fourier coefficients is determined. Since the Legendre functions are determined solely by the colatitude (or latitude in the case of **Spherepack**) the averaging occurs over the $N_{\max}$ parallels. All values along a parallel contribute equally, but different functions are employed for each of the Fourier coefficients previously computed. In this manner the data are averaged in a least squares sense to produce just enough coefficients to reproduce it [Swarztrauber 1993].

[24] See also [Blakely 1995] for additional commentary on zonal solutions.

Furthermore, each Legendre coefficient computed is the best possible regardless of the length of the dataset [Blakely 1995]. As indicated in equation 2-33 an infinite number of coefficients may be required to accurately represent some function on the sphere, but for the general case, a finite sum will suffice. The coefficients computed from the data available will allow the synthesis of that data to the degree permitted by the averaging process of the analysis.

As an aside, it is worth noting that the wavelength corresponding to each degree of expansion is roughly $\frac{2\pi R_E}{N}$, where R_E is the average radius of the earth, and N is the degree in question. For a circumference of about 40,000 km (given $R_E \approx 6371$ km), the second degree harmonic has a wavelength of about 20,000 km, while the tenth is about 4,000 km.

2.6 Implementation Approaches

This section is intended to outline some of the different techniques used by various authors in their attempts to implement efficient synthesis and analysis of spherical datasets. Most authors (all described here) employ fast Fourier transforms (**FFT**) in their codes, but even with this fairly recent development [Cooley and Tukey 1965] typical Fourier analysis on the sphere is still $O(N^3)$ in complexity.

Rather than beginning with Gauss methods which clearly pre-date the use of electronic computers, an early user of the FFT as described in a short paper by Ricardi and Burrows has been selected. None of the techniques will be discussed in detail, but hopefully, the reader will be left with some insight into the approach used by the different authors. Additional discussion of some of these techniques may be found in [Blais and Provins 2000] and [Blais and Provins 2002].

2.6.1 Ricardi Method

In 1972, a 2 page ‘short note’ described a recurrence technique for expanding a function in spherical harmonics [Ricardi and Burrows 1972].

Like other authors, they begin with a Fourier transform over the m coordinate. This leaves an expression of the form,

$$f_m^{e,o}(\theta) = \sum_n a_{nm}^{e,o} P_{nm}(\cos\theta) \tag{2-61}$$

Note that the $a_{nm}^{e,o}$ actually correspond to two coefficients, one even, the other odd.

The authors note that a Legendre transform (by means of computing an inner product) would then produce the desired coefficients. They avoid this procedure by noting that the associated Legendre functions have the property that when m is even, the $P_{nm}(\cos\theta)$ may be expressed as a finite series in $\cos p\theta$, and when odd, may be expressed as a finite series in $\sin p\theta$. The values of p are $p = n, n-2, \cdots$.

This means that $f_m^{e,o}(\theta)$ is either

$$\begin{aligned} f_m^{e,o}(\theta) &= \sum_p A_p \cos p\theta \quad m \text{ even} \\ f_m^{e,o}(\theta) &= \sum_p A_p \sin p\theta \quad m \text{ odd} \end{aligned} \tag{2-62}$$

Clearly, taking another Fourier transform will result in the computation of the A_p.

The desired coefficients are then given by expressions of the form,

$$a_{nm}^{e,o} = \frac{2n+1}{2}\frac{(n-m)!}{(n+m)!}\sum_p I_{nmp} A_p \tag{2-63}$$

for values of $n = m, m+1, \cdots$ (recall that the first step was to compute the m values, so now one is computing all n for a specific m).

The expressions of I_{nmp} are integrals of the form,

$$\begin{aligned} I_{nmp} &= \int_0^\pi \cos p\theta P_{nm}(\cos\theta)\sin\theta d\theta \quad m \text{ even} \\ I_{nmp} &= \int_0^\pi \sin p\theta P_{nm}(\cos\theta)\sin\theta d\theta \quad m \text{ odd} \end{aligned} \tag{2-64}$$

Careful (make that laborious) integration reveals that the I_{nmp} can be expressed in closed form, and not very arduous integration indicates a simple recursion for these terms. By noting that the I_{nmp} are zero for every other value, and using matrix formulation, the resulting matrices are relatively sparse.

This writer has not calculated the number of operations, but it was said by Colombo to be $O(N^3)$.

2.6.2 Colombo

In 1981, a report from Ohio State University described an $O(N^3)$ routine. This appeared to be an implementation of the Ricardi and Burrows algorithm, and was confirmed in a personal communication from Grafarend [Blais 2000] and passed to this writer. See for example, equations 1.17 and 1.18 in the report [Colombo 1981].

The analysis of a function $f(\theta_i, \lambda_j)$ sampled on an equi-angular basis is given as

$$\hat{C}^{\alpha}_{nm} = \frac{1}{4\pi} \sum_{i=0}^{N-1} \sum_{j=0}^{2N-1} \bar{P}_{nm}(\cos\theta_i) \begin{Bmatrix} \cos \\ \sin \end{Bmatrix} (mj\Delta\lambda) f(\theta_i, \lambda_j) \Delta_{ij} \tag{2-65}$$

where $\Delta\theta = \Delta\lambda = \pi/N$ and the θ_i and λ_j are point values which are centred in each equi-angular grid block. The $\bar{P}_{nm}$ are fully normalized associated Legendre functions, and

$$\hat{C}^{\alpha}_{nm} = \begin{cases} \bar{C}_{nm} & \alpha = 0 \\ \bar{S}_{nm} & \alpha = 1 \end{cases} \tag{2-66}$$

By substituting

$$\mathrm{X}^{nm}_i = \frac{1}{4\pi} \bar{P}_{nm}(\cos\theta_i) \Delta_{ij} \tag{2-67}$$

he simplifies the expression.

He notes that an equi-angular grid is symmetric about the equator and that

$$\begin{aligned} \mathrm{X}^{nm}_i &= \mathrm{X}^{nm}_{N-1-i} \quad n-m \ \ even \\ \mathrm{X}^{nm}_i &= -\mathrm{X}^{nm}_{N-1-i} \quad n-m \ \ odd \end{aligned} \tag{2-68}$$

so that equation 2-65 becomes

$$\begin{aligned} \hat{C}^{\alpha}_{nm} = \sum_{i=0}^{N/2-1} \Bigg(& \mathrm{X}^{nm}_i \left[\sum_{j=0}^{2N-1} \begin{Bmatrix} \cos \\ \sin \end{Bmatrix} (mj\Delta\lambda) f(\theta_i, \lambda_j) \right] \\ & + (-1)^{n-m} \mathrm{X}^{nm}_i \left[\sum_{j=0}^{2N-1} \begin{Bmatrix} \cos \\ \sin \end{Bmatrix} (mj\Delta\lambda) f(\theta_{n-1-i}, \lambda_j) \right] \Bigg) \end{aligned} \tag{2-69}$$

As for other methods, a (fast) Fourier transform becomes the first step. For all $0 \le n, m \le N$, two sums are computed, although the inner sum (the following two equations) is obviously the Fourier transform,

$$\begin{Bmatrix} a_m^i \\ b_m^i \end{Bmatrix} = \sum_{j=0}^{2N-1} \begin{Bmatrix} \cos \\ \sin \end{Bmatrix} (mj\Delta\lambda) f(\theta_i, \lambda_j) \tag{2-70}$$

and

$$\begin{Bmatrix} a_m^{N-1-i} \\ b_m^{N-1-i} \end{Bmatrix} = \sum_{j=0}^{2N-1} \begin{Bmatrix} \cos \\ \sin \end{Bmatrix} (mj\Delta\lambda) f(\theta_{N-1-i}, \lambda_j) \tag{2-71}$$

The second step is to add the contributions of the just-calculated Fourier coefficients with weights from the associated Legendre functions,

$$\hat{C}_{nm}^{\alpha} = \hat{C}_{nm}^{\alpha(i-1)} + K \left[\begin{Bmatrix} a_m^i \\ b_m^i \end{Bmatrix} + (-1)^{n-m} \begin{Bmatrix} a_m^{N-1-i} \\ b_m^{N-1-i} \end{Bmatrix} \right] \mathrm{X}_i^{nm} \tag{2-72}$$

This results in the calculation of all the C_{nm}^{α}.

There are N (fast) Fourier transforms, each of $O(N \log N)$ totalling $O(N^2 \log N)$ operations to be performed. To calculate the $\hat{C}_{nm}^{\alpha}$ terms requires a further N operations, resulting in a total operations count $O(N^3 \log N)$ for the method. Like other methods to be described, certain data values which also require an operations count $O(N^3)$ are computed once and saved for future re-use. The author describes the whole as an $O(N^3)$ algorithm.

The inverse transform is computed in a similar manner, and the number of operations is also $O(N^3)$. The author indicates that K is a proportionality constant. Δ_{ij} is defined as $\Delta\lambda(\cos\theta_i - \cos(\theta_i + \Delta\theta))$, which is the angular area of a surface element.

2.6.3 Driscoll and Healy, Jr.

This is a very brief summary of the method employed by Driscoll and Healy, Jr. to compute spherical harmonic transforms, as described in their paper [Driscoll and Healy 1994]. Their method is said to be exact in exact arithmetic for band-limited functions (i.e. those with a finite number of non-zero Fourier coefficients on the sphere).

They find an appropriate sampling of a function (on the sphere) for which an efficient transform can be developed. The method begins by finding an $O(N(\log N)^2)$ algorithm for the Legendre polynomial transform over $n = 2^k \leq N$ points arranged on an equiangular grid, using a data structure of size $O(N \log N)$. This is extended for the associated Legendre function transform over the sphere, and has the same order of complexity. The

inverse is done in $O(N^{1.5})$ time.

Some function $f(\theta, \lambda)$ is said to be band-limited so that its transform $\hat{f}(l, m) = 0$ if $l \geq b$. If sampled on a grid of points $i = 0, \cdots, 2b-1$, $j = 0. \cdots, 2b-1$ with $\theta_i = \pi i/2b$ and $\lambda_j = \pi j/b$ (notice that there are $2b$ points in both directions), then by weighting the samples of $f(\theta_j)$ by the appropriate a_j given in the following expression, the non-zero Fourier coefficients can be computed from them, and the function f can be recovered exactly. The expression given for the a_j, with n samples being a power of two is,

$$a_j = \frac{2\sqrt{2}}{n} \sin\left(\frac{\pi j}{n}\right) \sum_{l=0}^{n/2-1} \frac{1}{2l+1} \sin\left((2l+1)\frac{\pi j}{n}\right) \qquad j = 0, \cdots, n-1 \tag{2-73}$$

From this is obtained an equation describing the Legendre transform of function f as per[25],

$$\hat{f}(l, m) = \frac{\sqrt{2\pi}}{2b} \sum_{j=0}^{2b-1} \sum_{k=0}^{2b-1} a_j f(\theta_j, \lambda_k) \bar{Y}_l^m(\theta_j, \lambda_k) \tag{2-74}$$

with $l < b$, $|m| \leq l$, $\bar{Y}_l^m = (-1)^m Y_l^{-m}$ and

$$Y_l^m(\theta, \lambda) = (-1)^m \sqrt{\frac{(2l-1)(l-m)!}{4\pi(l+m)!}} P_l^m(\cos\theta) e^{im\theta} \tag{2-75}$$

For synthesis,

$$f(\theta, \lambda) = \sum_{l=0}^{b-1} \sum_{|m|\leq n} f(l, m) Y_l^m(\theta, \lambda) \tag{2-76}$$

Note that the sample count is somewhat confusing in their paper. In the case of the Legendre transform, the maximum degree computed from the n samples is $l < n/2$[26]. That is to say that there are n points along a meridian. Other points around the sphere that make up the equiangular grid mentioned earlier are used to form averages from which the Legendre transform can be computed. For the associated Legendre transform, $2b^2 = n^2$ data points are used, and the maximum degree (and order) computed is $l < b$[27]. Thus $2b = n$, and $l < n/2$.

They also prove that the convolution of two functions on the sphere is the product of their transforms (note that $m = 0$ for function $\hat{g}$).

[25] $\bar{Y}_l^m$ is the complex conjugate.

[26] Lemma 3, page 218.

[27] Theorem 3, page 215.

$$\widehat{(f*g)}_{lm} = 2\pi \sqrt{\frac{4\pi}{2l+1}}\, \hat{f}_{lm} \hat{g}_{l0} \tag{2-77}$$

This is an interesting conclusion as [Blais and Provins 2002, page 32] find that without **geodetic normalization**[28] as described in equation 2-32,

$$\widehat{(f*g)}_{lm} = \frac{4\pi}{2l+1}\, \hat{f}_{lm} \hat{g}_{l0} \tag{2-78}$$

which uses the fact that the Dirac kernel has the expansion $(2n+1)/4\pi$ and thus will preserve a function when convolved with a Dirac.

Note that the filter is axially symmetric (i.e. no change in longitude). Note also that

$$\widehat{(f*g)}_{lm} \neq \widehat{(g*f)}_{lm} \tag{2-79}$$

as convolutions on the sphere do not commute. The dual is indicated as the point-wise product of two functions on the sphere being the 'convolution' of their transforms. This convolution, like the inverse transform can be computed in $O(N^{1.5})$ time.

2.6.3.1 Improvements on the Algorithm

More recently, Healy and associates have re-worked the original algorithm to develop improved inverse and convolution routines. For N sample points, the cost of performing their fast Legendre transform is $O(N(\log N)^2)$, using a pre-computed data structure of $O(N \log N)$. Thus, for a function with harmonics of at most order N, their spherical harmonic transform is computed in $O(N^2(logN)^2)$ operations versus $O(N^3)$ required by direct computation. The performance, however is computer architecture dependent. They reported their work in an internal technical report at Dartmouth College's Department of Computer Science (PCS-TR94-222), and also in [Healy et al. 1998]. The explanation of their algorithm is much better in this paper, compared to that of [Driscoll and Healy 1994].

Healy and associates compared several variations of their algorithm, and found that the theoretically optimal algorithm was slower than several of the others. One caution that they noted in passing was that the storage requirements for the Legendre functions were formidable. For example, in one code, for a bandwidth of $n = 1024$, a pre-computed data structure of some 1.3 GBytes was required for one variation of the base algorithm. Other

[28] With **geodetic normalization** the expression becomes $\widehat{(\bar{f}*\bar{g})}_{lm} = \frac{4\pi}{\sqrt{2l+1}}\, \hat{\bar{f}}_{lm} \hat{\bar{g}}_{l0}$

variations made smaller storage demands, but even so were far too large for holding in commonly available computers. Of particular note is the fact that their codes are available for experimentation. An implementation is available [Moore et al. 1998] for experimental use. Several algorithms are included, and the sampling is done on Chebyshev nodes.

Also of note is the fact that the need for a power of two for the sample count may not be a requirement to use the algorithm. As of this writing, Blais and colleagues have experimented with forward and inverse transforms to degree and order 1024 on a unit sphere that excluded the poles when sampled. The maximum RMS error difference as defined by the square root of the sum of the squares of the differences of the cosine and sine coefficients (after synthesis and re-expansion) are approximately 10^{-12} in magnitude.

2.6.4 Mohlenkamp

[Mohlenkamp 1999] describes a method by which an expansion or synthesis can be accomplished in $O(N^{5/2} \log N)$ or $O(N^2(\log N)^2)$ from an equiangular grid of $2N^2$ points on a sphere. This second method is faster but less accurate than the first. Like the method of Driscoll and Healy, this is an improvement over the $O(N^3)$ operation count of earlier methods. Both methods used pre-computed associated Legendre functions. The calculations are done to a user-specified precision.

One variation that stands out in Mohlenkamp's method is the fact that he employs N Gaussian nodes for his integration along the meridians (and $2N$ points along the parallels). This allows the accurate integration of a polynomial of order $2N$ with only N points and implies that measurements not be made on an equi-angular basis, but at the zeros of the Legendre polynomials.

Like other authors, Mohlenkamp expects the (fast) Fourier transform to dispose of the longitudinal dependence. Doing this incurs $O(N^2 \log N)$ operations and leaves $2N$ problems indexed by $m: -N < m < N$ where for the expansion (i.e. analysis) problem, one computes N coefficients (for each m) $f(\theta_j, m)$. He then finds a way to reduce the problem to the application of matrices, and he takes advantage of the (as)symmetries across the equator ($\theta = \pi/2$) of the $P_{nm}(\cos\theta)$ when $n - m$ is odd versus even. Note that his sample implementation requires that a user add a suitable Fourier transform (such as an FFT) at the appropriate place in his code.

From the solution of certain differential equations (particularly Schrödinger's, which affords an asymptotic solution near the poles) an approximate solution yields an 'instantaneous frequency' that appears to model different values of the $P_{nm}(\cos\theta)$. These functions look like trigonometric functions, and this fact is a motivation behind the 'one-dimensional' algorithm. Mohlenkamp partitions the function and represents it in a localized trigonometric basis (actually, a local cosine basis). This allows the creation of sparse matrices which he says contributes significantly to the speed of the algorithms. The choice of partition (in the actual calculation) is a function of m and n. As the partition changes with n (for fixed m), the matrix adapts.

Like the previous method, Mohlenkamp has provided experimenters with a sample implementation, although it lacks the Fourier transform needed for processing the parallels [Mohlenkamp 2000].

2.6.5 Spherepack

Geophysical processes may be analysed with the **Spherepack** collection of FORTRAN 77 programs, which are publicly available [Adams and Swarztrauber 1997]. Both scalar and vector functions may be decomposed via spherical harmonic transforms. The computation of the required associated Legendre functions is provided, as are any required calculations of Gauss points and weights, or fast Fourier transforms.

The Spherepack collection allows spherical harmonic analysis on both Gaussian grids and equally-spaced grids. The means to transfer data between these two grids is also provided. Spherepack provides an exact harmonic analysis of a scalar function $f(\theta, \lambda)$ on the sphere, providing it is sufficiently smooth. To arbitrary precision, this means that there exists some N so that

$$f(\theta, \lambda) \approx \sum_{n=0}^{N} \sum_{m=0}^{n} P_{nm}(\cos\theta)\left(a_{m,n}\cos m\lambda + b_{nm}\sin m\lambda\right) \qquad (2\text{-}80)$$

where the $P_{nm}(\cos\theta)$ are the associated Legendre functions.

The coefficients (a_{nm}, b_{nm}) are given by the usual expressions for non-normalized values,

$$a_{nm} = \frac{(2n+1)(n-m)!}{2\pi(n+m)!} \int_0^{2\pi} \int_0^{\pi} f(\theta,\lambda) P_{nm}(\cos\theta) \cos m\lambda \sin\theta d\theta d\lambda$$
$$b_{nm} = \frac{(2n+1)(n-m)!}{2\pi(n+m)!} \int_0^{2\pi} \int_0^{\pi} f(\theta,\lambda) P_{nm}(\cos\theta) \sin m\lambda \sin\theta d\theta d\lambda \quad (2\text{-}81)$$

Here, equation 2-80 and equation 2-81 represent the synthesis of a scalar field given its spectrum, and the forward transform, or analysis of a scalar field respectively. Similar expressions may be derived for vector transforms of vorticity and divergence.

Many operations are provided in the collection. For example, the gradient of a scalar field can be computed from a vector field synthesis and the Laplacian of a scalar function can be computed as a suitably scaled synthesis of the original scalar function. All of these functions, and many others are provided by the collection.

For additional background, see [Swarztrauber 1979; Swarztrauber 1993] and [Swarztrauber 1996].

2.7 Various Codes for Legendre Functions and Transforms

FORTRAN code known as the Gathers' Legendre transform is available from the Oakridge National Lab in the USA. It may be acquired for $1300US. It was written in 1977 to run on an IBM 360. Routines in the package calculate the associated Legendre functions of the first kind, indefinite (multiple) integrals involving the Legendre polynomials, derivatives of the Legendre polynomials, spherical harmonic functions, and an expansion of an arbitrary (single valued) function. Other code to compute Legendre functions is available through Lawrence Livermore National Labs[29]. A set of FORTRAN codes to evaluate various Legendre functions or polynomials with real or complex arguments, some with derivatives and others with integrals is also available[30].

Codes attributed to **GNU** are available[31] and they are part of the GNU Scientific Library which is also available[32]. Other codes[33] allege to use extended range arithmetic (i.e. a combination of integer and float to represent numbers).

[29] ftp://ftp-icf.llnl.gov/pub/Yorick/doc/html_i/legndr_i.html

[30] http://iris-lee3.ece.uiuc.edu/~jjin/routines/routines.html

[31] http://www.computing.ethz.ch/sepp/gsl-1.1.1-mo/gsl-ref_122.html

[32] http://www.computing.ethz.ch/sepp/gsl-1.1.1-mo/gsl-ref.html#SEC_Top

[33] http://sunsite.univie.ac.at/statlib/cm/doc/fcnpak/archive

Reiji Suda of Nagoya University proposed the development of a fast spherical harmonic transform of time order $O(T^2 \log T)$ when at the Fields Institute, University of Toronto [Suda 2001]. In his IPSJ[34] abstract dated June 2001, and a second dated July, 2002 he indicated the use of ultra-spherical polynomials for the associated Legendre transform. The proposed method would run theoretically with computational complexity of $O(N^2 \log^2 N)$. He felt that this approach would be a better tradeoff between computational complexity and memory requirements than the direct method (of order $O(N^3)$). He published an algorithm [Suda and Takami 2002] and made two sample implementations (FORTRAN 90 and FORTRAN 77) available from his personal website[35]. Note that his website, which offers an online test system, only promises the precision of the transform in the 2-norm to be about 10^{-10}.

At NCAR is the library of routines known as **ALFPACK**, developed by Swarztrauber[36]. A complete list of his publications, many of which are available electronically including those cited earlier, are also available online[37].

Synthesis codes are available from Blais at the University of Calgary[38]. These are made up of two C programs, first of which reads a set of ASCII-formatted spherical harmonic coefficients and writes them out as a binary-formatted file. The second program reads this file, makes the appropriate geodetic normalization corrections and synthesizes the geoid undulation.

Other synthesis codes have been developed at the Ohio State University's Department of Geodetic Science and Surveying. See for example [Rapp 1982] which synthesizes to degree and order 180. Subsequent codes were extended to higher degrees, some of which are being used for experimentation with the weights described in [Driscoll and Healy 1994] by Blais and associates.

Finally, cosmic microwave background anisotropy researchers are now using fast spherical harmonic transforms thanks to the development of the **HEALPix** pixelization scheme for the sphere. The transforms are said to be slower than the Mohlenkamp routines as they scale asymptotically as $O(N^{3/2})$, but owing to the method of discretization used, they

[34] Information Processing Society of Japan

[35] http://www.na.cse.nagoya-u.ac.jp/~reiji/

[36] See ftp://ftp.ucar.edu/dsl/lib/alfpack/ and the README therein.

[37] http://www.scd.ucar.edu/css/staff/pauls/papers/

[38] http://www.ucalgary.ca/~blais/

deal with smaller datasets for the same degree and order. Sample codes which are available[39] are described in [Górski, Hivon, and Wandelt 1998; Hivon and Górski 1998; Wandelt et al. 1998]. See also [Bond et al. 1999] and [O'Mullane et al. 2001] for additional information. HEALPix and its use in this study are described in the sequel.

2.8 Notes on Using FFT´s, Public Codes and Power Spectra

Various codes were investigated during the course of this research, and C implementations were effected for several. As might be expected, the results were varied. Techniques were investigated to greater or lesser detail depending on this writer's available time and interest. The following comments briefly summarize some of the interesting findings.

During the course of early research, an $O(N^3)$ synthesis program was written using both simple coefficient multiplication and addition initially, then a discrete Fourier transform, and later fast Fourier transforms (FFTs). Obviously the latter implementation was superior in terms of speed, but all three codes were written so as to verify the correctness of the others. In addition, as certain derivatives were required for an investigation to be described in a later chapter, the writer had no choice but to write them as other codes known to the writer did not provide the required facilities. This program then provided the basic facility described in equation 2-33 (repeated here for convenience),

$$f(\theta,\lambda) = \sum_{n=0}^{\infty}\sum_{m=0}^{n}\left[\bar{a}_{nm}\bar{R}_{nm}(\theta,\lambda) + \bar{b}_{nm}\bar{S}_{nm}(\theta,\lambda)\right] \tag{2-82}$$

plus the addition of northward and eastward derivatives of the synthesized function.

The relationship between the summation implied in equation 2-82 and the Fourier transform was described in [Blais and Provins 2003]. Summarizing the expressions for a finite sum to N, the equation was re-written by swapping the n and m summations as per,

[39] http://www.eso.org/science/healpix/index.html

$$
\begin{aligned}
f(\theta,\lambda) &= \sum_{m=0}^{N}\left\{\left(\sum_{n=m}^{N}\bar{a}_{nm}\bar{P}_{nm}(t)\right)\cos m\lambda + \left(\sum_{n=m}^{N}\bar{b}_{nm}\bar{P}_{nm}(t)\right)\sin m\lambda\right\} \\
&= \sum_{m=0}^{N}\left\{A_m(\theta)\cos m\lambda + B_m(\theta)\sin m\lambda\right\} \\
&= \frac{1}{2}\sum_{m=0}^{N}\left\{(A_m(\theta)+iB_m(\theta))e^{-m\lambda} + (A_m(\theta)-iB_m(\theta))e^{+m\lambda}\right\} \\
&= \mathrm{Re}\Big[\,DFT(A_m(\theta)+iB_m(\theta))\,\Big]
\end{aligned}
\tag{2-83}
$$

with symbol 'Re' denoting the real part, and DFT indicating the discrete Fourier transform. [Rummel 1997] reached a similar conclusion when examining the expansion of the disturbing potential.

When introducing the fast Fourier transform, it is important to note that as one is computing a real function on the sphere, then the products of the $a_{mm}P_{nm}(t)$ and $b_{nm}P_{nm}(t)$ must have their imaginary components above the Nyquist flipped in sign[40]. Failure to make the correction results in an inaccurate synthesis. [Kanasewich 1981, page 45]

The second thing to note when employing the fast Fourier transform is that the energy of the spectrum is spread across both positive and negative frequencies. Thus the products mentioned in a previous paragraph must be so distributed before invoking an FFT. In other words, one half the energy in the fundamental, plus all its harmonics except for the Nyquist must be in the positive frequency set, and one half must be in the negative frequency set. As the DC and Nyquist frequencies are even functions, they are unaffected.

A final consideration when using publicly available codes is that the internal scale factors may not be the same between codes, and and will almost certainly provide results different from the geodetic formulation in equation 2-33. For example, tests with the Driscoll and Healy implementation on axially symmetric functions on the sphere suggested a correction factor of $2\sqrt{\pi}$. On the other hand, using Spherepack with the same dataset implied a correction of $2\sqrt{2}$. Martin Mohlenkamp's code, again with the same dataset had a scale factor of $\sqrt{2}$. Fortunately, for the latter two codes, the inverse and forward procedures were consistent.[41] The scale factors derived for each of these codes were those needed to correct for a geodetic normalization.

[40] Because of the circularity of FFTs, negative frequencies typically appear after the Nyquist. They are the complex conjugates of the positive frequencies for real data sequences.

[41] The Driscoll and Healy algorithm has been extensively tested by Blais' group.

For the purposes of this research, selected FORTRAN routines from the **Spherepack** package were interfaced to C. As indicated, corrections were needed when this code was used to synthesize geodetic coefficients generated by other programs. This was due to differences in normalization between **Spherepack** and those used in geodetic contexts. The corrections required are shown in **Table 2-1**.

Spherepack Corrections for Synthesis of Geodetic Data

Order	Coefficient	Correction
0	all	$*\,2\sqrt{2}$
1↔n	real	+2
	imaginary	–2

Table 2-1: *When synthesizing a set of coefficients computed by normal geodetic software, Spherepack must have products, sums or difference corrections applied to obtain the correct result.*

There are several descriptions of spherical harmonic spectra and their normalization. [Kaula 1966, page 98] defined the term **degree variance** or $\bar{\sigma}_n^2$, to describe the variances arising from the variations of the Earth's gravitational field, as per

$$\bar{\sigma}_n^2 = \sum_{m=0}^{n} \left[\bar{a}_{nm}^2 + \bar{b}_{nm}^2 \right] \tag{2-84}$$

Based on Kaula's definition, at least two definitions of **power spectra** were then given by subsequent authors. Those known to this writer, and used to illustrate items of interest in the sequel, were given by, [Wong et al. 1971, page 6231] and [Pollack 1973] Their respective definitions were[42]:

$$\begin{aligned} Power_n &= \frac{\bar{\sigma}_n}{\sqrt{2n+1}} \qquad Wong\ et\ al. \\ &= \bar{\sigma}_n \sqrt{2n+1} \qquad Pollack \end{aligned} \tag{2-85}$$

Both of these employ normalized coefficients in the geodetic sense. Pollack's has the unique characteristic that for point sources at the surface, which obviously would produce a singularity, the spectrum is uniform, just as the spectrum for a Dirac delta function is uniform. Example spectra for both normalization methods are illustrated in **Figure 2-1**.

[42] While these authors called $\bar{\sigma}_n$ a power spectrum for degree n, it might be more appropriate to call it an amplitude spectrum because of the square root.

EGM96 is shown to degree 100 and to degree 360. The normal field has been removed.

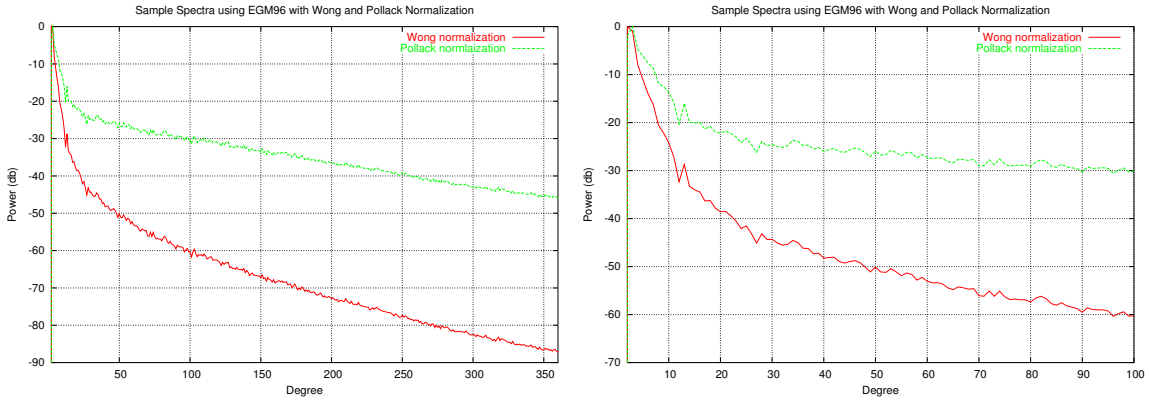

Figure 2-1: *Both Wong and Pollack's normalization of the corrected geopotential model EGM96 are illustrated. On the left, the field to degree 360 is shown, and on the right, the first 100 degrees are shown.*

2.9 Requirements for Wavelet Analysis

In order to implement the wavelet analysis technique which will be described in a later chapter, certain expressions involving spherical harmonics in a geodetic context were required. This section covers that material, which is in addition to the computational requirements coded in accordance with the material already described in this chapter.

The fundamental expression for the potential is indicated in [Pollack 1973], and also in [Heiskanen and Moritz 1966, page 59 and page 107] as that given in equation 4-1 and is repeated here for convenience.

$$V(r,\theta,\lambda) = \frac{GM}{r}\left\{1 - \sum_{n=1}^{\infty}\sum_{m=0}^{n}\left(\frac{a}{r}\right)^{n}\left[\bar{a}_{nm}\bar{R}_{nm}(\theta,\lambda) + \bar{b}_{nm}\bar{S}_{nm}(\theta,\lambda)\right\}\right. \qquad (2\text{-}86)$$

with θ as colatitude, λ as longitude, r as the spherical Earth radius (for surface measurements) or the radius at which measurements are taken (for an elevated surface), and a as the radial distance to the model body. This is the potential exterior to the sphere containing the source. It has units of work or energy (distance in metres times acceleration).

The gravitational vector is the radial derivative of equation 2-86, providing the directions of the normals for the reference surface and the anomalous surface are nearly coincident. This is the standard assumption for a spherical approximation and the expansion of the

disturbing potential [Heiskanen and Moritz 1966, section 2-14]. Because the same assumption is made for Pollack's models, then the vector magnitude will be given by the following equation which has units of acceleration in metres per second squared[43].

$$\begin{aligned} g &= -\frac{\partial V}{\partial r} \\ &= -\frac{GM}{r^2}\left[1 - \sum_{n=1}^{\infty}\sum_{m=0}^{n}(1+n)\left(\frac{a}{r}\right)^n\left[\bar{a}_{nm}\bar{R}_{nm}(\theta,\lambda) + \bar{b}_{nm}\bar{S}_{nm}(\theta,\lambda)\right]\right] \end{aligned} \tag{2-87}$$

The upward continuation of g is a straightforward computational exercise. The calculation of the two dimensional horizontal gradient is accomplished by calculating the changes to the gravity vector from that implied by a centred spherical source.

For the anomalous potential of the Earth, how the geoidal surface differs from the ellipsoid is described by [Heiskanen and Moritz 1966, page 112] as the change in the undulation divided by the change in arc length along the ellipsoid. This is the same as the change in the tangent along a curved surface, as described in [Protter and Morrey 1964, page 60].

For the wavelet transform of gravitation, a similar requirement exists. Specifically, the gradient of the gravity vector is needed, and this is given as the change in the magnitude of the gravity vector over some arc length, as per

$$\varepsilon = -\frac{dg}{ds} \tag{2-88}$$

In this case, g is the value of the gravitational field for the given potential, and $ds = Rd\theta$ is the arc length for some angular change of colatitude $d\theta$, and nominal radius R. The gradient is expressed in terms of latitude (ϕ) and longitude (λ) as,

$$\begin{aligned} \delta_N &= -\frac{1}{R}\frac{\partial g}{\partial \phi} \\ \delta_E &= -\frac{1}{R\cos\phi}\frac{\partial g}{\partial \lambda} \end{aligned} \tag{2-89}$$

Note that $d\phi = -d\theta$ and that $\cos\phi = \sin\theta$ in the following. Note also that as the expressions in equation 2-89 are taken with respect to the latitude, then this implies that the gravity has been described in terms of latitude, or rather that the associated Legendre functions are given in those coordinates. A simple calculation shows that the derivative of these functions with respect to colatitude is minus that of the derivative with respect to

[43] Acceleration measured in m/sec^2 corresponds to 100 cm/sec^2 or 100 gals (1 gal = 1 cm/sec^2).

latitude.

Thus the gradients become,

$$\begin{aligned} \textit{Eastward} \quad \delta_E &= -\frac{1}{r\cos\phi}\frac{\partial g}{\partial \lambda} \\ &= -\frac{1}{r\sin\theta}\frac{\partial g}{\partial \lambda} \\ &= -\frac{1}{\sin\theta}\frac{GM}{r^3}\sum_{n=1}^{\infty}\sum_{m=0}^{n}(1+n)\left(\frac{a}{r}\right)^n\left[\bar{a}_{nm}(-m)\sin(m\lambda)+\bar{b}_{nm}(m)\cos(m\lambda)\right]\bar{P}_{nm}(t) \end{aligned} \tag{2-90}$$

and

$$\begin{aligned} \textit{Northward} \quad \delta_N &= -\frac{1}{r}\frac{\partial g}{\partial \phi} \\ &= \frac{1}{r}\frac{\partial g}{\partial \theta} \\ &= -\frac{GM}{r^3}\sum_{n=1}^{\infty}\sum_{m=0}^{n}(1+n)\left(\frac{a}{r}\right)^n\left[\bar{a}_{nm}\cos(m\lambda)+\bar{b}_{nm}\sin(m\lambda)\right]\frac{\partial \bar{P}_{nm}(t)}{\partial \theta} \end{aligned} \tag{2-91}$$

Note that the eastward gradient has no meaning at the poles owing to the $\sin^{-1}\theta$ term, not to mention that the poles are single valued anyway. Notice also that this gradient has the dimensions of acceleration per unit distance. The derivative required in the previous expression for the North gradient is given by the recursions noted earlier.

Note that there is no derivative that can be calculated at $\theta = k\pi, k = 0, 1$ using any previously mentioned recursion. However, there is a simple recursion for certain values at those locations, with all others being zero. The specific $P_{nm}(\cos\theta)$ for which the derivatives are non-zero are, and the obvious recursion is given in **Table 2-2**.

The recursion for the normalized derivatives is (with starting value $\bar{P}'_{11}(\cos\theta) = \sqrt{3}$),

$$\bar{P}'_{n1}(\cos\theta) = \bar{P}'_{n-1\ 1}(\cos\theta)(-1)^{n\delta_{180,\theta}}\sqrt{\frac{(2n+1)(n-1)}{(2n-1)(n+1)}} \tag{2-92}$$

Also required was the magnitude of the gradient of gravitation. This is just the root of the summed squares,

$$\begin{aligned} M &= \sqrt{\delta_{N^2_{\theta,\lambda}} + \delta_{E^2_{\theta,\lambda}}} \\ &= \frac{GM}{r^3}\sqrt{E^2_{\theta,\lambda} + \frac{N^2_{\theta,\lambda}}{\sin^2\theta}} \end{aligned} \tag{2-93}$$

Values for $\mathbf{P'_{nm}}(\cos\theta)$ at the Poles

Degree (n)	$\theta = 0$	$\theta = \pi$
0	0	0
1	1	-1
2	3	3
3	6	-6
4	10	10
5	15	-15
n	$n + P'_{n-1\ m}(\cos 0)$	$-1^{\delta_{1,(n\%2)}}(n + P'_{n-1\ m}(\cos 0))$

Table 2-2: *A simple recursion for the derivatives of the $P_{nm}(\cos\theta)$ at the poles. The symbol % is a shorthand expression for modulus (i.e. the remainder function).*

where the terms $E_{\theta,\lambda}$ and $N_{\theta,\lambda}$ are the summations of the coefficients described in equation 2-91 and equation 2-90.

For completeness, note that the azimuth of the vector resulting from the combination of the northward and eastward gradients is the usual arctangent function, as per

$$D = \tan^{-1}\left[\frac{N_{\theta,\lambda}}{\sin\theta E_{\theta,\lambda}}\right] \tag{2-94}$$

With these mathematical tools, one can explore the efficacy of the wavelet transform approach as a means to uncover the Earth's structure.

2.10 Requirements for Geopotential Inversion

For inverting geopotential fields directly, there is a requirement for the continuation of the field and for expressing density variations as derived from the measured field. This section develops the equations necessary to downward continue the measured anomalous geopotential field to an arbitrary depth. in such a manner that the density variation of a shell of arbitrary thickness may be determined.

There is a theorem by Chasles, which is also known as **Green´s equivalent layer** [Heiskanen and Moritz 1966; Ramsey 1961], that says that any Newtonian potential V on an equipotential surface S will be the same as that of a surface layer of density μ,

$$\mu = \frac{-1}{4\pi G}\frac{\partial V}{\partial n} \tag{2-95}$$

where the partial derivative is taken with respect to the normal n [Heiskanen and Moritz 1966]. Furthermore, using Gauss' theorem the amount of matter contained within S is given by,

$$\iint_S \mu dS = \iiint_v \rho dv \tag{2-96}$$

Pail used the surface layer technique to consolidate all of the mantle into a single surface feature in order to reduce the amount of numerical work that he incurred. He concluded that the coefficients for the mantle with mean density $\bar{\rho}$ could be derived from the potential measured at radius R by placing the surface layer at some radius $\tilde{r} < R$. He quotes the following expression for surface layer density as a function of surface potential coefficients $\{\bar{a}_{nm}, \bar{b}_{nm}\}$ [Pail 1999, p. 18; MacMillan 1930],

$$\begin{bmatrix} \mu^{(c)}_{nm}(\tilde{r}) \\ \mu^{(s)}_{nm}(\tilde{r}) \end{bmatrix} = \frac{(2n+1)\bar{\rho}R}{3}\left(\frac{R}{\tilde{r}}\right)^{n+2}\begin{bmatrix} \bar{a}_{nm} \\ \bar{b}_{nm} \end{bmatrix} \tag{2-97}$$

where in the sequel, these will be given as $\bar{\mu}_{nm}(\tilde{r}) = \{\bar{\mu}^{(c)}_{nm}(\tilde{r}), \bar{\mu}^{(s)}_{nm}(\tilde{r})\}$. This equation implies the surface density layer coefficients are downward continued versions of the coefficients at measurement radius.

His alternate expression for a shell of known thickness relates the geopotential coefficients observed at radius R scaled to compute potential at some radius $r > R$, and downward continued to depth, to the equivalent density contrast coefficients for a shell of thickness $r_b - r_a$ as,

$$\begin{bmatrix} \bar{a}_{nm} \\ \bar{b}_{nm} \end{bmatrix} = \frac{3}{(2n+1)\bar{\rho}R^{n+3}}\int_{r_a}^{r_b}\begin{bmatrix} \bar{\rho}^{(c)}_{nm}(r') \\ \bar{\rho}^{(s)}_{nm}(r') \end{bmatrix} r'^{n+2} dr' \tag{2-98}$$

where in the sequel, these will be given as $\bar{\rho}_{nm}(r') = \{\bar{\rho}^{(c)}_{nm}(r'), \bar{\rho}^{(s)}_{nm}(r')\}$. This equation indicates that the coefficients observed at the measurement radius are upward continued versions of the coefficients due to the radially-dependent density.

Pail derived his expressions by use of a certain 'well-known' relation (see page 8 of his thesis, and its use on pages 14 and 18), quoted here as,

$$\frac{1}{\bar{R}_{nm}(\theta,\lambda)}\int_{\lambda'=0}^{2\pi}\int_{\theta'=0}^{\pi}\frac{\bar{R}_{nm}(\theta',\lambda')}{l}\,r'\sin\theta' d\theta' d\lambda' = \frac{4\pi}{2n+1}\left(\frac{r'}{R}\right)^{n+1} \qquad (2\text{-}99)$$

where $\bar{R}_{nm}(\theta,\lambda)$ corresponds to $\bar{P}_{nm}(\cos\theta)[\cos m\lambda + \sin m\lambda]$ (with a similar expression for $\bar{R}_{nm}(\theta',\lambda')$), l is the spherical distance between two points separated by angle α at radii r' and R, given as $l = \sqrt{r'^2 + R^2 - 2r'R\cos\alpha}$ and $r' < R$. This may be derived as follows (using $\bar{R}'_{nm}$ to represent $\bar{R}_{nm}(\theta',\lambda')$, $\bar{R}_{nm}$ to represent $\bar{R}_{nm}(\theta,\lambda)$ and σ as $\sin\theta d\theta d\lambda$, and quoting the relevant equations from [Heiskanen and Moritz 1966]).

$$\begin{aligned}
\frac{1}{\bar{R}_{nm}}\iint_{\sigma'}\bar{R}'_{nm}\frac{r'}{l}\,d\sigma' &= \iint_{\sigma'}\frac{1}{\bar{R}_{nm}}\bar{R}'_{nm}\left[\sum_{p=0}^{P}\sum_{q=0}^{p}\frac{1}{2p+1}\left(\frac{r'}{R}\right)^{n+1}\bar{R}_{pq}\bar{R}'_{pq}\right]d\sigma' && \textit{eqn. 1-83', page 33}\\
&= \sum_{p=0}^{P}\sum_{q=0}^{p}\frac{1}{2p+1}\left(\frac{r'}{R}\right)^{p+1}\iint_{\sigma'}\frac{\bar{R}'_{nm}}{\bar{R}_{nm}}\bar{R}_{pq}\bar{R}'_{pq}\,d\sigma' &&\\
&= \frac{1}{2n+1}\left(\frac{r'}{R}\right)^{n+1}\frac{R_{nm}}{R_{nm}}\iint_{\sigma'}\bar{R}'_{nm}\bar{R}'_{nm}\,d\sigma' && \textit{eqn. 1-68, page 29} \quad (2\text{-}100)\\
&= \frac{1}{2n+1}\left(\frac{r'}{R}\right)^{n+1}4\pi && \textit{eqn. 1-74, page 31}\\
&= \frac{4\pi}{2n+1}\left(\frac{r'}{R}\right)^{n+1} &&
\end{aligned}$$

One can deduce Pail's expressions for arbitrary and surface layer density distributions from the following. In addition to the expressions for $\bar{R}_{nm}$ and $\bar{R}'_{nm}$ above, let $\bar{C} = \{\bar{a}_{nm}, \bar{b}_{nm}\}$ be the measured coefficients.

$$\begin{aligned}
V(r,\theta,\lambda) &= \frac{GM}{R}\sum_{n=0}^{\infty}\sum_{m=0}^{n}\left(\frac{R}{r}\right)^{n+1}\bar{C}\bar{R}_{nm}\\
&= G\int_0^{2\pi}\int_0^{\pi}\int_{r_a}^{r_b}\frac{\rho(r',\theta',\lambda')}{l}\,r'^2\sin\theta' d\theta' d\lambda' dr'
\end{aligned} \qquad (2\text{-}101)$$

Let the density at arbitrary level r' be expanded into spherical harmonic coefficients as,

$$\rho(r',\theta',\lambda') = \sum_{n=0}^{\infty}\sum_{m=0}^{n}\bar{\rho}_{nm}(r')\bar{R}'_{nm} \qquad (2\text{-}102)$$

Inserting the expression for the expansion of $\rho(r',\theta',\lambda')$ into the second expression in equation 2-101, yields,

$$V = G \int_0^{2\pi} \int_0^{\pi} \int_{r_a}^{r_b} \sum_{n=0}^{\infty} \sum_{m=0}^{n} \frac{\bar{\rho}_{nm}(r')}{l} \bar{R}'_{nm} r'^2 \sin\theta' d\theta' d\lambda' dr' \tag{2-103}$$

Re-arranging terms and then inserting equation 2-99 gives

$$\begin{aligned} V &= G \int_{r_a}^{r_b} \sum_{n=0}^{\infty} \sum_{m=0}^{n} \bar{\rho}_{nm}(r') r' \left\{ \int_0^{2\pi} \int_0^{\pi} \bar{R}'_{nm} \frac{r'}{l} \sin\theta' d\theta' d\lambda' \right\} dr' \\ &= G \int_{r_a}^{r_b} \sum_{n=0}^{\infty} \sum_{m=0}^{n} \bar{\rho}_{nm}(r') r' \left\{ \frac{4\pi \bar{R}_{nm}}{2n+1} \left(\frac{r'}{R} \right)^{n+1} \right\} dr' \\ &= \frac{4\pi G}{R^{n+1}} \sum_{n=0}^{\infty} \sum_{m=0}^{n} \frac{1}{2n+1} \int_{r_a}^{r_b} \bar{\rho}_{nm}(r') r'^{n+2} dr' \bar{R}_{nm} \end{aligned} \tag{2-104}$$

Equating this to the first expression in equation 2-101, gives,

$$\frac{GM}{R} \left(\frac{R}{r} \right)^{n+1} \bar{C} = \frac{4\pi G}{(2n+1)R^{n+1}} \int_{r_a}^{r_b} \bar{\rho}_{nm}(r') r'^{n+2} dr' \tag{2-105}$$

For the potential V measured at $r = R$, and setting mass $M = \frac{4\pi R^3 \bar{\rho}}{3}$ (where $\bar{\rho}$ is the mean density to radius R), with re-arrangement results in

$$\bar{C} = \frac{3}{(2n+1)\bar{\rho}R} \int_{r_a}^{r_b} \bar{\rho}_{nm}(r') \left(\frac{r'}{R} \right)^{n+2} dr' \tag{2-106}$$

which with a re-arrangement of terms is equation 2-98. For the case where no integration is required because all mass is assumed to lie on the surface $\tilde{r}$,

$$\bar{C} = \frac{3}{(2n+1)\bar{\rho}R} \left(\frac{\tilde{r}}{R} \right)^{n+2} \mu_{nm}(\tilde{r}) \tag{2-107}$$

which when inverted is

$$\mu_{nm}(\tilde{r}) = \frac{(2n+1)\bar{\rho}R}{3} \left(\frac{R}{\tilde{r}} \right)^{n+2} \bar{C} \tag{2-108}$$

is equation 2-97.

In the case at hand, the anomalous potential on the surface of the sphere is expressed in spherical harmonic coefficients T_{nm}. The analysis undertaken within this research will show that when properly normalized, publicly available geopotential fields indicate that the mid to upper mantle may be described by layers of mass anomalies. Given Chasles

theorem, it seems reasonable that a surface layer density analysis might indicate the area distribution of non-point source mass anomalies.

The anomalous potential can be expanded for an arbitrary radius r outside of the masses contributing to that potential (see **Figure 2-2**) by [Heiskanen and Moritz 1966, page 88],

$$T(r,\theta,\lambda) = \sum_{n=0}^{\infty} \left(\frac{R}{r}\right)^{n+1} T_n(\theta,\lambda) \tag{2-109}$$

where $T_n(\theta,\lambda)$ is the Laplace surface harmonic of degree n,

$$T_n(\theta,\lambda) = \sum_{m=0}^{n} \bar{a}_{nm}\bar{R}_{nm}(\theta,\lambda) + \bar{b}_{nm}\bar{S}(\theta,\lambda) \tag{2-110}$$

This can be re-written in terms of the coefficients at radius r and those at radius R, as per,

$$T_{nm,r} = \left(\frac{R}{r}\right)^{n+1} T_{nm,R} \tag{2-111}$$

which indicates that the coefficients at $r > R$, are scaled versions of those at radius $r = R$.

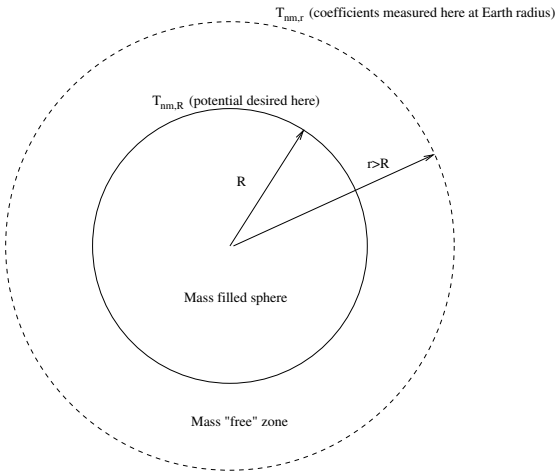

Figure 2-2: *Within the Earth radius shown here as r, at which the anomalous potential was measured, a mass-filled sphere is located (with radius R).*

Thus if one measured $T(r,\theta,\lambda)$ at some radius $r > R$, where R was the radius just enclosing the mass contributing to $T(r,\theta,\lambda)$, then the coefficients are known at $r = R$, as per,

$$T_{nm,R} = \left(\frac{r}{R}\right)^{n+1} T_{nm,r} \tag{2-112}$$

A justification for this in terms of convolutions on the sphere may be found in [Blais and Provins 2002].

For the purpose of this research, the portions of **EGM96** which correspond to individual anomalous zones, or layers indicating that substantial anomalous mass is to be found, are examined in the light of both surface layer density and radially constant shell density anomalies.

For the case of a surface layer at depth, one must correct the measured anomalous geopotential coefficients for the appropriate depth, and then compute the surface layer density that would create that field. Suppose that the layer in question was at $R < R_E$ (i.e. at some radius less than the nominal Earth radius). Then the coefficients that would be measured for masses within that radius would be as described in the extended Meissl scheme [Rummel 1997],

$$\bar{D} = \left(\frac{R_E}{R}\right)^{n+1} \bar{C} \tag{2-113}$$

where $\bar{D}$ indicates a set of coefficients which are downward continued versions of $\bar{C}$, as per equation 2-112.

Inserting $\bar{D}$ as the representative coefficient set for depth $R < R_E$ in equation 2-101 through to equation 2-107, computing the surface layer density in terms of $\bar{D}$, and then re-introducing $\bar{C}$ produces the following result.

$$\bar{D} = \frac{3}{(2n+1)\bar{\rho}R}\left(\frac{\tilde{r}}{R}\right)^{n+2} \mu_{nm}(\tilde{r}) \tag{2-114}$$

Therefore,

$$\begin{aligned} \bar{C} &= \frac{3}{(2n+1)\bar{\rho}R}\left(\frac{\tilde{r}}{R}\right)^{n+2}\left(\frac{R}{R_E}\right)^{n+1} \mu_{nm}(\tilde{r}) \\ &= \frac{3\tilde{r}}{(2n+1)\bar{\rho}R^2}\left(\frac{\tilde{r}}{R_E}\right)^{n+1} \mu_{nm}(\tilde{r}) \end{aligned} \tag{2-115}$$

or when inverted,

$$\mu_{nm}(\tilde{r}) = \frac{(2n+1)\bar{\rho}R^2}{3\tilde{r}}\left(\frac{R_E}{\tilde{r}}\right)^{n+1} \bar{C} \tag{2-116}$$

with $\bar{C}$ being the coefficients measured at R_E. Note that $\bar{\rho}$ is the mean density of the

sphere with radius R. This expression gives the surface layer density at an arbitrary radius $\tilde{r}$ less than the radius R which contains the masses. Obviously, if $\tilde{r} = R$, then the expression reduces to

$$\mu_{nm}(R) = \frac{(2n+1)\bar{\rho}R}{3}\left(\frac{R_E}{R}\right)^{n+1}\bar{C} \tag{2-117}$$

meaning the relevant coefficients from the surface measurements, downward continued to the desired depth can be converted to an equivalent surface layer of density $\mu_{nm}(R)$. By relevant coefficients is meant that set of coefficients most likely to have contributed to the zone of interest.

For the case of a shell of masses, equation 2-106 when expressed in terms of a downward continued set of geopotential coefficients results in

$$\begin{aligned}\bar{C} &= \frac{3}{(2n+1)\bar{\rho}R}\left(\frac{R}{R_E}\right)^{n+1}\int_{r_a}^{r_b}\bar{\rho}_{nm}(r')\left(\frac{r'}{R}\right)^{n+2}dr' \\ &= \frac{3R_E}{(2n+1)\bar{\rho}R^2}\int_{r_a}^{r_b}\bar{\rho}_{nm}(r')\left(\frac{r'}{R_E}\right)^{n+2}dr'\end{aligned} \tag{2-118}$$

Assuming that the density in the shell varies laterally and not radially yields,

$$\bar{C} = \frac{3R_E\bar{\rho}_{nm}}{(2n+1)\bar{\rho}R^2}\int_{r_a}^{r_b}\left(\frac{r'}{R_E}\right)^{n+2}dr' \tag{2-119}$$

or when inverted,

$$\bar{\rho}_{nm} = \frac{(2n+1)\bar{\rho}R^2}{3R_E\int_{r_a}^{r_b}\left(\frac{r'}{R_E}\right)^{n+2}dr'}\bar{C} \tag{2-120}$$

Letting $r_b = R$ be the upper limit of integration, and $\bar{\rho}$ is the mean density of the shell, results in,

$$\bar{\rho}_{nm} = \frac{(2n+1)(n+3)\bar{\rho}(R/R_E)^2}{3\left[\left(\frac{R}{R_E}\right)^{n+3} - \left(\frac{r_a}{R_E}\right)^{n+3}\right]}\bar{C} \tag{2-121}$$

This equation describes the spherical harmonic coefficients for a shell of thickness $R - r_a$ at radius R. These coefficients indicate a variable density and are derived directly from

the measured coefficients for a spherical Earth of radius R_E. Obviously, this is an invertible expression. That one is a function of the other is an important relationship. Clearly, if one knows what portion of the spectrum is strongly correlated with what depth, then the Earth's internal structure will be revealed in a manner not seen before.

2.10.1 Comments on Geopotential Inversion

The geopotential fields (EGM96, GEMT1, CHAMP) employed in this research are publicly available. They have been corrected for the effect of angular rotation, and include all normal corrections for topography, isostasy etc. For the purpose of this research, no additional corrections were required. The addition of higher resolution spectrum, say from topography, may prove to be useful for more detailed analysis of surface features, but this was not done.

In the chapter following the wavelet experiments, these fields were employed in two ways. In the first case, attempts were made to compute anomalous mass magnitudes using the fields in a global least squares inversion. Synthetic tests indicated that this would be possible under certain conditions, but these could not be guaranteed, nor could the instability of the process be overcome in a satisfactory manner. The alternative was to employ equation 2-121 once a satisfactory depth estimate had been made. The method became quite simple: interpret the spectrum as a series of anomalous layers having identifiable depths, and then use that equation to make density contrast estimates. Depth, thickness and spectral interpretation were the controlling parameters.

The steps for these experiments were as follows:

1 Normalize and display the spectrum in the manner to be described.

2 Interpret the spectrum as a series of layers at likely depths, based on a point source assumption, and subject to certain limitations also to be described.

3 For the case of identifiable anomaly inversion, compute the potential corresponding to the spectral components for the interpreted depth and identify anomaly extrema.

4 Given anomaly locations and depth, populate the normal equations and invert for mass magnitude.

5 For the case of variable shell density, use equation 2-121 with the spectral components for the interpreted depth to estimate density contrast.

3 Wavelets

3.1 Introduction

In an early attempt to achieve the primary objective, the use of wavelets was investigated. It was hoped that the use of a *signal processing* approach to potential field analysis might prove to be beneficial in this regard[44]. Accordingly, continuous, discrete and orthogonal wavelet approaches were studied. Finally an indirect approach to applying an analyzing wavelet to the gravitational field was considered.

This latter method might be called the Poisson kernel wavelet method. It is based on deriving an analyzing wavelet from the Poisson kernel, which itself is a smoothing function that satisfies desirable properties. It is an indirect method because at no time does one apply a specific wavelet, such as those to be described in the sequel; nevertheless, a wavelet based on sound physical principles, and one which has the property of identifying desirable features in the original data, is applied.

This chapter begins with some background on Fourier analysis to set the stage. By means of examples, each of the wavelet techniques mentioned earlier is described. The chapter closes with the description of the technique which promised to indicate not only the shape of a buried structure, but also to indicate the depth to such a body. It was the latter attribute of primary interest in this research.

The discussion in this chapter will not be a thorough, or exhaustive description, but should provide the reader with sufficient background for a following chapter.

3.2 Fourier Analysis

Signal analysis in its traditional form has involved the use of Fourier transforms which resulted from the work of Jean Baptiste Joseph Fourier who lived from 1768 to 1830. It was Fourier, who in his study of the theory of heat shortly after 1800, first expanded an arbitrary function as a series based on sinusoids [O'Connor and Robertson 1997]. Although not received well by his contemporaries, his development in this regard has withstood the test of time, and still enjoys widespread use. Useful reviews of Fourier techniques may be found in various publications, including the following small sampling [Blais 1988; Blais 1997; Carslaw 1930; Gonzalez and Wintz 1987; Kanasewich 1981;

[44] Wavelets are used in many areas, including data compression, matrix simplification, data combination, filtering and geophysical analysis.

Kay and Marple 1981; Marple 1987; Papoulis 1962; Priestley 1981; Robinson 1967], or [Oppenheim and Schafer 1975].

3.2.1 Periodic Functions

A function periodic in an interval T, which is expressible as

$$f(t) = f(t + nT) \quad n = 0, \pm 1, \pm 2, \cdots \tag{3-1}$$

can be expressed in terms of basis functions ($\vec{e}_n$) that are themselves periodic in an interval T [Kaiser 1994], as per

$$f_N = \frac{1}{T} \sum_{-N}^{N} c_n e_n \tag{3-2}$$

where e_n are basis vectors given by [Kanasewich 1981],

$$e_n(t) = e^{in\omega_0 t} \tag{3-3}$$

with $n\omega_0 = 2\pi n/T$, $n = 0, \pm 1, \pm 2, \cdots$. Such basis functions are more than orthogonal as through their inner product, one can see that they are also orthonormal (within the period T).

$$\langle e_n, e_m \rangle = T\delta_{nm} \tag{3-4}$$

As a result, the c_n terms may be computed by means of the inner product of the basis functions and the arbitrary function f_N, as per

$$c_n = \langle e_n, f_N \rangle_T = \int_{t_0}^{t_0+T} f_N(t) e^{-in\omega_0 t}\, dt \tag{3-5}$$

In the limit, $f_N \to f_\infty$ and,

$$|f|_T^2 = \frac{1}{T} \sum_{-\infty}^{\infty} |c_n|^2 \tag{3-6}$$

Given that the period of the function is T, then the result is a spectral expansion of f from the fundamental frequency $f_0 = 1/T$ to an upper limit based on the length T and the number of samples contained therein. T can be arbitrarily long, including an interval which is of infinite length. In other words, any function can be considered to be periodic if its support (i.e. non-zero length) equals the period.

The spectral lines so generated are multiples of the fundamental, meaning that the

decomposition is in terms of f's harmonic content. Each 'line' is an indication of the contribution that frequency makes to the overall energy in the period.

This analysis is highly beneficial for signal analysis and other purposes, as it has the capability of capturing frequency information in an entire dataset, and presenting it together. Thus it provides for a general analysis of frequency content over a fixed time interval. It has the disadvantage of not being selective in time. For example, it is not possible to determine if two signals occur simultaneously within a period, or are separated in time, both having occurred within the same period.

Fourier's spectral decomposition demonstrated that any periodic motion could be represented as a combination of simple harmonic functions. His transformation of a signal can be seen as the weighted contributions of sinusoidal functions which when summed will result in the reconstruction of a time (or spatial) domain signal. It is ideal for the analysis of stationary signals; but for those signals whose statistical characteristics vary with time, one requires a transformation which is time dependent, or just as non-stationary as the signal being analysed. Dennis Gabor proposed such an analysis tool in the late 1940's, the Short Time Fourier Transform (**STFT**) [Gabor 1946].

The windowed or short time Fourier transform of which Gabor's is one example, was intended to overcome the limitation of Fourier's more general transform. It was an attempt to provide insight into the properties of a signal as a function of both location and frequency. This was done by performing a Fourier analysis on the convolution of a window and the original dataset. Because the window had compact support, meaning that it was zero outside of some defined bounds, the resulting analysis provided insight into the local spectral properties of the signal.

3.2.2 Uncertainty

However, there was still some 'vagueness' in the analysis. Specifically, the desired localization in both time and frequency was not quite attainable. This is a result of requiring one full period of any signal in order to establish that the time signal contains that frequency. For a window of length T, the lowest frequency recognizable corresponds to $1/T$, with higher frequencies recognized up to $f_{Nyquist}$, that value being dependent on the sample rate. Large windows have good frequency resolution, but poor time resolution (i.e. event time localization). Short windows have improved time resolution, but poorer frequency resolution.

This poorly determined state is similar to that referred to as Heisenberg's uncertainty principle developed in 1927 [Schiff 1968]. The general condition is that the product of the time width of the window and its bandwidth is a constant which is lower bounded [Rioul and Vetterli 1991],

$$\Delta f \Delta t \geq \frac{1}{4\pi} \tag{3-7}$$

This then is the caveat with the windowed or short time Fourier transform. In effect, it is that if the windowed Fourier transform is used to analyse a signal containing frequencies having more than one cycle in the window (i.e. signal features shorter than the window length), then the analysis is underlocalized in time. In other words, like the general Fourier transform, one doesn't know when a feature occurred, just that it did occur. Similarly, if such a transform is used to analyse a signal containing events with a length longer than the analysis window, it is said to be overlocalized in time. Such events cannot be resolved by the transform.

In either case, the windowed Fourier transform (at least for a fixed length window) is inappropriate if used without altering the window length. It has difficulty dealing with local behaviour. As indicated, the balance between time and frequency resolution is controlled by the window function. One requires a scale independent transformation to deal with such behaviour. The wavelet transform is a tool that provides such a facility.

3.3 Continuous Wavelet Transforms

A scale independent transformation is one whose analyzing function offers high resolution for high frequencies and correspondingly appropriate resolution for low frequencies. While, the Fourier basis functions $e^{i\omega t}$ have very high frequency locality, and they are also orthogonal, it is the purview of wavelets to offer similar characteristics with the proviso of also offering scale dependent resolution.

A single wavelet function defines a family of wavelets by dilating and translating itself over the continuum of all possible values. Such functions are said to be *mother wavelets* or *analyzing functions*. Their stretching in time corresponds to a contraction in bandwidth, with translations corresponding to phase shifts, as might be expected. When used to transform a signal f, the resulting magnitude describes how much f is like the translated and dilated analyzing function. For most choices of analyzing wavelet g, an inverse is possible providing several requirements are met [Teolis 1998]:

- Every function f should be represented as a linear combination of dilated and translated versions of g over a large enough space of interest
- Each function should be recoverable from a knowledge of the inner products $\langle f, D_t D_s g \rangle$ where D_t indicates translation (t) and D_s the amount of dilation (s) of g
- The analyzing function g must have zero mean.

A function $\psi \in L^2(\mathcal{R})$[45] is defined as a wavelet if it fulfils the **admissibility condition**, meaning that it has finite energy [Mallat 1989b, p. 2097],

$$0 < c_\psi = 2\pi \int_{-\infty}^{\infty} \frac{|\hat{\psi}(\omega)|^2}{|\omega|} d\omega < \infty \tag{3-8}$$

and based on this definition, the **wavelet transform** as originally introduced by [Goupillaud et al. 1984] for seismic signal analysis, is given by

$$W(f)(s,t) = \frac{1}{\sqrt{c_\psi}} \frac{1}{|s|^{1/2}} \int_{-\infty}^{\infty} f(u) \psi\left(\frac{u-t}{s}\right) du \tag{3-9}$$

for $s \in \mathcal{R} \setminus \{0\}, t \in \mathcal{R}$[46]. The term s is known as the scale, while t is the amount of translation of the wavelet operator. Note that this expression is simply a convolution with a scaled operator (see for example **Figure 3-1**), which could be re-written as,

$$W(f)(s,t) = \frac{1}{\sqrt{c_\psi}} f * \psi_{st} \tag{3-10}$$

where

$$\psi_{st} = \frac{1}{|s|^{1/2}} \psi\left(\frac{u-t}{s}\right) \tag{3-11}$$

The inverse is given as [Daubechies 1992],

$$f(u) = \frac{1}{\sqrt{c_\psi}} \int_{\mathcal{R}} \int \psi\left(\frac{u-t}{s}\right) W(f)(s,t) \frac{dsdt}{s^2} \tag{3-12}$$

From these statements, one concludes that a wavelet has zero mean (because $c_\psi < \infty$) and hence it must oscillate. As well, because $\psi \in L^2(\mathcal{R})$, then ψ decays to zero at some point

[45] ψ is indicated to be a member of the set of square integrable functions over the space of reals.

[46] The expression $s \in \mathcal{R} \setminus \{0\}$ means that s exists in the space of all reals, with the exception of the value zero.

making it a wave of finite length (i.e. compact support), or a 'wavelet'.

Unlike the short time Fourier transform, the denominator in the expression of ψ in equation 3-9 indicates that the envelope function (containing the aforementioned oscillations) changes shape as the factor s, or scale, changes in magnitude. As s shrinks in magnitude, the width of ψ declines so that the frequency of oscillation increases, implying improved resolution at higher frequencies. It follows that scale changes affect a wavelet's spectrum with larger scales implying narrower spectra.

For example, for the **Mexican Hat wavelet**, defined as the second derivative of a normal distribution function,

$$\psi(t) = (1 - t^2)e^{-t^2/2} \tag{3-13}$$

the effect of scaling at five versus unity is illustrated in **Figure 3-1** following. Note that [Kumar and Foufoula-Georgiou 1997] show the Mexican Hat wavelet with the coefficient $2/\sqrt{3}\pi^{-1/4}$. See also **Figure 3-2** which illustrates a Mexican Hat wavelet at multiple scales and the corresponding spectra.

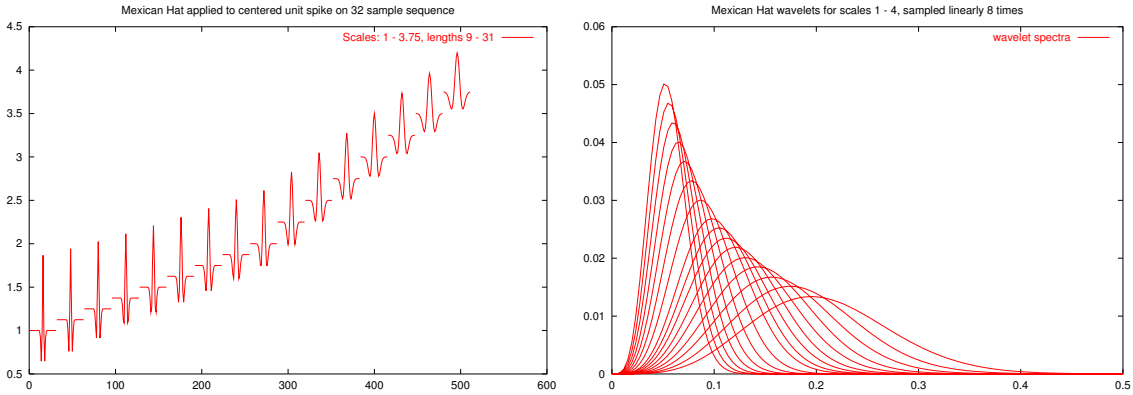

Figure 3-2: *A Mexican hat wavelet applied to a centred unit spike on a 32 sample dataset is shown (left). From left to right the wavelet increases in length, and decreases in overall amplitude. The position of the wavelet as it is presented from left to right results from the addition of the effective scale value to the result of the convolution. The lengths range from 9 to 31 samples, and the actual amplitudes range from 0.867 (bottom left) to 0.45 (top right). On the right are the corresponding spectra.*

An alternative is the **Morlet wavelet** given as

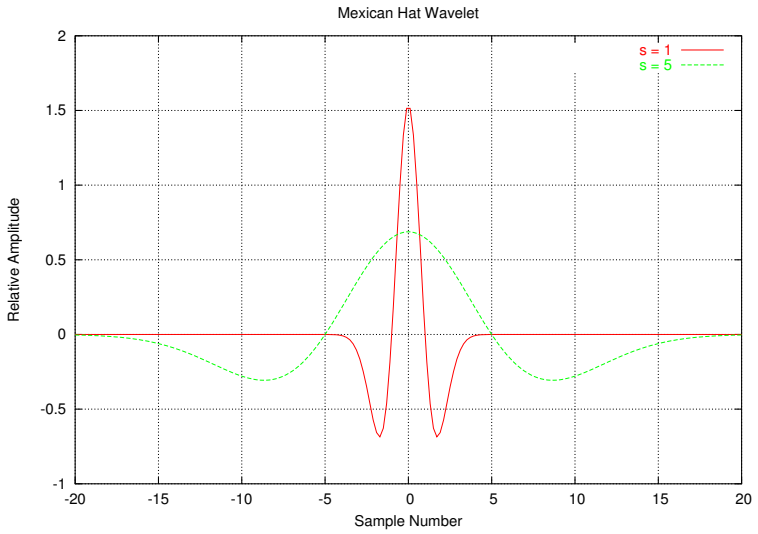

Figure 3-1: *A Mexican Hat wavelet with scale factor set to 1 and to 5. A large scale factor increases the length of the wavelet thus accommodating larger features. Smaller scale factors resolve finer features. Note that the amplitude of the scaled wavelet increases with smaller scale factors, implying constant wavelet energy.*

$$\psi(t) = \frac{1}{\sqrt{2\pi}} e^{-t^2/2} e^{-i\omega_o t} \tag{3-14}$$

which has the spectrum [Starck 2002],

$$\hat{\psi}(\omega) = e^{-2\pi^2(\omega-\omega_0)^2} \tag{3-15}$$

This wavelet has the advantage of being complex. This allows the determination of event phase as well as amplitude, a feature lacking in the symmetric Mexican Hat wavelet. Examples of Morlet wavelets for the same scales as before may be seen in **Figure 3-3**. Note that complexity may also be viewed as a disadvantage in that the computational requirements are doubled. Of course if fast Fourier transforms are employed, this additional cost is ameliorated.

There are several formulations for the Morlet wavelet. Another, from [Teolis 1998] gives the formula as:

$$\psi(t) = \frac{1}{\sqrt{\pi\gamma_{BW}}} e^{i2\pi\gamma_{CF}t-(t^2/\gamma_{BW})} \tag{3-16}$$

where γ_{BW} is the bandwidth and γ_{CF} is the centre frequency. The L_1 norm of $\psi(t)$ is

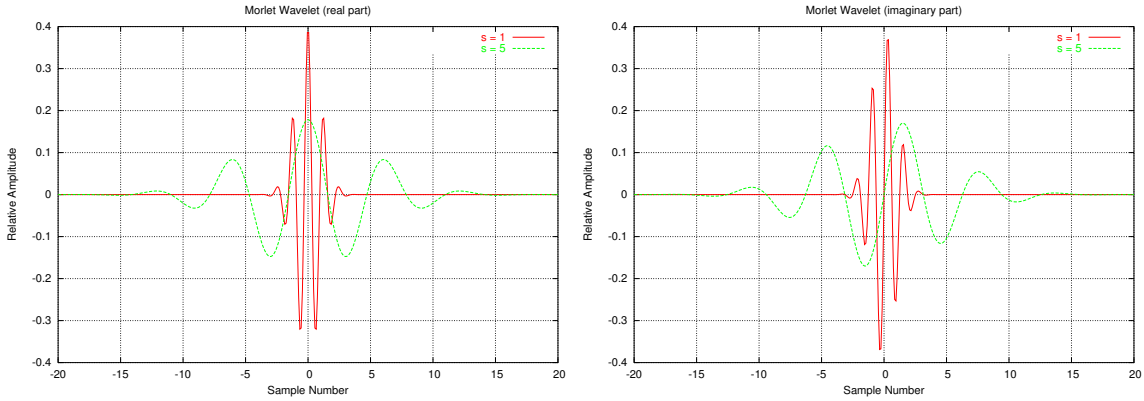

Figure 3-3: *The real part of a Morlet wavelet at scales one and five (left) versus the imaginary part (right).*

---

unity, and as a result, its Fourier transform has its maximum value (1) at γ_{CF}. Teolis notes that the Fourier transform of a Morlet wavelet is

$$\hat{g}_{Morlet}(\gamma) = e^{-\pi^2 \gamma_{BW}(\gamma-\gamma_{CF})^2} \tag{3-17}$$

The zero mean requirement is not satisfied for a Morlet wavelet, but he indicates that by choosing the product $\gamma_{BW} \cdot \gamma_{CF}^2$ large enough, the mean can be made arbitrarily small. The mean is unimportant if the signals being analyzed are in L^1 over $\mathcal{R}$, and have a zero mean.

The article by [Kumar and Foufoula-Georgiou 1997] shows the Morlet wavelet as

$$\psi(t) = \pi^{-1/4} e^{-i\omega_0 t} e^{-t^2/2} \qquad \omega_0 \geq 5 \tag{3-18}$$

Other wavelet examples, also from [Teolis 1998] are

- **frequency B-spline wavelet** given as

$$g_m(t) = (\gamma_{BW}/m)^{(1/2-m)} e^{i2\pi\gamma_{CF}t} \left(\frac{\sin\left(\frac{\pi\gamma_{BW}t}{m}\right)}{\pi t} \right)^m \qquad m = 1, 2, 3, \cdots \tag{3-19}$$

  These are simply B-splines designed in the frequency domain.

- **Shannon wavelet** given as

$$g_{Shannon}(t) = \gamma_{BW}^{-1/2} e^{i2\pi\gamma_{CF}t} \frac{\sin(\pi\gamma_{BW}t)}{\pi t} \tag{3-20}$$

Teolis notes that as the envelope of this wavelet is a sinc function, it has poor $1/t$ time decay.

3.4 The Discrete Wavelet Transform

In order to implement a continuous wavelet transform, it must be discretized. This creates the so-called **discrete wavelet transform** which can be implemented numerically. In the forward case, a single integral (equation 3-9) must be evaluated, and for the inverse case, a double integral with its additional cost must be computed (equation 3-12). Given that digitally, one is limited to discrete values on a grid (i.e. $G = \{(s_0^m, nt_0) | m, n \in \mathcal{Z}\}$[47]), with $s_0 > 1$ a fixed dilation step and $t_0 > 0$ a fixed start time, the question of invertability arises. Can the original signal $f(u)$ be completely represented by the following discrete basis functions?

$$\psi_{mn}^{(s_0,t_0)}(\bullet) = s_0^{-m/2}\psi(s_0^{-m}\bullet - nt_0) \tag{3-21}$$

The answer is that inversion is in fact possible, providing the wavelet basis functions $\psi_{mn}^{(s_0,t_0)}(\bullet)$ have certain properties. They must form what is called a **frame**, which implies that a bounded inverse operator exists [Kumar and Foufoula-Georgiou 1997].

By a suitable choice of scale and translation values, generally those which correspond to a dyadic analysis, the coefficients resulting from the transform indicate the intensity of the signal f at the scale s_0^m in the vicinity of time $nt_o s_0^m$. They provide similarity information about the discretized signal. Providing the so-called *frame* requirements are met, the inverse is guaranteed. Partial inversions or inversion with modified coefficients can be useful when studying specific aspects of a process as the effects of factors such as noise or interfering signals can be reduced.

One example of a discretized continuous wavelet transform is shown in **Figure 3-4**. A Mexican Hat wavelet is applied to a dataset similar to that found in [Mallat 1997]. The dataset which is shown at the bottom of the figure has been biased negatively to offset it from the result of the analysis. The scales employed were 1, 2, 4 and 8, with intermediate scalings known as **voices**[48]. A suitable number of voices per octave of analysis has the effect of meeting the frame requirements for inversion. If the most stringent frame needs are not met, then the wavelet coefficients are correlated over a neighbourhood which

[47] The term $\mathcal{Z}$ indicates the field of all integers.

[48] A 'voice' is an intermediate scaling of the analyzing wavelet. As typical scales are related by dyads (i.e. separated by factors of two, or octaves) a 'voice' would have some value between the current and next scale value.

tends to improve the resolution of sharp features in an analysis [Kumar and Foufoula-Georgiou 1997, page 393].

Different mechanisms are used when applying continuous wavelet transforms to discrete data. Some researchers employ zero padding as is commonly done for fast Fourier transforms, some assume periodicity, and others force the data to appear mirrored at the boundaries [Mallat 1997].

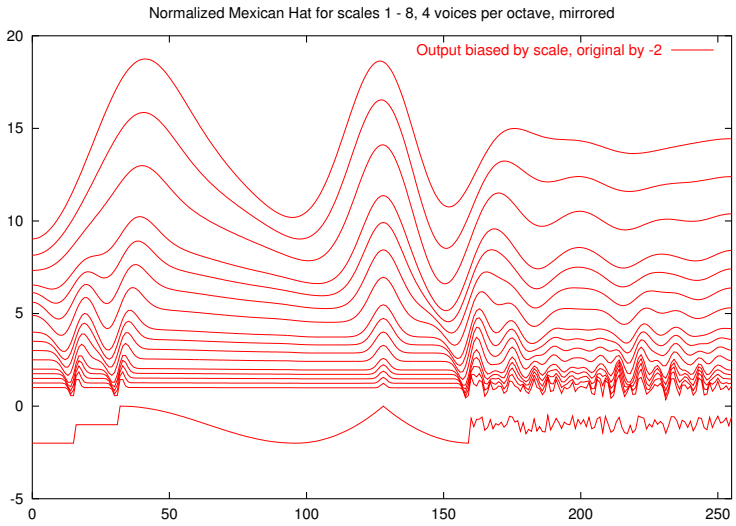

Figure 3-4: *A Mexican Hat is applied to the lower dataset (biased by -2). Each scale and voice (4 per octave) is biased by the effective scale factor to create the display. The data were mirrored about the endpoints.*

3.5 Multiresolution Analysis

Multiresolution analysis (**MRA**) is the technique of going from one resolution to another by building an image pyramid of a function represented in space or time.

In general, multiple resolutions can mean different colours, scale, time or other factors which make for different sets of observations [Blais 1997]. Multiple resolutions allow zooming in for enhanced information extraction. The detail required depends on the specific requirement.

Any equispaced data can be analyzed, placed into a pyramid or made into an orthonormal set (meaning that different coverages can be decoupled). Combinations of equispaced sequences can be made and varying scales of images can be synthesized. Data series can

be assimilated into processes. This means that everything relevant to a process can be extracted. Such an analysis can act as an aid in understanding a process, or can facilitate further processing of a dataset [Kumar and Foufoula-Georgiou 1997]. As indicated earlier, other applications include digital signal and image coding or compression. Some inverse problems with ill-conditioning can be handled. Wavelet transforms are information preserving, just as Fourier transforms are [Blais 1996].

As in many analyses, the objective of a multiresolution analysis is to approximate some signal $f \in V_0$[49] by some new signal $\bar{f} \in V_{-1}$ with minimal approximation error. The error is carried in the orthogonal space W_{-1}.

One can represent the projection as a Boolean sum,

$$f = P_0 f \oplus Q_0 f \tag{3-22}$$

This corresponds to a low pass smoothing step ($P_0 f$) and a high pass filtering step ($Q_0 f$) with a decimation of the result. One can represent the space V_0 by

$$V_0 = V_{-1} \oplus W_{-1} \tag{3-23}$$

The smoothing and filtering can be repeated again (and again ...) as per,

$$\begin{aligned} f &= (P_0 \oplus Q_0) f \\ &= (P_1 \oplus Q_1) P_0 f \oplus Q_0 f \\ &= P_1 P_0 f \oplus Q_1 P_0 f \oplus Q_0 f \end{aligned} \tag{3-24}$$

Pictorially, this looks like **Figure 3-5**. The definition of a multiresolution analysis is a nested sequence of spaces, as described in [Teolis 1998, page 92] is given by

$$L^2(\mathcal{R}) \supset \cdots \supset V_1 \supset V_0 \supset V_{-1} \supset \cdots \supset \{0\} \tag{3-25}$$

This says that there is a sequence of nested subspaces V_k which increase in resolution as k increases. These spaces contain improved representations of some function f with increasing k. The change in resolution will be uniform if the spaces are related by consistent dilation factors (usually two).

This is an MRA if several conditions are satisfied:

1 There must exist some function ϕ called a **scaling function** (sometimes called a **smoothing function**) which by integer translates, will form an orthonormal basis

[49] The symbol V is used in the context of an MRA to denote a space. While in the context of Newtonian potential the same symbol is used, there should be little chance of confusion.

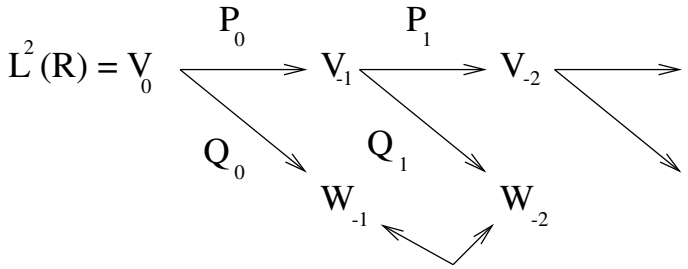

Figure 3-5: *Repeated application of projections onto subspaces of preceding superspaces shows repeated smoothing (into spaces V_{-n}) and loss of information (into spaces W_{-n}).*

---

for f in a subspace V_k. Only one basis function is required for each space, and they are related as per [Mallat 1989a],

$$\phi_{2^j}(\bullet) = 2^j \phi(2^j \bullet) \quad \forall j \in \mathcal{Z} \tag{3-26}$$

Thus if $\phi(\bullet)$ is a basis for V_0, then $\phi_{2^j}(\bullet)$ is a basis for V_{2^j}. An alternative definition from [Mallat 1997, page 225] is

$$\phi_{jn}(\bullet) = \sqrt{2^{-j}}\,\phi(2^{-j}(\bullet - n)) \quad \forall j \in \mathcal{Z} \tag{3-27}$$

where the family $\{\phi_{jn}\}_{n \in \mathcal{Z}}$ is an orthonormal basis of $V_j \ \forall j \in \mathcal{Z}$.

2 The union of the spaces is dense in $L^2(\mathcal{R})$,

$$\overline{\bigcup_{m \in \mathcal{Z}}} V_m = L^2(\mathcal{R}) \tag{3-28}$$

3 The spaces are independent of each other,

$$\bigcap_{m \in \mathcal{Z}} V_m = \{0\} \tag{3-29}$$

4 If signal $f(\bullet) \in V_0$, then dilating by 2^m will place it in V_m (i.e. $f(2^m \bullet) \in V_m$). All spaces of an **MRA** are scaled versions of the base space V_0.

5 [Chui 1992] adds a fifth condition[50], that being that $V_{j+1} = V_j \oplus W_j$, $j \in \mathcal{Z}$ where W_j is the orthogonal complement of V_j. He also points out an intrinsic property of wavelet spaces, which says that more and more variations of the projection of f (i.e. $P_j f$) are removed as $j \to -\infty$.

[50] Note that which space is subordinate to which sometimes is reversed in equation 3-25. [Mallat 1989a] shows the boolean sum as indicated here, but in [Mallat 1997] it is reversed.

Any set of vector spaces $V_{2j},\ j \in \mathcal{Z}$ satisfying these properties is said to form a multiresolution approximation of $L^2(\mathcal{R})$ [Mallat 1989a]. Implementation details for multiresolution filter specification are given, for example, in this latter paper, or more recently in [Keller 2000].

As indicated in equation 3-22, there are two aspects to an **MRA**. One smoothes by application of a low pass filter, and one highlights detail with a high pass filter. The smoothing step results in the ability to visualize a process at some resolution. In fact, each resolution is a scaled version of the base space V_0 (condition 4 above). What has been removed and set aside is the result of the filtering step at the preceding resolution.

If a function $f_m(t)$ is the representation of $f(t)$ at resolution m, then to get the function at the next higher resolution, one need only add that which was removed, as per

$$f_{m+1}(t) = f_m(t) \oplus f_m^{'}(t) \tag{3-30}$$

where $f_m^{'}(t)$ is the detail removed to obtain the 'view' of $f(t)$ at resolution m. The smoothed version of $f(t)$ at resolution m is computed by the action of a **smoothing function** ϕ upon $f(t)$ at the desired resolution, with $f_m(t)$ represented in terms of that function by,

$$f_m(t) = \sum_{n=-\infty}^{\infty} c_{mn}\phi_{mn}(t) \tag{3-31}$$

with

$$\phi_{mn}(t) = 2^{-m/2}\phi(2^{-m}t - n) \tag{3-32}$$

and coefficients computed by[51],

$$c_{mn} = \int_{-\infty}^{\infty} f(t)\phi_{mn}^{*}(t)dt \tag{3-33}$$

By contrast, the detail that has been removed is described by a weighted sum of orthogonal wavelets ($\Psi_{mn}(t)$), as per

$$f_m^{'}(t) = \sum_{n=-\infty}^{\infty} d_{mn}\psi_{mn}(t) \tag{3-34}$$

with the coefficients defined by,

[51] Shown here is the inner product of a function with the complex conjugate of the smoothing function. Typically, real wavelets and smoothing functions are used.

$$d_{mn} = \int_{-\infty}^{\infty} f(t)\psi_{mn}^{*}(t)dt \tag{3-35}$$

Often this detail is derived from a wavelet which is the first derivative of the smoothing function. A good example is the Haar wavelet described in a later section.

Examples of the application of smoothing and detail removal can be seen in **Figure 3-11** and **Figure 3-12**. The first shows the detail removed from successive applications of the wavelet, and the second shows the remainder which is the equivalent of applying the smoothing function at each of the scales illustrated.

3.5.1 Application and Results

A multiresolution analysis can be implemented in one or more directions. The decomposition is performed via quadratic mirror filters [Blais 1996], that is filters (H, a low pass smoothing filter, and G, a high pass detail recovery filter) that satisfy the condition that

$$H^{*}H + G^{*}G = I \tag{3-36}$$

where H and G and their transposed complex conjugates correspond to the conjugate mirror filter pair (in spectral response) [Mallat 1989a],

$$\begin{aligned} H(\omega) &= \sum_{n=-\infty}^{\infty} h(n)e^{-in\omega} \\ G(\omega) &= e^{-i\omega}H^{*}(\omega+\pi) \end{aligned} \tag{3-37}$$

This defines the filter pair (in time/space response).

$$g(n) = (-1)^{1-n}h(1-n) \tag{3-38}$$

with $g(n)$ being the high pass filter corresponding to $G(\omega)$. The filters h and g correspond to the smoothing and wavelet (detail) functions ϕ and ψ respectively. The bandwidth of the filters is approximately equal to $[-\pi, 0] \bigcup [0, \pi]$ for h and $[-2\pi, -\pi] \bigcup [\pi, 2\pi]$ for g in V_0 and $[-2^{-j}\pi, 0] \bigcup [0, 2^{-j}\pi]$ for h and $[-2^{-j+1}\pi, -2^{-j}\pi] \bigcup [2^{-j}\pi, 2^{-j+1}\pi]$ for g in subspace V_{2^j} [Mallat 1989a].

The relationship of the filters g and h to the detail and smoothing functions is [Li 1996a; Mallat 1997, pp. 228, 239],

$$\phi(x) = \sqrt{2}\sum_{n=-\infty}^{\infty} h(n)\phi(2x-n) \tag{3-39}$$

with

$$h(n) = \int_{-\infty}^{\infty} \phi(x)\phi(2x-n)dx \quad and \qquad \sum_{n=-\infty}^{\infty} h^2(n) = 1 \tag{3-40}$$

and

$$\psi(x) = \sqrt{2} \sum_{n=-\infty}^{\infty} g(n)\phi(2x-n) \tag{3-41}$$

with g defined as in equation 3-38 above.

In one dimension they act on a data sequence via,

$$\begin{aligned} H \cdot \{x_1, \cdots x_n\} &= \{r_1, \cdots, r_{n/2}\} \\ G \cdot \{x_1, \cdots x_n\} &= \{s_1, \cdots, s_{n/2}\} \end{aligned} \tag{3-42}$$

Reconstruction occurs under the mapping,

$$H^* \cdot \{s_1, \cdots s_{n/2}\} + G^* \cdot \{r_1, \cdots r_{n/2}\} = \{x_1, \cdots x_n\} \tag{3-43}$$

with '*' denoting the conjugate transpose.

The process is as follows

1 apply the low and high pass filters to the current sequence

2 decimate the result of the both filter operations by discarding every second sample, setting aside the decimated high pass result and creating a new sequence from the decimated low pass result

3 repeat the first two steps until decimation is no longer possible

Note that the effect of the low pass filter is to reset the bandwidth of the sequence to a lower value than the original sequence had. In this case it would be halved. Once the highest frequency is at one half the original Nyquist frequency, the data can be decimated without loss of information. Then the process can be repeated. For the data processed with the high pass filter, the bandwidth is also halved. Thus it too can be decimated without loss of information.

The process is similar to averaging, and then subtracting the average from the original to get the residual. The trend or low frequency component leads to data pyramids, and the

high pass detail leads to the wavelet transform. This procedure allows one to work at a resolution which is appropriate for the task. It also allows one to do some separation of signal (trend) and noise (residual).

Application of such filters results in a smooth approximation of the original signal, plus the residuals remaining at each step. So, for some signal S_0, application of a multiresolution analysis would result in

$$S_0 \rightarrow \left[S_k, R_k, R_{k-1}, \cdots R_2, R_1 \right] \tag{3-44}$$

Here S_k is the smooth function remaining after k smoothing operations, or applications of the low pass filter. The $R_i, i = 1, 2, \cdots, k$ are the residuals remaining at each step of the analysis. This is illustrated pictorially in **Figure 3-6**.

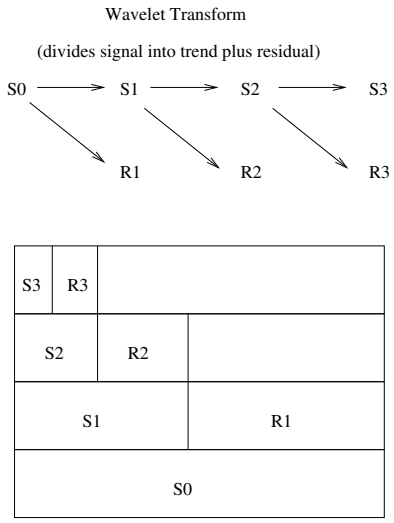

Figure 3-6: *The multiresolution wavelet transform is a method of separating the trend from the residual, using the previous trend as input to the next trend/residual estimate. The result is a vector comprised of the final trend component, plus the preceding residuals. The number of components in the whole is the same as the original vector length. Note that the final result is (as indicated in the text) the sequence* $\{S3, R3, R2, R1\}$.

A similar series of operations can be applied to two dimensional data. In this case, the filters are applied in both directions to decompose the original dataset into quadrants, one of which is then further decomposed, and so on. Pictorially, this looks like the illustration in **Figure 3-7** which shows a single step of decomposition. For the two dimensional case,

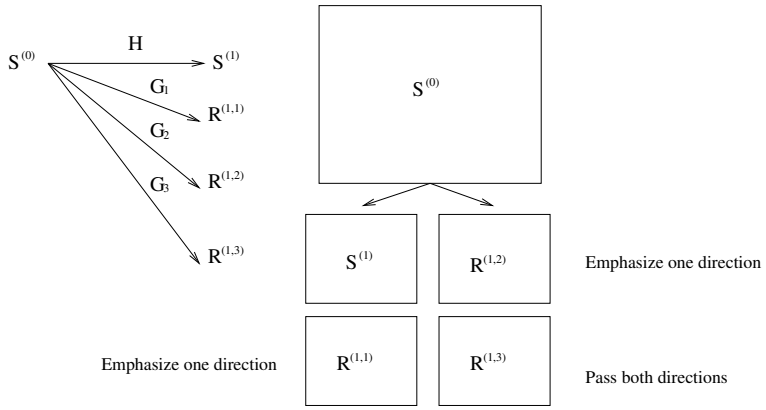

Figure 3-7: *A single step of a two dimensional decomposition is illustrated before (top) and after (bottom) application of multiresolution filter operators. The signal at the next lower resolution, or smoothed image, is seen in the northwest corner. The southwest corner has horizontal (vertical) emphasis; the northeast corner has vertical (horizontal) emphasis and the southeast corner shows both directions. The four smaller rectangles 'replace' the original signal after the single step. A succeeding step would be applied to the new 'signal'.*

---

a more concrete example is the following illustration **(Figure 3-8**) which shows the perspective view of a simple dataset made up of several unit height boxes one of which is surrounded by a fence, all of which lie upon a uniform background. After applying a single step of a Haar two dimensional transformation, the right hand side of the figure results. A miniature version of the original set of structures may be seen in the lower left hand corner, with the expected residuals in the other three corners.

Of particular note in **Figure 3-8** is the fact that there are many zero and near zero values remaining after even a single step in a multiresolution analysis. Data compression and numerical analysis algorithms can take advantage of this characteristic to afford *acceptable* answers for problems of considerable magnitude.

Unfortunately, while a multiresolution analysis is a useful tool for compression, or the simplification of numerical algorithms, it has the property of shrinking the spatial extent of anomalous features when used as a tool for say indexing image[52] databases. This property is inherent in the analysis of the data remaining at each succeeding step, as the

[52] Any two dimensional datasets could be indexed in this manner. The term *image* is being used loosely in this context.

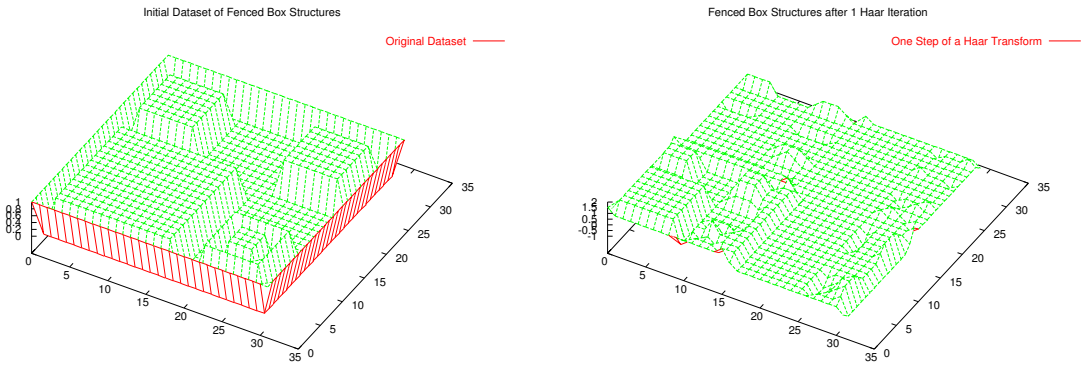

Figure 3-8: *A perspective view of a two dimensional dataset used to illustrate a Haar transform is shown on the left. A matching perspective view of a single step of the two dimensional transform applied to the first dataset is shown on the right. As indicated in* **Figure 3-7***, the 'signal' occupies only one quarter of the original image's space.*

---

smoothed image is always reduced in size compared to the original data sequence. This smoothing of the original dataset is much like viewing the original at increasingly greater distances; detail is lost to the eye, as the dataset shrinks in size. This is a normal feature of a multiresolution analysis.

It can be argued that this is entirely correct, but one could also argue that with a suitable microscope, the image size need not shrink. Such an imaginary device would allow an observer to better appreciate the effect of detail removal, or in other words, more clearly comprehend the increasingly gross structural aspects of a dataset.

The following illustrations show how one could establish context for features large and small. They are generated by expanding the coefficients, which were computed during the multiresolution analysis, in terms of the relevant basis functions at the appropriate level of detail[53]. There are two examples: both are for the one dimensional case, with one showing the detail removed at each scale, and the other illustrating the degradation of the smoothed data as the detail is removed. They clearly show varying levels of detail at the original, or unaltered scale. For reference see [Press et al. 1992].

Figure 3-9 illustrates the gravity response over the **Orphan Knoll**, a geological feature

[53] These basis functions were computed by performing inverse transforms on unit vectors, one for each desired basis function. Each basis function corresponds to one level of detail.

found in the Labrador Sea. It was examined by [Zhang 1993] in his PhD research. The model shown is a duplicate of the model that he used. A cross section over the model is shown in **Figure 3-10**. This cross section was used to generate **Figure 3-11** and **Figure 3-12** which illustrate a multiresolution analysis where the scale has been preserved. A Daub14[54] orthogonal wavelet [Daubechies 1988; Mallat 1997] was employed to ensure a near zero response when applying the high pass filter. This ensured that the low pass filter provided the best possible representation of the low frequencies at each scale. In other words, the wavelet applied had a sufficiently large number of vanishing moments to remove high frequency components successfully [Press et al. 1992].

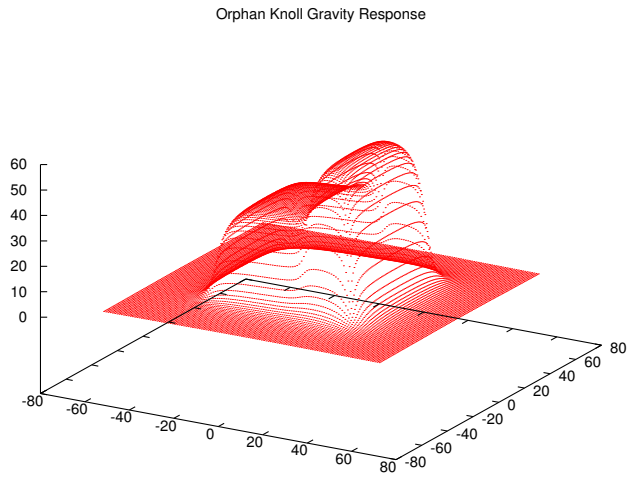

Figure 3-9: *This illustrates the Orphan Knoll gravity response as synthesized from assumed density information [Zhang 1993].*

3.6 Wavelets and Potential Fields

In the geodetic literature, there has been increasing use of wavelets for signal analysis and other purposes. For example, [Blais 1999] discusses multiresolution analysis in a geodetic context. The presentation by [Wang et al. 2001] discusses feature extraction using wavelet techniques with illustrations of the Orphan Knoll highlighted earlier and first attempts at global subsurface characterization. In [Blais and Provins 2001] there is a discussion of the application of symmetric wavelets used to highlight possible geological features. In [Blais and Provins 2000] and [Blais and Provins 2002] there is further

[54] A 'Daub14 wavelet' is one of a series of causal conjugate mirror filters developed by Ingrid Daubechies. Each has p vanishing moments and $2p$ samples. The Daub14 has 7 vanishing moments. As noted in [Liu and Sideris 2003b] the higher the number of vanishing moments, the more zeroed wavelet coefficients there are.

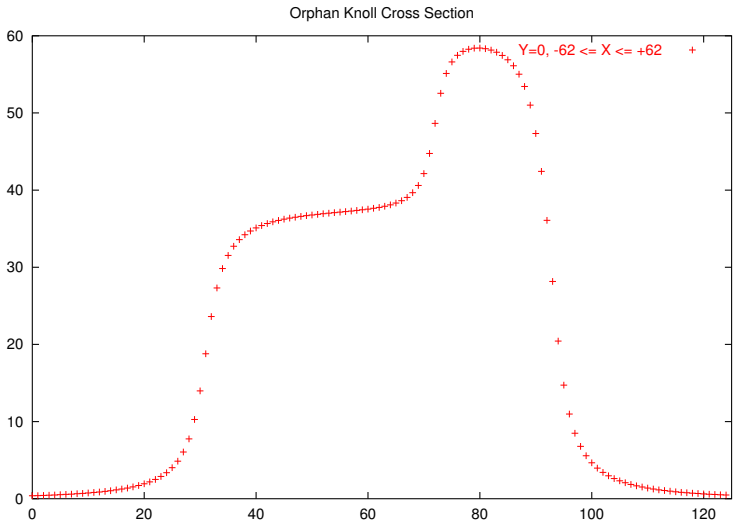

Figure 3-10: *This is a cross section of the gravity response synthesis of the Orphan Knoll geological feature in the North Atlantic Ocean.*

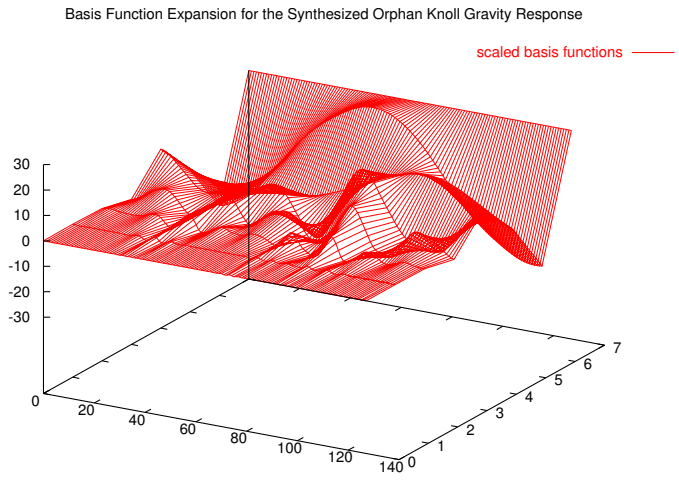

Figure 3-11: *This illustrates the expansion of the wavelet analysis of the cross section illustrated in* **Figure 3-10**. *A Daub14 wavelet has been employed. Highest frequencies are shown in the foreground, and the mean response is shown at the back.*

---

discussion of multiresolution analysis in spherical contexts, with emphasis on convolutions and the obvious relationship of these operations and spherical harmonic transforms.

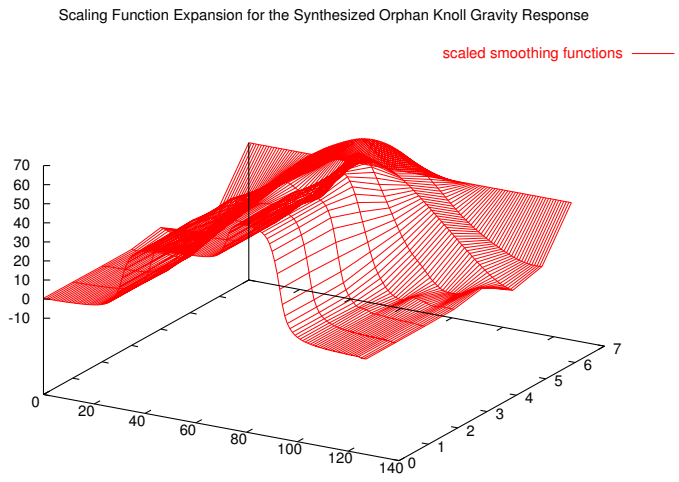

Figure 3-12: *This illustrates the progressive removal of the high (to low) frequency components in a spatially contextual manner. In the foreground is the original gravity field synthesis. At the back is the mean level of that synthesis.*

[Li 1996b] and [Li 1996a] discuss the combination of data having different resolutions and accuracies using wavelet transforms. In [Kotsakis and Sideris 1999] there is a discussion of using wavelet transforms as a tool for spectral gravity field modelling.

Very recently, wavelets have been used for the evaluation of terrain corrections [Liu and Sideris 2003a]. In another use, wavelet techniques have been employed to describe the Earth's gravitational field in terms of its wavelet coefficients to allow new data to be added to the model easily [Salamonowicz 2001]. [Grebenitcharsky and Sideris 2002] discuss the use of wavelets to provide information about the spatial distribution of irregularities when combining mountainous coastal data with smoother oceanic data.

In other work, attempts to identify plate boundaries have been reported in [Vecsey et al. 2000] and [Yuen et al. 2001]. The authors employed second, fourth and eighth order derivatives of a Gaussian function with emphasis on the first (the Mexican Hat described earlier). Unlike some of the authors cited earlier, this group applied their operators to Mercator projections of the geoid. Even with the associated distortion, they were able to identify subduction zones, such as was done in the non-distorted spherical basis and described in [Wang et al. 2001]. An example of the early experimentation by Wang and colleagues is illustrated in **Figure 3-14** in the sequel. It illustrates the wavelet gradient

magnitude computed at a resolution of 0.1° at a reference scale of one.

The use of wavelets is not confined to geodetic work. Geophysical exploration has also enjoyed benefit from their use. In [Gibert and Pessel 2001] the authors describe the use of continuous wavelet transforms to study self-potential[55] profile data. In a more theoretical sense, [Moreau et al. 1997] and [Moreau et al. 1999] describe the theory behind developing wavelets specifically related to the gravitational data. In a related paper the techniques described earlier are used to investigate the use of continuous wavelet transforms for the recovery of geometric characteristics of simple shapes. Using upward continuation and various wavelets, the shape, thickness and dip of simple causative bodies may be inferred [Martelet et al. 2001].

Other authors have developed similar techniques which are described in the sequel. These were employed in an attempt to realize the objective of this research: to create a realistic Earth model by making reasonable estimates of deep Earth mass anomalies as a contribution to the synthetic Earth project. The work published by the Australian researchers [Boschetti, Horowitz, and Hornby 1999; Boschetti, Horowitz, Hornby et al. 2000; Hornby, Boschetti, and Horowitz 1997; Hornby, Boschetti, and Horowitz 1998; Hornby, Boschetti, and Horowitz 1999; Hornby, Boschetti, Horowitz, and Archibald 1997a; Hornby, Boschetti, Horowitz, and Archibald 1997b] and [Boschetti, Hornby, and Horowitz 2000] is more oriented to exploration for economic minerals, but the technique described appears quite relevant to the objective of this research.

In the following section is a description of the work done in Australia. In this research, a development similar to that described by the Australians was employed. These researchers take a more practical approach to the problem of deciphering gravity data. Two sections describe that approach, and this is followed by the writer's thoughts on applying the technique to global geopotential fields. The following chapter describes the use of the technique for the interpretation of geopotential data for mass anomaly characterization.

3.6.1 Practical Application

Typically, an exploration geoscientist would employ either a visual, or traditional interpretive approach to delineating and mapping causative bodies, or more recently, would

[55] Self-potential is the potential developed in the Earth by electrochemical action between minerals and the solutions with which they are in contact.

use some form of an inversion approach in his attempt to comprehend the geology which induced the measured field. Background on the interpretation of potential field data through modelling is exemplified by [Jessel 1997] or [Blakely and Simpson 1986].

More recently, the work of [Hornby, Boschetti, and Horowitz 1999; Moreau et al. 1997; Moreau et al. 1999] combined with the work by [Mallat and Hwang 1992] and [Mallat and Zhong 1992] some of which has already been mentioned, has introduced the *signal processing* approach to interpretation. By employing the physics of the system to model or to influence the processing of the measurement, it is hoped that the characteristics of causative bodies will be revealed.

As seen earlier in equation 3-10, the continuous wavelet transform of some function f is,

$$W[f](s, x) = f * \psi_s(x) \tag{3-45}$$

for dilation s and translation x. In the detection of edges, [Hornby, Boschetti, and Horowitz 1999] observe that given a non-negative **smoothing function** $\phi(x)$ (to be defined in the sequel) whose integral is unity, and with a wavelet $\psi(x)$ derived from that smoothing function by taking its horizontal gradient (∇_x) as per,

$$\begin{aligned} \psi_s(x) &= s \frac{d}{dx}\left(\frac{1}{s}\phi\left(\frac{x}{s}\right)\right) \\ &= s \frac{d}{dx}\phi_s(x) \end{aligned} \tag{3-46}$$

then the transform is identical to,

$$W[f](s, x) = s\nabla_x f * \phi_s(x) \tag{3-47}$$

using the definition of convolution and the linearity of the derivative operator. This is sometimes called scale covariance under a gradient operation.

The consequence of this is that rapid changes resulting from convolving a scaled smoothing function with another function, is to highlight those changes as local maxima, by computing the gradient of the convolution. These local maxima correspond to the edges of a signal, after being blurred at scale s and are known as **multiscale edges** [Mallat and Zhong 1992].

3.6.2 Application to Potential Fields

The potential at z_0 (a reference elevation) can be described in the continuous case as,

$$V(x, y, z_0) = G \iint_{\mathcal{R}^2} \int_{-\infty}^{0} \frac{\rho(x', y', z')dx'dy'dz'}{[(x - x')^2 + (y - y')^2 + (z - z')^2]^{1/2}} \tag{3-48}$$

and the magnitude of the gravity at that point can be described by

$$g(x, y, z_0) = G \iint_{\mathcal{R}^2} \int_{-\infty}^{0} \frac{\rho(x', y', z')(z_0 - z')dx'dy'dz'}{[(x - x')^2 + (y - y')^2 + (z_0 - z')^2]^{3/2}} \tag{3-49}$$

which corresponds to the vertical derivative of the potential. This latter equation can be expressed in terms of a **normalized Green´s kernel** function for the vertical acceleration, given by,

$$K(x, y, z) = \frac{z/2\pi}{[x^2 + y^2 + z^2]^{3/2}} \tag{3-50}$$

Thus, the gravity magnitude is expressible as,

$$g(x, y, z_0) = 2\pi G \int_{-\infty}^{0} \rho(x', y', z')K(x, y, z_0 - z')dz' \tag{3-51}$$

which is a convolution over z. The function $K(x, y, z)$ has an integral of unity for all $z > 0$, implying compact support in the limit as $x, y \to \infty$.

Consider the scaling of $K(x, y, z)$ vertically,

$$\begin{aligned} K(x, y, sz) &= \frac{1}{2\pi} \frac{sz}{[x^2 + y^2 + (sz)^2]^{3/2}} \\ &= \frac{1}{2\pi s^2} \frac{z}{[(x/s)^2 + (y/s)^2 + z^2]^{3/2}} \\ &= \frac{1}{s^2} K(x/s, y/s, z) \\ &= D_s K(x, y, z) \end{aligned} \tag{3-52}$$

Thus the *horizontal* dilation of $K(x, y, z)$ is the same function as would be found at some scaled height sz. This is a two dimensional **smoothing function** like that indicated in equation 3-46. In other words, using the symbols of that equation, the dilation of $K(x, y, z)$ is,

$$K(x, y, sz) = \frac{1}{s^2}\,\phi\left(\frac{x}{s}, \frac{y}{s}\right) = \phi_s(x, y) \tag{3-53}$$

This function can be used in a wavelet analysis. Its two dimensional gradient ($\nabla_{xy}K(x, y, sz) \equiv \nabla_{xy}\phi_s(x, y)$) yields wavelets $\psi_s(x) = \nabla_x\phi_s(x, y)$ and $\psi_s(y) = \nabla_y\phi_s(x, y)$ by their definition. Each has zero mean and their support is finite, providing the underlying function converges to zero at a sufficiently great distance.

Therefore, the wavelet transform given by equation 3-47 for one dimension is the same as,

$$W[f](s, x, y) = s\nabla_x f * K(x, y, sz) = s\nabla_x f * K_s(x, y, z) \tag{3-54}$$

Thus both a smoothing function (ϕ) and a wavelet (ψ) are available. The effect of applying a smoothing function is directly related to the scale, which in turn is a function of the selected height above the reference. The wavelet function is related to the smoothing function by its first derivative.

[Hornby, Boschetti, and Horowitz 1999] show that the vertical acceleration at some elevation z can be computed from that at another level z_0 by convolution with the appropriately scaled smoothing function ϕ. They assert that this expression is comparable to the expression in equation 3-47, so that by choosing a scale factor of

$$s = \frac{z}{z_0} \tag{3-55}$$

one finds the horizontal derivative of the vertical acceleration (g_z, which is a function of $K(x, y, z)$) to be the wavelet transform for scale s (in one dimension),

$$W[g](s, x) = \frac{z}{z_0}\,\nabla_x g_z(x, y) \tag{3-56}$$

Since the expression is the same for the y direction, the two dimensional transform becomes,

$$W[g](s, x, y) = \frac{z}{z_0}\,\nabla_{xy} g_z(x, y) \tag{3-57}$$

As Hornby and colleagues conclude, the wavelet transform of the vertical acceleration at arbitrary elevation (which is equivalent to a single scale), can be obtained by upward continuing the measured gravity data to level $z = sz_0$, computing the two dimensional

gradient and then scaling by s. These steps correspond to applying a suitably scaled wavelet (scaled by $s = z/z_0$, the upward continuation step) to a data set to achieve a continuous wavelet transform. By using several scale factors (i.e. elevations), sufficient information may be derived to analyze the properties of the body which generated the original, measured gravity field. The effect of the analyzing wavelet is quite visible. There is a clear correspondence between horizontal gravity gradients and the wavelet transform of planar sources [Hornby, Boschetti, and Horowitz 1999].

The difference in the transforms for each scale selected corresponds to the detail removed (or added, depending on the direction of continuation) between chosen scales. Since no indication has been given of whether or not the wavelet forms a frame with the requisite characteristics, the question of invertability is not answered, nor is it relevant for the purpose of this research. The transform described here was intended for information extraction from geopotential fields: depth estimates and possibly shape analysis.

With regard to **shape analysis**, [Mallat and Zhong 1992] show that the evolution of wavelet local maxima across scales characterize the local shape of irregular structures. They observe that the maxima of the absolute value of the first derivative of $f * \phi_s(x)$ (for one dimension) are sharp variation points. These are easily selected by the modulus of the transform $|W[f](s, x)|$ which is easily extended to two dimensions. Furthermore, the values of the **modulus maxima**[56] vary across changing scale values. This evolution is dependent on the Lipschitz regularity of the signal. Examine again **Figure 3-4** for an illustration of how the maxima of the analyzing wavelet's actions change with scale.

A function is said to be uniform Lipschitz α for $\alpha \in (0, 1]$, in the interval (a, b), if there exists some constant K, independent of location (within the interval) so that for all $x_i, x_j \in (a, b)$,

$$|f(x_j) - f(x_i)| \leq K|x_j - x_i|^{\alpha} \tag{3-58}$$

An example function is a unit step, for which $\alpha = 0$. The derivative of such a function, a Dirac delta, has $\alpha = -1$. In fact, using the definition given by [Mallat and Hwang 1992, page 619], one can show that the Lipschitz regularity α, indicates the differentiability of a function. The primitive (i.e. integral) of a function Lipschitz α at a point is Lipschitz $\alpha + 1$ at the same point, but it's derivative need not be Lipschitz $\alpha - 1$ at that point. It is only bounded by $\alpha - 1$ [Hornby, Boschetti, and Horowitz 1999].

[56] Modulus maxima means the extrema of the modulus of the wavelet transform.

Distribution f, whose integral F is Lipschitz α, is Lipschitz $\alpha - 1$, by definition. See [Mallat and Hwang 1992] and [Hornby, Boschetti, and Horowitz 1999]. Thus the value of $\alpha = -1$ for a point source in one dimension, and -2 in two dimensions. This behaviour can be related directly to source body configuration by a study of the modulus of the wavelet transform [Hornby, Boschetti, and Horowitz 1999]. In particular, these authors prove that if the density is Lipschitz uniform regular at some depth, then given the vertical acceleration (gravitational attraction) the modulus maxima has the value,

$$|W[f](s,x)| \leq K(s+s')^{\alpha-1}s \tag{3-59}$$

where $s = z/z_0$ and $s' = -z'/z_0$, with z' the depth below z_0. This says that by examining the variation of the modulus maxima, one can make estimates of s and s', as well as the Lipschitz exponent α, which indicates the type or shape of the source body.

For various body shapes, Hornby and colleagues provide an analysis of the modulus maxima to be expected. In particular, they note the expected result for spherical bodies, and how one can interpret their depth from the measured values. The expression given, and that employed in this work was (for one dimension)

$$x = \pm(s - z_d)/2 \tag{3-60}$$

where $s = z$ is the scale used in the wavelet analysis, $z_0 = 1$ is the **normalized** height of the measurement surface above the body, z_d is the depth to the source below the reference surface and x is the horizontal offset to the wavelet modulus maxima. This expression is easily derived from the expression for the vertical acceleration due to a point source [Hornby, Boschetti, and Horowitz 1999, page 184].

Hornby notes that the anomalous body produces a diagnostic shape in the graph of the gravity function. While this has been known for many years (see for example [Dobrin 1960] or [Telford et al. 1976]), the use of wavelets introduces a vertical variation of the field through reformulation of the available information. This in turn may be investigated through the horizontal gradient to highlight edges at varying scales. By means of wavelets, Hornby and colleagues have provided a sound basis for the interpretation of potential field data.

3.6.3 Application to Global Potential Fields

The theoretical development in the Moreau papers substantiates the work of Hornby and colleagues. Thus it makes sense to apply the more direct method described by the latter

authors to interpret gravity anomalies on a global basis. The method is simpler to implement, and the two are fundamentally the same.

The preferred method of dealing with global data is via spherical harmonics. They can be used to describe all manner of data on a sphere, as indicated elsewhere in this document. In particular, they may be used to describe the **anomalous potential**, which is that potential of the gravitational field dissimilar to that expected from the **normal field**, defined by a specified ellipsoid.

For the anomalous potential, the spherical harmonic coefficients are well known via many different models, each generally improving on its predecessors. Similarly, gravitational models based on well-known body types can be developed for experimental use.

The signal processing approach used in the Poisson kernel continuous wavelet analysis of either measured or modelled data is as follows:

1 Initialize the radius of computation, say at the spherical Earth's mean radius R_E.

2 In spherical approximation, compute the two dimensional horizontal gradient of gravitation at the current height (i.e. the current level of upward continuation). This is estimated from published coefficients by modifying them as if to compute the magnitude of the gravitational attraction g from the anomalous potential T as described in equation 2-87. The gradients are then given by equation 2-90 and equation 2-91. By taking these gradients, the **detail** at the current scale or relative height is computed.

3 Synthesize the field described by the spherical harmonic representation.

4 Compute the magnitudes (scaled by s) of the extrema of the synthesized field and note the extrema locations.

5 Increment the height and thus effect an **upward continuation** or **smoothing** of the gravitational spectrum when these steps are next iterated.

6 Repeat steps two through five until all scales of interest are determined.

7 Estimate depths and allied parameters. This may be done graphically by plotting the positions of the extrema versus their relative magnitude. Finding the regression line through these points then indicates relative depth. Further detail is provided in the next chapter.

The described process is relatively easy to implement, although there are certain numerical problems to overcome which will be mentioned in due course. Typical of geophysical interpretations, graphical methods are employed and it will be seen that for simple bodies the technique is sufficiently robust for depth estimation. Unfortunately, for complex mass assemblages (which tend to be the norm in the real world) the method appears inappropriate. These issues will be described in the sequel.

It should be noted that some early work in the area of global feature extraction was done by the author in some of the work mentioned earlier [Wang et al. 2001]. In that work global datasets using both **EGM96** and the very high degree model described in [Wenzel 1998a] were employed using an early version of the technique described in this chapter. The approach used was an approximation for a single scale. The deflections of the vertical for the undulation at ground level (scale equal to one) were computed, their magnitudes were found, and the extrema were displayed. The result for **EGM96** is shown in **Figure 3-13**. To the degree that the transform was computed, the results appeared promising in that subterranean features were nicely highlighted - particularly on Wenzel's dataset shown in **Figure 3-14**. An additional test employing a multiresolution analysis using low order Daubechies orthogonal wavelets over the Orphan Knoll was also completed, with somewhat ambiguous results.

3.7 Summary

This chapter reviewed the basic theory of continuous wavelets and their discretized implementation. It also covered multiresolution analysis using orthogonal wavelets and smoothing functions. Examples shown illustrated the application of these transforms to general datasets and synthesized gravity anomalies.

The text returned to the continuous case to observe the relationship that wavelets have to gravity data. This was shown by virtue of the effect of smoothing when altering the reference surface elevation. The importance of the wavelet modulus maxima was highlighted as a tool which allows one to characterize a body at depth. The important aspect for this research was that depth could be determined for certain body shapes.

Using this, and the assumption that anomalous bodies can be characterized by the simplest of models (a point source), the next chapter explores the use of the technique to realize the primary objective.

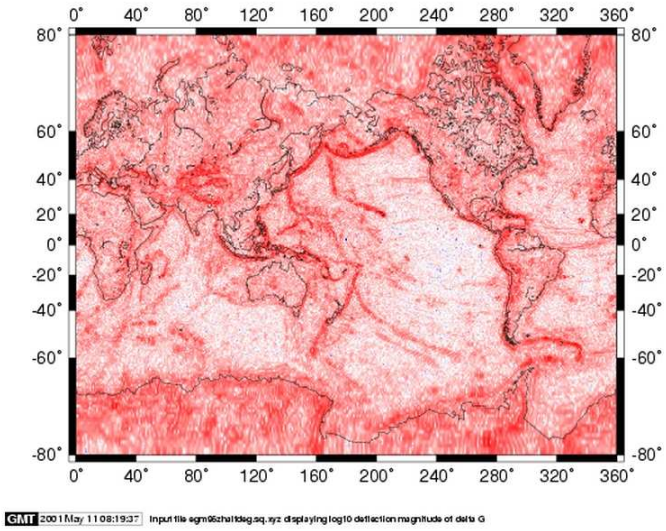

Figure 3-13: *Using* **EGM96***, the wavelet transform magnitude is seen to show some features, but less clearly than in* **Figure 3-14***. A scale of one was employed (i.e. no upward continuation).*

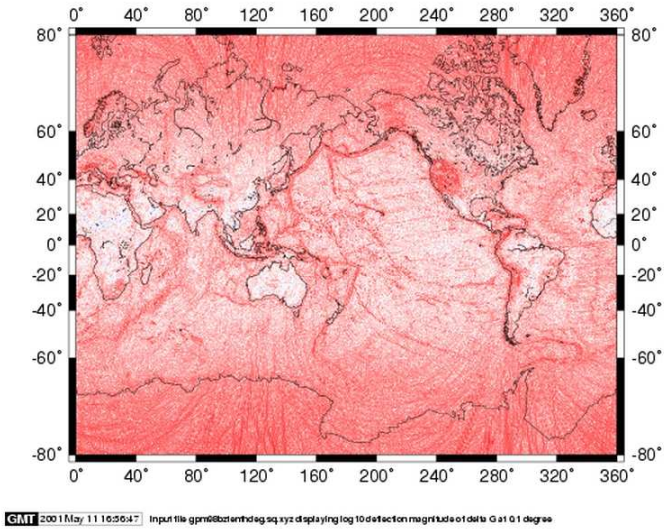

Figure 3-14: *Using Wenzel's 0.1° geopotential model (***GPM98B***) the wavelet transform magnitude is seen as very fine curvilinear features over the Earth. A scale of one was employed (i.e. no upward continuation).*

---

4 Using Wavelets for Anomaly Characterization

Use of wavelet transforms should allow one to make estimates of depth for mass anomalies reflected in the geopotential field's surface expression. Given some estimate of depth, one should then be able to make some assessment of mass for each surface geopotential anomaly. This then will result in a map of Earth structure that matches (to some degree) the measured field. This chapter demonstrates the capability the wavelet transform affords in delineating that structure. As will be seen, under ideal conditions, the method works reasonably well. In realistic conditions however, it proves to be inadequate.

The theories developed by Moreau and associates, Hornby and colleagues, and quite recently by [Abdelrahman et al. 2001] are intended generally for seeking out, and characterizing shallow bodies of exploration interest. Such bodies would typically be within a few kilometres of the Earth's surface (for the deepest mines), and for economic reasons would be as shallow as possible. In this research, the primary interest lay in modelling the Earth's deep structure so as to synthesize the Earth's geopotential field. Consequently there was the wish to test the theories of some of the previously mentioned authors for their applicability in this endeavour. If successful, then one might expect that a better knowledge of the crust and mantle might result. The most obvious characteristic would be a consistent and plausible depth estimate for causative bodies based upon the surface measurements of the gravity field. While other characteristics (shape, orientation etc.) might also be possible, the focus on depth, followed by mass and the resulting *fit* to the measured field was the primary objective.

In this chapter, reference is made to the work of Bowin as described in [Bowin 2000]. His interest was in attempting to describe some of the major geoidal features in terms of structure on the core/mantle boundary, with shallower anomalous masses contributing to the balance of the geopotential field. His models and those of Lithgow-Bertelloni were provided to the author for experimental use. While reference is made to some of their work in this chapter, it is not until the next that they were used to any extent. Accordingly, a greater description of their activities and models is deferred until then.

The next section begins with a review of a small set of models, one of which will be used here and in the following chapter. This is followed by a discussion of the convergence of the spherical harmonic spectrum for a point source. An additional consideration is the cost of calculating the spectrum for experimental purposes. The 'meat' of the chapter is

comprised of attempting to estimate the depth of a buried source using the wavelet transform procedure described in the previous chapter. Both simple and complex body assemblages are considered, and an attempt to estimate the depth of the principal cause of the South American high is made. Some conclusions about the usefulness of the wavelet technique for depth estimation end the chapter.

4.1 Modelling the Potential Field on a Global Basis

To model bodies at depth, one needs a method to synthesize that which is measured at the surface. [Pollack 1973] provided several models of various shaped bodies in terms of spherical harmonic coefficients. Without going into detail, quoted here are his model descriptions, with corrections[57]. This paper described how one might represent the gravitational potential field in terms of three rudimentary models. These included a point mass, a spherical cap and a spherical rectangle[58]. The representation was in terms of the generated spherical harmonic coefficients for an arbitrary placement of these ideal bodies.

Pollack's paper describes the normalized spherical harmonic coefficients in terms of potential for each body using the expression found in [Heiskanen and Moritz 1966, page 59]

$$V(r,\theta,\lambda) = \frac{GM}{r}\left\{1 - \sum_{n=1}^{\infty}\sum_{m=0}^{n}\left(\frac{a}{r}\right)^{n}\left[\bar{a}_{nm}\bar{R}_{nm}(\mu,\lambda) + \bar{b}_{nm}\bar{S}_{nm}(\mu,\lambda)\right]\right\} \qquad (4\text{-}1)$$

where

r	radial distance from the origin to the point of observation
a	radius of the sphere upon which the models are placed
θ	colatitude of observation point (θ' for the model)
λ	longitude of observation point (λ' for the model)
μ	$\cos\theta$ ($\mu' = \cos\theta'$ for the model)
$\bar{a}_{nm}, \bar{b}_{nm}$	coefficients of the normalized spherical harmonic expansion of the gravitational potential as per [Heiskanen and Moritz 1966]

[57] There were some typographical errors in Pollack's paper, which have been corrected in this document. Perhaps not surprisingly, when developing codes to exploit these models, typographical errors were also encountered in several reference texts.

[58] The spherical cap is a circular surface and the rectangle is a zone defined by two colatitudes, and a lune.

$\bar{R}_{nm}(\mu,\lambda), \bar{S}_{nm}(\mu,\lambda)$ normalized spherical harmonic functions of degree n and order m

The models are well described by Pollack, with the coefficients for each given in terms of the coordinates of the anomalous body at (a, θ', λ').

Point Mass

$$\begin{bmatrix} \bar{a}_{nm} \\ \bar{b}_{nm} \end{bmatrix} = \frac{-1}{2n+1} \begin{bmatrix} \bar{R}_{nm}(\mu',\lambda') \\ \bar{S}_{nm}(\mu',\lambda') \end{bmatrix} \tag{4-2}$$

Spherical Cap

$$\begin{bmatrix} \bar{a}_{nm} \\ \bar{b}_{nm} \end{bmatrix} = \frac{P_{n+1}(\gamma) - P_{n-1}(\gamma)}{(2n+1)^2(1-\gamma)} \begin{bmatrix} \bar{R}_{nm}(\mu',\lambda') \\ \bar{S}_{nm}(\mu',\lambda') \end{bmatrix} \tag{4-3}$$

Spherical Rectangle: m = 0

$$\bar{a}_{n0} = \frac{P_{n-1}(\mu_1) - P_{n+1}(\mu_1) + P_{n+1}(\mu_2) - P_{n-1}(\mu_2)}{(2n+1)^2(\mu_1 - \mu_2)} \bar{P}_{n0}(\mu') \tag{4-4}$$

Spherical Rectangle: n, m > 0

$$\begin{bmatrix} \bar{a}_{nm} \\ \bar{b}_{nm} \end{bmatrix} = \frac{\int_{\mu_1}^{\mu_2} \bar{P}_{nm}(\mu')d\mu'}{m(2n+1)(\gamma_2-\gamma_1)(\mu_1-\mu_2)} \begin{bmatrix} \sin(m\lambda_2) - \sin(m\lambda_1) \\ \cos(m\lambda_1) - \cos(m\lambda_2) \end{bmatrix} \tag{4-5}$$

In these expressions, the angle of the generating cap is α, with $\gamma = \cos\alpha$.

Note that the expression for the spherical rectangle contains a term additional to that indicated by Pollack ($\bar{P}_{n0}(\mu')$). Apparently, it was missed in transcription, but is easy enough to determine. The expression shown for that model will resolve to that of the spherical cap if the rectangle is 2π radians in width, and has $\mu_1 = 1$ (i.e. the rectangle starts at the pole). Pollack's expression will not. Note also that both the spherical cap and the spherical rectangle (for $m = 0$) generate the same potential as the point source as $\gamma \to -1$ (cap) and $\mu_1 \to 1, \mu_2 \to -1$ (rectangle).

With the exception of the spherical rectangle, for $n, m > 0$, these expressions are easy to evaluate. The rectangle is more involved, as it requires the numerical solution of the integral,

$$\int_{\mu_1}^{\mu_2} \bar{P}_{nm}(\mu')d\mu' \tag{4-6}$$

This may be done using an extended arithmetic machine such as **GNU MP**, or via recursions such as described by [Paul 1978]. Note that if the former method is employed, considerable care must be taken to ensure adequate precision is carried, and that the expressions used for the integration lack typographical error. The process is also expensive computationally, as is illustrated in **Figure 4-1**.

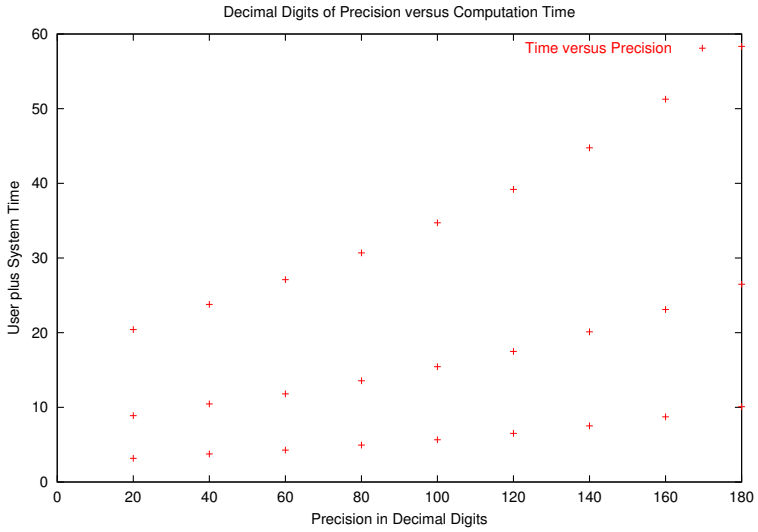

Figure 4-1: *Direct calculation of the integrals of the P_{nm} functions for various degrees of decimal precision can be costly. Shown here are the times in seconds to calculate these functions to degree and order 36, 48 and 60 on a 300 Mhz Pentium II processor.*

4.2 Potential for a Point Mass

The first problem investigated was that of the convergence of a spherical harmonic model to a field that is truly representative for that model. Authors [Heiskanen and Moritz 1966, page 245] hint at the need for high degree summations, owing to slow convergence, and one might surmise that Pollack's models were not used, or at least cited in the literature as being used, because of this problem. The capabilities of commonly available computing facilities of his day were not as well developed as they are today[59] [Dongarra 2003].

[59] There were very some capable computers available at the time, such as those produced by CDC for scientific work. More commonly available however, were those from IBM, such as the 370 with a MFLOP rating of about 1.2. Today's Sony Playstation 2 is comparable to that machine at 0.995 MFLOPs.

It is instructive to see the degree of convergence, or lack thereof as a function of anomaly depth versus degree. This was accomplished by computing the measured surface potential via both Pollack's expressions and from geometric considerations. For a point mass, this also confirmed that the calculation via spherical harmonics was correct. In **Table 4-1** is illustrated the effect as a function of depth, for varying degrees of expansion, the relative error that may be incurred, The relative error indicates the difference between an exact, geometric potential versus that determined from a spherical harmonic expansion. The same information is shown graphically in **Figure 4-2**.

Geometric Potential versus Spherical Harmonic Potential

Depth (km)	Relative Error by Degree (%)					
	36	**72**	**90**	**144**	**180**	**360**
1600	0.002	0.000	0.000	0.000	0.000	0.000
1400	0.010	0.000	0.000	0.000	0.000	0.000
1200	0.045	0.000	0.000	0.000	0.000	0.000
1000	0.182	0.000	0.000	0.000	0.000	0.000
800	0.702	0.006	0.001	0.000	0.000	0.000
600	2.585	0.074	0.012	0.000	0.000	0.000
400	9.105	0.884	0.276	0.008	0.001	0.000
200	30.765	9.771	5.507	0.986	0.313	0.001
100	55.727	31.550	23.739	10.112	5.725	0.333

Table 4-1: *A comparison of potential computed via spherical harmonics versus that determined from geometric considerations. Measurable error is observed at shallower depths.*

It is evident that anomalies too near the surface require high degree spherical harmonic expansions. For moderately deep anomalies, say greater than several hundred kilometres, the computing demands are ameliorated considerably, as the highest degree required is substantially less.

As might be expected, gravitational fields exhibit similar characteristics. **Figure 4-3** illustrates the convergence of the gravitational field for point sources at various depths. A surface source forms a singularity, and hence is not shown. The RMS difference between a synthesized gravitational field and a geometrically-generated field, over a specified

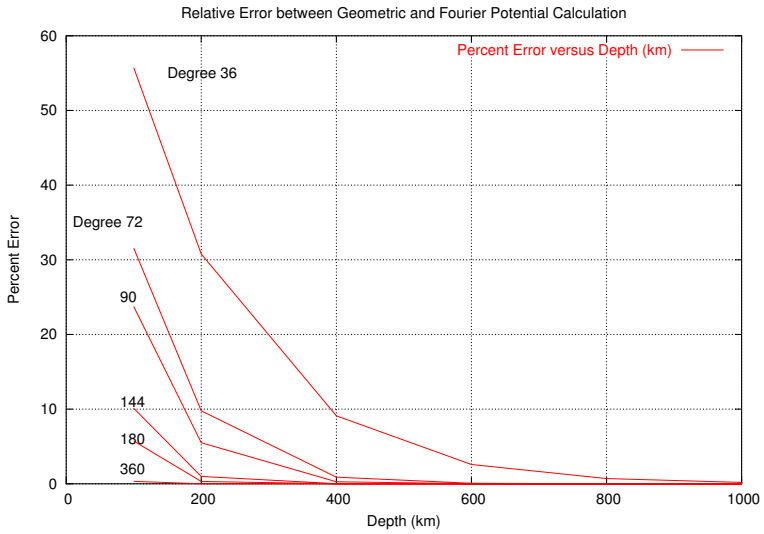

Figure 4-2: *Shown is the relative error between a geometric calculation and Pollack's point source calculation of potential for depths to 1600 km.*

spherical rectangle, has been computed.

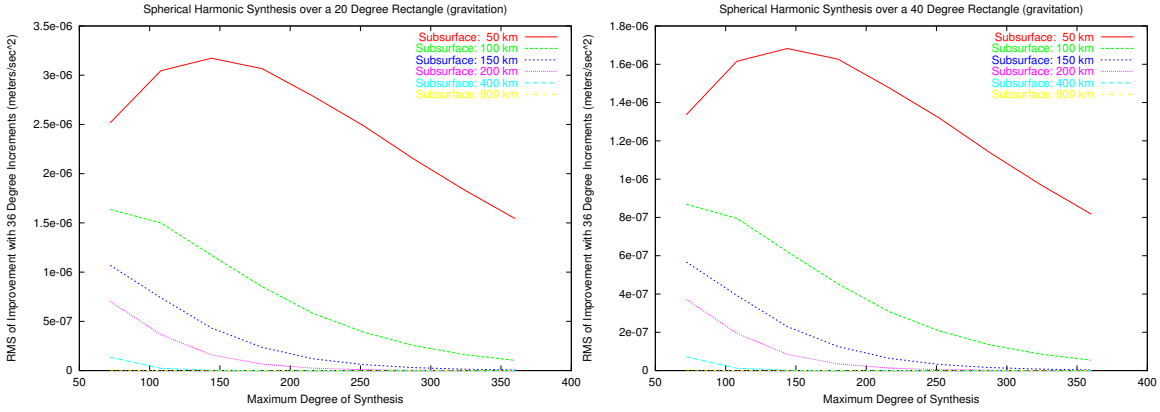

Figure 4-3: *Convergence of a spherical harmonic synthesis of gravitation with increasing degree/order for the attraction due to a 10^{17} kg mass at various depths. On the left is a 20° spherical rectangle centred on a point source, and on the right is a 40° rectangle. No surface anomaly is shown as the calculation diverges with increasing degree.*

The dependency of the gradient on degree and order is illustrated in **Figure 4-4**. Only the 20° spherical rectangle is shown. Clearly the gradient values are both small and decrease rapidly with increasing degree.

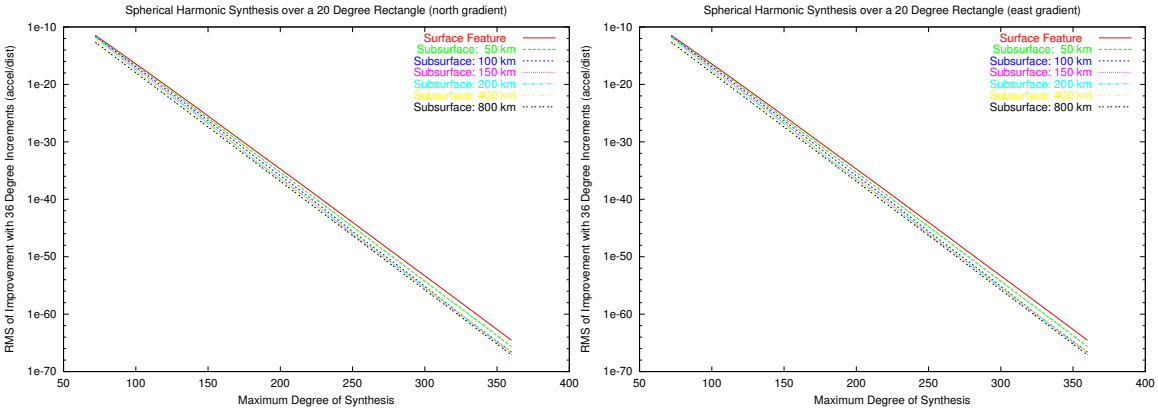

Figure 4-4: *The convergence for a synthesis of gradients of gravitational attraction for various degree/order and depths. On the left is illustrated the dependency of the northward gradient of gravitation for point mass anomalies at various depths. The right illustration is for the eastward gradient. The mass size was 10^{17} kg.*

It is apparent that using Pollack's synthesis mechanism for moderately deep bodies should be satisfactory if degree and order 360, a common value until quite recently, were used. This was confirmed numerically, and is shown here graphically by further geometric versus synthesis comparison at that degree. For example, for a single point source buried at a depth of 100 km, with measurements taken at the surface, and again at 100 km elevation, **Figure 4-5** shows that the potential computed by both methods is virtually identical.

For gravitational attraction, as seen in **Figure 4-6**, there is some observable discrepancy for the surface measurement within 1° of the anomaly. This amounts to an order of magnitude difference ($1.48*10^{-5}$ for geometrically computed values of $6.672*10^{-4}$, versus synthesized values of $6.524*10^{-4}$). This falls to two orders of magnitude difference by 1° and greater. For a higher measurement elevation (or a deeper body depth), the difference is a minimum of 4 orders of magnitude. Computing the gravitational attraction to degree and order 1440 caused the difference to fall to between 7 and 8 orders of magnitude, as might be expected.

4.2.1 Computational Considerations

Evidently, for minimal error, a high degree is required. At the same time, computational costs imply that a low degree is desired. Since the synthesis of a set of spherical

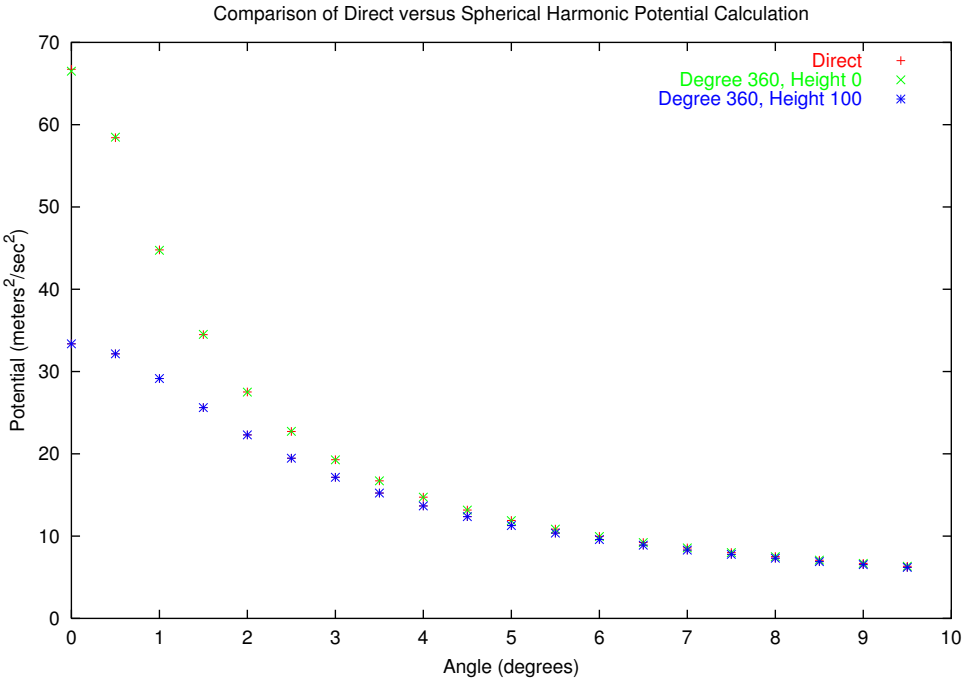

Figure 4-5: *To degree and order 360, the potential measured at the surface, and at an elevation of 100 km for a point source of 10^{17} kg at 100 km depth appears coincident for the spherical harmonic and direct calculation methods.*

---

harmonic coefficients is $O(N^4)$ in the most naive implementation, computational cost can become extremely high for even moderate degree/order syntheses. Although codes to degree and order 1800 have been developed (e.g. [Wenzel 1998a]), they are expensive to run.

As illustrated in earlier figures, by degree and order 360, the synthesis for moderately deep bodies (say in excess of 50 km) converges rapidly for the quantities derived from the potential described by the models used. Accordingly, a maximum degree/order of 360 was selected as a compromise. To maximize performance the codes developed by this author made use of fast Fourier transforms to reduce the order of computation to $O(N^3)$. This was the least possible without employing codes such as those developed by [Mohlenkamp 1997] or [Healy et al. 1998] which have their own computational idiosyncrasies (mainly very large storage and memory requirements).

For the fast Fourier transform (FFT), the publicly available **FFTPACK** codes were selected. These are supplied as single precision FORTRAN functions. To increase

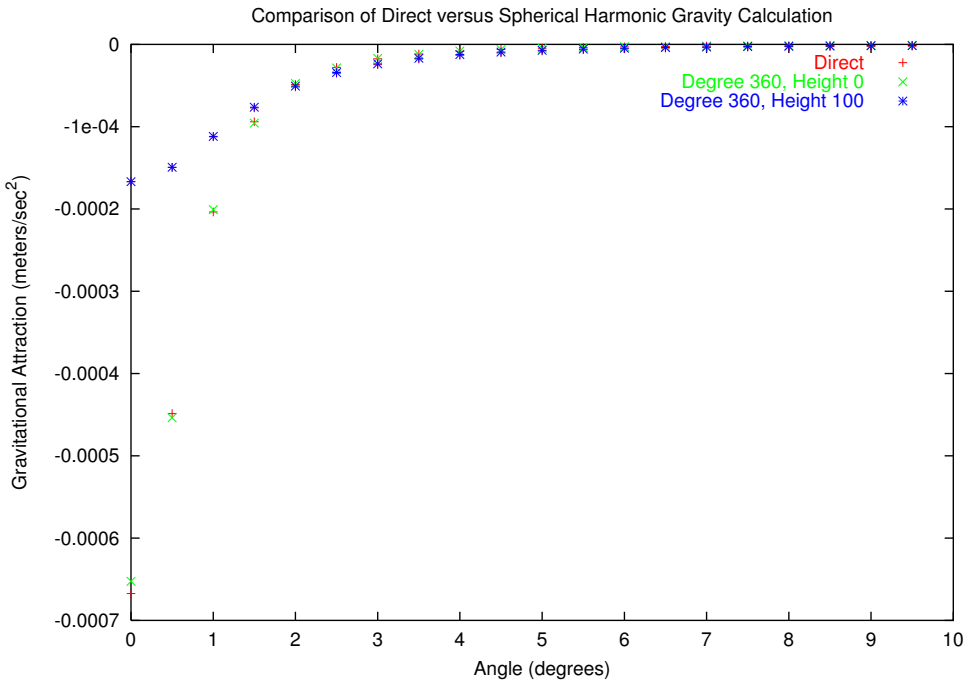

Figure 4-6: *For the same parameters as in* **Figure 4-5**, *the gravitational attraction deviates for measurements close to the buried source.*

---

numerical accuracy and to make them compatible with other codes developed for this research, the author did a conversion to C, and forced all real variables to double precision. The required routines were then packaged as a single library to be linked with other codes as required.

Employing an FFT in a spherical harmonic synthesis requires a reorganisation of the order of operations from that which appears to be most obvious from the summation described in, for example, equation 2-86. It is evident that a Fourier transform is being executed but its implementation is not immediately clear. Satisfying the conditions described in the chapter on spherical harmonics will ensure that the FFT can be used to reduce the order of computations from $O(N^4)$ to $O(N^3)$.

4.3 Synthetic Examples using Wavelets

The first modelling program was used in part to ensure the correctness of the algorithm. Some early program results are shown here. All computations were performed with double precision arithmetic and to maximum degree and order 360. The mass of the point source was 10^{17} kg, and the anomalous body was placed (for convenience) at a colatitude and longitude of 90°. The following illustrations, and all other synthetic tests were made

by analyzing single anomalies, or multiple anomalies arranged in a line through which cross sections were made. Only multiple body assemblages required some interpretation to select the orientation of the sectional 'slice'.

In **Figure 4-7** are illustrated the potential computed from point masses at two different depths, but measured at an elevation superior to the Earth's surface. In **Figure 4-8** are illustrated the corresponding gravitational attractions for the point source bodies of **Figure 4-7**. For one of the bodies, the eastward and northward gravitational gradients for an elevated measurement level (i.e. upward continued from the Earth's surface) are illustrated in **Figure 4-9**. Finally, in **Figure 4-10** is illustrated the magnitude of the gradient for the same body.

All illustrations were generated over a 20° by 20° rectangular surface and have had hidden lines removed for clarity. Readers are assured that the gradient figures are as asymmetrical as expected, and that the northward and eastward gradients had identical (or nearly so – some numerical imprecision results from differing order and content of calculations) values.

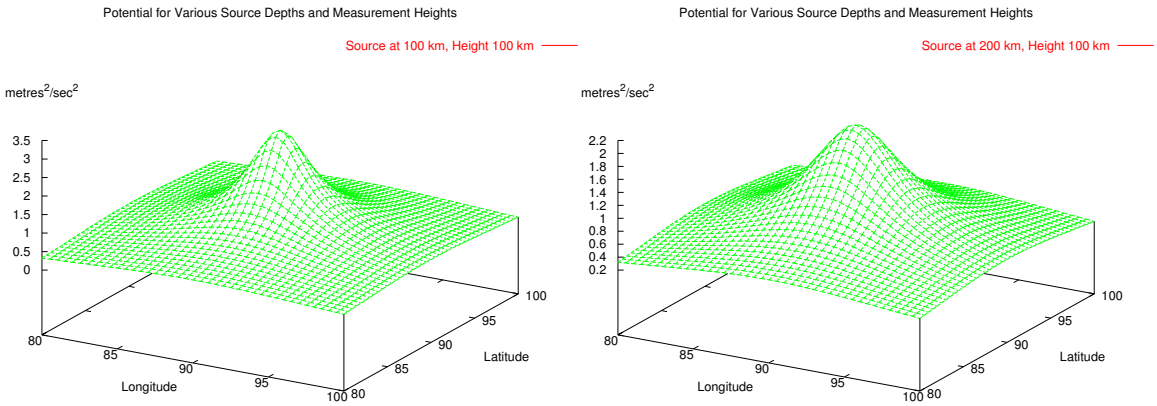

Figure 4-7: *An example of the potential calculated from a Pollack point source body at two different depths, and measured at some elevation above the Earth's surface.*

Using the wavelet technique described earlier, depth estimates resulting from several analyses for a single point mass were made and are illustrated in the following figures. They show the interpretation of the modulus maxima (i.e. location and magnitude) computed from the wavelet transform. The horizontal axis is given in terms of sample number while the vertical axis is the scale or dilation applied for each transform step. **Figure 4-11** illustrates points at depths of 50 and 100 km, while **Figure 4-12** is for depths of 200

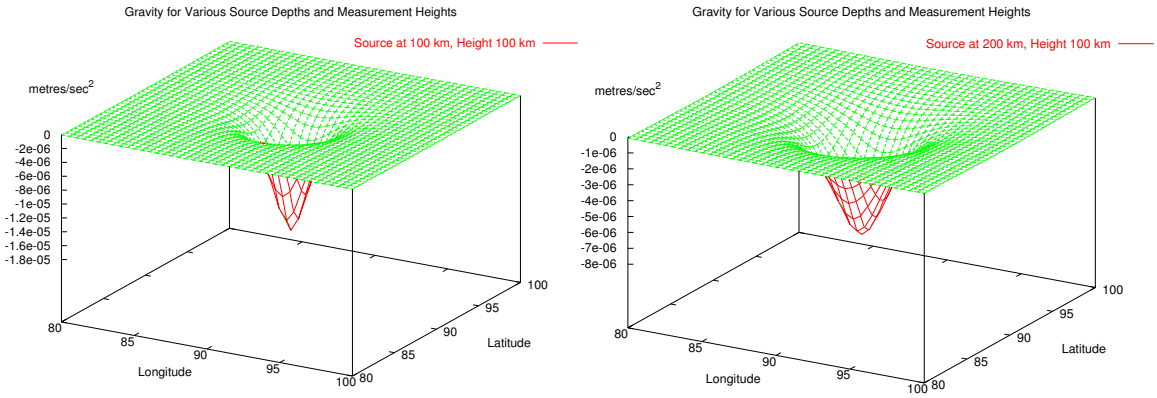

Figure 4-8: *An example of the gravitational attraction due to a Pollack point source body at two different depths, and measured at some elevation above the Earth's surface.*

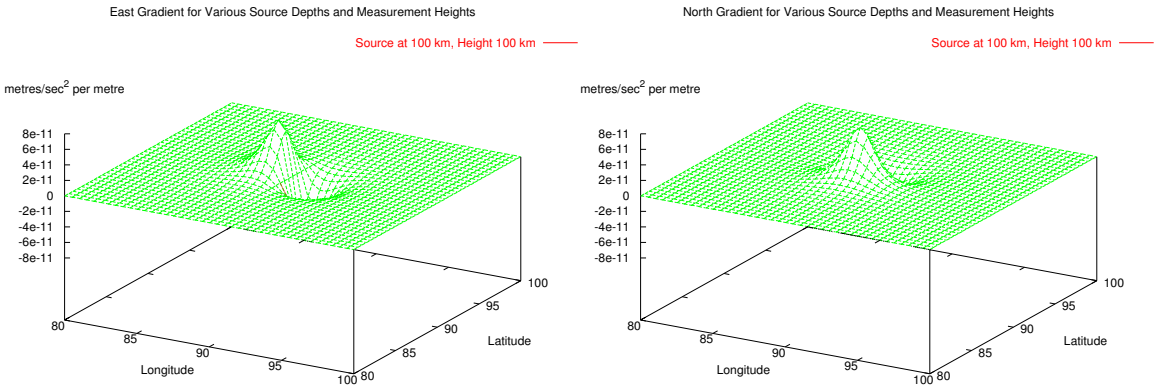

Figure 4-9: *An example of the gravitational gradients calculated from a Pollack point source body at a single depth, and measured at some elevation above the Earth's surface.*

---

and 400 km. Lastly, **Figure 4-13** is for a depth of 800 km. The estimated depths resulted from a least-squares analysis of the best fit line through the samples having the highest magnitude. No attempt was made to interpolate for a better estimate of where that point might lie. The heights to which continuation was taken were {0, 50, 10, 150, 200, 300, 400, 500}. Extending this list to {0, 50, 10, 150, 200, 300, 400, 600, 800, 1000, 1200, 1400, 1600, 1800, 2000} made no appreciable difference to the depth estimate. See **Figure 4-14**. As the gradient magnitude is symmetrical about the point source, only one half is shown.

The intercept at sample 180 is a measure of the depth to the source body. As noted

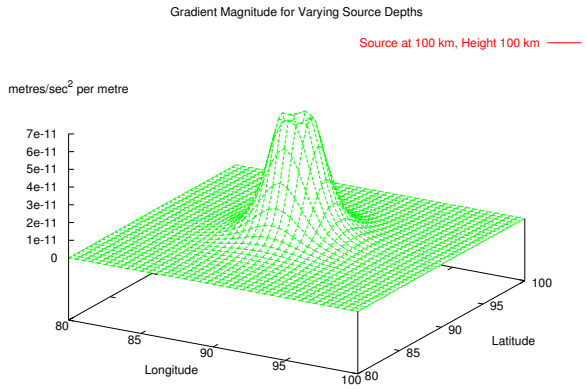

Figure 4-10: *An example of the magnitude of the combined gradients (effectively the magnitude of the wavelet transform of the gravitational attraction for an unspecified scale factor) calculated from a Pollack point source body at a single depth, and measured at some elevation above the Earth's surface.*

---

earlier in equation 3-60, the positions of the wavelet maxima are related to the source depth via (for a cross section through the source),

$$x = \frac{(s - z_d)}{2} \tag{4-7}$$

where z_d is the depth below the measurement surface to the body in question, and s is the **normalized** dilation factor for the wavelet transform which is given by,

$$s = \frac{z}{z_0} \tag{4-8}$$

with $z_0 = 1$. This term is Hornby's expression [Hornby, Boschetti, and Horowitz 1999, page 184]. Since the depth to the body (z_d) is unknown, and by implication, the height of the measurement surface relative to the body (z_0) is also unknown, and only the height above the measurement surface (z) is known, the scale or dilation becomes a relative measure. One can arbitrarily set $z_0 = 1$ to parameterize everything to a scale relative to the unknown source depth. Thus the intercept is an indirect measure of depth. Actual depth estimates require a knowledge of the intercept and an estimate of the distance between the intersection of the left and right gradient maxima lines (although for these experiments, as was indicated earlier only one line was required due to near perfect symmetry).

For example, if for the experiment the point source was placed at 90° colatitude (i.e. on the equator), and the synthesis was computed to degree and order 360, then the samples

would be taken at 0.5° intervals. For a nominal Earth radius of 6378 km, this corresponds to approximately 55.7 km between samples. If the best estimate of the line fitting the data points was for example,

$$s = 0.019069x - 2.506281 \tag{4-9}$$

as it was for the first 400 km deep experiment (see the following figures), then the intercept would be,

$$(1 - 0.019069*180 + 2.506281)*6378 \tag{4-10}$$

In other words, the distance below the $z_0 = 1$ level multiplied by the Earth's radius is the depth to source. The number 180 in the previous equation appears as the point source was placed at the 181st sample (counting from zero). The error of the estimate increases with increasing point depth, as shown in **Table 4-2**.

First Attempt Depth Estimates (km) for Single Points

Actual Depth	Estimated Depth	Standard Deviation
50	58.7	±20.2
100	102.5	±36.2
200	228.4	±32.6
400	471.6	±32.6
800	958.1	±32.6
1600	1934.6	±36.2

Table 4-2: *For a single mass anomaly, depths were estimated using the largest observed value for analysis.*

As an illustration of the effect of increasing the height to which the measurements are upward continued, see **Figure 4-14**, which shows the same point mass situated at a depth of 1600 km. The left figure has a maximum continuation height of 500 km, while the right has been taken to 2000 km. Note the change in the slope and intercept. Based on the intercept, the estimated depth for the lesser of the continuation heights is 2072.7 ±38.1 km, while that for the greater continuation height is 1934.6 ±36.2 km. Examining the figures, it is apparent that the intercept can be greatly affected by the point distribution. A better estimate would be one where the horizontal coordinate (x in the example calculation shown in equation 4-9) was unity. This point is within or very near the set of measurements, and thus suffers less from the sensitivity of estimates due to slope error.

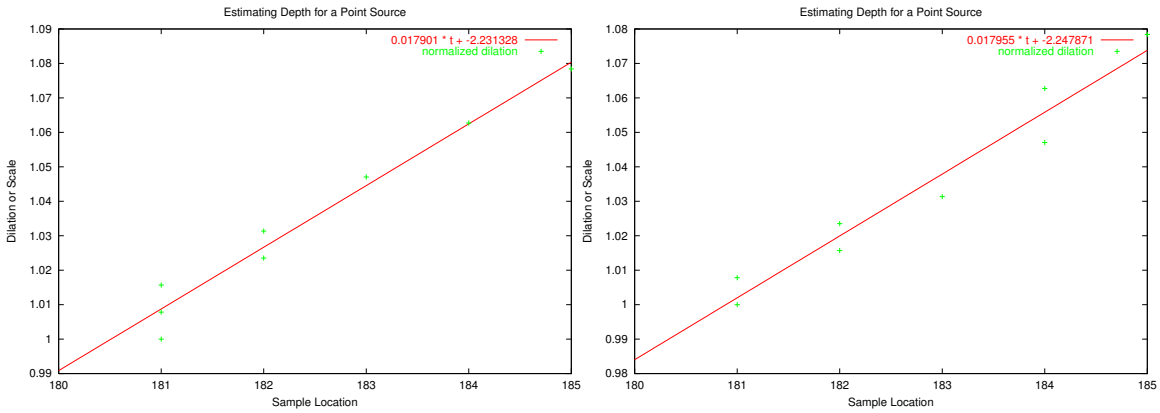

Figure 4-11: *Fifty and one hundred kilometre depths for a single point source.*

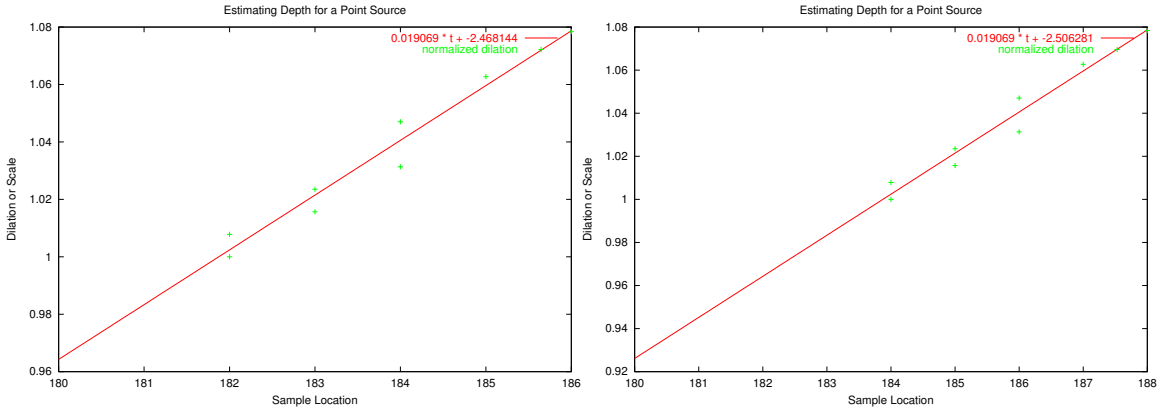

Figure 4-12: *Two and four hundred kilometre depths for a single point source.*

Furthermore, the point at which the regression line crosses the horizontal axis equals the depth to the source body. The depth estimates for the previous examples using that value are illustrated in **Table 4-3**. The additional experiment for a body at 1600 km with upward continuation to 2000 km had depth estimates of 2072.7±38.1 km using the intercept and 1898.7 km using the horizontal axis as the reference.

Anticipating that a better estimate of the peak location might improve the accuracy of the depth estimates, a simple parabolic interpolation around the highest magnitude observed was performed for selected depths. This didn't have the desired effect, although the standard deviations were improved for the most part. These are illustrated in **Table 4-4** for selected point source depths. As well, in **Figure 4-15** for depths of 1600 km and 200 km,

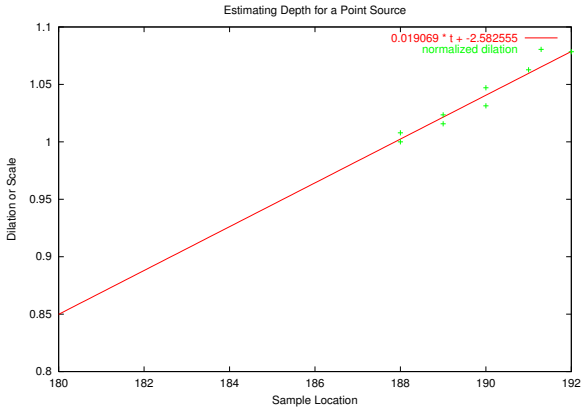

Figure 4-13: *Eight hundred kilometre depth for a single point source.*

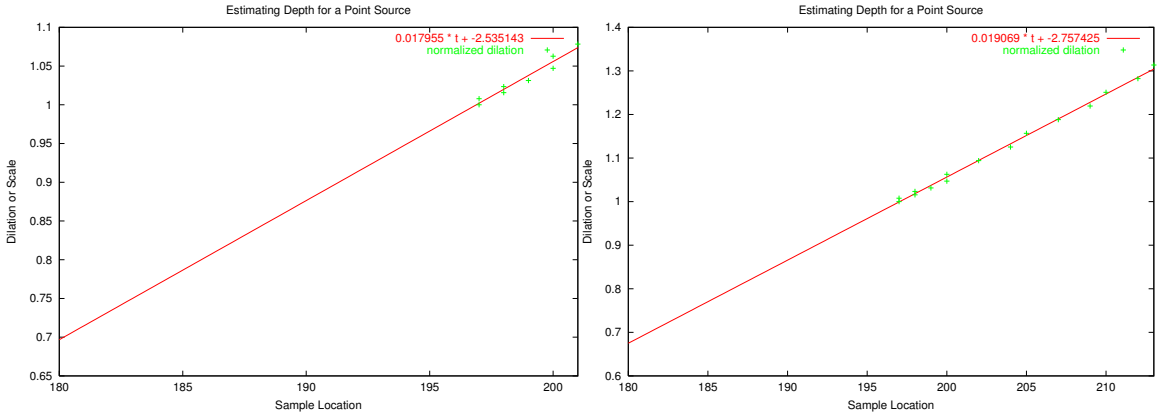

Figure 4-14: *The left hand illustration shows the depth estimate for a point source at a 1600 kilometre depth upward continued to 500 km. The right hand figure is the same body upward continued to 2000 km.*

one can see the improvement in the line fit. Part of the problem associated with finding the maximum of the transform is the sampling of the field. For example, for a depth of 100 km, with 0.5° sample spacing at the equator, **Figure 4-16** shows how well the magnitudes for various upward continuation heights are defined. On the other hand, for a deeply buried body, the sampling frequency appears to be quite adequate. This is illustrated in **Figure 4-17**.

4.4 Estimating Depth in More Complex Situations

This section will consider the problem of making depth estimates when there is more than one body in the study area. It will be seen that this seriously complicates the issue, and that the interpretation requires greater care. Whether it would be possible to automate

Modified Depth Estimates for Single Points (km)		
Actual Depth	**Estimated Depth**	**Standard Deviation**
50	56.9	±20.2
100	99.1	±36.2
200	208.7	±32.6
400	431.5	±32.6
800	877.1	±32.6
1600	1881.4	±36.2

Table 4-3: *Errors incurred when making depth estimates using a different reference point at which to make that estimate.*

Parabolic Depth Estimates (km) for Single Points			
Actual Depth	**Depth from Intercept**	**Depth from Unit Dilation**	**Standard Deviation**
100	117.8	106.8	±40.9
200	265.0	235.3	±18.3
400	495.4	442.7	±19.5
800	983.9	887.2	±20.0
1600	2064.7	1896.8	±21.9

Table 4-4: *Errors incurred when using a parabolic fit to make depth estimates.*

this process is currently an outstanding problem.

Previous illustrations were the gradient and magnitude graphs for a single body. Consider the case where there are 2 bodies in moderately close proximity. Let one be at a depth of 100 km, and the second at a depth of 200 km, and let them be separated by 5°, using the Earth centre as the coordinate reference. Let each have a mass of 10^{20} gm. These characteristics are outlined in **Table 4-5**.

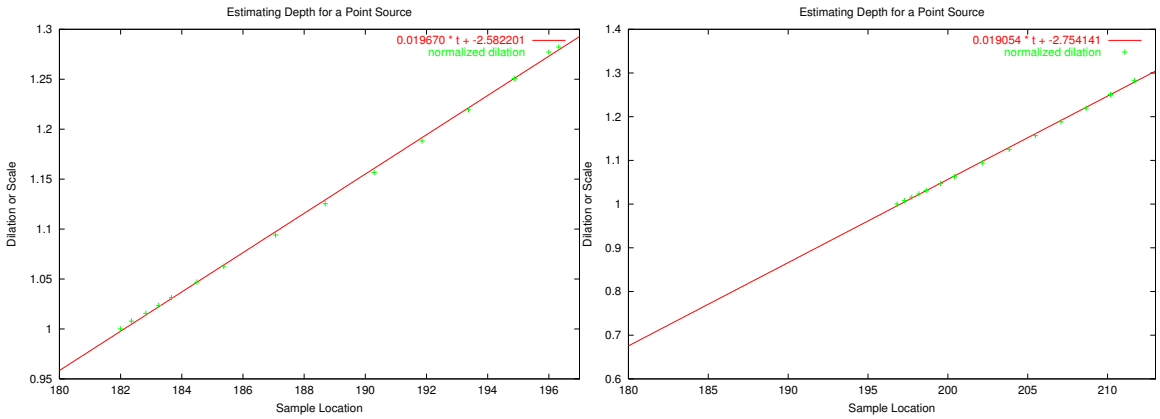

Figure 4-15: *On the left is a body buried at 200 km, and on the right the depth is 1600 km. Using parabolic interpolation of the three points encompassing the maximum observed gradient magnitude, less variation about the line fit is observed. This suggests an improved depth estimate might result.*

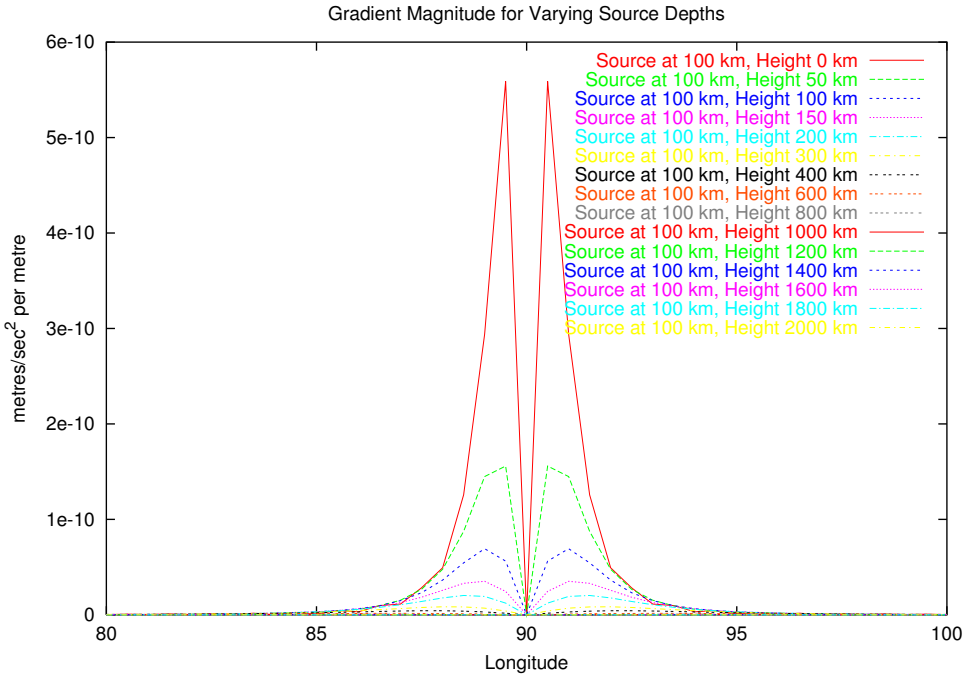

Figure 4-16: *For 0.5° sampling, the definition of the magnitude of the gradient (i.e. the wavelet transform) is less than ideal for a shallow body at low heights above the measurement surface.*

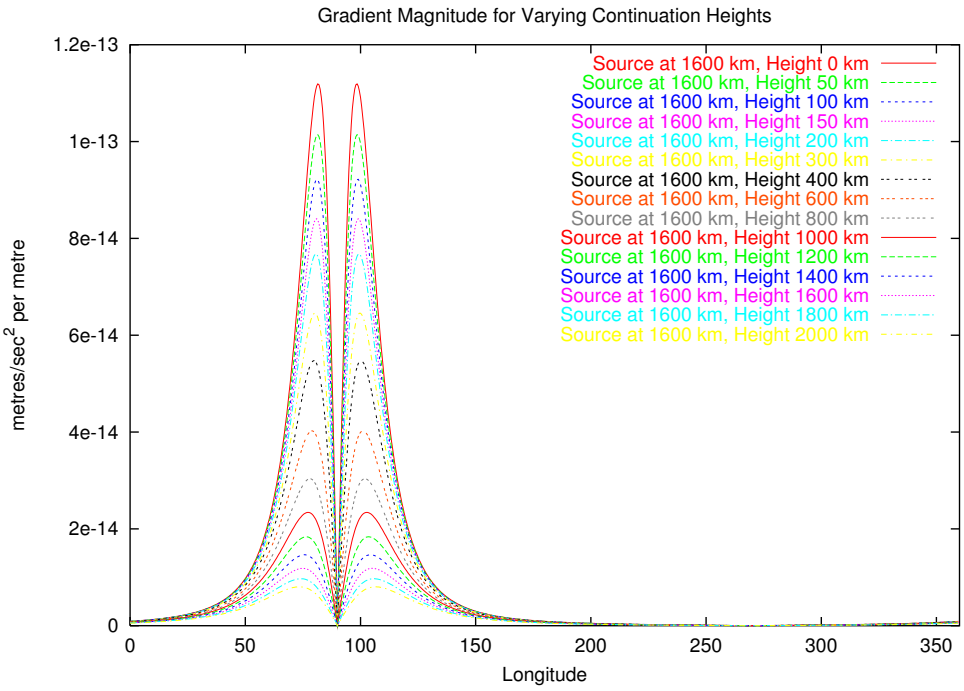

Figure 4-17: *For 0.5° sampling, the definition of the magnitude of the gradient (i.e. the wavelet transform) appears to be satisfactory for a deeper body.*

Two Body Problem

Latitude	Longitude	Depth (km)	Mass (gm)
0.	140.	100.	10^{20}
0.	145.	200.	10^{20}

Table 4-5: *A simple two body problem for testing the wavelet technique.*

The potential generated by such a simple model is shown in **Figure 4-18** and the gradient is illustrated in **Figure 4-19**. Evidently, the gradient is easily interpreted as to where it crosses the horizontal axis. Thus the magnitude for at least one scale (i.e. scale = 1) is easily determined. Given that the peaks of the magnitude diverge with increasing scale, it should be recognized that complications will quickly result.

As well, as the bodies become closer, it becomes increasingly difficult to separate them, as is illustrated in **Figure 4-20** and **Figure 4-21**. In **Figure 4-22** one can see the wavelet transforms for the two-body problem synthesized to degree and order 360. To keep the profiles in a displayable range, they are shown in two overlapping illustrations. The continuation height of 200 km is common to both. In **Figure 4-23** one can see the two body

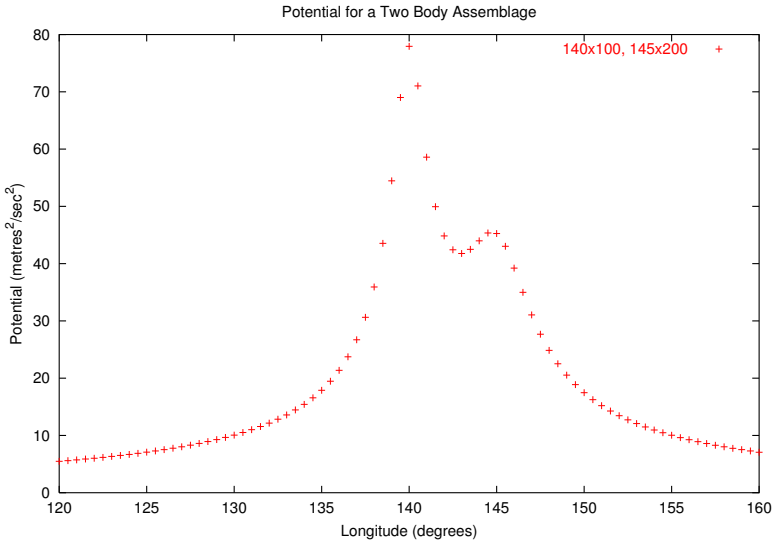

Figure 4-18: *The potential generated by the two mass anomalies described in the text.*

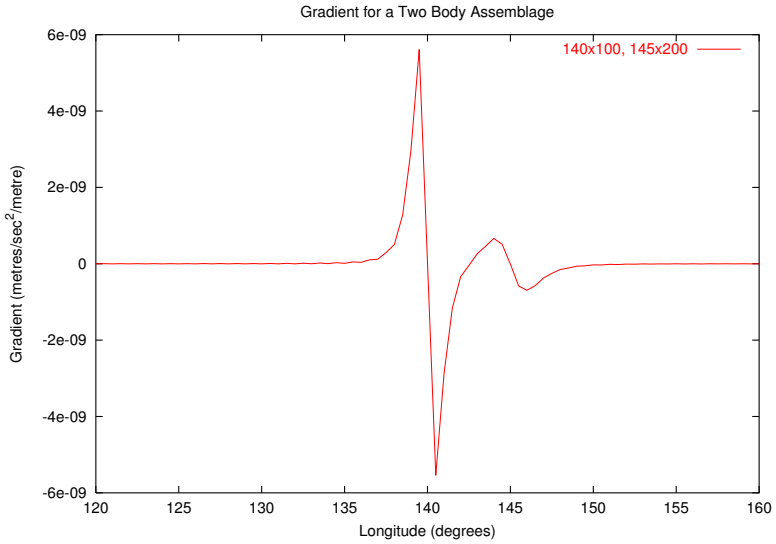

Figure 4-19: *The gradient generated by the two mass anomalies described in the text.*

---

problem with the maxima and minima displayed for analysis. The minima have been scaled by -1 so that they can be easily selected for display. Normally, they would be positive numbers. The drift in their location is an indication of the difficulty in identifying the number and locations of point sources as the transform proceeds through different dilations.

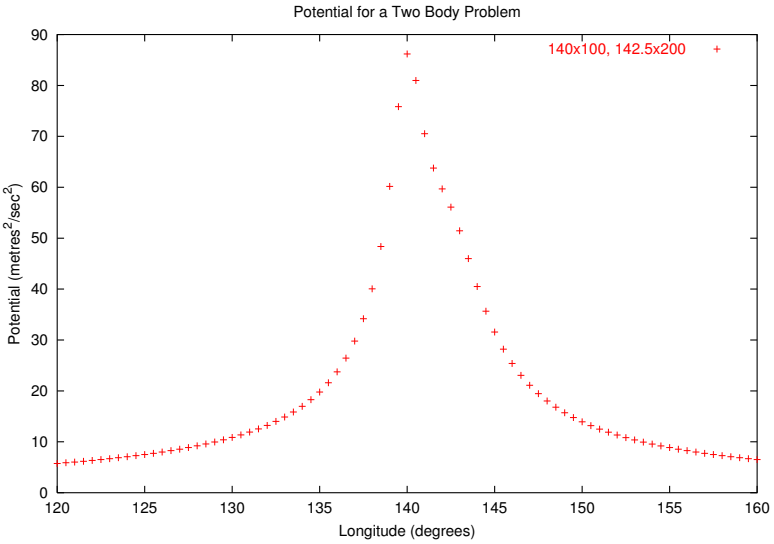

Figure 4-20: *Separating the bodies by smaller angular amounts increases the difficulty in recognizing their existence. This is illustrated in this graph of potential for 2 bodies separated by 2.5°, with all other parameters as before.*

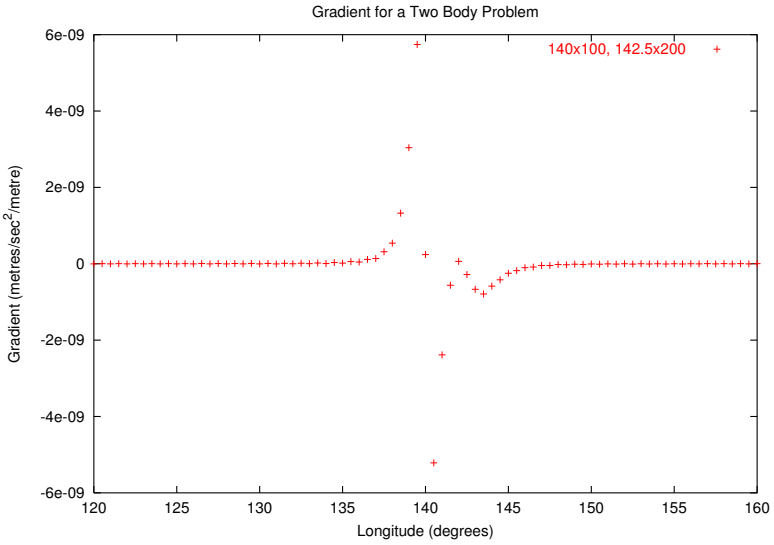

Figure 4-21: *With the same parameters as* **Figure 4-20***, this illustrates the gradient calculation for decreasing separation.*

At a higher degree, better resolution is achieved, albeit at the expense of computational cost. **Figure 4-24** illustrates the same two body problem synthesized to degree and order 1440 (i.e. 0.125° resolution). The peak definition is much improved, and combined with the identification of the peak maxima (see **Figure 4-25**), and the corresponding

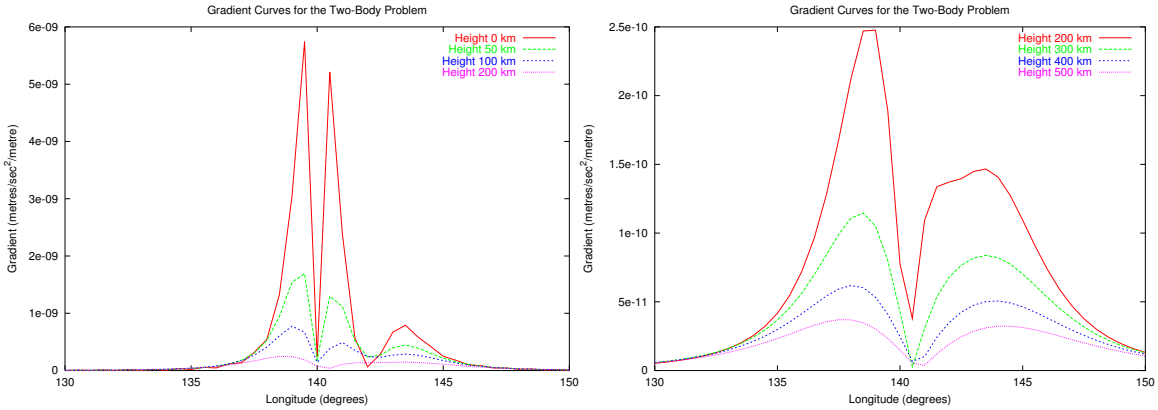

Figure 4-22: *The gradient magnitudes for various continuation heights for the two-body problem. The degree and order for the synthesis was 360.*

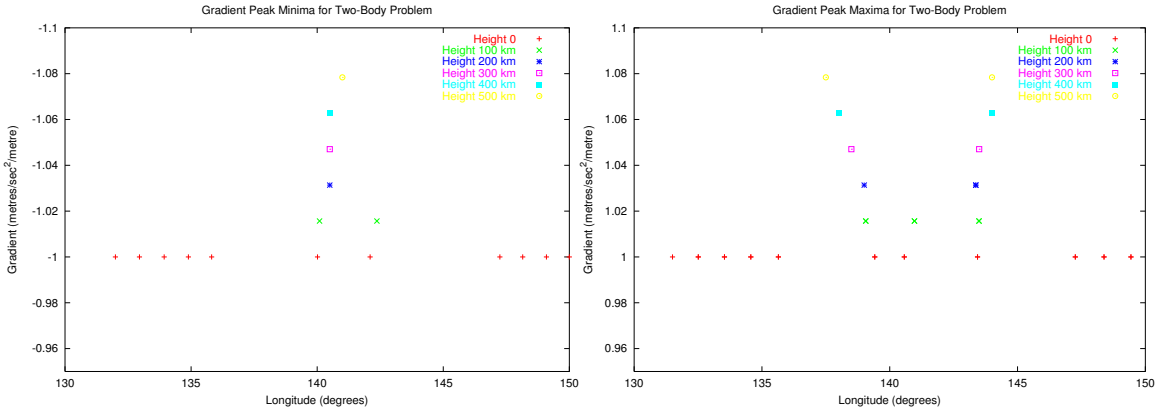

Figure 4-23: *For the same two bodies separated by 2.5°, and differing in depth by 100 km., the interpretation of depth and source location becomes much more difficult. The degree and order for the synthesis was 360.*

intervening minima, make interpretation somewhat easier. Applying the techniques described earlier for estimating depths, one is able to make up to three estimates for the left hand body. In **Figure 4-26** are shown the gradient maxima at upward continuation heights ranging from 0 to 200 km. These correspond to all but one of the peaks identifiable in **Figure 4-24** and **Figure 4-25**. The 200 km peak on the right hand side of that figure is sufficiently influenced by the adjacent body that the peak location is unusable. This is easily seen when plotting the estimated line which fits the data points. The slope is inordinately in error. Deleting the point corrects the problem. To be fair, one must note that this is an interpretation issue, but it is readily identified as an error of some sort. By referring back to the gradient curves, it is easily seen.

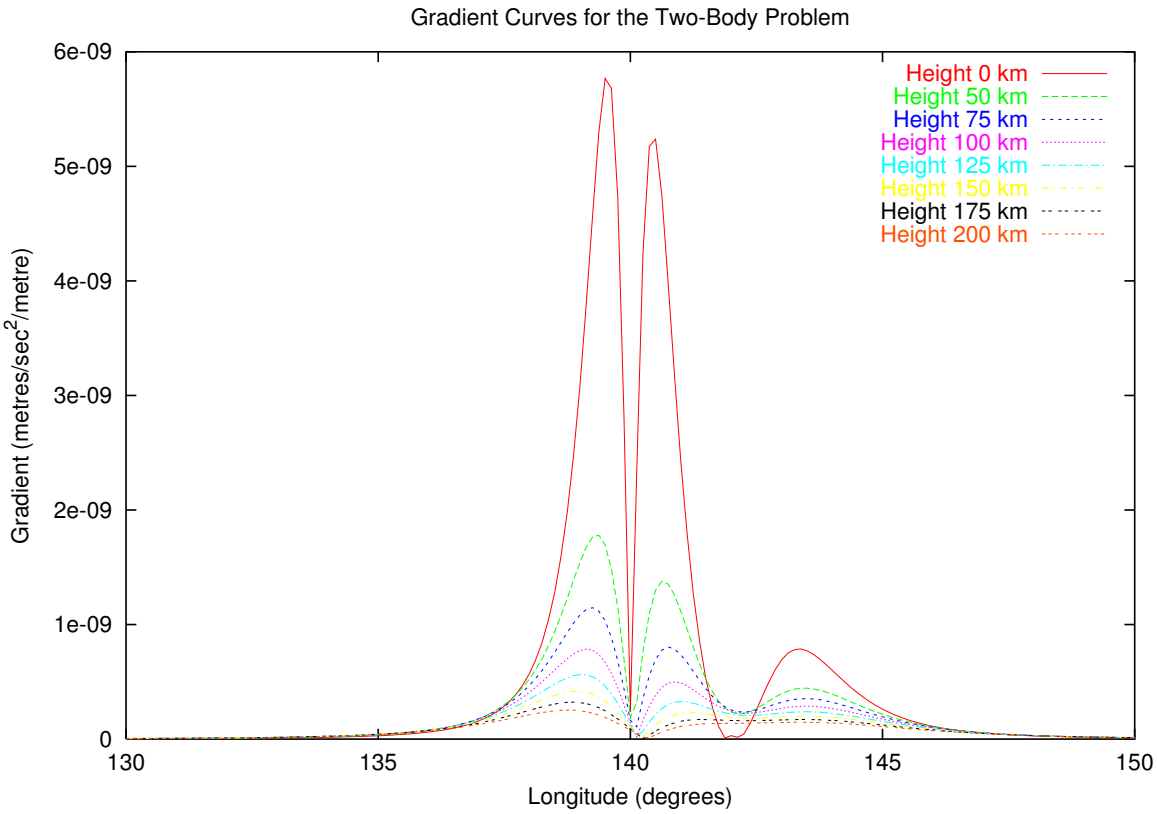

Figure 4-24: *Defining the anomaly to a higher degree (here to degree and order 1440) enables the interpreter to better comprehend the anomalous feature. This is the same two-body problem as in the previous illustrations.*

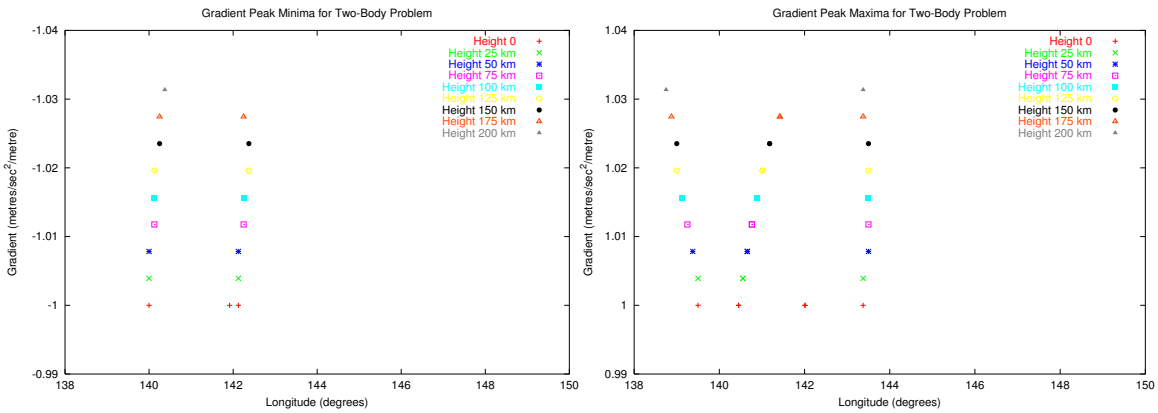

Figure 4-25: *The minima (left) and maxima (right) that correspond to the gradient curves illustrated in* **Figure 4-24**.

Even with this *correction*, it is obvious that the two slopes do not agree, which isn't surprising as it should be obvious that one is not dealing with a single point source.

Nevertheless, one can find that the intersection of the two regression lines occurs at a depth of 89 km. Using the offset technique, that is using the point at which the regression lines cross the scale = 0 line, yields estimates of 99.7 km and 86.9 km for a mean value of 93.3 km. Finally, as one can note that the minimum in the gradient curve seems to be well positioned over the longitude 140° mark, one can estimate, from the left hand curve that the depth is 99.7 km, on the presumption that it is more reliable.

A significant factor in the interpretation is the ability to resolve the anomalies so that good estimates of gradient maxima magnitude and location can be made. A second and equally important factor is the ability to isolate at least one half of the wavelet transform from the effects of adjacent bodies.

A rudimentary examination of gradient maxima shown in the right hand side of **Figure 4-25** indicates that without taking some corrective action for the influence of the dominating body to the left, any depth estimate will be inordinately high. This requires a mass estimate, and then the insertion of an appropriately signed mass at the prescribed depth and location to remove the effect of the dominant body.

A rough calculation using the measured potentials between 135° and 140° suggests a mass of about $1.5*10^{17}$ kg. While this is 50% too high because the second body is a also a contributor, it must be accepted. As might be expected, if the mass and depth are correct, a negative mass will exactly remove the effects of a positive mass. Error in either of these quantities causes the exercise to be frustrating. Only by successive mass reductions can one remove the effects of the erroneously high mass estimate. These manifest themselves as negative potential, which of course is not possible except in the case of the anomalous potential. Note that the assumed mass geometry will also affect the outcome of this step. In these experiments, only the simplest shapes (point sources) were used[60].

A second attempt which utilizes the apparent fact (deduced from **Figure 4-18**) that the right hand body has roughly one half the potential of the first allows for a better result. Clearly this is highly interpretive, but like most geophysical analyses, there is a requirement to achieve some reasonable resolution to the problem at hand. Assuming that the right hand body contributes about one half the potential can be realized by an anomaly of

[60] In the paper [Hornby, Boschetti, Horowitz, and Archibald 1997a] is an illustration of how the most unusual geological interpretations can fit the measured potential field. The fact that anything (the head of Mickey Mouse® with appropriate ear and brain density in the cited reference) can produce the observed field suggests that the simplest models should be used.

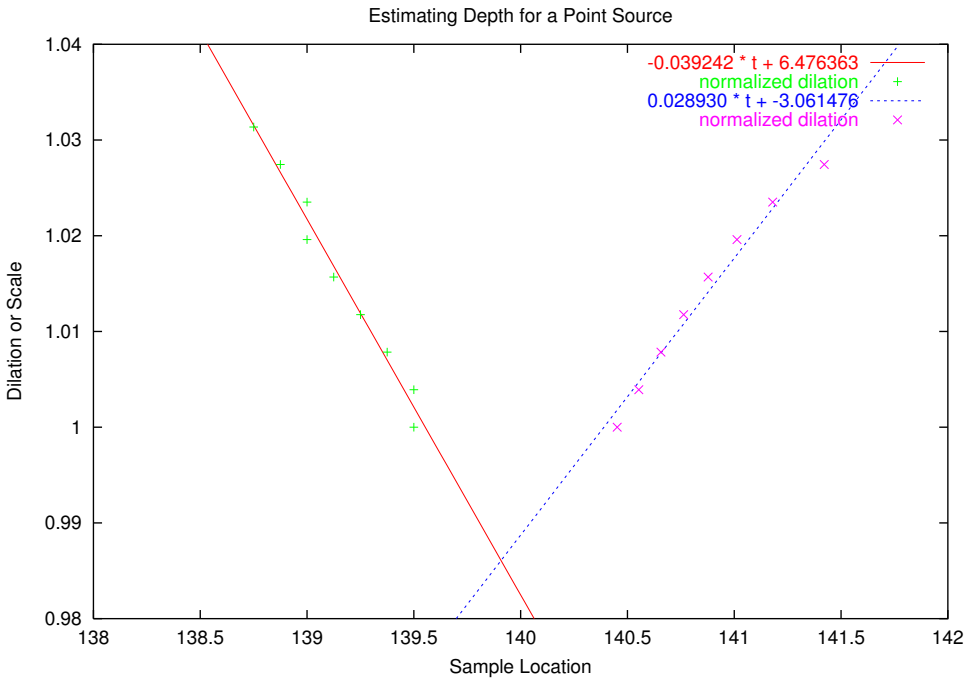

Figure 4-26: *The interpretation of the left body in the two body problem. The degree and order for the synthesis was 1440. Without this degree of resolution (0.125°), and the use of smaller continuation heights, the difficulty of interpreting is increased.*

---

one half the mass at the same depth, or the same mass at twice the depth (or any of a very large number of variations, keeping in mind that depth and the *width* of the associated surface expression are related).

Using these two extremes results in several mass estimates with associated error in the estimated potential. Two tests were conducted: the first used potential measurements across the pair of bodies (from 130° to 150°), and the second reduced the affect of the second body by dropping potential values from 140° to 150°. The results are in **Table 4-6**.

Two Body Mass Estimates Given One Body's Depth Estimate

Range of Potentials	Depth 1 (km)	Depth 2 (km)	Mass 1 (gm)	Mass 2 (gm)	RMS Difference in Potential
130° - 150°	93	186	$0.85*10^{20}$	$1.11*10^{20}$	0.216
	93	93	$1.04*10^{20}$	$0.58*10^{20}$	0.735

Two Body Mass Estimates Given One Body's Depth Estimate

Range of Potentials	Depth 1 (km)	Depth 2 (km)	Mass 1 (gm)	Mass 2 (gm)	RMS Difference in Potential
130° - 140°	93	186	$0.84*10^{20}$	$1.18*10^{20}$	0.079
	93	93	$0.72*10^{20}$	$1.33*10^{20}$	0.147

Table 4-6: *Mass estimates with associated error in the estimated potential.*

One of these stands out with much lower error in the estimated potential, although two others are close. One can select the former and use the mass estimated for the left hand body to remove its effect.

The result is illustrated in **Figure 4-27**. There is clearly a residual anomaly in the potential after adding the negative mass at longitude 140°.

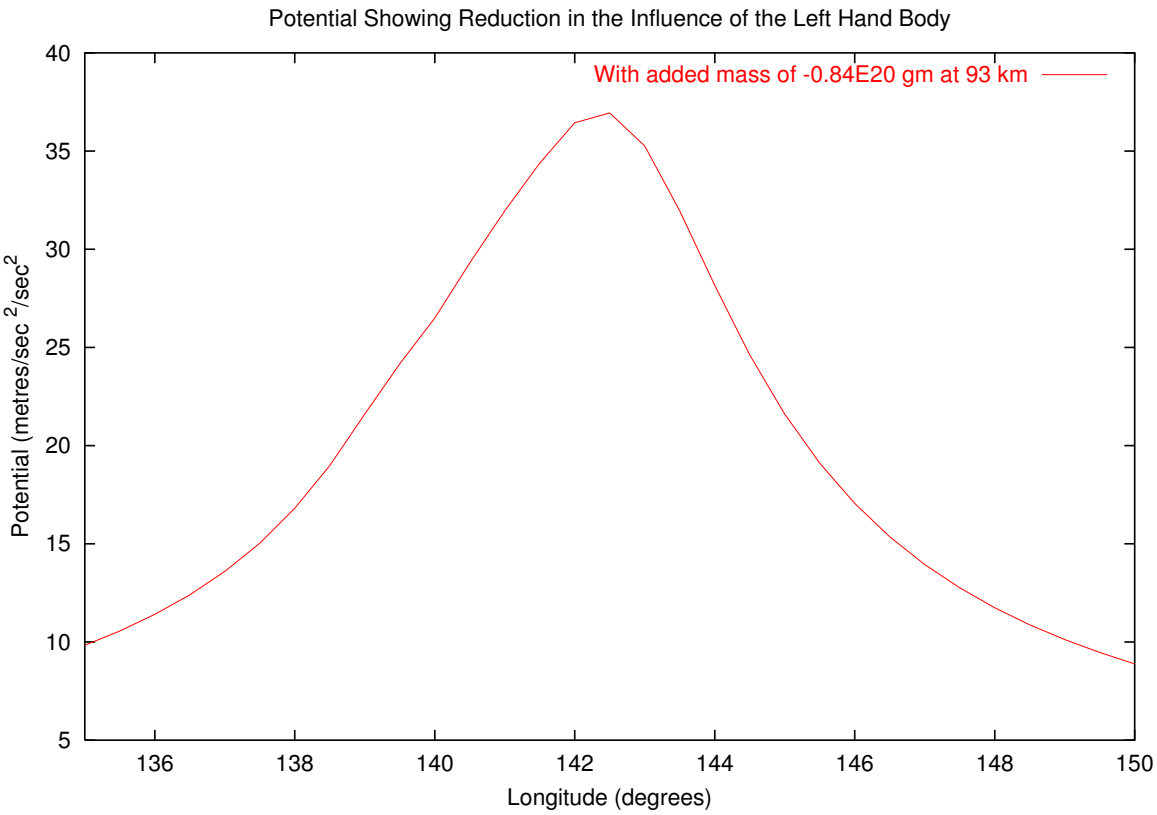

Figure 4-27: *A negative mass of -0.836*$*10^{20}$ *gm has been added at longitude 140°. A residual anomaly is clearly visible.*

In the following figures (**Figure 4-28** and **Figure 4-29**) are the gradient and gradient

maxima/minima curves. It is evident that the right hand body is now better defined[61] so that a depth estimate may be made.

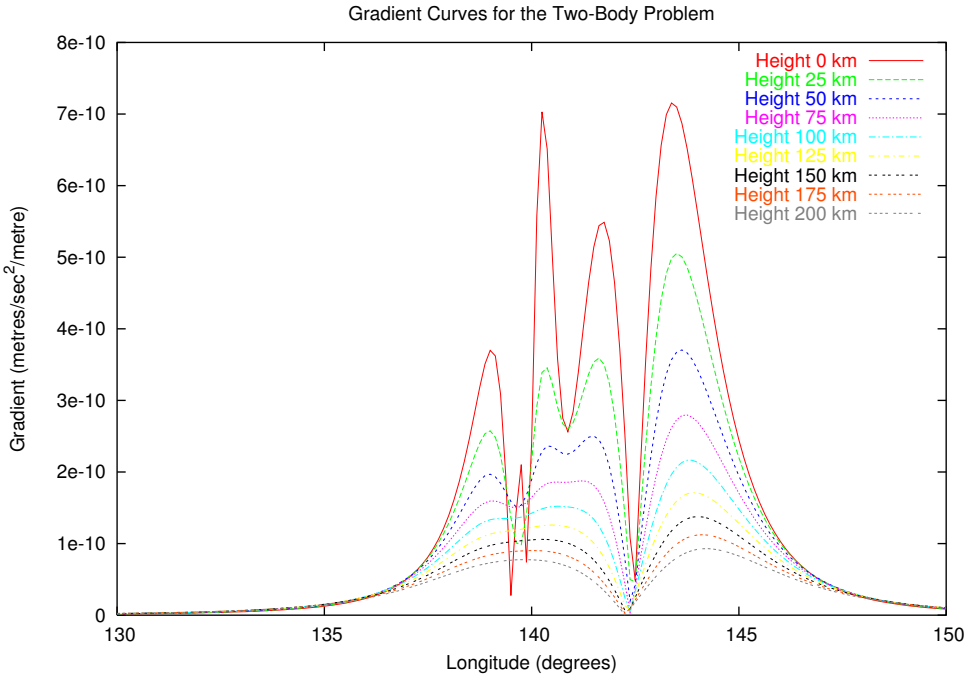

Figure 4-28: *The left-most body has been subtracted after estimating a depth, assuming a depth for the presumed second body, and then estimating masses for both. While complicated in appearance, probably due to inadequate mass removal, the right-most transform curves now appear to be reliably interpretable.*

The interpretation of these curves is that the right hand body is probably located nearer to 142.5° (previously presumed to be at 142°). As well, one can compute from the regression lines that the second body is somewhere between 216.2± 7.4 and 199.3± 7.4 km below that location. These figures come from the two methods described earlier for the right most line shown in **Figure 4-30**. The left hand line is presumed to be less reliable as it is evidently still influenced by the remnants of the first body. It suggests depths of 121.9 and 142.1 km with a standard deviation of ± 16.4 km.

Using the mean of the two presumably more reliable depth estimates, one can calculate the mass for the two bodies, based on the measured potentials as in **Table 4-7**.

The potential across the two bodies after these calculations compares favourably with the

[61] At least on the right hand side.

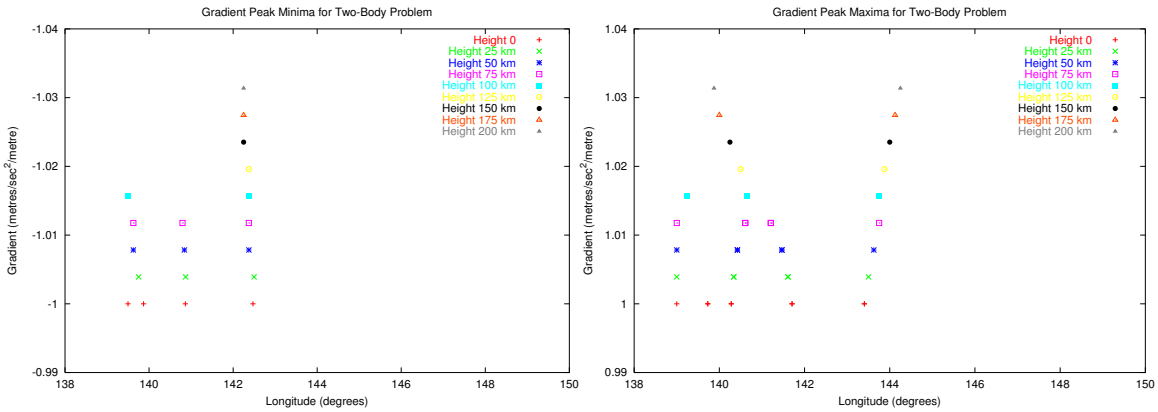

Figure 4-29: *On the left are the minima for the gradients across the two body problem after the left most body has been removed by subtracting an estimated mass at its estimated depth. On the right are the maxima for the same two bodies. The right-most gradient peaks now resemble the left-most in the previous analysis, and appear to be interpretable. These curves correspond to the transforms shown in* **Figure 4-28**.

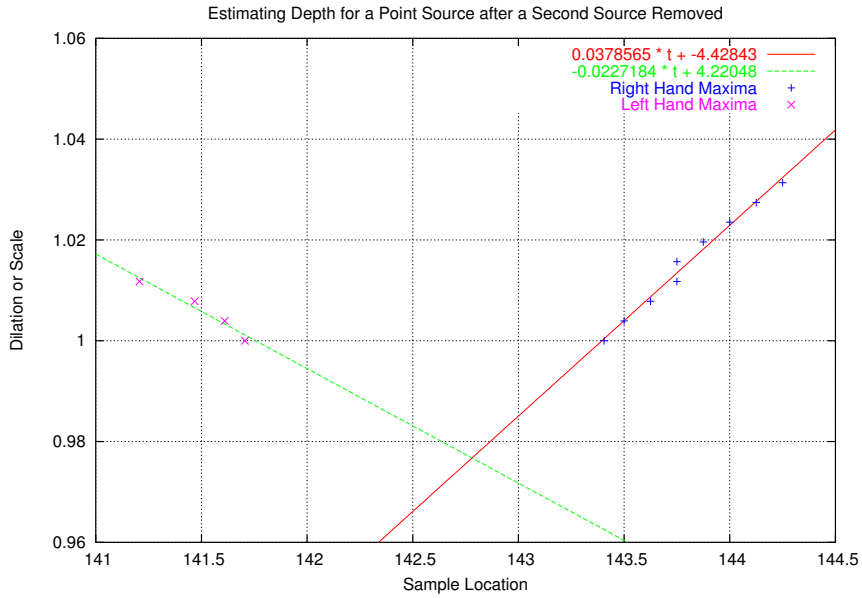

Figure 4-30: *The interpretation of the second (right hand) body after removing the left hand feature. Note that the left-most regression line is based on fewer points because there was a lack of local maxima attributed to the left had side of the local minima.*

---

measured values, as seen in **Figure 4-31**. The standard deviation for the difference in

potential along the entire parallel is $4.031*10^{-3}$ with the largest difference occurring at 140°. That value was 1.70 when the actual maximum was 86.2. Adjacent difference values were at least an order of magnitude smaller.

Two Body Problem: Estimated Depths and Masses

Colatitude	Longitude	Depth (km)	Mass (gm)
90.000	140.0	93	$9.377*10^{19}$
90.000	142.5	200	$1.046*10^{20}$

Table 4-7: *Using measured potentials, and presumably reliable depth estimates, masses are estimated.*

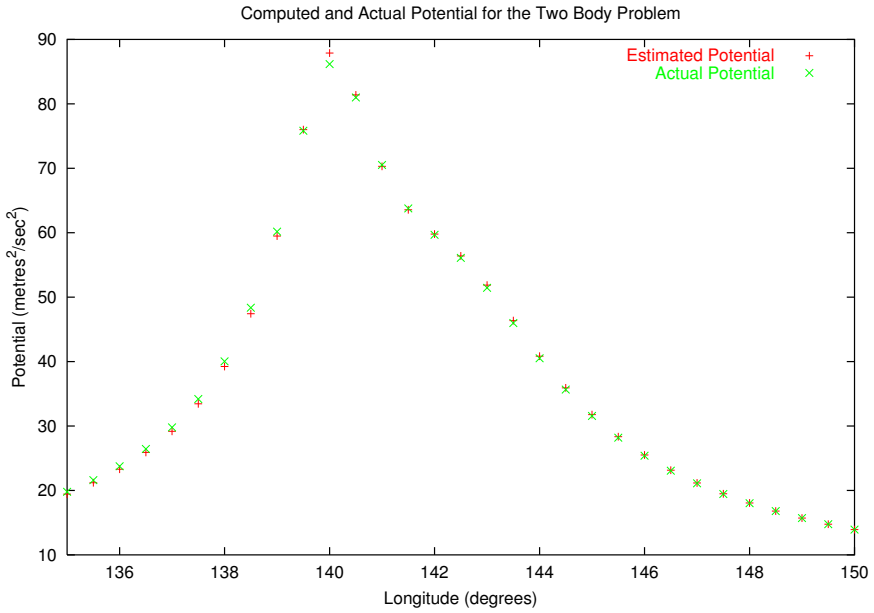

Figure 4-31: *After estimating the depth and mass for the two bodies, one can compare the potential as originally measured and that computed for the interpreted model.*

When performing the least-squares analysis of the gradient maxima, no weights were assigned to individual samples. This might be counter intuitive as the wavelet transform clearly is affected by the degree of smoothing that the scaling due to measurement elevation contributes. Obviously, a transform taken at a higher elevation is 'further away' from the body of interest. Furthermore, an examination of the gradient curves, such as **Figure 4-24** for example, indicates a decrease in the sharpness of local extrema, which

could easily contribute to error in locating that point.

Isolated bodies show very little extrema location variation at small scales and would not benefit greatly from such a procedure (see the interpretation in **Figure 4-15**). Complex assemblages such as that of **Figure 4-24**, and which is interpreted in **Figure 4-26**, have the additional complication of adjacent body interference which cannot help but influence the position of the extrema. On the right hand side of that figure, it is quite obvious that weighting according to dilation would not be free of that effect, and hence erroneous values would result.

4.5 The South American High

One of Bowin's areas of interest was the South American High, centred roughly at 110° by 290° [Bowin 2000]. His research and a description of how it was used in this research are described in the following chapter. In **Figure 4-32** are illustrated the **GEMT1** and **EGM96** geopotential models over that anomaly. See [Marsh et al. 1987] and [Lemoine et al. 1998] for model details. The former model is a considerably simplified synthesis compared to the latter. Obviously an analysis of deep-seated bodies would need the de-emphasis of the higher spectral components in order to obtain an interpretable wavelet transform of the low frequencies. A cross section of the potential at colatitude 110° is illustrated in **Figure 4-33**.

Choosing a dataset for the transform can be approached in several ways. Firstly, because the GEMT1 model is inherently smoother, owing to the averaging of the limited data available at the time the model was created, it would provide a good starting point. Alternatively, the EGM96 model could be truncated at a suitably low degree, much as Bowin did in his analysis, or it could be filtered with an appropriately shaped Butterworth operator.

As has been seen, using a low degree (e.g. degree 36) model yields very poor results for the wavelet transform because of the associated coarse sampling of the field. The better alternative is to use a high degree model with appropriate filters applied to reduce the complexity. This complexity is highlighted in **Figure 4-33** where the EGM96 model is shown in profile across the South American high in question.

Truncating the model to a lower degree greatly simplifies the analysis. In **Figure 4-34** are shown two truncations. One is to degree 36, and the other to degree 10. As Bowin

points out, the contribution to the Earth's geoid anomalies show little change with the addition of spherical harmonic components in excess of 10. In fact, the largest contributions come from degrees 2 and 3, and the power spectra for the Earth range over some 8 orders of magnitude to degree 10. Thus it is not unreasonable to employ a spectrum of maximum degree 10, or possibly even less.

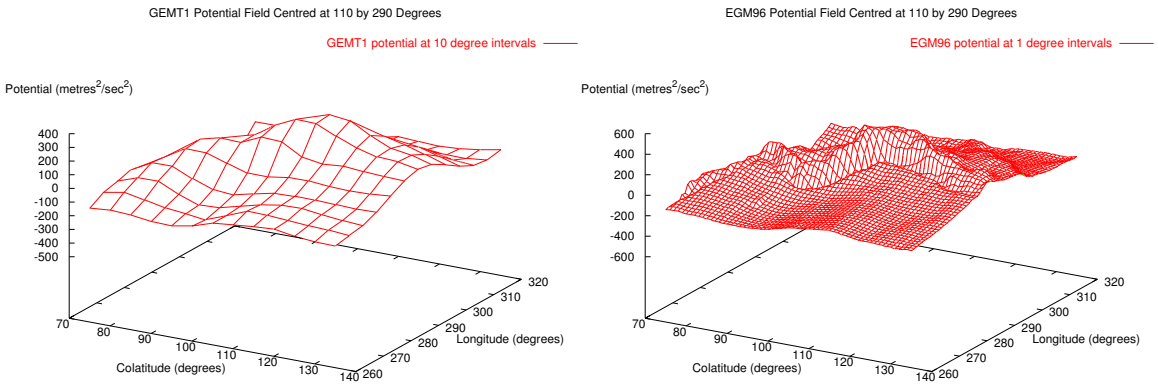

Figure 4-32: *On the left is the GEMT1 geopotential model over the South American high. On the right is the same anomaly synthesized from EGM96. Note the complexity introduced by the latter field description.*

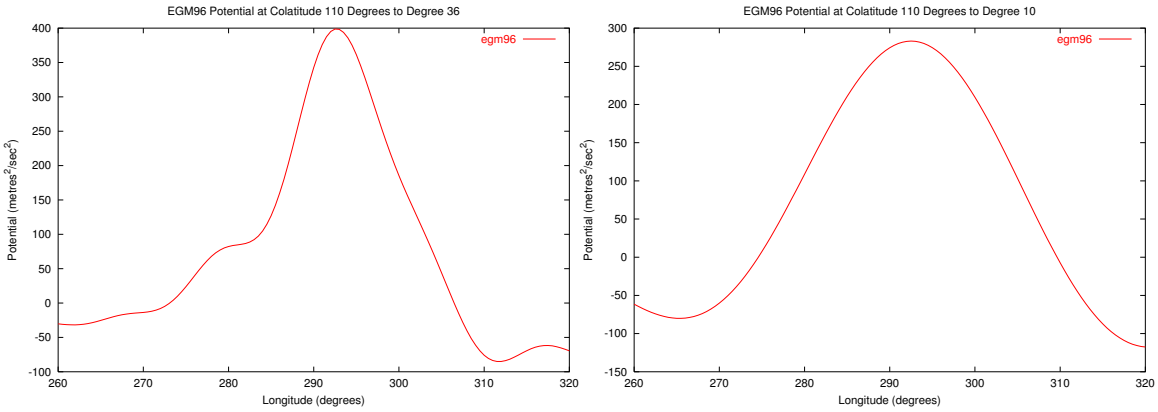

Figure 4-34: *Both figures show the same profile as illustrated in* **Figure 4-33**. *On the left, the EGM96 spectrum has been truncated at degree 36, and on the right, to degree 10.*

Interpreting the filtered high requires an appropriate choice of continuation heights. Using heights similar in range to those employed for shallower anomalies, such as the 100 or 200 km deep bodies of the demonstration studies, proves inadequate for a much deeper body. This is illustrated in **Figure 4-35** where one can see the gradients over the anomaly of interest. Careful study indicates that they do not converge at a reasonable

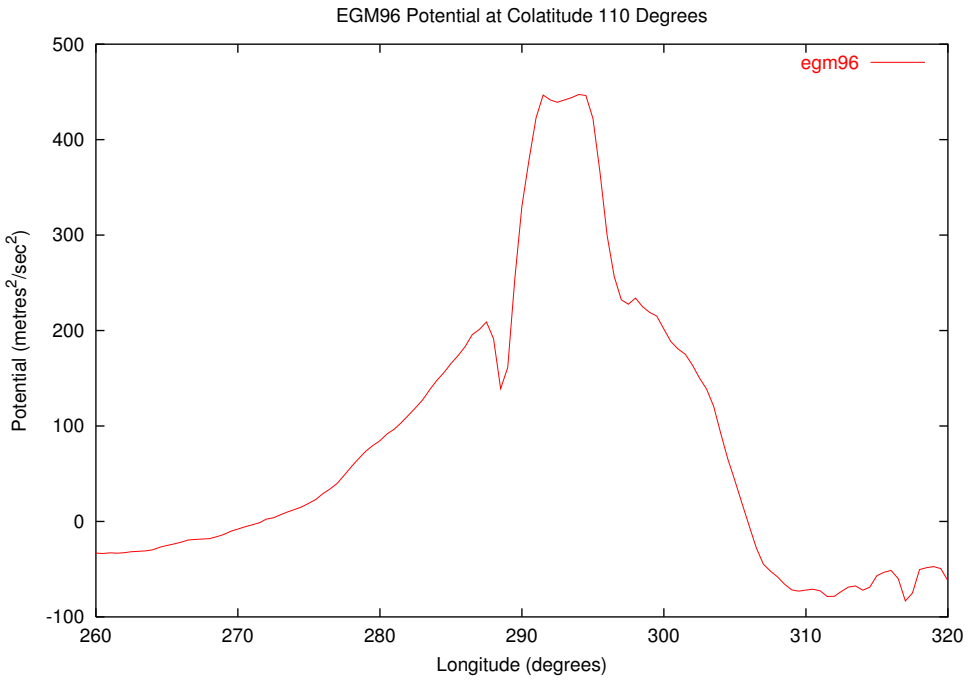

Figure 4-33: *A cross section of the potential illustrated in the previous figure taken at colatitude 110°.*

---

depth, but the convergence rate is not as easily seen as in earlier experiments. This may be due to the influence of other nearby anomalies, and so the depth at intercept is meaningless. The depth computed from the scale zero value is likely more indicative of the true depth. The scale zero depth is estimated to be in the range 2415 to 2476 metres.

Using continuation heights ranging from 0 km to 2000 km gives similar results. The high side of the anomaly, that is, the magnitude of the gradient to the right in the figure still suggests an impossibly large depth (anywhere from 42,000 to 62,000 km). The zero scale intercept gives about the same values as before: 2397 to 2470 km. To illustrate the problem, see **Figure 4-36**. In this figure one can see the both sides of the anomaly. If it were due to a point source, without being affected by adjacent bodies, the two lines would converge to intersect at the approximate depth of that body. The line on the right hand side clearly has the wrong slope, indicating external influences.

The position of the anomaly is less in doubt. Its location is close to 293.25±0.25°. This is evident from the gradient display in **Figure 4-35**. It is surmised that the transform magnitudes are being influenced by other sources. That these exist are evident in **Figure 4-37** where at least two others are apparent.

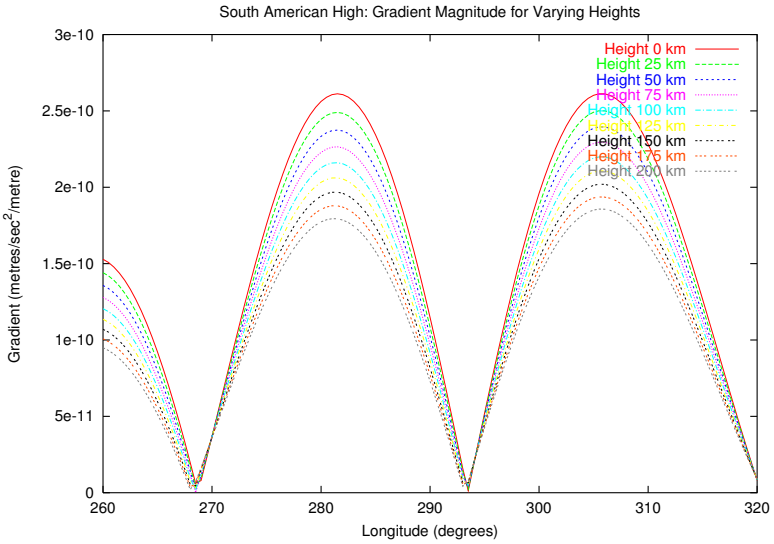

Figure 4-35: *The South American High passed through the wavelet transform at continuation heights which are too small to dramatically indicate the causative body's depth.*

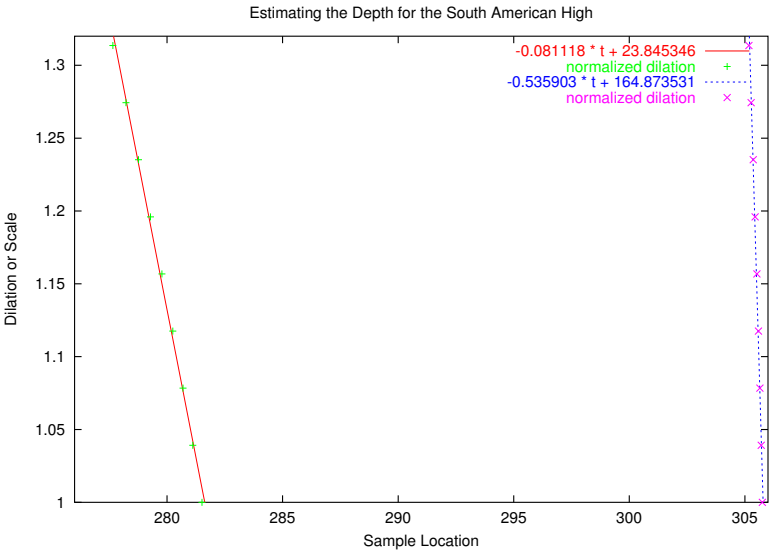

Figure 4-36: *The two lines shown are used to estimate depth to point sources. The right hand regression line has a slope suggesting that it influenced by another anomaly. Thus the depth estimate is questionable.*

Four views of the South American high synthesized to degree 10 from EGM96 are shown in **Figure 4-38**. From the top left, they are taken from the west through to the south (bottom right) at 30° intervals. This figure illustrates the complexity that remains even

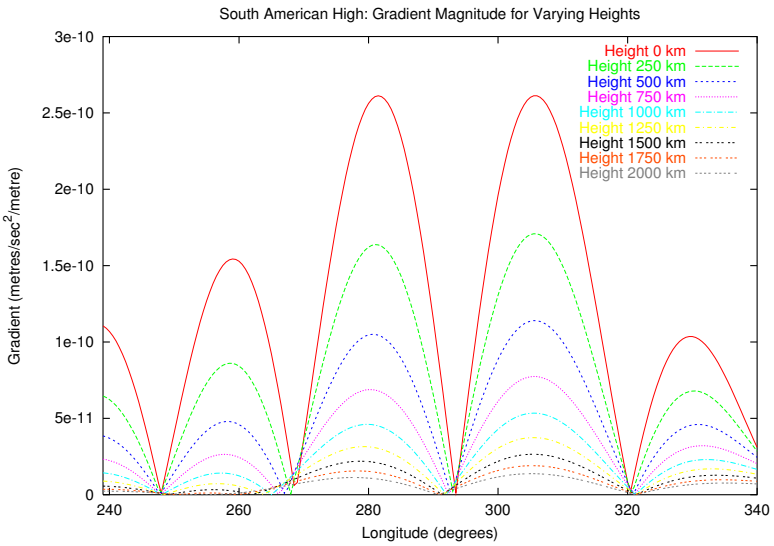

Figure 4-37: *The wavelet transform of the high on or near 293° longitude may be influenced by the adjacent sources evident in this illustration. Both to the right and left are other causative bodies, of lesser magnitude, but necessarily influential.*

---

though the shallowest features have been removed by truncation filtering. For comparison the original, unfiltered gradient magnitudes are shown in **Figure 4-39**. The same views are shown, and in the same order. Clearly the truncation at degree 10 has had a dramatic effect.

There is always the concern that simple truncation will induce ringing in the synthesized result. To ascertain whether or not that is an issue one can undertake to properly filter the EGM96 spectrum by applying a **Butterworth filter**. This filter was a low pass filter with a 10 degree cutoff, and a 36 db per octave slope. No significant differences appear when comparing the illustrations in **Figure 4-40** and **Figure 4-38**. To be fair, the Butterworth filtered data seems slightly less complicated. The interpretation is not significantly enhanced though.

Lastly, an attempt to estimate a mass for a causative body at about 2400 km was made. This turned out to be grossly in error. Using Bowin's estimate of about 1200 km was also erroneous. Arbitrarily selecting 600 km provided a reasonable match to the filtered potential curve. The three estimates are shown in **Figure 4-41**.

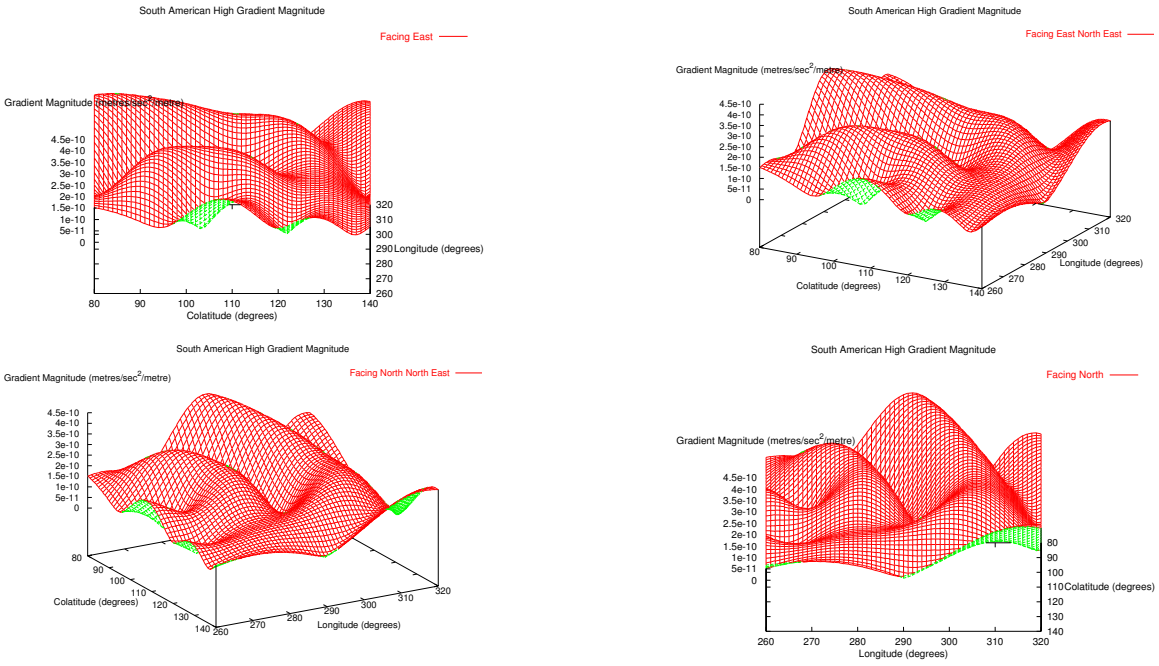

Figure 4-38: *Four views of the South American high gradient magnitude. From the top left the views are taken from the west looking east, from the west south west looking east north east, from the south south west looking north north east and from the south looking north.*

4.6 Final Comments

This chapter considered an approach to depth estimation that depended on wavelet transform analysis based on a Poisson kernel smoothing function and derived wavelet. Fundamentally, this is a signal processing approach to wavelet analysis not having any concern for frames and inversion. In theory, it can provide more than just depth information as the 'structural index', or 'Lipschitz regularity' can indicate some of the properties of a causative body. For simple anomalies, the depth is easily extracted from the potential field, albeit with some error, but for more complex body assemblages, the technique proves to be problematic.

Limitations observed in this chapter included numerical issues, and in particular, precision issues as the spherical harmonic expansion requires a relatively high degree for reasonable accuracy. Good interpretation of the resulting transforms also requires a relatively high degree of expansion in order to achieve a reasonable estimate of wavelet transform maxima locations. These needs impose computational requirements that may exceed the capability of available machinery.

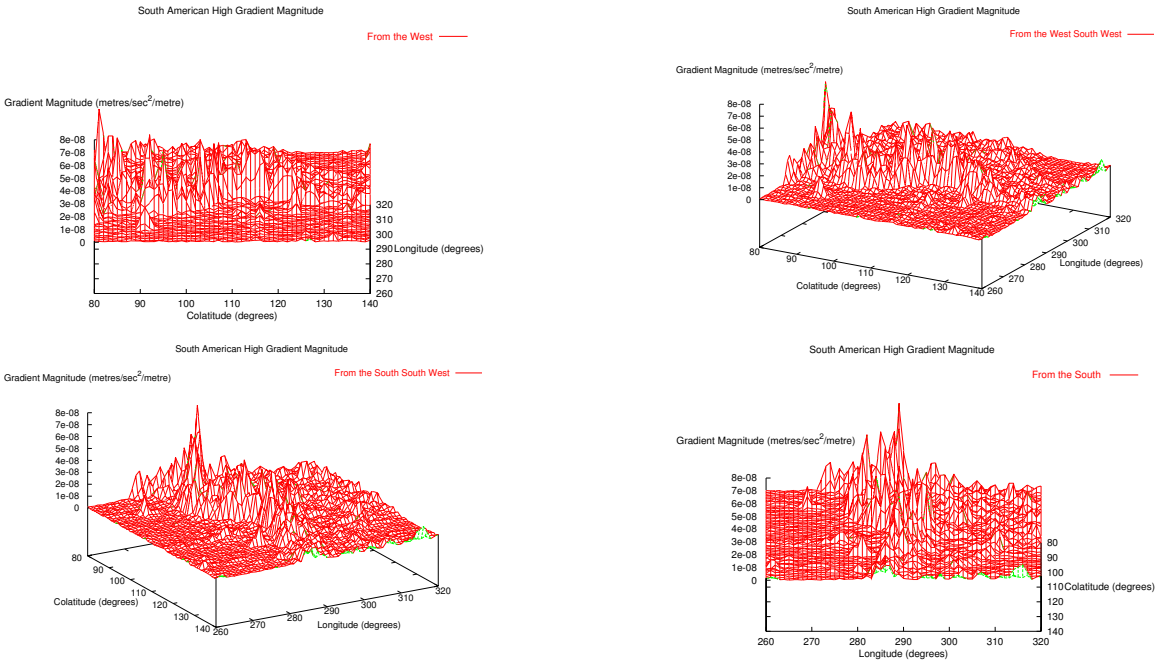

Figure 4-39: *The same four views of the South American high gradient magnitude, but using the full spectrum available from EGM96. From the top left the views are taken from the west looking east, from the west south west looking east north east, from the south south west looking north north east and from the south looking north.*

From a geophysicist's point of view, the interpretation of the two body problem, and particularly the South American high problem *might* be satisfactory. This is particularly true for one experienced in exploration geophysics, where all interpretations are made with compromise and are subject to business constraints. From a researcher's point of view, the results are less satisfactory as ideally one wants to understand as much as possible so as to quantify the Earth's characterization in a repeatable manner.

In the opinion of this writer, the wavelet technique is not the answer for deep mantle characterization. For shallow bodies, particularly in an exploration context where local gravity anomalies may be isolated from the background, the technique might be very useful. As the literature has indicated, not only can depth and mass be estimated, but so can a body's gross characterization, as described by the Lipschitz regularity [Hornby, Boschetti, and Horowitz 1999], or by the "structural index" associated with Euler deconvolution [Blakely 1995], neither of which were discussed in this document.

Given the frustration experienced in trying to interpret depths, and ultimately masses for

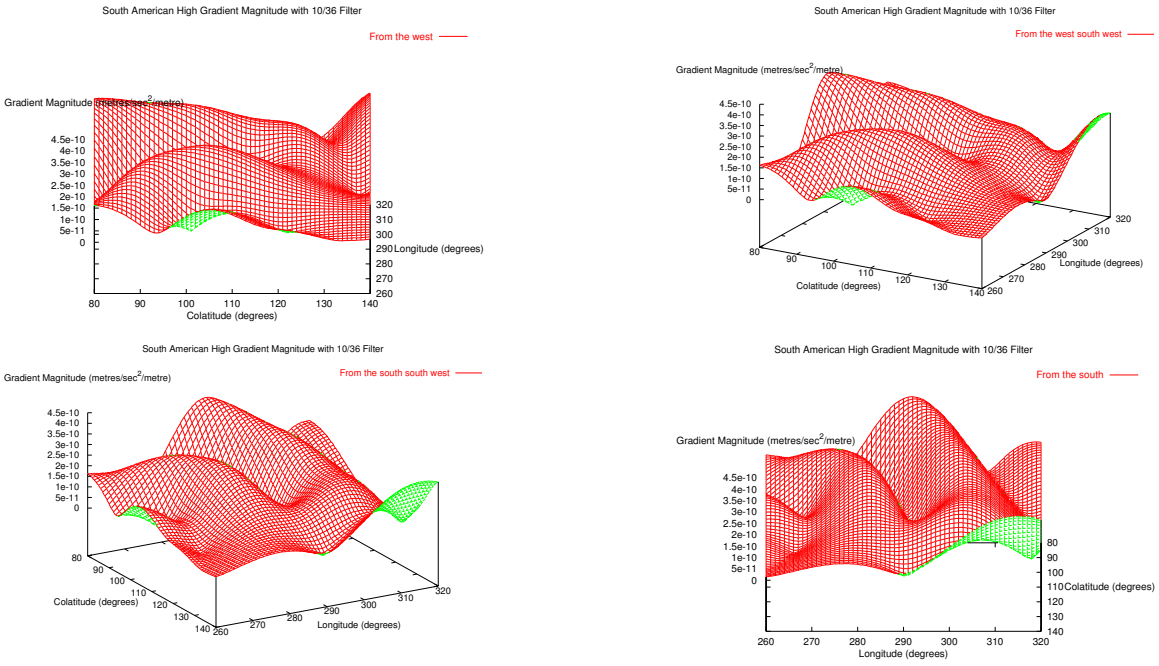

Figure 4-40: *Four views of the South American high gradient magnitude. From the top left the views are taken from the west looking east, from the west south west looking east north east, from the south south west looking north north east and from the south looking north. These illustrations have been filtered with a Butterworth low pass filter with a 3 db cutoff of 10 degrees, and a 36 db/octave slope. The images are not significantly different from* **Figure 4-38**.

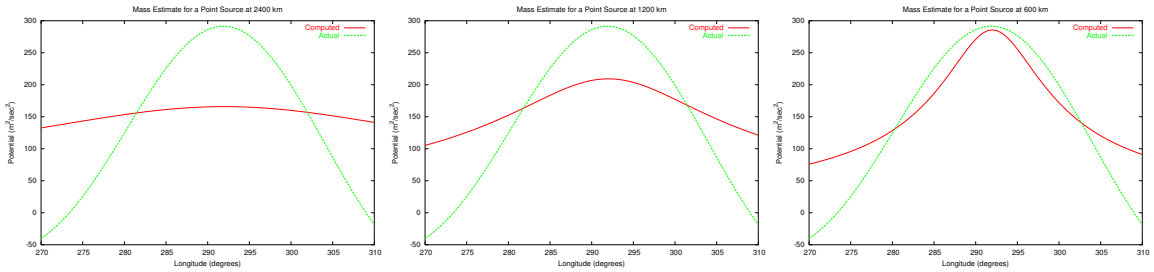

Figure 4-41: *Three estimates of masses that might reflect a point source interpretation of a profile over the South American high. On the left is a mass of $5.964*10^{21}$ at 2400 km which is clearly too deep. At the center is a mass of $3.763*10^{21}$ placed at Bowin's depth of 1200 km. At the right is a mass of $2.568*10^{21}$ placed at 600 km. All masses are in grams.*

---

body assemblages (i.e. 2 or more) in synthetic cases, or for the case of the South

American high, it was deemed prudent to explore other methods of estimating depth, mass and possibly mass distribution to characterize deep mass anomalies and ultimately generate a synthetic Earth model.

5 Estimating Anomaly Depth, Mass and Distribution

In this penultimate chapter the objective is achieved. For a modest portion of the spherical spectrum, mass anomalies are identified both geographically and by depth, and an estimate of their mass is made. This set of mass anomalies have a corresponding surface potential which resembles that of publicly available geopotential models. In addition, a continuous mass anomaly representation is computed for the same and other depths. This model, which represents a variable density contrast, complements the discrete mass model and can be improved easily as better spherical harmonic spectra are derived. For the portion of the spectrum that is examined, these models and their spectral representation provide a contribution to the synthetic Earth project for the mid and upper mantle. This complements the crustal models mentioned earlier.

The result is achieved in a circumspect manner. On the assumption that if anomaly locations and depths can be determined, then it should be possible to compute their masses and contributing potential. To do so requires that certain problems of inversion be identified. The result of this investigation establishes the 'bounds' for reliable mass estimates. Once this is completed, then the procedure of indicating anomaly spatial location using the characteristics of the spherical spectrum is reviewed and shown to be effective for a specific type of mass. Both of these steps are performed using synthetic data.

Given geographic location and depth, a model of the mid to upper mantle is generated and is shown to be similar to the measured field, as exhibited in recent geopotential models. Noting that these mantle anomalies, and in fact all mass anomalies, are not the same as the mass type employed in the study, an attempt is made to ascribe some sense of their breadth and possible density characteristics. This latter exercise results in a direct link between a continuously variable density contrast for a specific depth and shell thickness, and the measured geopotential field as interpreted as a depth-dependent function.

To be more specific, this chapter deals with the following subjects:

1 A review of recent Earth models

2 Establishing inversion bounds

- Describing the basic mathematical framework for inverting potential to mass
- Reviewing some experimental results for inversion of point masses whose surface potential is assumed known

- Noting the effect of the normally-used spherical coordinate system in polar regions when making reliable mass estimates
- Noting the effect of proximity to other masses when identifying each mass' location and the ability of performing a satisfactory inversion
- Proposing the use of an alternative discretization of the sphere to limit the effect of the '**polar problem**' and establishing some limits for anomaly identification and inversion
- Establishing the limitations for the aforementioned inversion by reviewing error incurred due to erroneous depth and/or location estimates
- Noting the effect of precision problems in the inversion results, if any
- Describing an appropriate method for determining the most likely position of mass anomalies

3 Spectrum exploitation

- Exploiting a characteristic of the spherical spectrum to make depth estimates for bodies at varying depths, assuming a simple mass model
- Estimating possible mass anomaly characteristics (geographic location and depth) as interpreted from publicly available geopotential models
- Employing the previously interpreted characteristics to estimate anomaly mass size and the similarity of their associated spectrum to the publicly available spectra

4 Altering the model assumptions

- Demonstrating a technique for indicating mass anomalies' possible size and density characteristics in a manner which is linked directly to the measured geopotential field

5 Summarizing the experimental results and noting the field generated from the interpreted model more closely matched the published fields than those of other recent researchers

5.1 Recent Models

By introduction to gravity field modelling, this section describes the work of Carl Bowin [Bowin 2000], and alludes to the preceding work of C. Lithgow-Bertelloni and her colleagues [Lithgow-Bertelloni, Richards et al. 1993; Ricard et al. 1993] and [Lithgow-Bertelloni and Richards 1998]. These researchers made estimates of the mantle and crust

composition in terms of mass anomaly structures, with the latter group modelling plate subduction over the millennia and the former testing an hypothesis counter to the status quo. Their models were used as a starting point in researching methods to estimate anomaly depth.

But their work has been preceded by earlier research into the possible cause of geoid anomalies. Early work on the correlation of geoid highs to subduction zones was completed by [McKenzie 1977; Morgan 1965; Parsons and Daly 1983] who concluded that excess mass existed beneath the highs, but that thermal modelling over estimated that mass by a significant amount. These researchers took surface deformation into account while [Chase 1979; Crough and Jurdy 1980] did not when engaged in similar studies. A follow-on study by [Hager 1984] also related the geoidal highs to viscosity contrast in the upper mantle.

Other work done at about the same time included that of [Dziewonski, Hager, and O'Connell 1977] who noted a negative correlation between velocity anomalies deeper than 1100 km and degrees 2 and 3 of the geopotential spectrum. [Hide and Horai 1968] examined the spectrum and concluded (as did Bowin later) that the lowest degrees of the spectrum were likely due to the core mantle boundary and its topography. Later [Khan 1977; Lambeck 1976], indicated that the Earth's spectrum could be described by a non-unique random distribution of density anomalies with no spatial coherence. Their study of the spectrum found that sources were generally shallow, except for the lowest (< 7) degrees. As noted elsewhere in this document, the spectral interpretation is blind to spatial dependencies.

In the study of subduction zones, [Chase 1979] examined them in the context of lower mantle convection and slab existence. He found that while contributing to the geoid, they did not dominate the low-degree (long wavelength) geoid. In related studies, [Richards and Hager 1984] found a good fit between seismic velocity in the lower mantle and the lowest two degrees of the geopotential. These seemed to correlate well with ancient plate positions. Past subduction zones also showed as lows [Chase 1985] and these might be due to the concentration of old lithospheric slabs in the mid mantle [Hager 1984].

Bowin was a much more recent researcher who proposed and substantiated the idea that large scale geoidal structures could be caused by deep-seated mass anomalies. These anomalous bodies were proposed to exist at the core/mantle boundary, and were the result

of topography on that surface. Other anomalous bodies were suggested to exist at shallower depths. He argued that since gravity varied as the reciprocal of distance squared, while potential (and undulation) varied only as the reciprocal of distance, then gravity features were more likely to reflect nearby anomalous bodies. On the other hand, features reflected in the potential must reflect more deeply seated bodies.

He observed that the lowest degree (2 and 3) contributions to potential dominated, and that for degrees in excess of 10, very little change occurred from their contributions. Intermediate values made smaller but observable contributions. Bowin concluded that the low degree harmonic coefficients were sufficient to specify the regional geoid, and suggested that some very deep anomalies dictated the lowest degree (2 and 3) contributions, while some shallower bodies determined the intermediate contributions. He added that the intermediate degree contributions to the geoid seemed to reflect plate subduction zones and indicated that shallow crustal bodies contributed to the larger gravity anomalies. By means of the ratio of the gravity to geoid anomalies for presumed point sources, he estimated the depth to several major anomalous bodies, including the South American high which he concluded had a maximum depth of about 1200 km [Bowin 2000, page 366].

To support his hypothesis, Bowin obtained a model set of 9274 5° spherical cubes derived from a study of plate reconstruction done by C. Lithgow-Bertelloni. This dataset gave slab location estimates at 20 depths. He observed that the model did not reflect the geoid very well, (see **Figure 5-18** or **Figure 5-19**), but when a **dynamic topography**[62] solution set of coefficients was added, then a better match was achieved. Using these cubes, he created two new models, one of which contained masses not deeper than 800 km and the other not deeper than 1400 km. These also contained four masses at the core/mantle boundary: beneath New Guinea, Iceland, Crozet and and the Indian Ocean. The range of densities used in the models was $0.5*10^{-4}$ to $0.225*10^{-2}$ gm/cc. In terms of a 5° pixelization of the Earth, the coverage over the sphere for Bowin's mass anomalies is shown in **Table 5-1**. While not a perfect match to the observed geoid, Bowin felt that they were a viable alternative to the **dynamic topography** model which has been in vogue for some 15 or more years. In this research, Bowin's deeper model was used for early experiments

[62] Dynamic topography relates thermal flow and geoid anomalies. Positive density anomalies, presumably blocks resulting from subduction, flow through a viscous medium as they descend. Bowin, who cites [Pekeris 1935], notes that this will induce negative boundary deflections at the surface, and at interior density boundaries within the mantle. This combination will result in a complex geoid anomaly. Determining the amount of dynamic topography requires an accurate knowledge of the density structure of both the crust and mantle [Lithgow-Bertelloni and Richards 1998].

Mass Anomaly Coverage by Depth		
Count	**Depth (km)**	**Percent Coverage**
7	72.5	0.27
105	217.5	4.05
98	362.5	3.78
92	507.5	3.55
220	652.5	8.49
383	797.5	14.78
324	942.5	12.50
274	1087.0	10.61
282	1232.0	10.88
326	1377.0	12.58

Table 5-1: *The mass anomalies are distributed irregularly with depth and the coverage is particularly thin at shallow depths. The 'percent coverage' figure indicates the percentage of the some 2592 5° spherical rectangles that contain a mass anomaly.*

in depth estimation.

The distribution of Bowin's masses are shown in **Figure 5-1** where they are seen as a function of latitude. Shown in **Table 5-2** is a breakdown of Lithgow-Bertelloni's mass anomalies, which were used as a basis for Bowin's models. The table gives an indication of the distribution of mass magnitudes, and indicates the number of masses, their mean separation and the standard deviation about that mean. The distribution is illustrated in **Figure 5-2** which shows mass size versus latitude, and geographic distribution.

5.2 Potential Field Inversion

5.2.1 Inversion of Point Masses

To generate a synthetic Earth model, mass anomalies which create a matching geopotential field were sought in this research. Assuming the anomalous bodies were placed and sized satisfactorily, then the primary objective would be achieved. To some degree and order, a field matching recent published fields would result, and some indication of the mantle (and possibly the crust's) geology would also be realized.

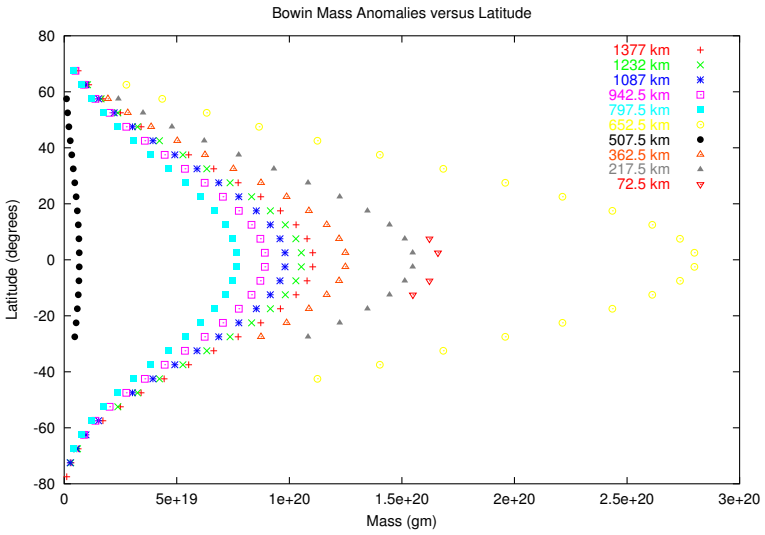

Figure 5-1: *Bowin's masses, which were derived from Lithgow-Bertelloni's mass model, are shown as a function of latitude. Bowin included four additional masses in his dataset (not shown here) which he placed near the core/mantle boundary.*

The observations and assumptions at hand were two-fold: first, recent geopotential fields were available (e.g. **EGM96**), and second, two recent models of subducted blocks which had sunk deep into the mantle were available. It seemed reasonable that one might be able to expand on the work of the creators of these models to find other anomalous masses, or unexpected changes in lithologic density, and to estimate their depth and magnitude.

An obvious thing to do, was to see if given the model which indicated both depth and mass, one could compute one of those parameters, given the other and the potential field that one would measure at the surface. To the best of the knowledge of this writer, all masses in the models were treated as points, although they were indicated to be cubes 5° on the side. Thus the earliest experiments undertaken after discarding the wavelet technique as inappropriate for the purpose were to see how successfully one might invert the field.

The standard method for solving problems when one has some measurements and a model describing the physical situation, is to use least-squares to estimate the parameters that match those measurements. For the problem at hand

Lithgow-Bertelloni's Mass Anomaly Characteristics

Depth	Number of Masses	Mean Minimum Separation Angle (°)	Mean Mass (gm)
72.5	503	0.69±0.49	$1.952*10^{16}$±$2.066*10^{16}$
217.5	503	0.69±0.49	$6.292*10^{16}$±$6.657*10^{16}$
362.5	520	0.71±0.57	$5.790*10^{16}$±$6.734*10^{16}$
507.5	118	1.60±3.22	$7.156*10^{16}$±$7.368*10^{16}$
652.5	424	1.18±1.04	$1.529*10^{17}$±$1.321*10^{17}$
797.5	228	2.45±2.55	$4.700*10^{17}$±$6.329*10^{17}$
942.5	204	2.81±3.39	$6.055*10^{17}$±$6.527*10^{17}$
1087.5	205	2.92±3.50	$4.626*10^{17}$±$5.175*10^{17}$
1232.5	211	2.18±3.25	$4.486*10^{17}$±$4.621*10^{17}$
1377.5	216	1.65±2.19	$3.915*10^{17}$±$3.426*10^{17}$
1522.5	191	1.96±1.70	$3.955*10^{17}$±$3.880*10^{17}$
1667.5	204	2.01±2.37	$4.563*10^{17}$±$4.249*10^{17}$
1812.5	219	1.61±1.89	$5.123*10^{17}$±$4.997*10^{17}$
1957.5	211	1.71±2.38	$5.987*10^{17}$±$6.228*10^{17}$
2102.5	197	2.34±3.05	$7.083*10^{17}$±$7.805*10^{17}$
2247.5	197	2.25±3.42	$7.930*10^{17}$±$1.019*10^{18}$
2392.5	203	1.94±3.13	$6.738*10^{17}$±$9.869*10^{17}$
2537.5	191	1.97±3.20	$7.414*10^{17}$±$9.898*10^{17}$
2682.5	189	1.97±3.27	$7.714*10^{17}$±$9.561*10^{17}$
2827.5	174	1.98±3.53	$9.228*10^{17}$±$1.242*10^{18}$

Table 5-2: *The mass distribution in Carolina Lithgow-Bertelloni's 20 mass anomaly files. Each line corresponds to a single data file. The mean angle is the average angular separation of each mass anomaly to its closest neighbour. Masses are in grams with the smallest being $3.371*10^{12}$ and the largest being $8.545*10^{18}$.*

$$K\vec{f} = \vec{d} \tag{5-1}$$

where K is a design matrix yet to be described, $\vec{f}$ is a vector of unknown masses, and $\vec{d}$ is a vector of potential measurements, given a sufficiently large set of observations, one could perform an inversion, as indicated in equation 5-2 to make such an estimation.

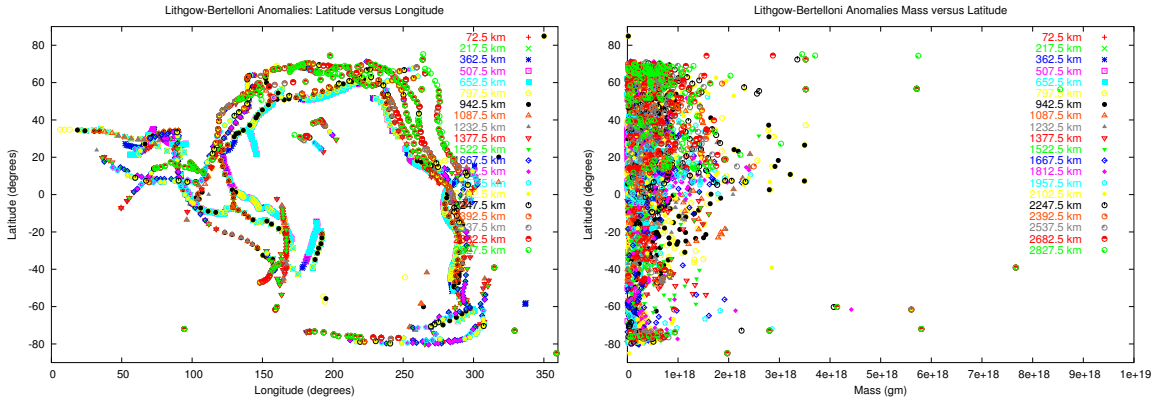

Figure 5-2: *The geographic distribution of Lithgow-Bertelloni's mass anomalies (left) and their magnitude versus latitude (right). The range of values runs from 10^{12} to 10^{18} grams.*

The solution to equation 5-1 for the case where the number of observations exceeds the number of unknowns is given by

$$\vec{f} = (K^T K)^{-1} K^T \vec{d} \tag{5-2}$$

This is the least-squares method formulation as described in [Blais 1988; Meju 1994; Menke 1989] and others.

The problem to be solved is linear. Given a set of measured potentials, and the coordinates of some mass anomaly, the inversion is straightforward. Using a spherical coordinate system, for a mass at subsurface coordinate Q (M_Q), the associated potential at some surface location P is given by,

$$V_P = \frac{GM_Q}{|P - Q|} \tag{5-3}$$

with G being the gravitational constant $6.67259 * 10^{-11} m^3/kg/sec^2$. This is expressed in the continuous case as

$$V = G \iiint_v \frac{\rho}{l} \, dv \tag{5-4}$$

with dv some volume element (sometimes called a voxel), ρ the density of that voxel and l the distance separating the voxel and the point of observation, with the integration being carried out over all space containing mass.

It follows that given the locations of measurement points and the subsurface locations of mass anomalies, the design matrix K can be populated easily. For both the regular case, where masses and observations are distributed uniformly, although not necessarily at the same locations, and the irregular where observations and masses may be positioned arbitrarily, the populating of K can be described by,

$$K_i = \sum_{j=1}^{N} \frac{GM_j}{|l_{i-j}|} \tag{5-5}$$

Thus the contribution to K for the observation at station i is the sum of all contributions from masses M_j to station i, divided by the distance separating the mass and the observation location. This formulation applies to the discrete point masses used in the sequel. Obviously, extended masses would require an additional degree of discretization.

For the problems examined in this research, the observations were regularly distributed on the sphere on an equiangular basis, and the masses were either regularly distributed (for synthetic tests) or irregularly positioned for geopotential field inversion. Certain difficulties manifested themselves with equiangular surface and mass spacing when performing initial synthetic tests. These were alleviated by altering the spacing strategy to that of an equal spherical angle. This problem is described in detail in the sequel.

Suitable codes for experiments in this regard were written with the highly efficient Lapack++ library [Dongarra et al. 1996] on both Intel IA86 and HP/Compaq/DEC-Alpha architectures. Other codes (for smaller problems) were written in **GNU Octave**[63].

5.2.2 Designing Suitable Experiments

It was with the numerical techniques just described that the suggestion of a colleague to attempt to resolve masses at unspecified locations, but within narrow depth ranges, was undertaken. Early experiments in this regard employing simple models of buried masses at known locations were promising. Without constraints, small numbers of masses could be recovered acceptably well, having RMS error two orders of magnitude less than the average mass size. With single constraints, this was improved by an order of magnitude. Thus encouraged, a code which could employ some or all of Bowin's model as constraints was constructed. The balance of all possible mass locations for one or more depths, were assumed to be filled with unknowns and inversion was attempted.

[63] **GNU Octave** is a high level interpreted language intended for numerical computations. It is uses **gnuplot** for two and three dimensional display, and is generally compatible with **Matlab**, an interpreted, commercial code available from The MathWorks, Inc.

This had the unfortunate effect of requiring a significant re-coding of the problem to effect a solution, as the memory requirements for a direct inversion became substantial, except for the least number of constraining 'known' masses. Another problem hinted at earlier was the effect of matrix conditioning which caused the reliability of the inversion to be in doubt. Instead, purely synthetic test codes were developed to study the problem more carefully.

Since the densities of Bowin's mass anomalies were modest (see **Table 5-3**), the code designed allowed for both positive and negative deviations from the **PREM** value for a chosen depth. The range selected was between plus and minus Bowin's largest density value.

Density Variations for Bowin's Mass Anomalies (gm/cc)
$0.1166*10^{-02}$
$0.1332*10^{-02}$
$0.2250*10^{-02}$
$0.5000*10^{-04}$
$0.6660*10^{-03}$
$0.8375*10^{-03}$
$0.8658*10^{-03}$
$0.9990*10^{-03}$

Table 5-3: *Densities used in Bowin's mass anomaly analysis.*

For the experiments, the Linux function **rand**(3) which provides a uniformly random sequence of integers between 0 and the value defined for **RAND_MAX**[64] was used. Alternatives include **random**(3) and **plfg** which was developed by Ken Tan (see [Tan and Blais 2000]), who developed the latter code for a parallel implementation of a random number generator. An equivalent function was employed when **GNU Octave** was used.

One of several codes developed was created to synthesize a randomly distributed field of density contrasts for one or more shells at depth. An example test was for the Bowin's deepest shell at 1377 km, and had the density contrast characteristics shown in **Table 5-4**.

The autocorrelation of the densities had a mean and standard deviation of $-1.9298*10^{-4} \pm$

[64] RAND_MAX has the value 2147483647 on typical IEEE 754 32 bit machines.

Synthetic Shell of Masses: Density Contrast Range (gm/cc)		
Minimum	**Maximum**	**Mean**
-0.00199902	0.00199286	$1.79556*10^{-5}$

Table 5-4: *The density characteristics for a sample synthetic model of mass anomalies.*

0.0138, after discarding the zero lag value which was unity. In other words, the mean of the autocorrelation function, apart from the zero lag value, was close to zero. Besides fully populated shells, other codes allowed partial population, or population restricted to narrow zones.

5.2.3 Experimental Inversion Results

To reduce computational time, and to take advantage of the facilities immediately available, the problem examined was reduced from a shell of unknown masses to those lying solely on a great circle, by suitable modification of inversion programs already written.

A typical pseudo-random dataset was created with the property that anomalous masses exist only along a great circle passing through the poles. A line drawing illustrating one such dataset and its randomness is shown in **Figure 5-3**. The vertical axis is that of the size of the masses which are placed at 5° intervals at a depth of 1377 km. The horizontal axis is the sample number for samples starting at the north pole, and proceeding to the south pole before returning to the origin. The individual masses have density contrasts within the range ± 0.002 gm/cc.

Computing the potential for the masses in **Figure 5-3** and then performing a standard inversion resulted in **Figure 5-4** where the potential is seen to be well resolved whenever the surface sample interval is less than the subsurface mass position interval of 5°. The individual mass elements are resolved to within about 5 orders of magnitude, while the potentials are resolved to within 6 or 7 orders of magnitude. The values for various surface sampling intervals are shown in **Table 5-5**. As a matter of interest, with sufficient over sampling, the parameter resolution matrix[65] was found to be the identity matrix.

A subsequent experiment involving two layers of randomly chosen masses at depths of

[65] Parameter resolution matrix calculations were done for cases where the surface sample interval was twice that of the subsurface. Only a single shell of masses was considered.

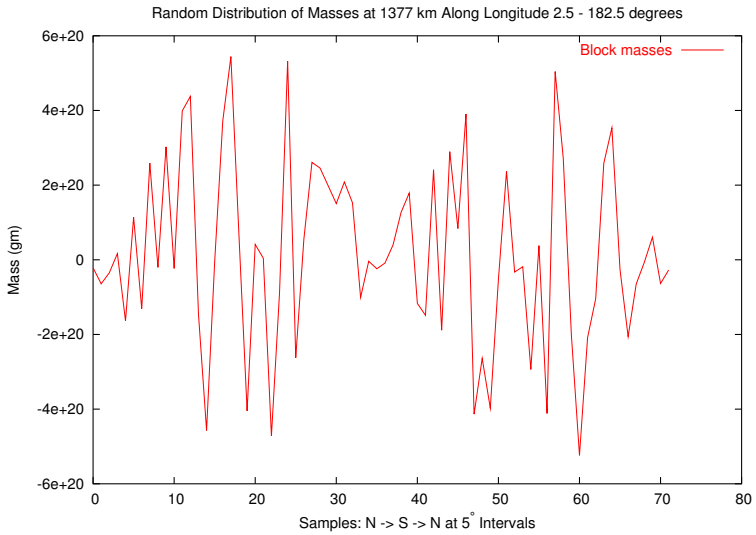

Figure 5-3: *Random masses at 1377 km placed at 5° intervals. The masses are placed along a great circle passing through the poles. The lines are used to highlight the mass size and distribution.*

1377 km and 1232 km was singularly unsuccessful when simultaneous inversion was attempted. The data are illustrated in **Figure 5-5**, and the surface potential in **Figure 5-6**. The masses were set at 5° intervals along a polar great circle.

In this experiment, the masses returned from the inversion step were wildly in error with differences having the same order of magnitude as the computed masses. The potential associated with the computed masses however, suggested that acceptable masses had been determined. The difference in potential resulting from the true masses versus the computed masses was some 6 orders of magnitude (i.e. the true and computed potential was nearly the same), with an RMS difference of $1.475464 * 10^{-4}$. Experiments like this were performed to the finest degree allowed by models like **EGM96** (i.e. 0.5°).

For single shells of masses (i.e. a set of masses with random magnitude, but on a regular grid), inversion could be both successful and unsuccessful. Experimentation revealed that the 'degree' of success was a function of mass location. It was later determined that mass anomaly positioning using the standard spherical coordinate system was affecting the inversion results negatively. As will be seen, this was a function of anomaly proximity in the polar regions. After this '**polar problem**' described in the next section was identified and dealt with, reasonable inversions of synthetic mass anomaly assemblages for fixed depths became reliably invertible. In various tests, as much as 25% of the regularly

RMS of the Mass and Potential Difference by Surface Sample Interval (gm)

Surface Interval (°)	RMS of Mass Differences	RMS of Potential Differences
5	$3.474161*10^{22}$	$3.195533*10^{0}$
4.5	$2.471824*10^{14}$	$3.447001*10^{7}$
4	$3.286231*10^{14}$	$3.760962*10^{7}$
3.5	$1.704014*10^{14}$	$2.741021*10^{7}$
3	$2.537612*10^{14}$	$3.184918*10^{7}$
2.5	$1.673274*10^{14}$	$5.952656*10^{7}$
2	$2.168901*10^{14}$	$5.488175*10^{7}$
1.5	$3.082822*10^{14}$	$1.981722*10^{7}$
1.25	$1.963754*10^{14}$	$2.368938*10^{7}$
1	$2.679974*10^{14}$	$4.050323*10^{7}$

Table 5-5: *For masses of magnitude 10^{20} grams placed along a great circle at a subsurface spacing of 5°, with various surface sample intervals, the RMS of the differences between actual and computed mass sizes and their geopotential are illustrated. The computed masses differ from the true values by 6 orders of magnitude (RMS), and the potential by 7.*

gridded masses could be randomly removed, and still result in a satisfactory inversion of the remainder.

Other problems to be discussed in the following text included error in the estimated depth and error in the estimated position.

5.2.4 Problems Associated with Neighbour Proximity

During inversion experiments, some difficulties were observed when trying to resolve individual masses. Errors associated with estimating mass magnitudes for bodies at known depths seemed to have significant variation. This was judged to be a function of latitude as may be seen in **Figure 5-7** following. That figure shows the absolute value of the differences between computed and actual mass magnitudes for a synthetic analysis where bodies were placed in a spherical shell at an 11.25° subsurface sample interval, with a known depth of 1377 km. The errors shown are those greater than 10^{20} grams. Typical errors ranged from $10^{14}\leftrightarrow10^{20}$ grams with a mean of $3.4*10^{19}$ grams. Of interest is the fact that error increased closer to the poles which results from the inability to

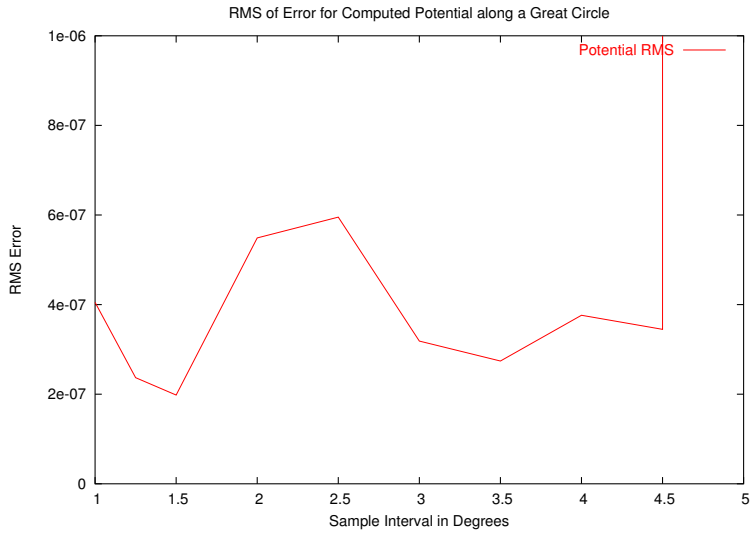

Figure 5-4: *Without a priori information, arbitrary weighting or Tikhonov regularization, subsurface masses at a fixed depth can be acceptably well resolved providing the surface sampling interval is less than the subsurface interval.*

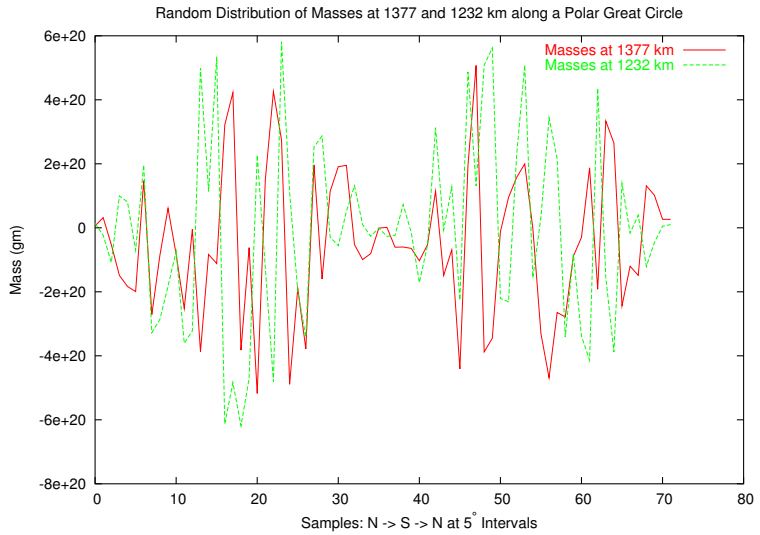

Figure 5-5: *Masses at 5° intervals at the depths of 1377 and 1232 km are illustrated. These are along the great circle passing through the poles, and running along longitude 2.5/182.5°.*

---

resolve masses at that depth with such small angular separations.

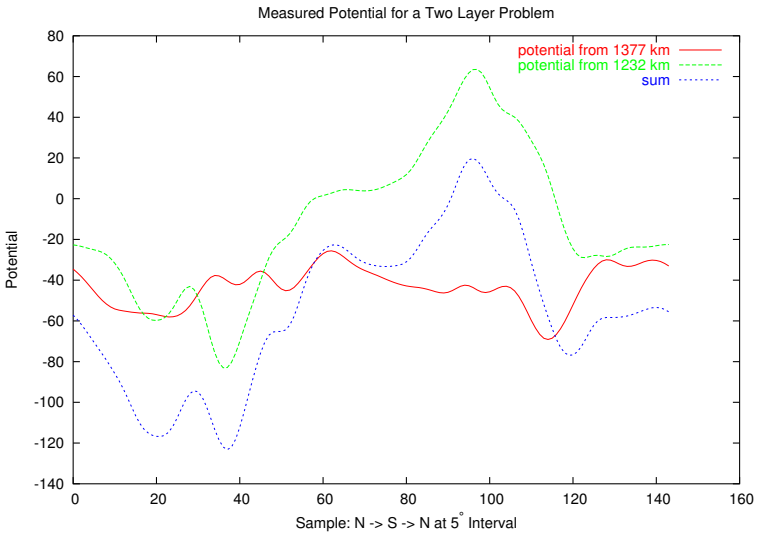

Figure 5-6: *The potential for each, and for the sum of two layers of masses set on a 5° grid along a polar great circle.*

This was determined to be a result of the discretization employed in traditional spherical harmonic analysis/synthesis codes, and which had been carried over to this analysis of mass magnitude. These codes generally employ what is known as an equiangular sampling (i.e. sample separation in latitude equals that in longitude), although the method as described in [Driscoll and Healy 1994] is an exception. Masses on some grid, and at some depth appear from the surface to be separated by an approximate angular separation Λ of

$$\Lambda = \tan^{-1} \frac{(R_E - D_{body})\theta \sin \alpha}{D_{body}} \tag{5-6}$$

where R_E is the Earth's nominal radius, D_{body} is the mass depth, θ is the angular separation of masses at depth referenced to the Earth's centre and α is the latitude. Thus for $\theta = 11.25°$ and $D_{body} = 1377$ km., the approximate separation of masses referenced to the surface is 35.5° or 982 km. At 11.25° from the pole, the apparent separation becomes 7.9° or 192 km, which is somewhat less than the surface sample interval of 244 km at the same latitude. This resolution problem, as a function of latitude is illustrated in the same figure.

To see the problem from a slightly different perspective, one might inquire as to what angular separation is needed between adjacent mass anomalies to allow one to recognize that two masses existed. Visually, or numerically, a minimum in the potential would be

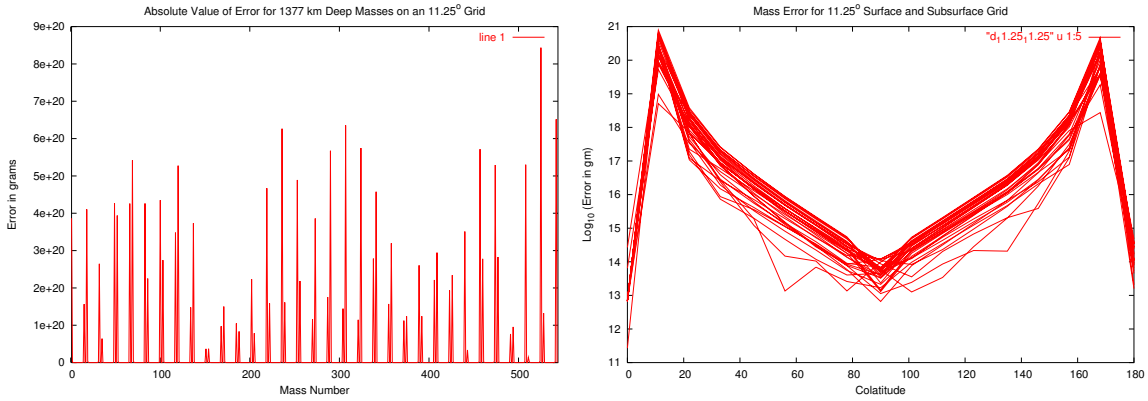

Figure 5-7: *A shell of masses buried at a depth of 1377 km with an angular separation of 11.25° is inverted to estimate mass size using a grid identical to the subsurface grid and error is incurred. On the left, the errors in excess of 10^{20} grams are shown for masses ordered by colatitude for each longitude. On the right all errors are shown as a function of colatitude, illustrating the resolution problem discussed in the text.*

---

required to identify two adjacent local maxima (assuming positive mass anomalies, as Bowin and Lithgow-Bertelloni did).

One can find such a minimum in the two dimensional case by computing the potential due to each, summing them and locating the minimum numerically as was done later in this research, or visually as shown in the sequel. For two bodies of relative mass M_1 and M_2 (where $M_2 = kM_1$) which are situated at depths z_1 and z_2 with separation L, one need only solve the potential expression,

$$V = \frac{M_1}{\left(z_1^2 + L^2\right)^{1/2}} + \frac{kM_1}{\left(z_2^2 + (L-x)^2\right)^{1/2}} \tag{5-7}$$

for a local minimum situated between them. This turns out to be the value of x, where,

$$\left(z_2^2 + (L-x)^2\right)^{3/2} x = k(L-x)\left(z_1^2 + L^2\right)^{3/2} \tag{5-8}$$

This is most easily seen graphically for varying masses, depths and separations, or may be solved numerically if a line search is performed to locate the point of equality. Graphical solutions are shown in **Figure 5-8** and **Figure 5-9**. In the first figure, for various angular separations, the potential due to a combination of two non-identical masses at

different depths is shown. It may be seen that for large enough mass differences, large enough depths and small enough angular separations, one quickly loses sight of the second mass. The second figure shows a close-up view for masses at two different depths and a fixed mass ratio. For the 1000 km deep bodies, it is apparent that at least 20° separation is needed to observe the presence of the second body. This fact is in keeping with the previously observed need for larger angular separation to minimize mass estimate error when body location is known. See for example **Table 5-8** which illustrates the problem from a different perspective. A more definitive measure of acceptable resolution follows in the next subsection. There, an alternative pixelization of the spherical surface that affords the opportunity to establish how close two bodies may be and still permit a satisfactory inversion, is described.

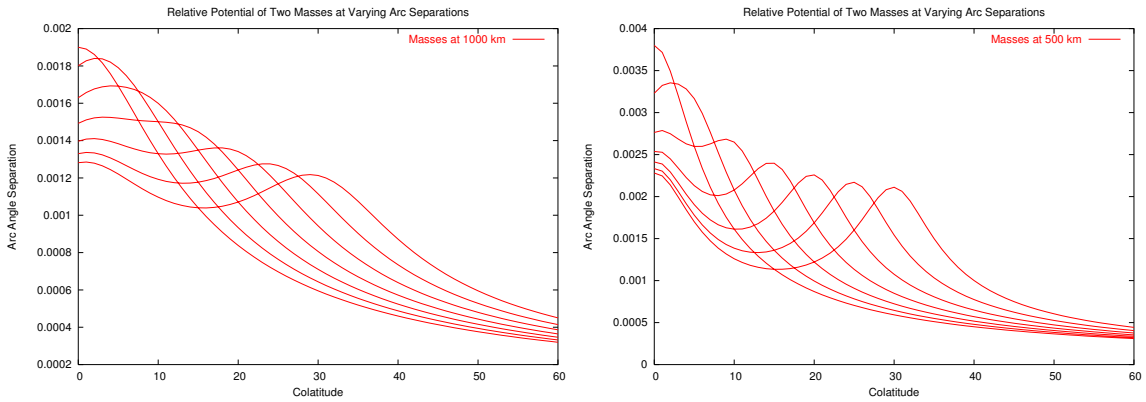

Figure 5-9: *close-up of masses at 1000 km (left) and 500 km (right) where the mass ratio is 0.9. Angles in degrees.*

It should be noted that if one somehow knew the exact positions and depths of two or more masses that were so close that their individual extrema could not be identified, they were still successfully inverted in synthetic tests.

5.2.4.1 An Alternative Discretization

It was noted earlier that for a spherical harmonic analysis to an arbitrary maximum degree and order, the ability to separate individual potential anomalies is determined by that degree/order cut-off. Anomalies that occur more frequently than the cut-off degree and order are simply aliased as they would be by an harmonic analysis on the line or plane. The cut-off degree and order in turn is determined by the surface sampling interval. Thus for a 0.5° sampling interval, one should not expect a higher frequency (or

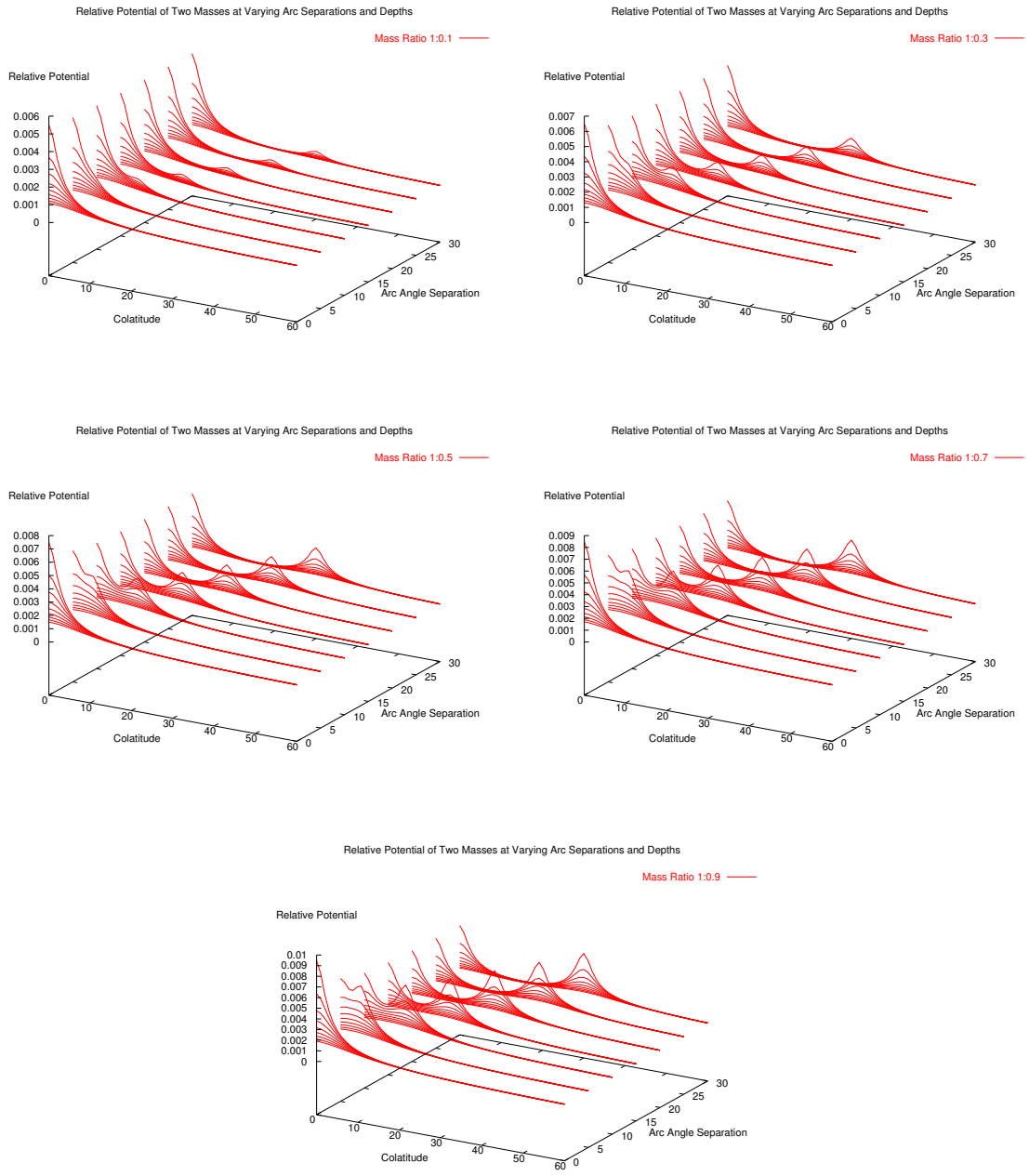

Figure 5-8: *From top to bottom, left to right the mass ratios are 1:0.1, 1:0.3, 1:0.5, 1:0.7 and 1:0.9. Depths range from 200 to 1000 km and the angular separation ranges from 0° to 30°. Mass pairs are at the same depth. Where definite peaks are seen, then simple inversion will suffice providing the mass separation at depth corresponds to the peak separation. Closer masses are partially separable, but increased mass estimate error is incurred.*

---

degree/order) than 360, simply because of the usual requirement that it takes at least two

samples to define a sinusoid.

But there is catch, so to speak. While 0.5° from East to West at the equator is a moderately large distance (about 55 km), it is a very short distance 0.5° south of the north pole (about 0.5 km). Thus the anomaly resolution of a spherical analysis is somewhat variable. Except for order zero analyses (i.e. symmetrical about the poles) which can have uniform sampling from north to south upon synthesis, all non-zero order analyses sample more frequently near the poles, than near the equator. Diagrams illustrating this are found in [Heiskanen and Moritz 1966, page 26].

Thus near the poles, one should expect to see preserved by a spherical harmonic analysis more high frequency anomalies than near the equator. As well, one should expect that high frequency anomalies in the equatorial regions would be aliased. What results is a mean spectrum for the sphere [Swarztrauber 1979]. Given that, one might assume that one could better approximate the subsurface if the Earth was composed of a more uniform distribution of mass anomalies. In other words, if the distribution of masses was not less than some interval corresponding to the average sampling interval of a typical spherical harmonic analysis, then a more reliable inversion might result.

It is interesting to see how close those samples can be for some depth, but still allow an inversion with an acceptable error. Clearly, it would be advantageous if a uniform discretization of the sphere existed, with the meaning of *uniform* to be equal or nearly equal spherical angular separation between sample points. Several pixelizations have been reported in the literature. These include equidistant cylindrical projections (which corresponds to the equal divisions of latitude and longitude normally associated with spherical harmonic analysis), quadrilateralized sky cube projections (a cube is projected onto the sphere to generate 6 equal areas which may be subdivided in a hierarchical lattice), and the *igloo* projection which possesses exact azimuthal symmetry at each latitude. These pixelizations are described in whole or part in [Crittenden and Turok 1998] and [Bond et al. 1999]. One other uniform discretization is that of the regular partitioning possible with the icosahedron, a polyhedron made up of twenty equilateral triangular faces. Recursive partitioning of these faces leads to the spherical quad tree data structure [Tan, Blais, and Provins 1999].

An alternative, known as **HEALPix**, is also mentioned in Crittenden's article, and is introduced in [Bond et al. 1999] as using a rhombic dodecahedron[66] as its base. A

HEALPix pixelization provides a **uniform pixelization** of the sphere and it may be divided hierarchically while remaining azimuthal as required for rapid spherical harmonic analysis. This pixelization is also equiangular along the parallels, but unlike that used in typical spherical harmonic analysis, it is also equiangular from a spherical angle perspective. This ensures consistent surface sample spacing. Because of this uniformity, HEALPix is ideal for verifying the proximity problem described earlier. Details of the implementation are best described by the authors in [Górski, Hivon, and Wandelt 1998; Górski, Wandelt et al. 1999; Hivon and Górski 1998] and [Wandelt et al. 1998].

The name **HEALPix** is an acronym for **H**ierarchical **E**qual **A**rea iso-**L**atitude **P**ixelization as applied to the sphere. It provides a near-isometric discretization of the sphere and as indicated in its name, the pixels are centred on equal areas, which is ideal for spherical analysis. FORTRAN 90 code is available from the authors, and some of this was ported to C to establish the error bounds discussed earlier. The base pixelization is made up of the 12 sides of the dodecahedron mentioned earlier. Each face may be subdivided into 4 new faces (replacing the previous faces), and this is done in powers of two. The parameter *nside* is that which the authors use to determine the number of pixels and their distribution. It indicates how many pixels are to be found along the side of one of the 12 base divisions of the sphere.

Shown in **Table 5-6** is how *nside* affects the pixel count and the mean spherical angle between pixel centres as computed from the ported code. As can be seen in the table, the mean angle between pixel centres is fairly consistent. The same information is shown graphically in **Figure 5-10**. Evidently, the HEALPix sampling is a uniform discretization. Using it should allow the estimation of inversion error as a function of mean pixel separation versus surface grid interval with depth variation.

To establish the error bounds for mass separation, codes from the **HEALPix** sample implementation were adapted so that they might be used with the author's inversion codes. Tests for various depths and separation angles were then run to estimate mass size using synthetic data. As before, it was observed that bodies that were too close together for a particular depth were not inverted correctly, with the error increasing as they became closer. For some depths, the demarcation of good or correct inversion versus poor or

[66] The dodecahedron is one of the five Platonic solids: the tetrahedron (4 sides), the hexahedron or cube (6 sides), the octahedron (8 sides), the dodecahedron (12 sides) and the icosahedron (20 sides) [Selby 1964, page 15]. The rhombic dodecahedron is a 12 sided polyhedron with each face being an identical rhombus. Not all vertices are the same as some join 3 and others 4 faces. The internal angles for each rhombus are 70.53° and 109.47°.

HEALPix Mean and Minimum Angular Separations (°)

Number of sides	Pixel Count	Mean Angle	Standard Deviation	Closest Angle
1	12	58.19	0.00	58.19
2	48	28.49	0.90	27.59
3	108	18.78	1.06	17.26
4	192	14.11	0.86	12.64
5	300	11.28	0.70	9.98
6	432	9.41	0.60	8.21
7	588	8.07	0.51	6.99
8	768	7.07	0.45	6.09
9	972	6.28	0.40	5.39
10	1200	5.66	0.36	4.83
11	1452	5.15	0.33	4.38
12	1728	4.72	0.30	4.00
13	2028	4.36	0.28	3.69
14	2352	4.05	0.26	3.42
15	2700	3.78	0.24	3.19

Table 5-6: *Average and minimum angular separation in degrees for the closest pixels in the HEALPix spherical decomposition for various side counts.*

incorrect inversion was quite clear, while for others it appeared blurred. The potential computed from the computed masses generally closely matched the actual potential quite well even though the masses were quite erroneous.

For a wide range of depths, the correlation coefficient between computed and actual mass for various spherical angles of separation is tabulated in **Table 5-7**. The limits of resolution for the depths used are fairly clear with the general rule being that deep bodies require more separation than shallow bodies, which is to be expected. The table forms a useful guide for resolving mass anomalies from geopotential fields. Assuming that some measure of depth has been established, then bodies spaced wider than the "cut-off" suggested in the table should be successfully inverted.

Note that spherical angles imply a specific separation, irrespective of the location on the sphere. Because geographical coordinates converge towards the poles, the separation of

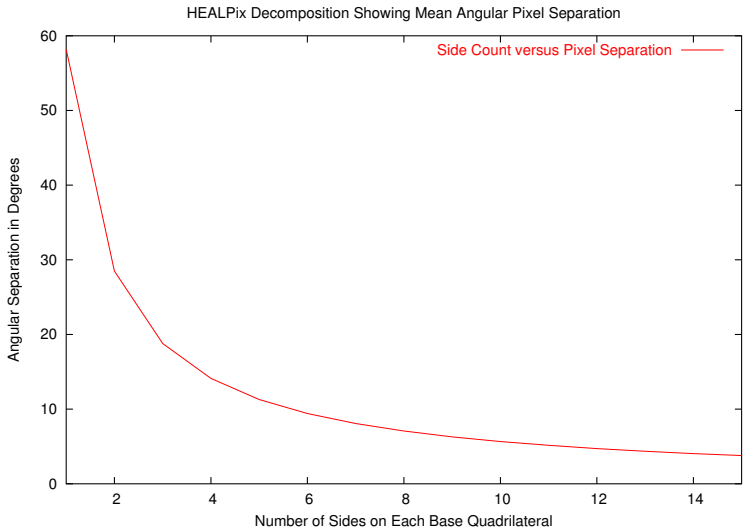

Figure 5-10: *An illustration of the average angular separation for the closest pixels in a HEALPix decomposition for various values of the number of side divisions.*

---

surface points is not constant. For example, points at 10° colatitude and separated by 10° along a parallel are only 1.73° (or about 193 km) apart, while the same points at the equator are spaced by 6.81° (about 758 km). To achieve the same surface spacing for the first pair, the separation along the parallel would need to be about 40°. It follows that to achieve a satisfactory inversion of buried masses given their potential, the closer to the pole that these masses lie, the less frequently they should occur in a spherical coordinate system.

5.2.5 Other Possible Error Sources

It is reasonable to assume that no matter what procedure might be used to estimate depth, or the geographical location of an anomalous body, some error is to be expected. These two error sources and the error associated with the measured potential are the subjects of this section.

In an early experiment, where the objective was to determine the effect of mis-positioning mass anomaly geographic locations, it was observed that errors of several degrees had a not-insignificant effect on the geopotential field. The results for one experiment involving a regular grid of surface points at 11.25° intervals, and a regular grid of buried masses at 30° intervals, offset from the poles and the prime meridian by 20° is shown in **Table 5-8**.

Correlation of Computed and Actual Masses for Various Depths

	Depth (km)							
Angle (°)	**3000**	**2000**	**1000**	**500**	**250**	**125**	**62**	**31**
28.49	9.99e-01	9.99e-01	9.99e-01	9.99e-01	9.99e-01	9.99e-01	9.99e-01	9.99e-01
18.78	9.99e-01	9.99e-01	9.99e-01	9.99e-01	9.99e-01	9.99e-01	9.99e-01	9.99e-01
14.11	9.99e-01	9.99e-01	9.99e-01	9.99e-01	9.99e-01	9.99e-01	9.99e-01	9.99e-01
11.28	9.99e-01	9.99e-01	9.99e-01	9.99e-01	9.99e-01	9.99e-01	9.99e-01	9.99e-01
9.41	3.28e-01	9.99e-01	9.99e-01	9.99e-01	9.99e-01	9.99e-01	9.99e-01	9.99e-01
8.07	2.15e-02	9.99e-01	9.99e-01	9.99e-01	9.99e-01	9.99e-01	9.99e-01	9.99e-01
7.07	1.80e-02	9.99e-01	9.99e-01	9.99e-01	9.99e-01	9.99e-01	9.99e-01	9.99e-01
6.28	-1.80e-03	9.34e-01	9.99e-01	9.99e-01	9.99e-01	9.99e-01	9.99e-01	9.99e-01
5.66	-6.66e-05	-1.26e-02	8.93e-01	9.53e-01	9.78e-01	8.99e-01	9.18e-01	8.88e-01
5.15	2.08e-02	1.60e-02	1.10e-02	4.83e-01	7.61e-01	8.37e-01	8.74e-01	8.98e-01
4.72	-1.14e-02	1.73e-02	-1.20e-02	5.51e-02	1.94e-02	3.29e-02	6.76e-02	1.39e-02
4.36	-4.77e-04	-2.00e-04	-1.05e-02	-4.99e-03	-8.94e-03	2.22e-02	7.31e-03	2.02e-02

Table 5-7: *These are the correlation coefficients between the actual and computed masses on a* **HEALPix** *grid, for the indicated depths and spherical angles of separation. Notice that shallower mass assemblages are resolvable at smaller angles, as expected.*

For 0.5° of position error, the potential computed from inaccurate masses is very close to the correct potential. By 2.5° it begins to deteriorate with the potential for 1000 km deep masses having an unexpectedly large standard deviation. For 0.5°, the ratio of computed to actual masses is not particularly good, and deteriorates for greater location error with an error of nearly 50% with a 2.5° location error. Notice that at shallower depths the mass ratio tends to approach unity. This likely reflects better geometry. Curiously, the **spectral norm**, which is the ratio of the highest to lowest singular value of the normal equation matrix, decreases for greater location error.

This test was performed prior to recognizing the '**polar problem**'. A subsequent test over a broader range of location errors, and which also examined the effect of error in depth estimate as well as observation error was completed using the **HEALPix** discretization. This provided a more reliable measure of the effects of mis-positioning for both position and depth. In **Table 5-9** the mean location error has been set to a random value having a mean of 0.05° or 0.1°. The average depth error was given random values

Effect of Positioning Error on Mass and Potential Calculations

Depth (km)	Mean Location Error (degrees)	Spectral Norm	Mass Ratio	Potential Ratio
1500		$2.125*10^4$		
1000	0	$1.850*10^3$	1.0	1.0
500		$9.803*10^1$		
1500		$6.016*10^2$	0.866±1.285	1.000±0.013
1000	0.498±0.288	$2.984*10^2$	1.361±3.236	0.995±0.106
500		$8.246*10^1$	0.952±0.307	0.972±0.350
1500		$1.323*10^2$	0.661±0.753	1.000±0.031
1000	2.491±1.443	$7.681*10^1$	1.309±2.784	0.962±4.271
500		$3.912*10^1$	0.794±1.096	0.977±0.657
1500		$8.908*10^1$	-0.154±4.408	2.169±23.452
1000	4.989±2.886	$5.865*10^1$	0.801±1.069	0.839±3.869
500		$3.874*10^1$	0.703±0.950	0.989±3.690

Table 5-8: *The table illustrates the effect of geographic location error on the norm of the normal equation matrix, and on the ratio of the computed to actual masses and their surface potentials. Note that the* '**polar problem**' *has had an effect on the inversion results, making them much less reliable. See* **Table 5-9** *for comparison.*

with means of 0.5% and 1%. Lastly, the observed potential was assigned mean errors of about 0.5% and 1%. The depths selected encompassed the depths of real anomalies identified later in this document. Also shown are the spectral norms for the design matrices. While all combinations of these parameters were used, only a small selection is shown. The test used masses on a regular grid having randomly assigned values near 10^{20} grams, a value near that used by Bowin. In the test shown, the true value of the gravitational constant (**G**) was used. Other tests employed a value of $G = 1$ with and without unit valued masses. These resulted in identical results indicating that the inversion procedure did not suffer from numerical precision problems. The precision of the values in the table is about 7 digits, with only 3 shown owing to the size of the table.

A review of the whole table indicates several items of note:

- the **spectral norm** declines from values of near 1100 for the deepest masses, to about 35 for the shallowest. This is consistent whether or not any dithering of the three parameters has occurred.
- As may be observed in the previous table, given perfect data and knowledge of mass location and depth, a perfect inversion can be performed.
- The ratio of the computed to true masses appears to be fairly good, although an examination of actual values (not shown) indicate that when dithering occurs, the computed masses are only accurate to from 1 to 3 decimal places. This is consistent for all variations and the greatest accuracy occurs for the shallowest anomalies.
- For the degree of dithering tested, the computed to actual potential ratio is generally good, with 2 to 3 decimal places of consistency.

The inversion step is sensitive to the three parameters shown which is a good indicator that this is not a well-posed problem; nevertheless, the inversion can still provide some insight into the underlying geology of the mid to upper mantle.

5.2.6 Peak Searches

Gravity anomalies are associated with masses. There can be no offset between the geographic location of the anomaly and the underlying mass. Point masses have the property that the anomaly's extremum lies directly over the body. Extended masses also underly observable anomalies, but a suitable extremum may be difficult to identify.

Note that where two mass anomalies lie in close geographic proximity, there may be an apparent offset of the extrema for both masses. This was illustrated earlier in the figures for relative potential of two masses: **Figure 5-8** and **Figure 5-9**.

A code was written to locate potential extrema. It employed a simple test for locating those points, and had a refined location mechanism for making a better estimate of the extremum coordinates. The test was to perform a least-squares fit of a two-dimensional paraboloid to the 9 or 25 points which were centred on the possible extremum.

After testing with 2 small, synthetic datasets to ensure code correctness, the code was applied to the geopotential field from **EGM96** and several spectrally delineated versions of that geopotential model. It was not surprising that as the spectrum widened, the number of extrema increased. What was surprising was that the number of extrema on the

Effect of Location, Depth and Potential Variation using HEALPix Surface Coordinates

Depth (km)	Mean Location Error (°)	Mean Depth Error (%)	Mean Potential Error (%)	Spectral Norm	Mean Mass Ratio	Mean Potential Ratio
2000	0	0	0	1.117e+03	1	1
1000	0	0	0	1.041e+02	1	1
500	0	0	0	4.501e+01	1	1
250	0	0	0	3.637e+01	1	1
2000	0.050±0.028	0	0	1.110e+03	1.026±0.196	0.999±0.000
1000	0.050±0.028	0	0	1.041e+02	1.002±0.020	0.998±0.011
500	0.050±0.028	0	0	4.502e+01	1.001±0.016	0.998±0.050
250	0.050±0.028	0	0	3.641e+01	1.001±0.022	1.004±0.027
2000	0.100±0.057	0	0	1.099e+03	0.997±0.388	0.999±0.001
1000	0.100±0.057	0	0	1.041e+02	1.004±0.041	0.998±0.020
500	0.100±0.057	0	0	4.510e+01	1.003±0.034	1.006±0.183
250	0.100±0.057	0	0	3.650e+01	1.003±0.044	1.009±0.067
2000	0	0.501±0.288	0	1.081e+03	1.017±1.437	1.000±0.001
1000	0	0.501±0.288	0	1.038e+02	1.006±0.028	0.998±0.022
500	0	0.501±0.288	0	4.499e+01	1.001±0.008	1.004±0.060
250	0	0.501±0.288	0	3.636e+01	1.000±0.003	1.000±0.002
2000	0	1.002±0.577	0	1.040e+03	0.865±1.296	1.000±0.003
1000	0	1.002±0.577	0	1.035e+02	1.014±0.070	0.998±0.035
500	0	1.002±0.577	0	4.498e+01	1.002±0.018	1.043±0.576
250	0	1.002±0.577	0	3.636e+01	1.000±0.006	1.000±0.005
2000	0	0	0.558±0.279	1.117e+03	0.908±1.791	1.000±0.004
1000	0	0	0.558±0.279	1.041e+02	1.056±0.512	1.000±0.006
500	0	0	0.558±0.279	4.501e+01	0.966±0.442	1.001±0.027
250	0	0	0.558±0.279	3.637e+01	1.043±0.394	0.999±0.006
2000	0.049±0.028	0.998±0.575	0.992±0.566	1.134e+03	0.781±4.373	1.000±0.008
1000	0.049±0.028	0.998±0.575	0.992±0.566	1.044e+02	0.995±0.277	1.012±0.161
500	0.049±0.028	0.998±0.575	0.992±0.566	4.521e+01	0.914±0.909	0.999±0.035
250	0.049±0.028	0.998±0.575	0.992±0.566	3.663e+01	1.039±0.395	1.000±0.016
2000	0.099±0.057	0.998±0.575	0.992±0.566	1.126e+03	0.726±8.364	1.000±0.008
1000	0.099±0.057	0.998±0.575	0.992±0.566	1.046e+02	0.994±0.276	1.011±0.152
500	0.099±0.057	0.998±0.575	0.992±0.566	4.557e+01	0.945±0.596	1.008±0.133
250	0.099±0.057	0.998±0.575	0.992±0.566	3.695e+01	1.078±0.787	1.001±0.029

Table 5-9: *This is a sample of the inversion tests run to examine the effect of dithering the average location and depth of a presumed mass anomaly. As well, the observed potential was dithered to see what effect this parameter had on the computed masses and their potential.* **HEALPix** *surface coordinates were used to avoid the '***polar problem***'. For this example, the surface was sampled with 'nside' = 4 (about 14.1° spacing) and subsurface was sampled with 'nside' = 3 (about 18.8°). The true value of the gravitational constant (G = 6.672590e-17 m^3/kg/sec^2) was used.*

---

full field was less than that of some of the narrower spectral ranges. This must be due to some cancellation mechanism resulting from *conflicting* coefficients in the spectrum, when synthesized. Recall that the **dynamic topography** thesis indicated that this might be expected.

The number of extrema found as a function of data points examined is illustrated in **Table 5-10**. The peak finding was limited to the 9 point paraboloid least-squares fit in this table. Changing the size of the interpolant from 9 points to 25 points provided some different peak locations. The error in fit increased for finer resolution geopotential fields for larger paraboloids, as might be expected. For fields up to degree and order 100, the fit was very good.

Duplicate peak indications are common in such analyses. A shell script to remove these was written. It performed a sort based on peak coordinates, and then tested for peak proximity, rejecting those that were too close ($< \approx 0.2°$). Subsequent experiments found that such a simple test was inadequate, and suitable C code was written to test all possible combinations of points for duplicates, and to ensure that the minimum spacing between extrema did not fall below a user-defined threshold (initially set to 6° which was adequate for depths within the range 1000 to 2000 km).

Note that extrema searches in polar regions were inclined to locate an overabundance of peaks. This likely resulted from the spherical harmonic expansion characteristics described earlier. Spherical harmonics generate anomalies in the polar regions of apparently the same frequency as those in the equatorial region. In a spatial sense these are of much higher frequency because of the spatial sample interval difference between polar regions and equatorial zones.

Once the duplicates were removed, shell scripts were used to reformat the peak locations so that an inversion procedure might be applied, given a depth estimate, which is the subject of the next section. In **Figure 5-11** is shown the result of peak finding for the 2↔11 degree range, and the 12↔27 degree range in the **EGM96** geopotential field. The maxima are shown as black dots, and the minima are white. These figures were generated with **GMT**[67] version 3.3.4 [Smith and Wessel 1998].

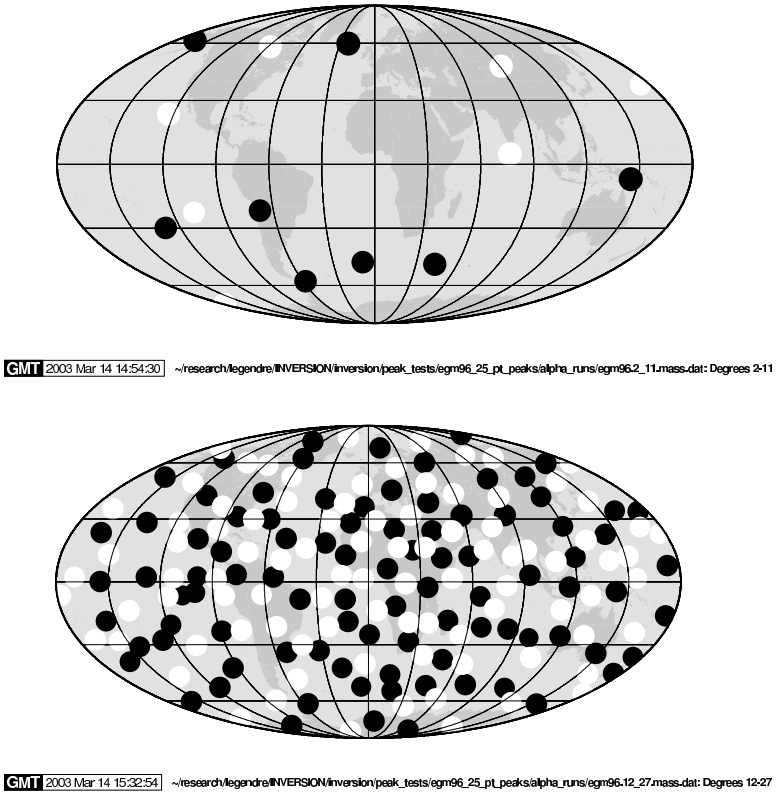

Figure 5-11: *Shown are probable mass locations for the 2↔11 degree range (upper) and the 12↔27 degree range (lower). There are 15 masses in the former range and 184 in the latter, As the spectral range increases, the number of possible mass anomalies increases rapidly. Black "dots" are positive anomalies, while "white" are negative.*

5.2.7 Final Comments on Inversion

This section, and its subsections discussed the problems associated with inverting a geopotential field, on the assumption that some model of a mass anomaly was made, and

[67] Generic Mapping Tools: a marvellous toolkit for high quality maps and other diagrams.

EGM96: Full and Partial Spectrum Extrema Counts

Data Point	Cumulative Extrema Found					
Count	**Full**	**2-11**	**12-27**	**28-102**	**102-296**	**297-359**
12996	153	0	10	95	679	2443
25992	298	0	21	203	1390	4996
38988	392	1	33	312	2105	7545
51984	465	1	43	422	2766	10104
64980	551	2	56	540	3446	12668
77976	647	3	65	680	4160	15279
90972	713	3	75	820	4843	17859
103968	819	3	87	959	5471	20443
116964	971	4	98	1106	6200	22975
129960	1141	5	108	1254	6991	25487
142956	1346	6	114	1414	7721	28028
155952	1430	7	124	1552	8480	30635
168948	1482	8	131	1668	9221	33222
181944	1536	9	139	1798	9976	35769
194940	1606	10	150	1935	10663	38342
207936	1749	11	161	2076	11319	40906
220932	1883	14	173	2203	11970	43476
233928	1993	14	183	2316	12655	46090
246924	2068	15	193	2426	13373	48686
259920	2227	16	208	2541	14129	51294
259920	2235	16	208	2544	14156	51368
259920	2239	16	208	2549	14187	51450
259920	2239	16	208	2549	14187	51450

Table 5-10: *Extrema found in the entire geopotential field described by* **EGM96** *or one of its spectral subsets, where the degree/order range has been limited.*

---

that each mass' geographic location and depth was known. Given this information, an inversion is possible in principle.

Problems identified included what has been referred to here as the '**polar problem**'. The

proximity of masses is problematic for two reasons. Firstly, individual anomalies cannot be readily identified for possible inversion. Secondly, bodies placed on a regular grid using a standard spherical coordinate system for positioning are not spaced consistently when moving from equatorial to polar regions where they are too close for successful inversion.

This problem affected the ability to define the bounds one would require for successfully inverting a publicly available geopotential field. By employing an alternative discretization, **HEALPix** in this case, the so-called '**polar problem**' was eliminated. Tests to define what if any anomaly location error, or depth estimate error could then be run reliably.

Because the problem is not well-posed, any small error in either of these parameters results in some error in estimated mass. In a table which showed several variations of these, as well as possible error in the observed potential, it was noted that masses were accurate only from 1 to 3 decimal places. The potential associated with the computed masses was similarly affected. No problems associated with precision were observed in tests designed to highlight such difficulties.

Lastly, a procedure to estimate anomaly location was described and for certain limited ranges of a spherical harmonic spectrum (the reasons for which are deferred to the next section), the locations of mass anomalies were mapped and displayed.

5.3 Using the Spectrum to Estimate Depth

Given a reliable depth, standard inversion techniques can be used to estimate mass (assuming a simple model is acceptable). Obviously, it is then critical for any structural assessment that a depth value be available. The question then becomes one of how to estimate that causative body's depth so that its mass can be determined.

As can be seen in **Figure 5-12**, the differences in the spectra for bodies at varying depths are not overly great. Given the disappointing results of wavelet analysis for making such estimates however, these differences appear to be all that remains for exploitation. As will be seen, they turned out to be beneficial, although the result still contained some ambiguity.

From the spectrum one can make a depth estimate, providing one makes a simplifying

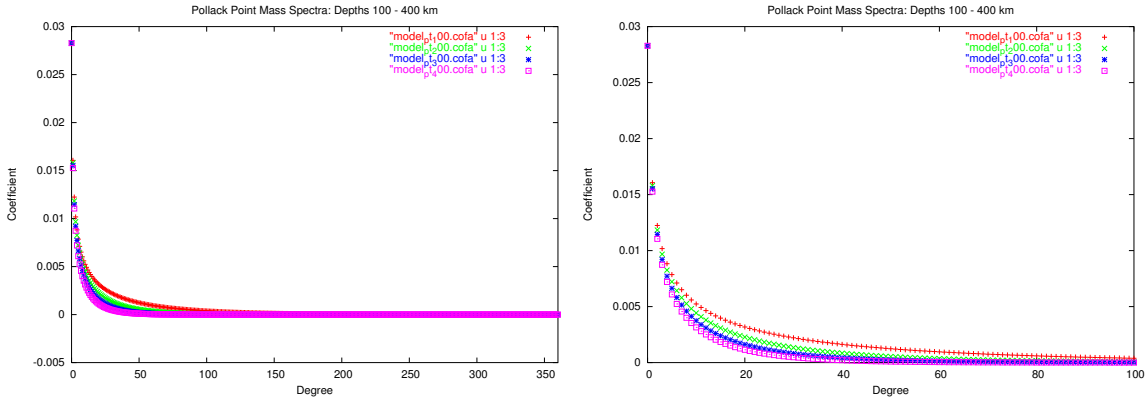

Figure 5-12: *The spherical harmonic spectra of a body at four depths: 100, 200, 300 and 400 km. Substantial spectral overlap indicates little opportunity for spectral decomposition. On the left is the full spectrum, and on the right is a close-up of the first 100 degrees.*

---

assumption about the masses under consideration. Furthermore, one must ignore the fact that some mass anomalies will be hidden from view in the spectrum, and thus impossible to recognize. This means that one will be characterizing the Earth in a 'deficient' manner (i.e. a model will result, but it will not be complete). However, at least with some form of depth estimate, and an analysis of the surface potential irregularity, one can 'spot' mass anomalies, their magnitudes and their locations in a repeatable manner.

Recall Pollack's models, and in particular his equation for the potential of a point mass, equation 4-2. Notice that the spectrum of the potential falls off as a function of degree n, as per

$$spectrum\ (n) \propto \frac{1}{2n+1}\left(\frac{a}{r}\right)^n \tag{5-9}$$

Recall also the **degree variance** definition for the potential from the normalized spectrum as given by [Kaula 1966, page 98] in equation 2-84 with corresponding definitions of the power spectrum using geodetic normalized spectral coefficients given by [Wong et al. 1971, page 6231] and [Pollack 1973] in equation 2-85. Of particular interest is the characteristic of these power spectra for bodies at fixed depths. In **Figure 5-13** is illustrated the power spectra for masses of random density contrast (within the range of ± 0.002 gm/cc) using both Wong's and Pollack's normalization. Notice that for point masses, the Pollack normalization exhibits a linear trend as a function of degree when plotted against power, with the slope being a function of depth of burial. Please also note that as might

be expected, single masses exhibit the same linear power versus degree characteristic shown in the figure.

The spectrum for single masses, having the characteristic indicated in equation 5-9, thus has the root of Kaula's degree variances in similar proportion,

$$\bar{\sigma}(n) \propto \frac{1}{\sqrt{2n+1}} \left(\frac{a}{r}\right)^{n/2} \tag{5-10}$$

so that by applying Pollack's suggested normalization (i.e. multiplying by $\sqrt{2n+1}$), the following power function with respect to degree n is indicated,

$$\bar{\sigma}(n) \propto \left(\frac{a}{r}\right)^{n/2} \tag{5-11}$$

For a mass at the surface, which would indicate a singularity in the spectrum, the spectrum is uniform for all degrees, just as the Fourier spectrum of a Dirac function is. The Pollack normalized spectra follows a homogeneous power law (i.e. ab^c) similar to those described in [Schroeder 1991, chapter 4].

A natural question would be to ask what characteristic does a field like **EGM96** exhibit when viewed in terms of its so-called power spectrum. This is answered in **Figure 5-14** where that geopotential model has been corrected for the normal field to degree 8.

Given this spectral display, and that of the random masses arranged in a shell, one can measure the characteristics of their respective linear features. The result is shown in **Table 5-11** which tabulates the masses at Bowin's depths which were used in the shell models, plus the most obvious lineament of the EGM96 spectrum.

The regression line fit to the slopes of the preceding synthetic data study was slightly parabolic, as per,

$$slope = -1.38151 * 10^{-07} * depth^2 - 0.00133843 * depth - 0.00331638 \tag{5-12}$$

where 'slope' is measured in decibels per degree, and 'depth' is in km. Adding the additional constraint that the surface have zero slope because all harmonic degrees are equally represented at that depth [Pollack 1973, page 1764], and adding additional information about the slopes for single buried masses over a broader depth range (see **Table 5-12**) results in the following equation,

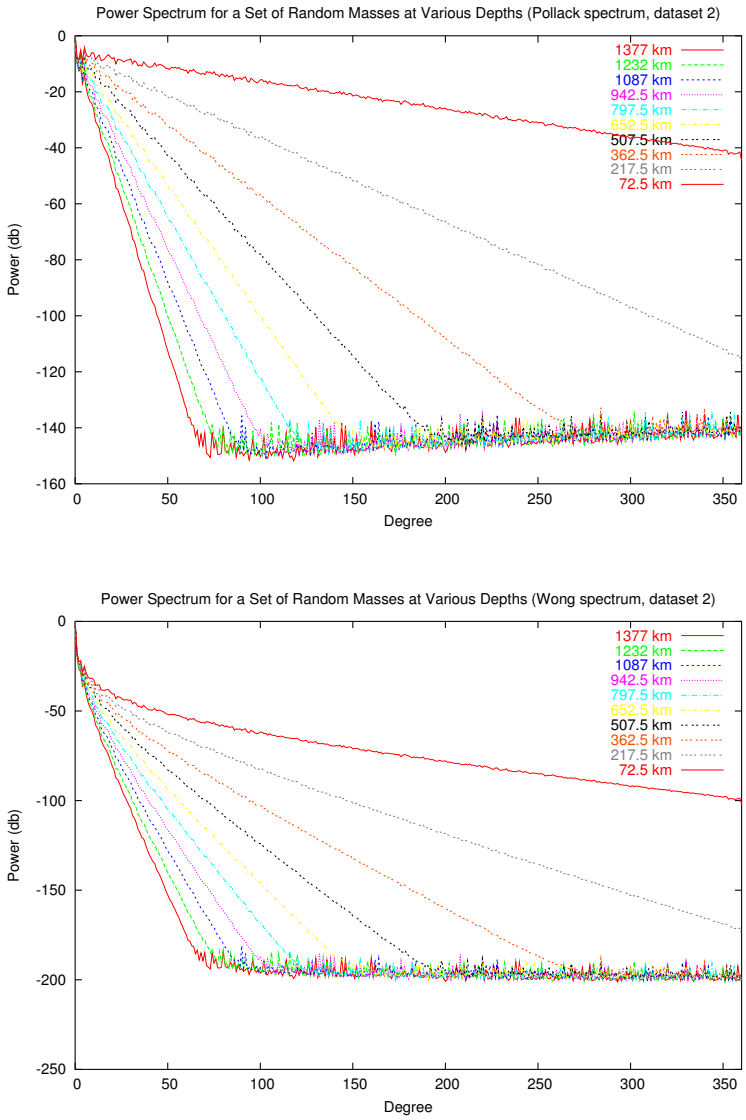

Figure 5-13: *The power spectra for datasets made up of a random set of masses contained within the density contrast range of ± 0.002 gm/cc, having different depths. These illustrate Pollack normalization (top) and Wong normalization (bottom). Single masses at the depths shown exhibit the same characteristic.*

$$slope = -1.91098 * 10^{-07} * depth^2 - 0.00127453 * depth - 0.00902622 \quad (5\text{-}13)$$

with an RMS fit of ±0.0114685. Inverting this expression so that depth can be determined from measured slope, one has (where the radical is real),

$$depth = \frac{0.00127453 \pm \sqrt{0.00127453^2 + 4 * 1.91098 * 10^{-07} * (-0.00902622 - slope)}}{-2 * 1.91098 * 10^{-07}} \quad (5\text{-}14)$$

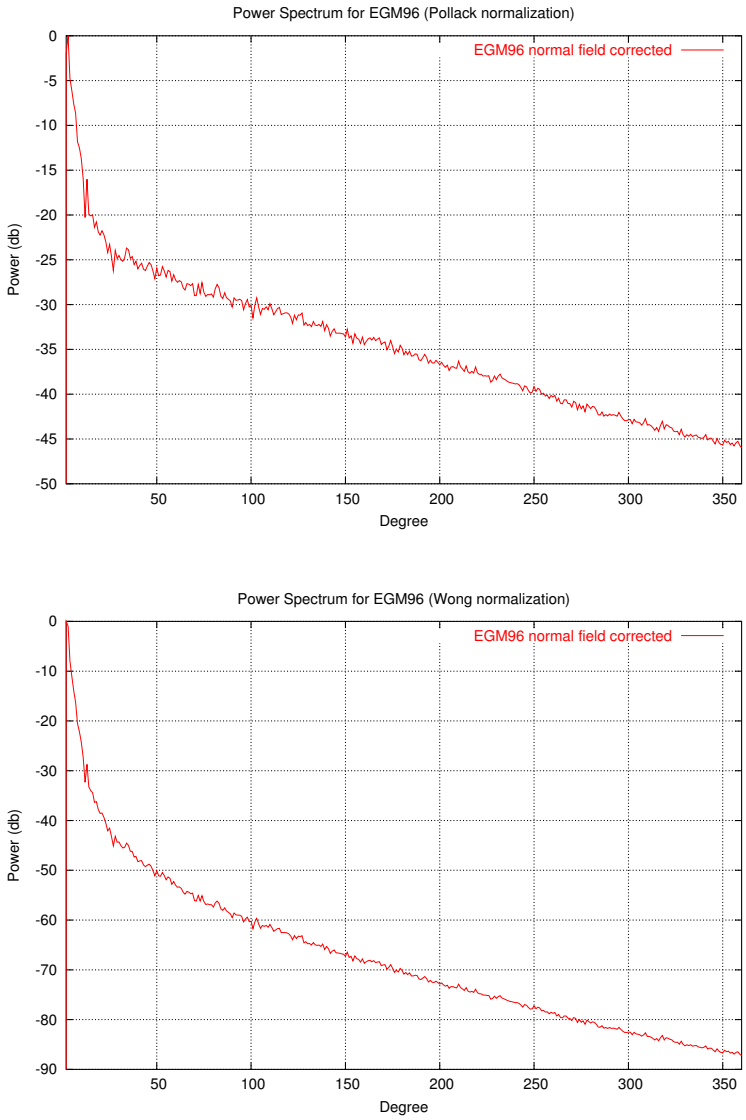

Figure 5-14: *Geopotential field EGM96 is shown with Pollack normalization (top) and Wong normalization (bottom) after being corrected to degree 8 for the normal field. Note the apparent linear features in the upper image.*

This is illustrated in **Figure 5-15**. Note that the estimated slope for degrees 50 to 350 of geopotential model EGM96 indicated earlier as -0.063655, corresponds to a depth of about 42.6 km.

Shown in **Figure 5-16** is the **EGM96** power spectrum from degree 2 to degree 102 with regression lines over three possible depth zones. That there are 2 lines over the middle zone reflects the inclusion or exclusion of degree 27 in the second and third zone. The spectrum between degrees 2 and 259 is shown in **Figure 5-17**. Depth estimates made by

Power Spectral Decay for Random Masses at Depth with Pollack Normalization

Depth (km)	Start Degree	End Degree	Slope	Intercept	RMS
1377	10	65	-2.108498	-6.483956	0.715606
1232	10	70	-1.862298	-6.428508	0.682542
1087	10	80	-1.622151	-6.395910	0.605898
942.5	10	97	-1.387754	-6.409862	0.579932
797.5	10	120	-1.152760	-6.702502	0.851110
652.5	10	140	-0.938112	-6.320963	0.521751
507.5	10	180	-0.719759	-6.384600	0.526288
362.5	10	260	-0.507356	-6.433044	0.484305
217.5	10	360	-0.301810	-6.286295	0.419965
72.5	10	360	-0.099525	-6.284648	0.419194
egm96 (corrected)	50	350	-0.063655	-24.0536	0.395040

Table 5-11: *Decay characteristics of the power spectra of Pollack-normalized random mass fields for various depths. For comparison, a sample line characteristic of* **EGM96** *is included. The RMS value indicates the 'fit' of the data to the regression line.*

Power Spectral Decay for Single Masses at Depth with Pollack Normalization

Depth (km)	Start Degree	End Degree	Slope	Intercept	RMS
3200	0	20	-6.0524	0.0136988	0.0420106
1600	0	50	-2.50885	0.00337255	0.0666596
800	0	100	-1.16355	-0.0163561	0.0762518
400	0	200	-0.56227	-0.0188264	0.0651609
200	0	300	-0.276818	0.00830768	0.00947161
100	0	300	-0.137298	-0.00479047	0.0419473

Table 5-12: *Decay characteristics of the power spectra of Pollack-normalized single mass anomalies for various depths.*

---

using equation 5-14 with the slopes indicated in **Figure 5-15** suggest that the deepest causative bodies are located in the upper half of the lower mantle. Depth estimates made

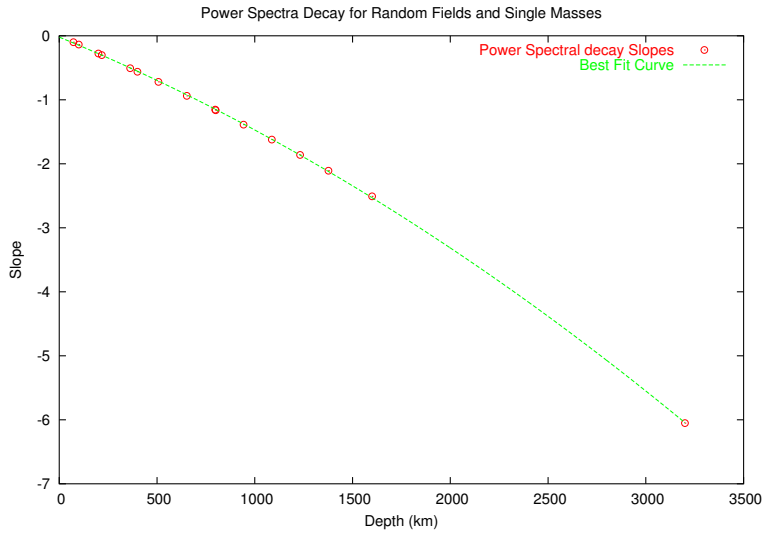

Figure 5-15: *The combination of single masses, plus random fields, with the best fit curve. Pollack normalization employed.*

---

from the whole spectrum are shown in **Table 5-13**.

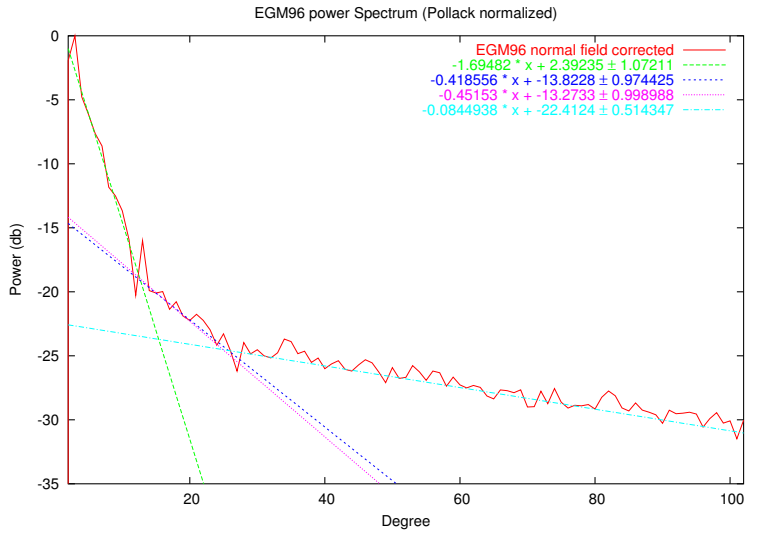

Figure 5-16: *Piece-wise linear regressions are overlaid on the* **EGM96** *power spectrum between degrees 2 and 102. These quasi-linear trends are indicative of anomalous masses arranged in shells.*

As a matter of interest, one might like to do a visual comparison of the mass anomalies that were reported in [Lithgow-Bertelloni, Richards et al. 1993; Ricard et al. 1993] and

Depth Estimates from the Power Spectrum of EGM96

Slope	Depth (km)	Equivalent Radius (km)	Degree Range Low	Degree Range High
-1.69482	1130.9	5247.	2	11
-0.418556	307.2	6071.	12	27
-0.45153	330.8	6047.4		
-0.0844938	58.7	6319.4	28	102
-0.0839344	58.3	6319.9		
-0.0649262	43.6	6334.6	102	296
-0.0647521	43.4	6334.7		
-0.0483362	30.7	6347.4	297	359

Table 5-13: *Slopes taken from* **Figure 5-17** *suggest mass anomalies at the depths shown. Pairs of slopes are from different interpretations of the regression lines set to segments of the* **EGM96** *spectrum. These do not correlate with anomalies derived from other geophysical measurements.*

[Lithgow-Bertelloni and Richards 1998] with the spectrum of a field like **EGM96**. The aforementioned authors indicated a good correlation with current geopotential fields, but the interpretation that has been placed on **EGM96** does not seem possible in **Figure 5-18**, except perhaps for the latter half of the spectrum. Between degrees 150 and 360, one might interpret the curve as being sufficiently linear to estimate a depth of burial of about 64 km. This is about 8.5 km shallower than Lithgow-Bertelloni's shallowest masses. As well, **Figure 5-19** which uses the same scale as **Figure 5-16**, shows a close-up of Lithgow-Bertelloni's summed masses. Notice that the power drops much more rapidly than is evident in **EGM96**, suggesting that while the geophysical analysis done by that group may be plausible, it does not completely reflect the measured spectrum.

Examining **Figure 5-18** one can see a curvilinear shape to the normalized spectrum, which is of some interest. One can surmize that some combination of mass anomalies can produce such an effect through a summation process. This effect can be demonstrated in **Figure 5-20** where one can see identical masses at different depths, and non-

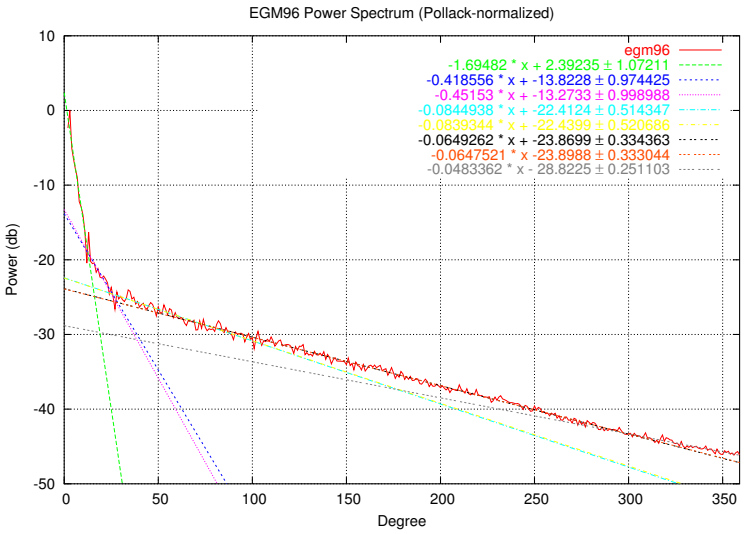

Figure 5-17: *For degrees 2 to 359, piece-wise linear regressions are overlaid on the* **EGM96** *power spectrum.*

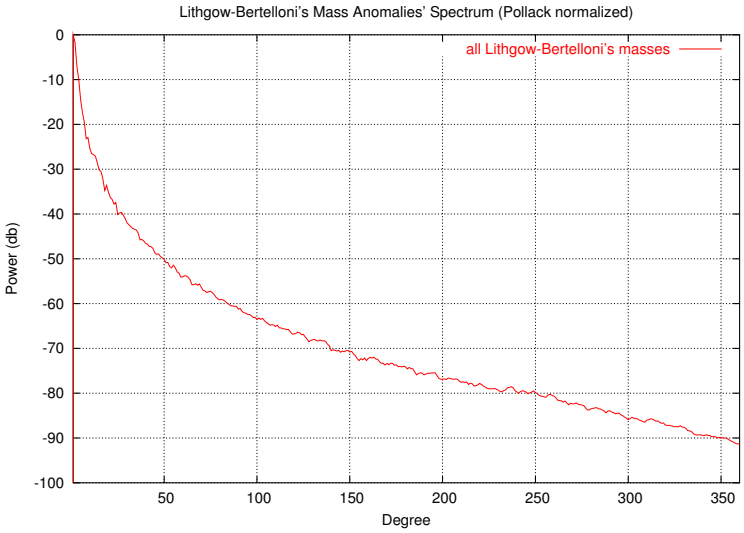

Figure 5-18: *The power spectrum for the sum of all Lithgow-Bertelloni's 20 spherical harmonic amplitude spectra. Using the observed correspondence of slope and depth, the approximate slope of the spectrum between degrees 150 and 360 which is -0.09141±0.00049 indicates a depth of 64.06 km, just 8.5 km shallower than the mass anomalies closest to the surface in her model.*

---

identical masses at different depths (and their inverse). It is apparent that deeper masses

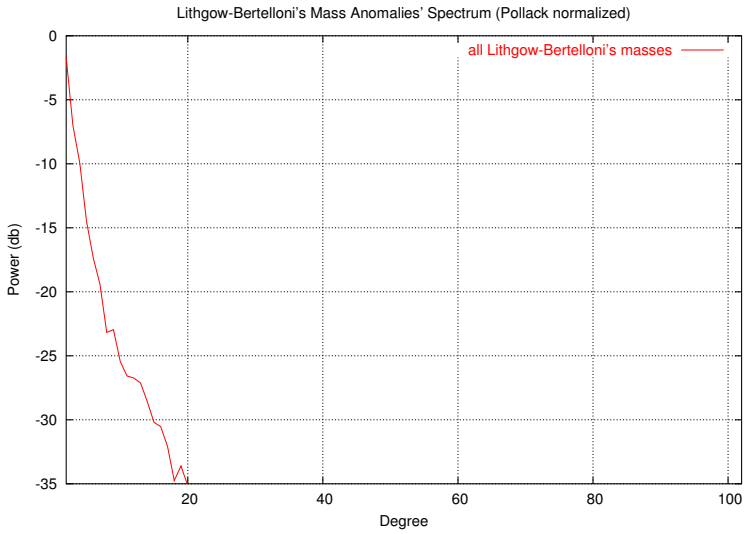

Figure 5-19: *This is a close-up of that pictured in* **Figure 5-17***, and has the same scale as* **Figure 5-16***. A visual inspection suggests that Lithgow-Bertelloni's model could yet be improved.*

---

influence the lowest degrees, but that their influence is lost if shallower masses have a greater magnitude. This is the spectral characteristic alluded to earlier: depths can be estimated, but not all masses are visible.

Finally, the supposition that phase difference in the spectrum of each mass anomaly allows for a sharper demarcation of the individual power spectra is examined. An encouraging result can be seen in the multi-images of **Figure 5-21**. Except for the two polar cases with angular separations of 0° (top left) or 180° (bottom right), the slope expected for each of the masses is fairly represented in the combined power spectrum, albeit with some error around the point of intersection. Notice also that the smoothness of the intersecting spectra is a function of the angular separation, with the degree of 'roughness' increasing with that angle. At the maximum possible angular separation, the noise level becomes unexpectedly high, for numerical reasons. An examination of the spectral coefficients reveals that the non-zero order coefficients are either zero, or are very small.

5.3.1 Earth Characteristics from Geopotential Spectra

The reason for exploring the spectrum was to see if it could be used to make better depth estimates for mass anomalies. To that end, it can be seen that masses subject to the initial requirements, that being that they be treated as point masses, could be seen to have a

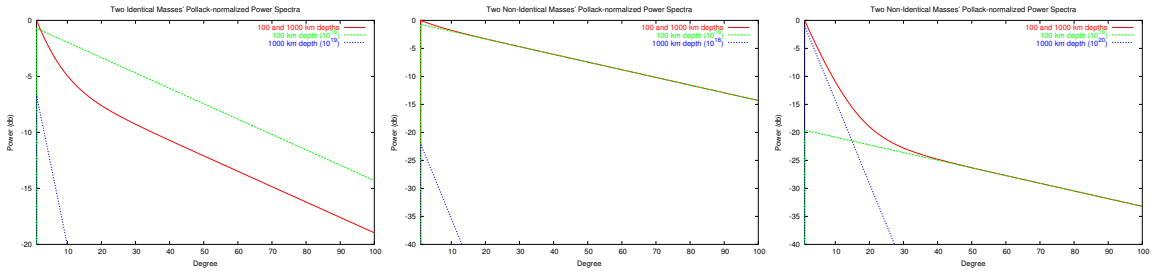

Figure 5-20: *On the left are two masses of size 10^{19} grams at the depths 100 and 1000 km. At higher degrees, the power spectrum resembles the shallower mass. At low degrees, the spectrum approaches the slope of the deeper mass. In the centre are two masses at depths of 100 and 1000 km, with magnitude 10^{19} grams and 10^{18} grams respectively. The deeper mass makes little contribution to the overall spectrum. On the right the masses are reversed and it can be seen that the larger but deeper mass has a stronger influence on the lowest degrees of the power spectrum. The shallower mass still influences the highest degrees.*

---

particular characteristic when the spectrum was viewed in a certain manner. Also seen was the fact that there is still ambiguity, in that some point masses will always be hidden by other masses (larger and shallower) in their joint spectrum. Nevertheless, this *tool* as it were, does promise to give insight into the makeup of the Earth. To that end, the **EGM96** geopotential field can be examined to see what one might learn from it.

By careful selection of the mass anomaly locations, even if positions are in error by a small amount, the possibility of re-creating the measured field may be possible. Given the locations and a depth estimate, mass magnitudes can be determined, and a synthetic field having a geological basis may result.

The first inversion was performed on the lowest degree range observed for that field: 2↔11. Recall that two different interpolating procedures were tried: 9 and 25 point. Generally, these agreed, with the exception that the former found an additional point. The fifteen mass locations shown in **Figure 5-11** are tabulated in **Table 5-14**. Note that these anomalies were interpreted to lie at 1131 km, as suggested by the normalized spectrum shown in **Figure 5-16**. Inversion of the spectrum indicated that the masses were 1 to 2 orders of magnitude larger than those Bowin, and 4 to 5 orders of magnitude larger than those of Lithgow-Bertelloni (all of whose 20 shells tended to be smaller by about that amount). Recalculating the geopotential field from the estimated masses indicated a

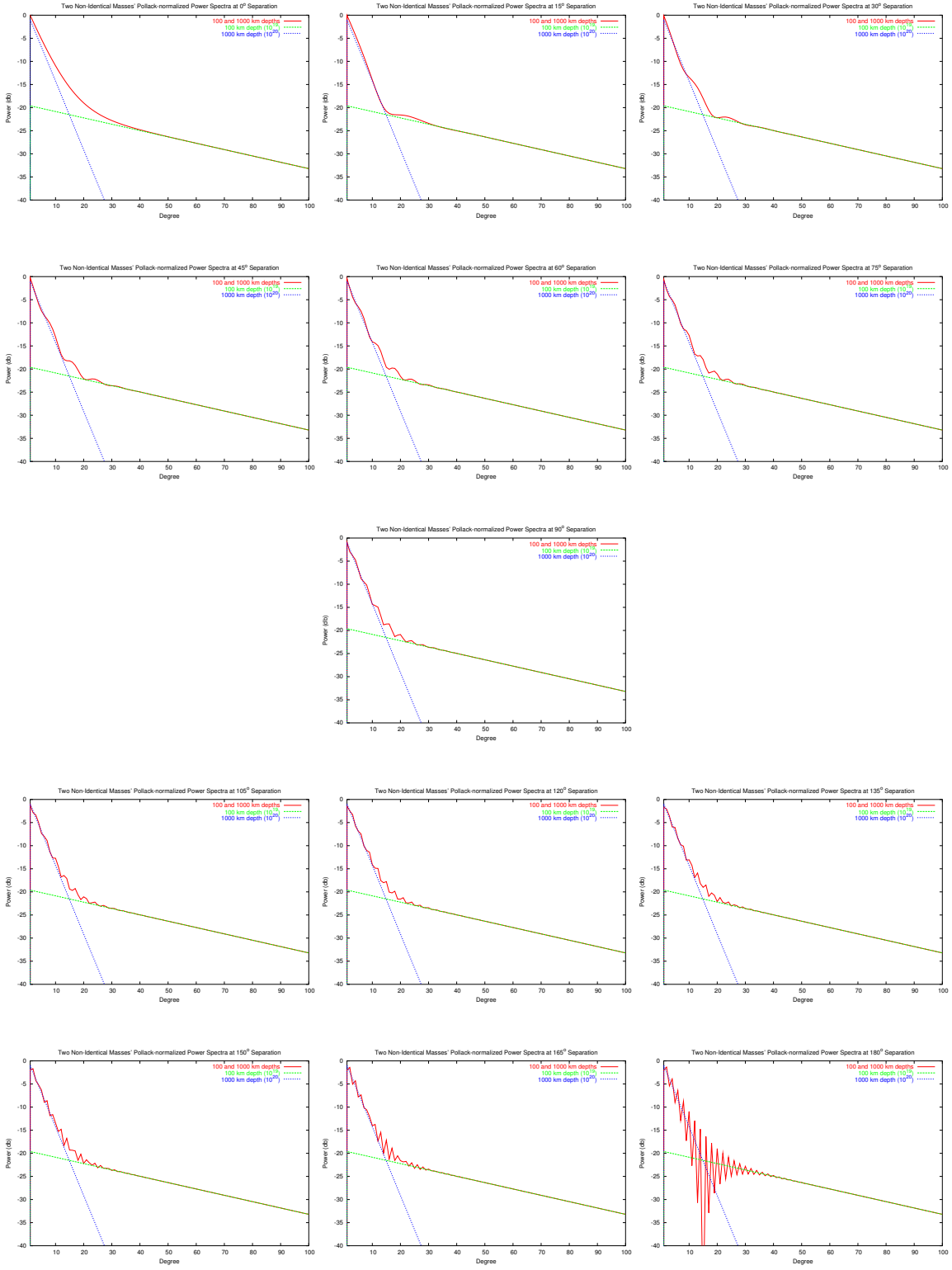

Figure 5-21: *Two masses, the first being 100 km beneath the North pole with magnitude 10^{19} grams, and the second at 1000 km beneath the surface with magnitude 10^{20} grams, with varying angular separation. From the top left,*

the latitude of the deeper mass varies from 0° to 180° difference. Note the sharp demarcation corresponding to the slopes of the mass anomalies, except where the masses are both beneath the North pole.

---

match with a correlation coefficient of 90%, however, the re-computed geopotential had a standard deviation about the mean (0.931) of 121.798 on a 2° equiangular sample interval. The minimum potential difference between the correct and computed potential due to the inverted masses was -518.77 and the maximum was +431.16, strongly suggesting that the correlation coefficient was not a reliable indicator of an accurate inversion.

Performing an inversion on the degree range 12↔27 resulted in a potential field that correlated with the original to 86%. The mean value and standard deviation of the differences between the computed and true potential values were 0.156±14.740. The minimum and maximum differences were -73.23 and +108.24 respectively.

Attempting the simultaneous solution of the two layers (depths 1131 and 320 km) gave an excellent geopotential match (98.7%), but the masses were (at times) markedly different from the individual solutions. The duplicates discarded (all from the 12↔27 degree range) were identical to the individual runs - which might be expected as the peaks used were from those runs. The mean and standard deviation for the differences between actual and computed potential were 0.059±44.592 with minimum and maximum differences of -299.10 and +216.56 respectively.

As an example of the differences possible from the two approaches, in **Table 5-15** are shown those calculated from an individual run, versus the combined run for degree range 2↔11. Note the relative error for the two attempts, and whether or not a high was expected. For the other dataset (degree range 12↔27), 58 of the 184 masses disagreed in sign with the presumed sign of the anomaly in the combined case (31.5%), while only 4 of the 184 disagreed in the range restricted case (2.2%).

If the two independent mass analysis runs are combined (i.e. the files are concatenated), and the power spectrum is computed, **Figure 5-22** results. The slopes are not what was expected however. Over the first range, a slope of -1.78 per degree (compared to about -1.69 per degree observed for **EGM96**) and for the second range, a slope of -0.57 per degree (compared to the range -0.419↔-0.452, or near about -0.435 per degree for **EGM96**) were observed. The observed slopes suggested depths of 1181 and 412 km

9 Point versus 25 Point Mass Estimates at 1131 km

Colat	Lon	9 Pt. Masses (gm)	25 Pt. Masses (gm)
138.12	43.76	$+1.445077*10^{22}$	$+1.437910*10^{22}$
85.23	76.68	$-2.391181*10^{22}$	$-2.499971*10^{22}$
42.67	91.20	$-3.310169*10^{20}$	$-7.159362*10^{21}$
96.93	145.63	$+2.370215*10^{22}$	$+2.456003*10^{22}$
52.26	173.94	$-1.231404*10^{21}$	$-5.973212*10^{20}$
162.24	180.08	$-1.764103*10^{22}$	$-1.734742*10^{22}$
28.32	197.65	$+5.046133*10^{21}$	$+5.714147*10^{21}$
119.87	230.66	$+1.968236*10^{21}$	$+1.531852*10^{21}$
66.69	236.89	$-1.216150*10^{22}$	$-9.141775*10^{21}$
112.39	252.57	$-1.157434*10^{21}$	$-7.250776*10^{20}$
32.02	272.11	$+2.951412*10^{21}$	$-1.560431*10^{22}$
111.48	292.05	$+5.372541*10^{21}$	$+1.392713*10^{21}$
66.38	296.90	$-2.446202*10^{21}$	
147.70	302.11	$+5.743403*10^{20}$	$+2.168099*10^{21}$
30.08	336.90		$+2.317899*10^{22}$
137.02	351.35	$+4.665534*10^{21}$	$+2.632707*10^{21}$

Table 5-14: *For the degree range 2↔11, masses were estimated at the locations of the extrema in the geopotential field as shown in* **Figure 5-16**. *Each interpolant found one additional extremum. The addition of these points in each inversion is the cause of the difference in mass size for the common locations. Duplicate extrema (there was an instance near colatitude 147.7, longitude 302) are not shown. The coordinates shown are those found for the 9 point interpolant. For the coordinates of the 25 point interpolant, see* **Table 5-15**.

respectively.

The simultaneous solution for the same degree ranges is shown in **Figure 5-23** for two choices of datasets. It is obvious that the choice of data to include in the linear analysis is critical to the interpretation. For the case where the data was analyzed for linear features only to degree 27, the first range shows a slope of -1.96 which is a higher in magnitude than that observed (-1.69), and the second is -0.38, compared to that observed in **EGM96**

Selected Range versus Combined Analysis for 1131 km

Colatitude	Longitude	Estimated Mass		High/Low	Relative
		2↔11 Degree Range	Combined Run	Expected	Error
138.13	43.76	$+1.437910*10^{22}$	$+1.172515*10^{22}$	H	-0.18457
85.23	76.68	$-2.499971*10^{22}$	$-1.835775*10^{22}$	L	-0.26568
42.68	91.21	$-7.159362*10^{21}$	$-1.821100*10^{22}$	L	+1.54366
96.91	145.62	$+2.456003*10^{22}$	$+1.871427*10^{22}$	H	-0.23801
52.26	173.96	$-5.973212*10^{20}$	$-4.691477*10^{21}$	L	+6.85419
162.24	180.10	$-1.734742*10^{22}$	$-1.232662*10^{22}$	L	-0.28942
28.32	197.64	$+5.714147*10^{21}$	$+6.007909*10^{21}$	H	+0.05140
119.88	230.66	$+1.531852*10^{21}$	$-2.728807*10^{21}$	L	-2.78138
66.68	236.88	$-9.141775*10^{21}$	$-9.852181*10^{21}$	L	+0.07770
112.40	252.57	$-7.250776*10^{20}$	$+6.579872*10^{20}$	H	-1.90747
32.03	272.11	$-1.560431*10^{22}$	$-1.192218*10^{22}$	L	-0.23596
111.49	292.05	$+1.392713*10^{21}$	$+1.432038*10^{22}$	H	+9.28236
147.69	302.08	$+2.168099*10^{21}$	$+3.757541*10^{21}$	H	+0.73310
30.08	336.90	$+2.317899*10^{22}$	$+1.501331*10^{22}$	H	-0.35228
137.02	351.36	$+2.632707*10^{21}$	$-3.603731*10^{20}$	H	-1.13688

Table 5-15: *Example mass values interpreted from* **Figure 5-16** *resulting in a depth of 1131 km obtained by analysing only the degree range 2↔11, versus those found in a combined run with masses interpreted to exist at depth 320 km, and thus for the range of degrees 12↔27. Whether or not a local high was expected is noted, and is based on the peaks determined in the combined run. In the case of the single range run, errors were incurred at longitudes 230.66 and 252.57. On the other hand, the simultaneous run had a single error at longitude 351.36. Finally, the relative error is shown. Coordinates are those of the 25 point single degree range run.*

(-0.435). The intersection point is at (9.4, -14.9) with the last point attributed to the first line at degree 12. Only points to degree 27 were included. Ignoring degrees 11 and 12 which may have influenced the slope calculation, made negligible difference to their values (a change of about +0.01 at most). The slope -1.96 suggests a depth of 1284 km, or about 150 km (about 13%) deeper than expected. The slope -0.38 suggests a depth of 279 km, which is also 13% shallower than the interpreted depth. Adding additional points to the interpretation of the data in terms of 2 linear sets results in slopes of -1.96

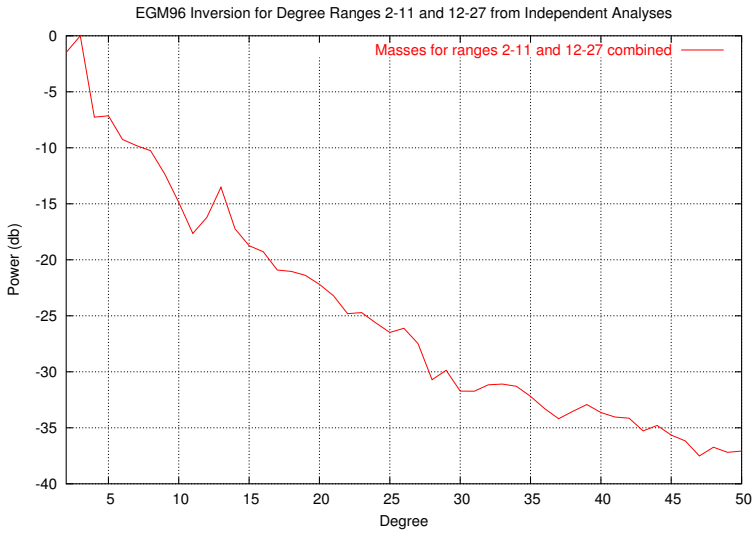

Figure 5-22: *The potential resulting from two independently run peak and mass analyses were combined to produce this power spectrum. It shows some of the character seen in the EGM96 spectrum over the degree ranges 2↔11 and 12↔27, but the slopes computed over the degree ranges are erroneous (see the text).*

---

and -0.44 for depths of 1284 and 322 km respectively.

Examining each of the assemblages of computed masses independently of the other, where the masses were determined from the spectrum range of degrees 2↔27, with the assumed depths 1131 and 320 km, indicates that the slopes determined from **EGM96** are repeatable. **Figure 5-24** shows four graphs. There are two each for the depths 1131 and 320 km, with one of each of these pairs showing the normalized spectrum for degrees 2↔100 and one for the range 2↔11 (for depth 1131) and 12↔27 (for depth 320). The slopes of the lines are nearly identical to those seen in **Figure 5-17**. The spectrum over the reduced degree ranges is sufficiently 'noisy' to account for the slope discrepancies observed in the earlier text.

It is likely that there is some interaction between the two spectra that might explain the slope discrepancy. Earlier tests indicated that single masses or masses situated on a uniform grid, with varying mass values had well defined slope characteristics. The interpretation and inversion of the lower degrees of **EGM96** resulted in multiple masses at two depths, with a non-uniform distribution. For a single mass M, the observed potential was

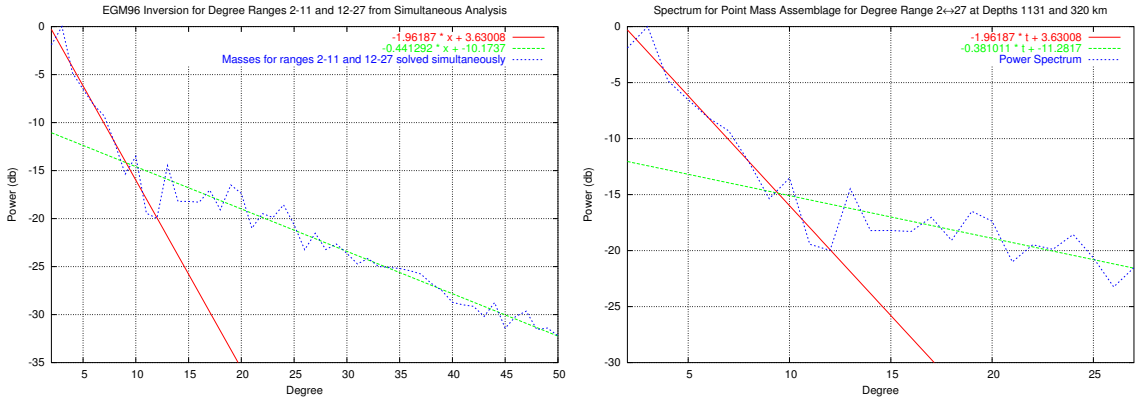

Figure 5-23: *This illustration of a combined solution for degree ranges 2↔11 and 12↔27 shows some of the characteristics of the* **EGM96** *power spectrum. The piece-wise linear regressions indicate a possible depth interpretation not unlike that of* **EGM96** *for the higher degree range, but is in error for the deeper masses. On the left, the higher degrees have been interpreted to degree 50 when computing the regression line. On the right, the higher range was restricted to degree 27.*

$$V = \frac{G}{R_E}\sum_{n=0}^{\infty}\sum_{m=0}^{n}\frac{M}{2n+1}\left(\frac{a}{R_E}\right)^n(\bar{a}_{nm}\bar{R}_{nm} + \bar{b}_{nm}\bar{S}_{nm}) \tag{5-15}$$

This has a clearly defined relationship between depth and degree, in the form of the power law discussed earlier. Multiple masses M_k have a slightly different form,

$$\begin{aligned} V &= \frac{G}{R_E}\sum_{n=0}^{\infty}\sum_{m=0}^{n}\sum_{k=1}^{N}\frac{M_k}{2n+1}\left(\frac{a}{R_E}\right)^n(\bar{a}_{nm,k}\bar{R}_{nm} + \bar{b}_{nm,k}\bar{S}_{nm}) \\ &= \frac{G}{R_E}\sum_{n=0}^{\infty}\sum_{m=0}^{n}\frac{1}{2n+1}\left(\frac{a}{R_E}\right)^n\left(\left(\sum_{k=1}^{N}M_k\bar{a}_{nm,k}\right)\bar{R}_{nm} + \left(\sum_{k=1}^{N}M_k\bar{b}_{nm,k}\right)\bar{S}_{nm}\right) \end{aligned} \tag{5-16}$$

where the coefficients $\bar{a}_{nm}, \bar{b}_{nm}$ are dependent on the mass distribution (i.e. mass location) and the mass magnitude. This affects how they sum. Note also that there is power in the lower degrees for both mass assemblages, and consequently, both sets of masses will impact the spectrum of the other. The potential for impact is visible in **Figure 5-24**. Notice the amount of power in the lower degrees of the 12↔27 degree range spectrum compared to that of the deeper bodies. Obviously the summation grows even more complex when mass assemblages at multiple depths are involved in the spectrum calculation.

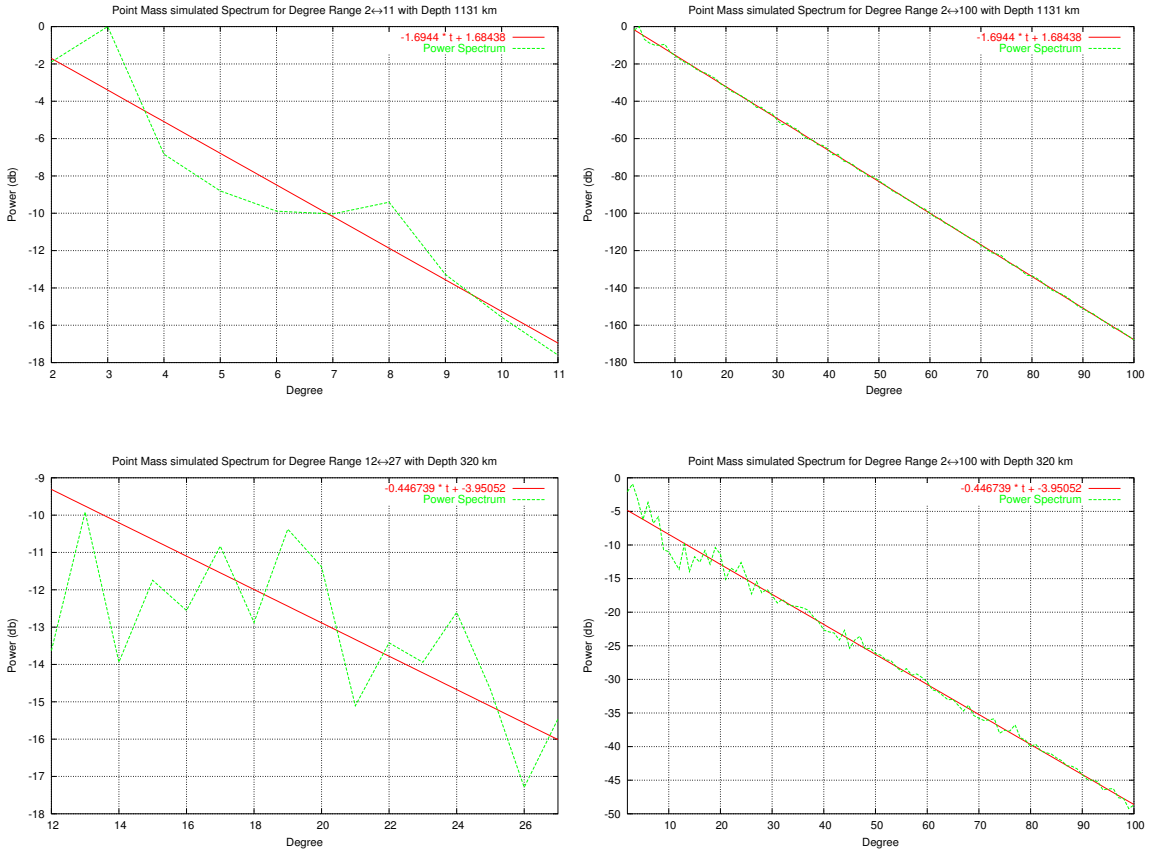

Figure 5-24: *The result from the peak analysis for each of the degree ranges identified (i.e. 2↔11 and 12↔27) in the normalized spectrum for* **EGM96** *have been combined, and the masses computed from the potential field over the entire degree range. The regression lines over degrees 2↔100 for the power spectrum for each of the mass assemblages were then determined, and are shown in the illustrations. Depth 1131 km for degrees 2↔11 and 2↔100 are at the top (left and right), and for the same ranges, the masses at depth 320 km are shown at the bottom. The slopes computed are very close to those interpreted in the normalized* **EGM96** *spectrum.*

5.3.2 A Modern Geopotential Field

This section examines the **CHAMP** or **CHA**llenging **M**inisatellite **P**ayload geopotential field. **CHAMP** is a German small satellite mission for geo-scientific and atmospheric research and applications[68]. In particular, the **CHAMP** mission will generate a highly precise gravity field. As well, datasets may be obtained up to degree and order 140 (at the time this document was written). Note that the analysis is complete only to degree

[68] http://op.gfz-potsdam.de/champ/index_CHAMP.html

and order 120, with degree 140 complete for only selected orders.

Figure 5-25 shows the **CHAMP** field normalized both via Pollack and Wong normalization (as done before). In the same illustration is included the **EGM96** field with Pollack normalization. A close-up of degrees 2 through 40 are shown in **Figure 5-26** where the interpretation of the **EGM96** field has also been included. Of particular interest is the unexpected divergence of the fields above degree 40, below which their power spectra are nearly identical. The upward concave shape is puzzling as it clearly does not follow the Pollack model. One might conclude that a sub parallel line might be ascribed to degrees $35 \leftrightarrow 80$. This would correspond to bodies at a slightly deeper depth, but a deeper depth following a shallower depth makes little sense. How to explain the upward trend after degree 80 is not immediately apparent, but [Roland and Denker 2002] suggests that it is due to the fact that CHAMP is a satellite only mission, and therefore tends to lose power at the higher degrees. This may be compounded by too optimistic error estimates. This will be a subject for further investigation.

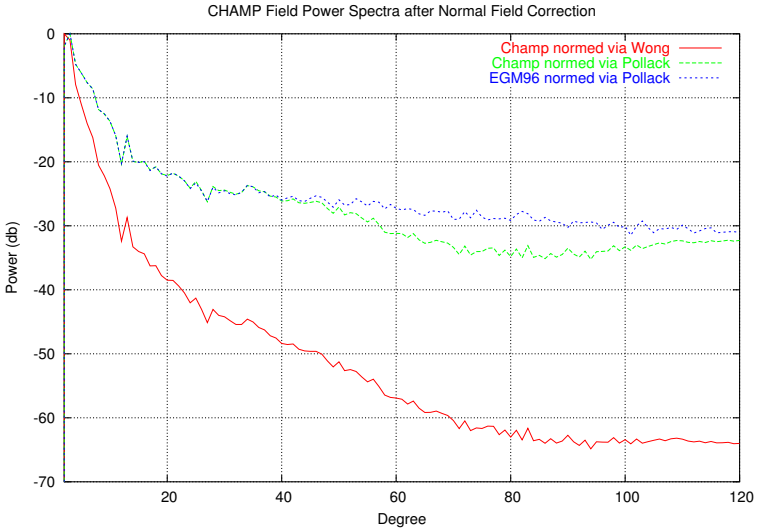

Figure 5-25: *This is the recently released CHAMP geopotential field to degree and order 120. Shown is the field normalized via Pollack and Wong and for comparison, EGM96 normalized via Pollack. Note the EGM96 and CHAMP fields are virtually identical to degree and order 40, before an unexpected divergence occurs. This divergence may have implications for higher degrees.*

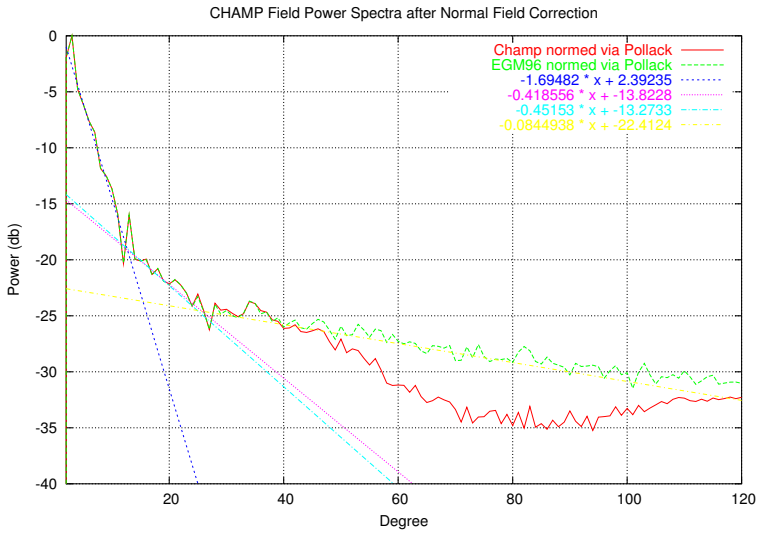

Figure 5-26: *Shown are both* **CHAMP** *and* **EGM96** *geopotential fields. To the degree that depths have been interpreted, and masses estimated, the fields are identical.*

5.3.3 Final Comments on Spectrum-based Depth Estimates

This section discussed the use of the spectral representation of the measured geopotential field to estimate the depth of buried masses. Although the spectrum for bodies buried at various depths changes very little, particularly for increasingly deep bodies, that there is a change afforded an opportunity for exploitation. To take advantage of the spectrum as a possible depth estimator, a particular assumption had to be made, and the limitations of this assumption had to be recognized.

While it is highly unlikely that any body causing a recognizable surface expression is spheroidal, this was the mandatory assumption that was required. Using the well-documented model for a point source, which from a gravity-inducing perspective is identical to a uniform spherical source, the effect of depth as a function of spectral characteristics was examined using synthetic data. It was demonstrated with additional synthetic studies that certain bodies would be 'lost' using the model. Larger shallower masses were seen to always mask deeper and smaller bodies. As well, individual sources were seen to be invisible in the spectrum. This is a consequence of a global 'Fourier' analysis, unlike the spatially sensitive wavelet analysis technique.

The point source model study was extended to an examination of two publicly available geopotential fields, which for low degree and order, exhibited characteristics similar to

those observed in the synthetic studies. Interpreting the resulting spectra provided estimates for possible depths of burial for bodies at two levels. Using the peak-finding methods and inversion procedure discussed in the previous section, the masses corresponding to the extrema observed in the surface geopotential were computed. Re-computing the surface potential from the interpreted masses showed a good match to the observed fields in terms of cross correlation; however, the individual potential fields showed discrepancies, which are summarized in **Table 5-16**. As well, the slopes (and thus the presumed depths) of the masses in the re-computed geopotential were observed to be in error. This is believed due to the impact that each set of masses had on the other when their respective spectra were summed. As well, the datasets used to estimate the slopes were small. Extending these to higher degree resulted in a near reproduction of the interpreted slopes from **EGM96**.

Point Mass Synthesis Summary (depths in km, potential in $(m/sec)^2$)

Degree	Interpreted		Estimated		Correlation	Potential Discrepancy		
Range	Slope	Depth	Slope	Depth		Mean±Std. Dev.	Min	Max
2↔11	-1.69	1131	-1.78	1181	90%	0.931±121.798	-518.77	+431.16
12↔27	-0.44	320	-0.57	412	86%	0.156±14.740	-73.23	+108.24
2↔27	-1.69	1131	-1.96	1284	98%	0.059±44.592	-299.10	+216.56
	-0.44	320	-0.38	279				

Table 5-16: *Running independent mass analyses from the potential computed from the indicated degree range gave good results in terms of correlation between synthesized and actual potential (first two lines). The mass analysis, and subsequent potential recalculation gave an even better correlation (third line), but in all cases, there was substantial discrepancies between the real and synthesized potentials.*

To the extent that the model assumptions can be accepted, a repeatable synthetic field can be generated, and an indication of the mid to upper mantle geology is indicated. Comparison of actual to computed geopotential from interpreted mass anomalies indicate that the field is not an accurate reproduction of the original, however. Furthermore, each of the mass assemblages interpreted and synthesized from the **EGM96** spectrum clearly has an impact on neighbouring degree ranges. This could make the original interpretation questionable. Even so, the apparent linearities are quite evident and suggestive of some form of layered Earth structure.

5.4 What Shape if not a Point

5.4.1 Variable Density Contrast

The simplifying assumption made in the previous analysis of depth was that the anomalies observed in the geopotential field were due to point masses. This was both convenient, and in fact necessary as the shape of the spectrum relied on this assumption. Of course, it is highly unlikely that any anomalies are due to point masses, and since one would like some insight into what their possible shapes might be, this section attempts to elucidate on that subject by further experiment.

As noted earlier, there is a theorem by Chasles, which is also known as Green's equivalent layer [Ramsey 1961], that says that any Newtonian potential V on an equipotential surface S can be represented outside of that surface by a surface layer of density μ on that surface,

$$\mu = \frac{-1}{4\pi G}\frac{\partial V}{\partial n} \tag{5-17}$$

where the partial derivative is taken with respect to the normal to the equipotential surface [Heiskanen and Moritz 1966]. Furthermore, using Gauss' theorem the amount of matter contained within S is given by,

$$\iint_S \mu dS = \iiint_v \rho dv \tag{5-18}$$

[Pail 1999] used the surface layer technique to consolidate all of the mantle into a single surface feature in order to reduce the amount of numerical work that he incurred.

In this section, using the expressions derived in chapter 2 for surface and shell layers, graphic illustrations of density variation at depths identified earlier will be seen. To begin, **Figure 5-27** shows the result of deriving a surface layer density at the greatest depth examined with the point source model (1131 km). The dataset employed was **EGM96** between degrees 2 and 11, and the synthesis was taken to 0.5°. A visual comparison with the top half of **Figure 5-11** is favourable, but should not be expected to be identical, as the downward continuation step alters the relative weights of coefficients as they contribute to the surface density synthesis. Note that a surface layer density is simply the result of a mathematical equivalence, and has no known relationship to real gravitational potential fields; nevertheless, it is instructive to see that it does reproduce the measured field, and when compared to the next figure, gives reassurance of its correctness

(insofar as the model assumptions allow). **Figure 5-28** is the shell model for the same depth, with a shell thickness of 150 km.

The contrast between the continuous shell and the point mass models shown in **Figure 5-11** is more evident in **Figure 5-29** which is a rendition of how density varies at a depth of 320 km when considered as a 150 km thick shell (the thickness used by other researchers). A comparison with the lower half of **Figure 5-11** shows clear differences.

Noteworthy is the fact that the density contrast variations are less than ±0.004 gm/cc for the 1131 km deep model and ±0.002 gm/cc for the 320 km deep model. This latter figure is approximately 0.025 times the variation assigned in [Ricard et al. 1993] (0.08 gm/cc). [Bowin 2000] quotes a density of about 0.0004 gm/cc to depth 670 km, and then 0.0024 gm/cc for deeper bodies for one model (to 800 km, except for 4 masses at the core/mantle boundary). In his second model (to depth 1400 km, with the same 4 masses), his density range varies over 0.00005↔0.00225 gm/cc. The density contrast computed by the modelling procedure described in this thesis for the 320 km shell model is within the range of both Ricard and Bowin's experiment. For the case of the deeper shell, the density contrast is nearly twice the highest figure used by Bowin and about 0.05 of that used by Ricard and colleagues. The mean density of the 320 km shell was 3.620 gm/cc and that of the 1131 km shell was 4.697 gm/cc. However, it must also be noted that the shell thickness has a direct bearing on the density contrast computed by the technique employed here, just as the size of the 'blocks' employed by other researchers must also affect the apparent contrast.

The **EGM96** geopotential model was interpreted as being composed of 5 zones. The third had an estimated depth of 58 km. Inverted as density contrast for a shell of 150 km thickness about a mean density of 3.370 gm/cc, this relatively shallow model is illustrated in **Figure 5-30**. Reducing the shell thickness to 25 km results in **Figure 5-31**. In this case, owing to the reduced thickness, the density contrast range rises in value to -0.0187507↔0.0170367 gm/cc from -0.00586163↔0.00535551 gm/cc around a mean density of 3.377 gm/cc. Although not apparent to the eye, the images are slightly different owing to the variable contribution of the denominator of equation 2-121.

The penultimate layer which is interpreted from degree range 102↔296 as being associated with the depth 43 km is seen in **Figure 5-32**. The density contrast range for a layer of 15 km thickness is higher than before: -0.089985↔0.163997 gm/cc around a mean

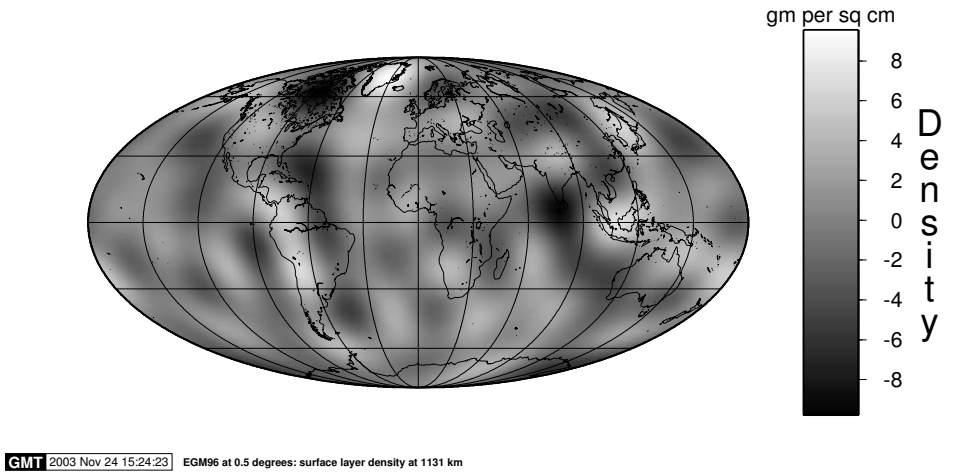

Figure 5-27: *This is an illustration of a surface layer density distribution at a depth of 1131 km using* **EGM96** *between degrees 2 and 11, as per the depth analysis performed earlier.*

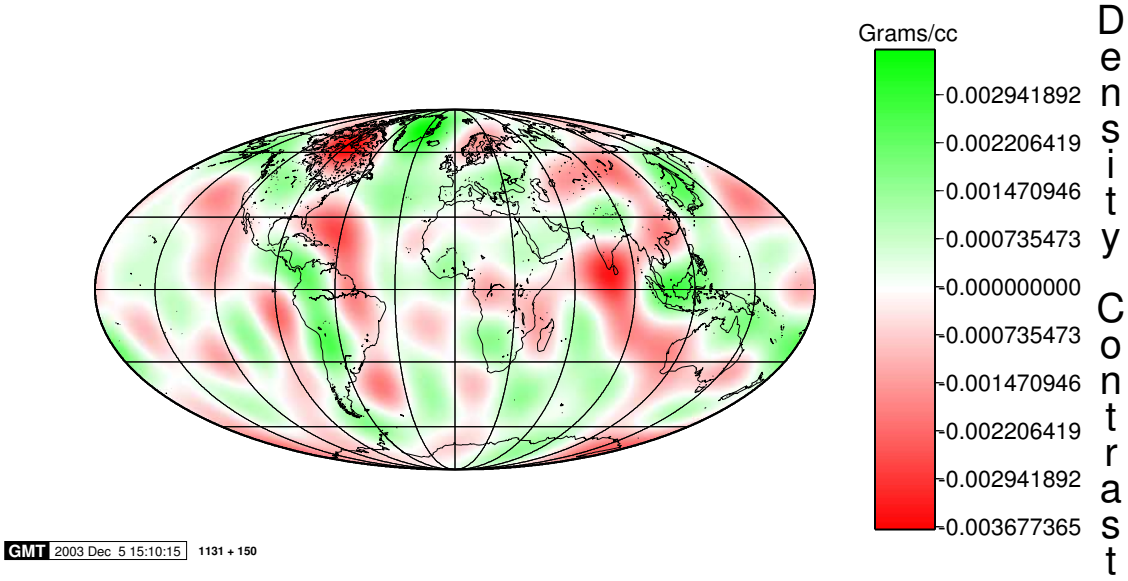

Figure 5-28: *The variation in density at 1131 km for a 150 km thick shell produced from downward continued geopotential coefficients from the range 2↔11, as interpreted previously. The density contrast ranges from -0.00371927↔0.00363546 gm/cc, corresponding to a mass variation of* $-1.875*10^{23} \leftrightarrow 1.833*10^{23}$ *grams.*

---

density of 3.379 gm/cc. The mass range corresponding to this density contrast range is $-6.7913*10^{23} \leftrightarrow 1.2377*10^{24}$ grams.

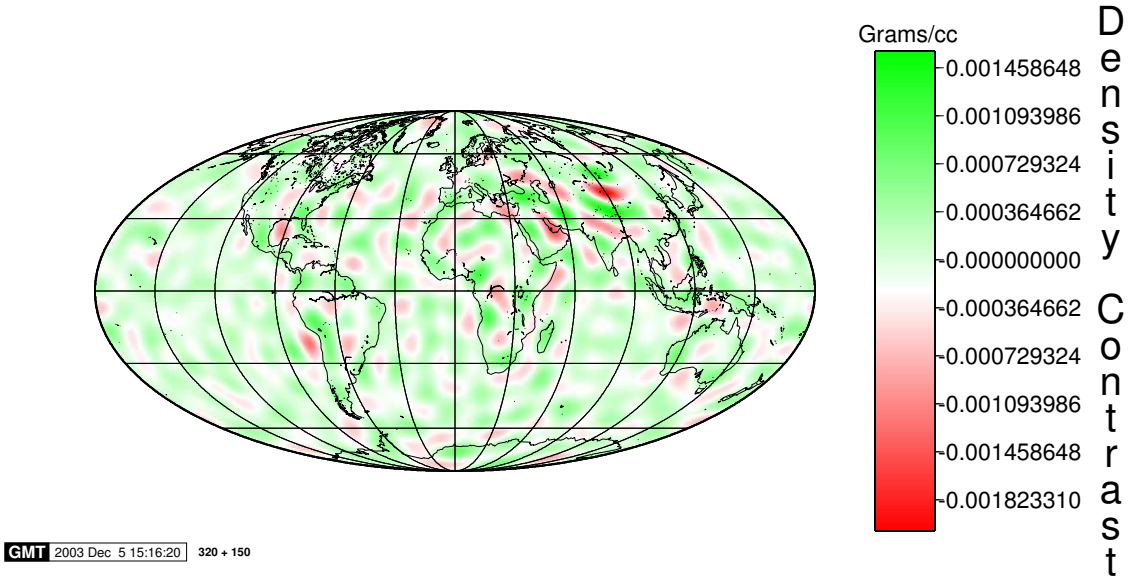

Figure 5-29: *This figure illustrates the variation in the density of a 150 km thick shell when geopotential coefficients estimated at the Earth's surface are downward continued to a depth of 320 km. The range of contrast is -0.00205883↔0.00158779 gm/cc which corresponds to a mass variation of* $-1.389*10^{23} \leftrightarrow 1.072*10^{23}$ *grams.*

The last layer, illustrated in **Figure 5-33**, is 12 km thick at 31 km depth, which is near the mean depth of the **Mohorovičić discontinuity**. The mean density is 3.359 gm/cc, and the density contrast range is -0.0457247↔0.0480633 gm/cc. This corresponds to a mass range of $-2.7725*10^{23} \leftrightarrow 2.9143*10^{23}$ grams.

5.4.2 Error Associated with Variable Density Contrast

The error associated with the analysis of the previous section is as variable as the density structure that was defined. That is to say, the error in the calculation of the density contrast is a function of several factors: depth, shell thickness and the measured spherical harmonic coefficients. Of the three, the coefficients affect the computed contrast in the most direct manner. Just as the equations indicate, an error in the potential coefficients is mapped directly to a corresponding error in the density coefficients.

The other factors affect the contrast calculation as a function of degree. Depth errors have the most pronounced effect, and for bodies assumed to lie at greater depths than they actually do, the error increases non-linearly with degree. For bodies assumed to lie at

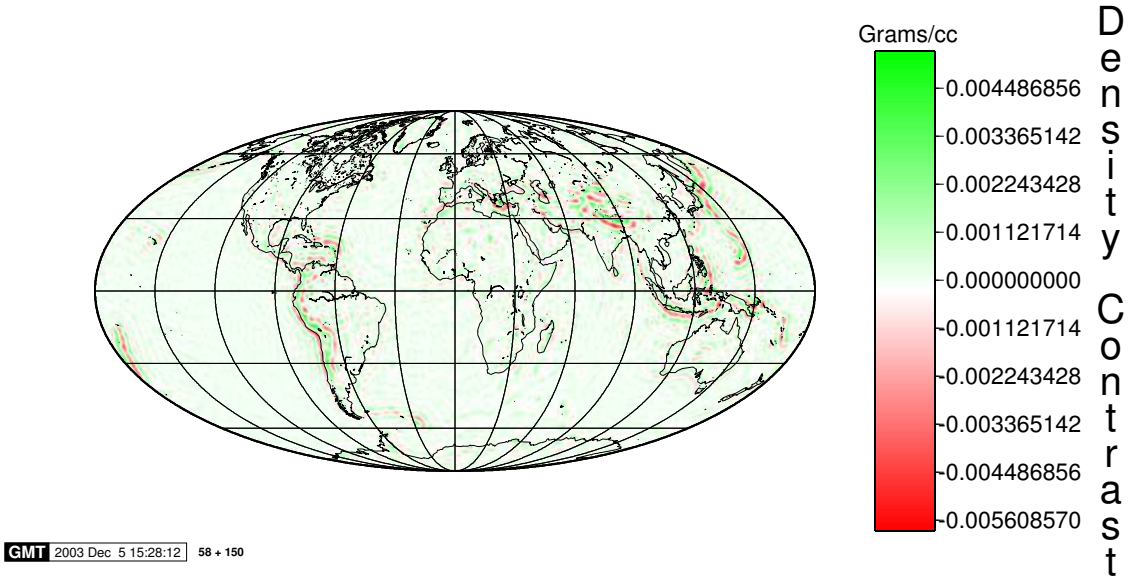

Figure 5-30: *This figure illustrates the variation in the density of a 150 km thick shell when geopotential coefficients estimated at the Earth's surface are downward continued to a depth of 58 km. The range of contrast is -0.00586163↔0.00535551 gm/cc which corresponds to a mass variation of* $-4.309*10^{23} \leftrightarrow 3.937*10^{23}$ *grams.*

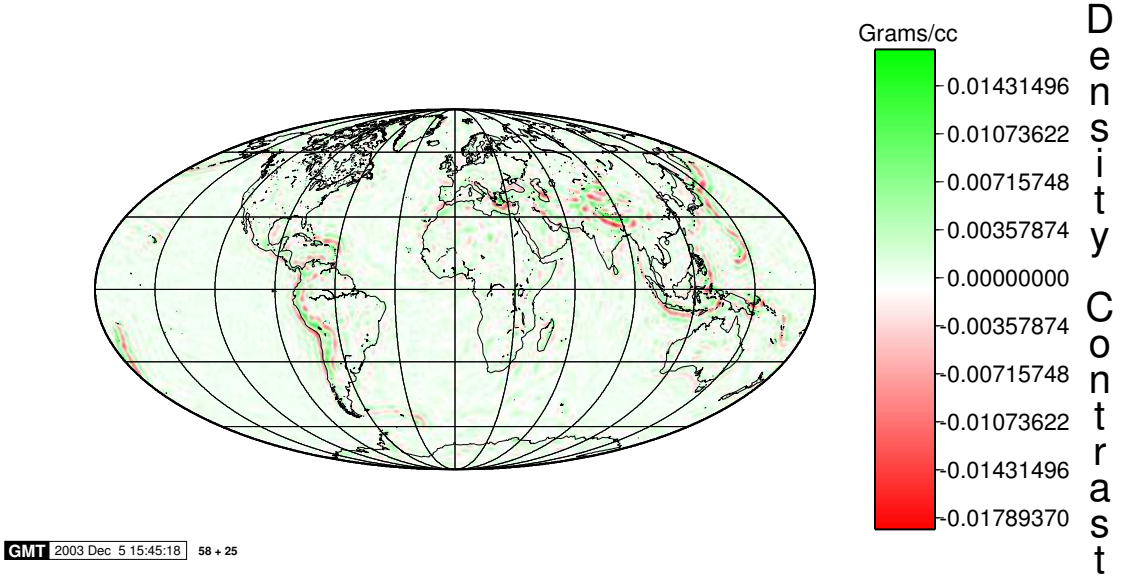

Figure 5-31: *This figure illustrates the variation in the density of a 25 km thick shell when geopotential coefficients estimated at the Earth's surface are downward continued to a depth of 58 km. The range of contrast is*

-0.0187507↔0.0170367 gm/cc which corresponds to a mass variation of -2.343∗10^{23}↔2.129^{23} grams.

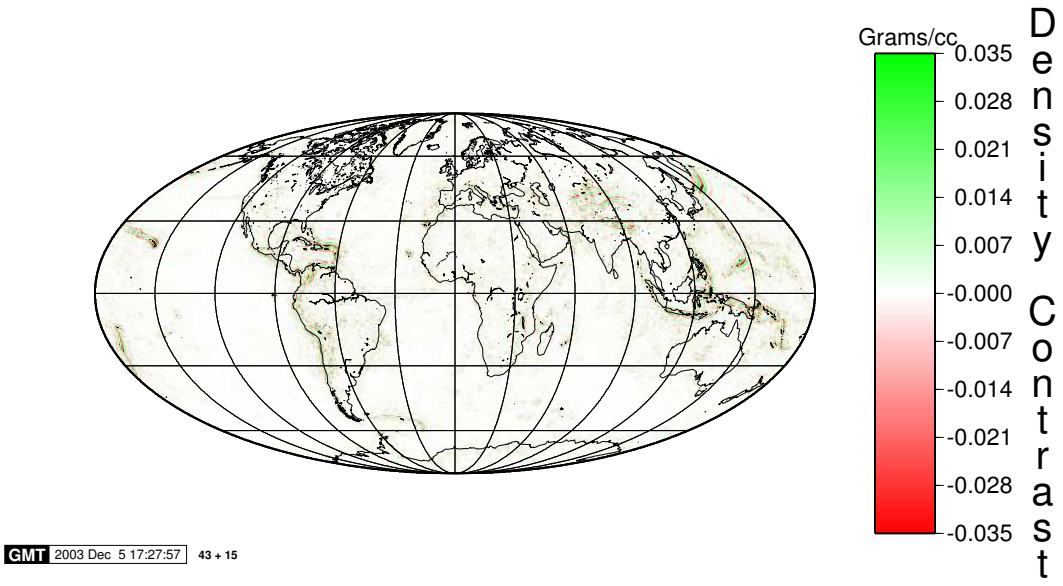

Figure 5-32: *This illustrates the variation in density contrast of a 15 km thick shell at 43 km, as interpreted from EGM96's spectrum. The contrast range is -0.089985↔0.163997 gm/cc which corresponds to a mass range of -6.7913∗10^{23}↔1.2377∗10^{24} grams. The range of data samples shown has been reduced to highlight low amplitude features.*

shallower than correct depths, the non-linear effect is greatly reduced, but still can be substantial. Error in shell thickness is greatest at the lowest degrees, falling rapidly to an inconsequential value for high degree. Illustrations of the effects of depth and thickness error on the computed coefficients show these effects clearly. The following figures have been selected to cover the range of depths interpreted from the normalized **EGM96** spectrum.

In **Figure 5-34** the effects of depth and thickness error are illustrated for the shallowest shell depth: 31 km, with a 12 km thickness. Errors of 1% and 10% for both depth and thickness are shown. As the degree range for this layer is presumed to be the highest, the figures cover the entire spectrum. The maximum error in the computed coefficients occurs at degree 360 and ranges from about 1.75% to approximately 19% if the error is to assume the body is deeper than the correct depth. Should the error assume a shallower

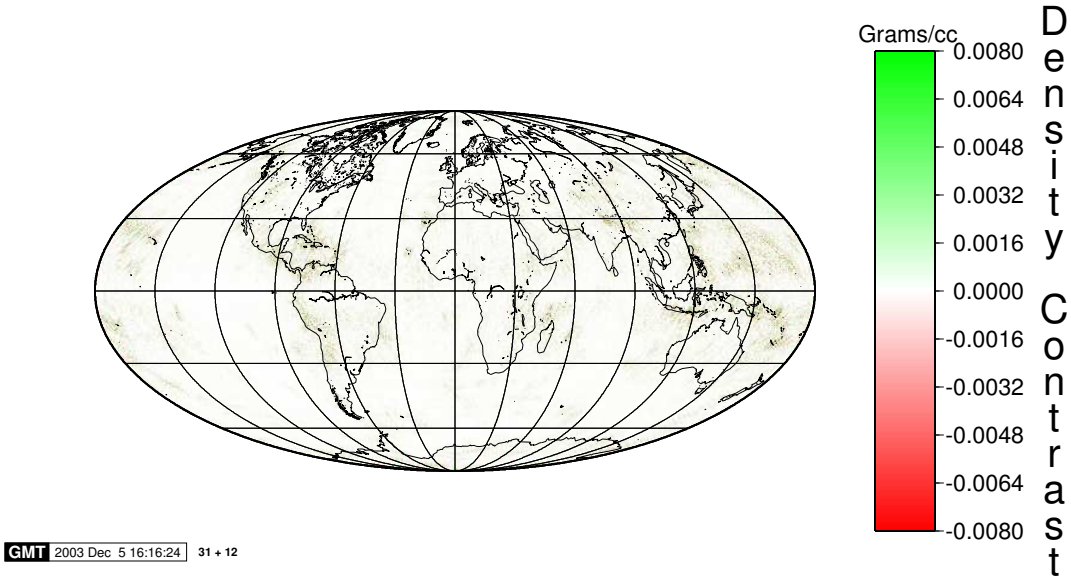

Figure 5-33: *This illustrates the variation in density contrast of a 12 km thick shell at 31 km, as interpreted from EGM96's spectrum. The contrast range is -0.0457247↔0.0480633 gm/cc which corresponds to a mass range of -2.7725∗10^23↔2.9143∗10^23 grams. The range of data samples shown has been reduced to highlight low amplitude features.*

---

body, the maximum error ranges from -1.75% to about -16%. The thickness error is much smaller, ranging from a maximum of approximately ±1% for a 1% error in thickness to about +11↔-9% for a 10% error in thickness. It declines to about ±0.7% for a 1% error in thickness to the approximate range -6%↔+7%. The thickness error range maximum appears to be independent of the depth or shell thickness, but the rate of decay is not, as it decays more slowly with thinner shells.

Figure 5-35 shows similar calculations for the greatest depth that was interpreted: 1131 km. A 1% error in depth becomes a maximum at degree 11 (the highest used for that depth) of ±2.5%. An error of 10% translates to an error range of -23% to +30% for the highest degree. The thickness error has initial values similar to the 31 km depth layer, but declines to a range of about ↔0.8% by degree 11 for a 1% thickness error, and -7.5% to +9% for a 10% error.

Figure 5-36 illustrates the relative error for a depth of 320 km for the same depth and thickness errors. For a 1% error in depth, the relative error ranges over ±1.5% at the maximum degree of interest (27). For a 10% error in depth, the error ranges over

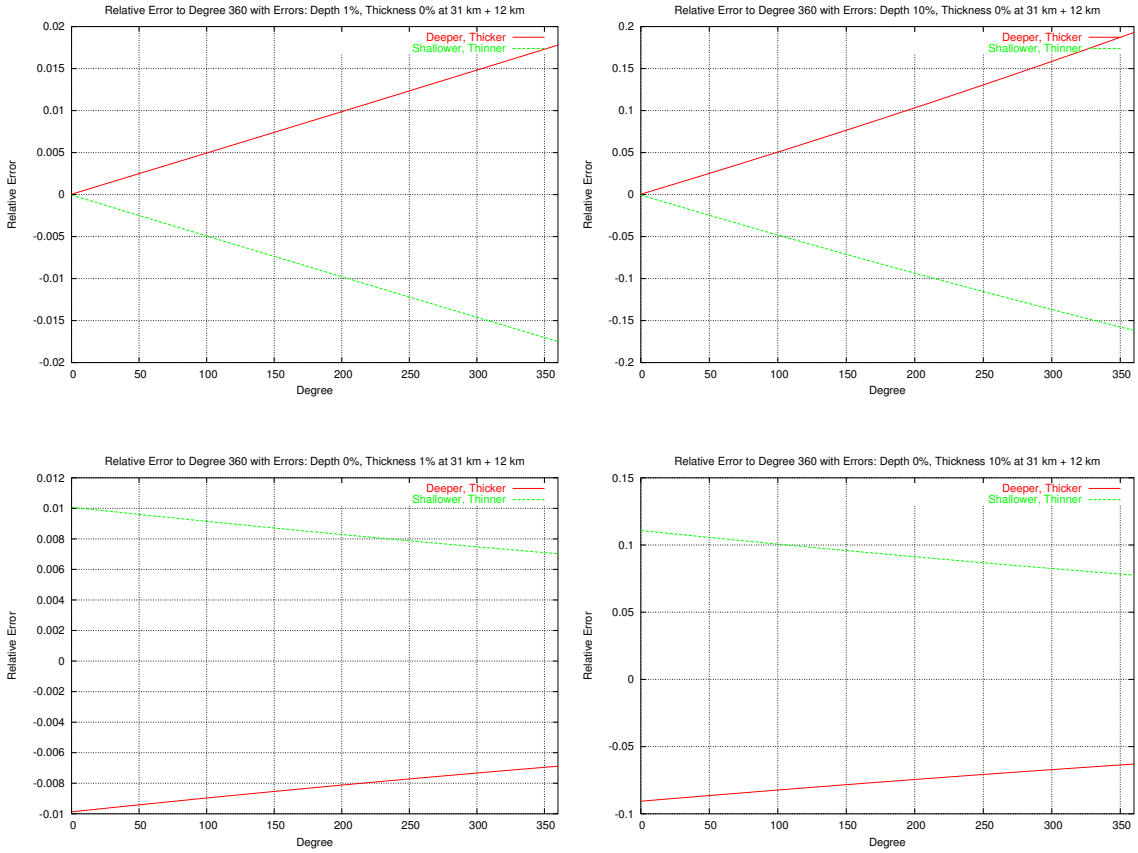

Figure 5-34: *Relative depth errors of 1% and 10% are shown in the top half (left and right respectively). Relative thickness error for the same percentages is shown in the bottom half. The layer is at 31 km and has a 12 km thickness.*

-14%↔+16% at the maximum degree. The thickness error has about the same maximum range, and declines to ±0.65% for a 1% thickness error. The range is about -13%↔+16% for a 10% thickness error. The same figure also shows the effect of depth and thickness error to degree 360, to highlight graphically the non-linear characteristic of both the depth and thickness error curves as a function of degree.

The question remaining is what effect the errors just described have on the computed density contrast. This may be determined through experiment. For example, a 10% increase in the presumed depth for a layer at 31 km compared to the presumed depth results in an apparent contrast range of -0.00854694↔0.00790712 gm/cc versus the presumed range -0.0457247↔0.0480633 gm/cc cited earlier. This corresponds to about a 16 to 18% change in the contrast. The mean value of the difference was $-3.421*10^{-5}\pm6.145*10^{-3}$.

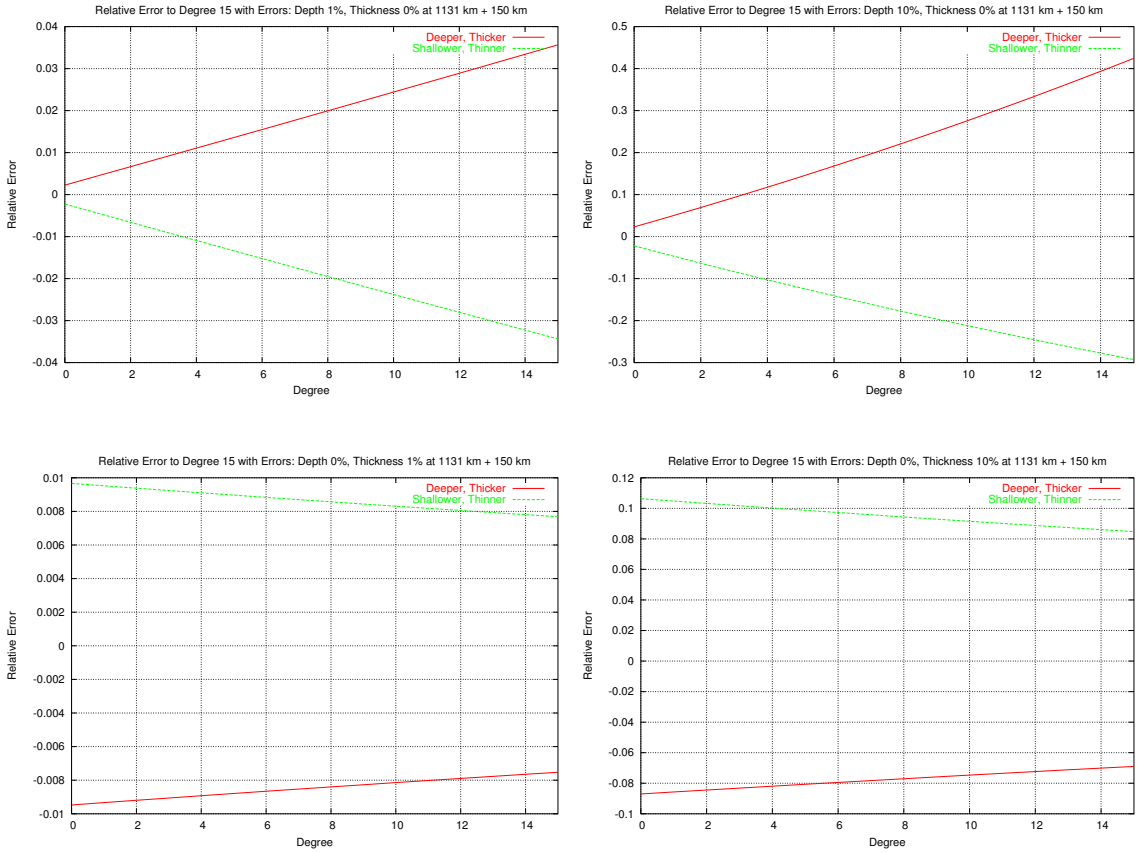

Figure 5-35: *For a depth of 1131 km, depth error of 1% (top left) and 10% (top right) are shown. Thickness error of 1% (bottom left) and 10% (bottom right) are also shown.*

The change in density contrast for other selected depths is given in **Table 5-17**.

It seems that the density contrast has its greatest change when the apparent depth is altered, while holding the thickness constant. See for example the first two lines for the deepest layer (1131 km) in **Table 5-17**. The contrast changes by 18.4 to 23.4% for a change in depth of ±10%. On the other hand, a 10% change in thickness for a fixed depth results in a small change in contrast (relatively speaking). For the same depth, see lines three and four which show a change of 7.5 to 9.3%.

Altering both depth and thickness has a more dramatic effect. A shallower shell sees its contrast change from 10.8% (thinner) to 24.7% (thicker). A deeper shell has the contrast change from 14.2% (thicker) to 34.9% (thinner).

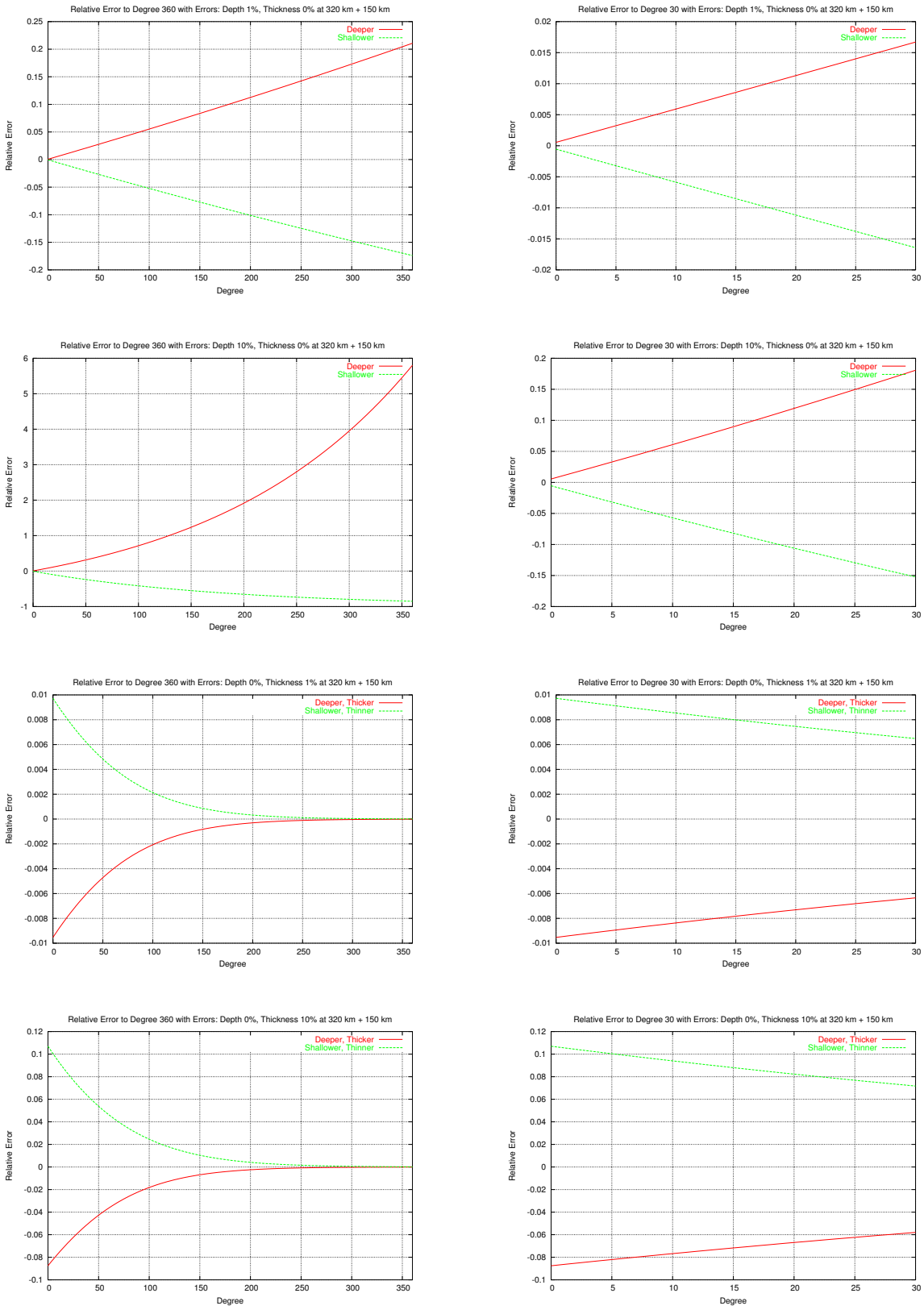

Figure 5-36: *Depth errors of 1% and 10% (top) and thickness errors of 1% and 10% (bottom) for a depth of 320 km. The left side goes to degree 360,*

while the right is to 30.

Density Contrast Change for 10% Depth and Thickness Errors (km)

Nominal Depth	Nominal Thickness	Selected Depth	Selected Thickness	Nominal Range (gm/cc)	Difference Range (gm/cc)	Difference (%)
31	12	34	12	-0.04572↔0.04806	-0.00854↔0.00790	17.5
		28			-0.00789↔0.00846	17.4
		31	13		-0.00251↔0.00262	5.5
			11		-0.00311↔0.00298	6.5
320	150	352	150	-0.00205↔0.00158	-0.00023↔0.00029	14.3
		288			-0.00025↔0.00019	12.1
		320	165		-0.00012↔0.00009	6.0
			135		-0.00012↔0.00015	7.4
1131	150	1244	150	-0.00371↔0.00363	-0.00086↔0.00086	23.4
		1018			-0.00068↔0.00067	18.4
		1131	165		-0.00028↔0.00027	7.5
			135		-0.00034↔0.00034	9.3
		1018			-0.00040↔0.00039	10.8
			165		-0.00092↔0.00090	24.7
		1244			-0.00052↔0.00052	14.2
			135		-0.00127↔0.00129	34.9

Table 5-17: *For selected depths and shell thicknesses the density contrast range of the presumed shells and the difference in contrast between the presumed and erroneous shells (with 10% error) are illustrated. The difference in the range is also given as a percentage.*

To summarize, for up to a 10% error in estimating thickness or depth, one should expect the density contrast computed to be in error within the range 7.5↔34.9% for the deepest layer in this study (1131 km). As expected from the preceding graphs, thickness error has the least effect as it ranges over a change of a little less than a factor of two for the three depths shown in the table. The effect of depth error appears to decline from the deepest to the mid-range depth, but curiously increases for the shallowest layer. This may be due to increased sensitivity of the measured coefficients to shallow bodies.

The effect on the density contrast changes is most easily seen graphically, as in **Figure 5-37**. For a depth 1131 km, the 9 variations shown in **Table 5-17** are illustrated. The middle figure is identical to **Figure 5-28**, and the others are variations of depth and thickness. Notice that the anomaly on the west coast of South America is a high in the middle figure. As the thickness for this presumably correct shell is varied, it shows a much lower density contrast for a thicker shell (middle right), and an unexpected sign reversal for a thinner shell (middle left).

When the shell is assumed to be deeper than it is, the synthesis of the difference also changes sign. The deepest and thinnest (bottom left) is about one third in value, but opposite in sign. The thicker shell at the same depth is also opposite in sign, and up to one sixth the magnitude. This suggests an over-compensation due to increased depth. In other words, a deeper shell requires a higher density to produce the same surface field. Thus the difference between the 'correct' and 'erroneous' shells results in a polarity reversal. If the difference had not been exhibited, this would be self-evident.

The synthesis of the difference between the presumed 'true' depth and shallower depths (top row) also show a high, but the contrast is reduced by a factor of about 10 for the thinnest shell (top left) to about a factor of 4 for the thickest (top right). This indicates that for a shallower depth (by 10% in this case) and a ±10% change in shell thickness, the anomaly is reduced in magnitude, but still evident. Using an argument opposite to that of the deeper shell, one might realize that a shallower body requires a lower density to produce the surface field.

It is apparent that interpreting the depth is most important if one is to specify the density contrast with certainty. The contrast resulting from an interpretation still provides insight into the local Earth structure, however.

5.4.3 South American High re-Visited

In the vicinity of the South American High near 290° longitude and 110° colatitude, it is evident that the major feature is deep-seated (in excess of several hundred kilometres), with a narrow 'high' positioned in the shallow upper mantle. This is illustrated in **Figure 5-38** which shows each of the depths analyzed from the spectrum. At about 1130 km, the major high is centred at 112° by 294°. At the shallower depth of 320 km, the anomaly becomes less diffuse, concentrating itself near 103° by 288°.

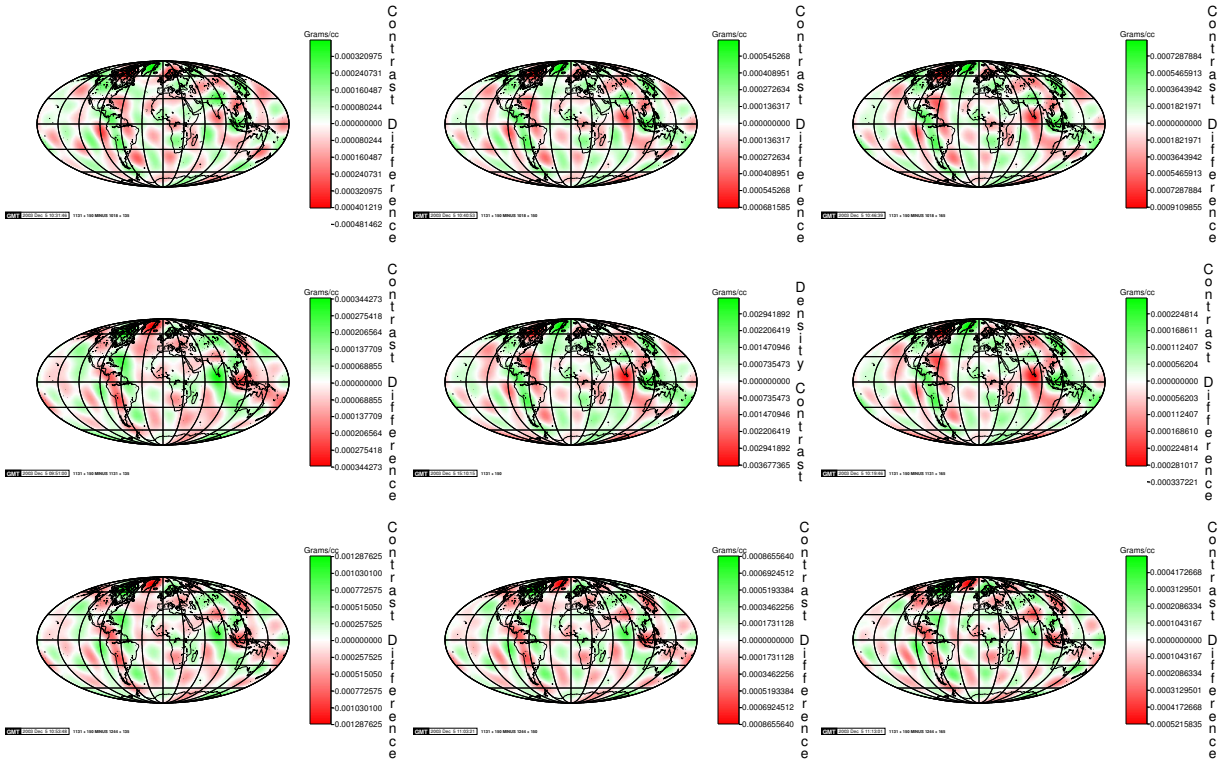

Figure 5-37: *This is an illustration of the synthesis of the difference between the depth and thickness of a shell interpreted from* **EGM96** *to exist at 1131 km with a 150 km thickness, and variations on the depth and thickness by ±10%. From left to right, the shell thicknesses have values of 135, 150 and 165 km. From top to bottom, the shell depths have values of 1018, 1131 and 1244 km. The middle figure has no depth or thickness correction applied and is identical to* **Figure 5-28**.

Two images of the density structure near 58 km are shown in the figure. One assumes a 150 km shell thickness, and the other a 25 km thickness. While they appear nearly identical, as indicated earlier they are only insofar as the general features are concerned. The difference in thickness affects the density contrast with the thinner shell showing an expected higher contrast. Owing to the formula used to calculate the density, the relative contribution for coefficients varies according to shell thickness and degree; nevertheless, the feature sets are similar, with both showing a high which tends to follow the coastline. This corresponds to the subduction zone where the Nazca and South American plates meet. The figure suggests an excess of mass in the near upper mantle beneath their point of contact.

The final two portions of **Figure 5-38** are for the shallowest zones interpreted in EGM96.

There seems to be little contribution at the 43 km depth, and almost none at the shallower depth (31 km)[69].

5.4.4 The Core/Mantle Boundary

As a last example of inversion, the following illustration examines Bowin's thesis that four masses at the core/mantle boundary (approximate depth 3000 km) would satisfy to some degree the lowest degrees of the measured field. The masses were positioned at the locations noted in **Table 5-18**. The density contrast observed from the use of the lowest degrees (2 and 3) of the observed field is illustrated in **Figure 5-39**. There, the four anomalies noted in **Table 5-18** are observed along with other substantial anomalies not matched to his deep masses.

The range for the density contrast was found to be -0.00294708↔0.00279903 gm/cc with an average density of 7.759 gm/cc. The mass variation for the shell was $-8.9731*10^{22}\leftrightarrow 8.5224*10^{22}$ grams. These values are one to two orders of magnitude smaller than Bowin's. This suggests that the assumed (for this example) shell thickness may be too large. Further investigation may be warranted.

Bowin's Core/Mantle Boundary Mass Anomalies

Latitude (°)	Longitude (°)	Mass (gm)	Location
-4	142	$0.5000*10^{22}$	New Guinea
5	77	$-0.9422*10^{23}$	Indian Ocean
55	-23.5	$0.1100*10^{24}$	Iceland
-52.5	50	$0.7200*10^{23}$	Crozet Is.

Table 5-18: *Bowin placed four substantial masses at the core/mantle boundary in addition to his shallower masses. These were intended to demonstrate that a restricted set of mass distributions might generate a geopotential field similar to that which is observed.*

[69] Note that the **GMT** labels under each image are for the data processor's use, and their content is irrelevant to the content of this document.

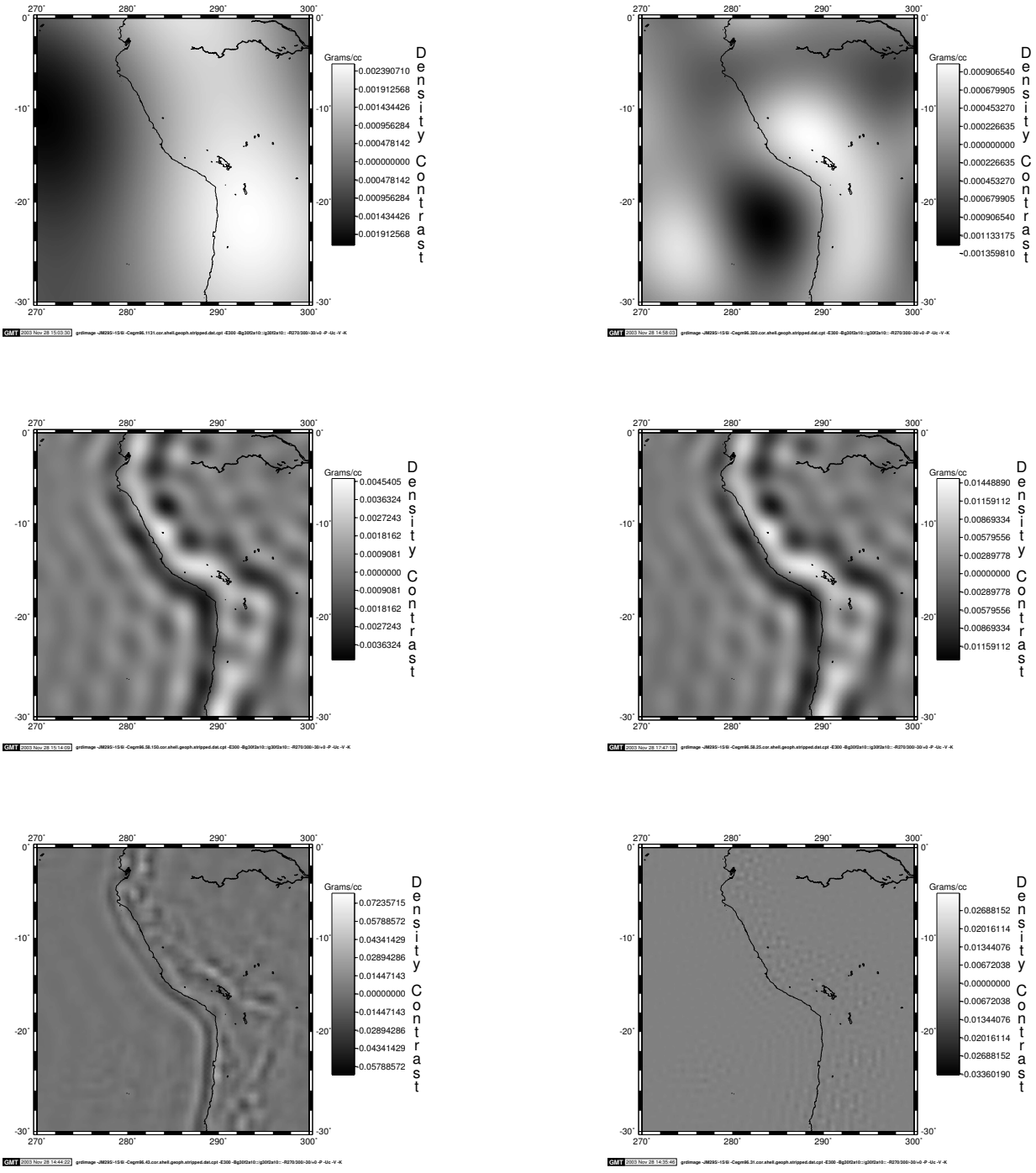

Figure 5-38: *The South American high as interpreted from EGM96 at 1131 (top left) and 320 (top right) km, with 150 km thicknesses. The centre images show two shells at 58 km with a 150 (left) and 25 (right) km shell thicknesses. The shallowest shells are interpreted to lie at 43 (bottom left) and 31 (bottom right) km with 15 and 12 km thick shells respectively.*

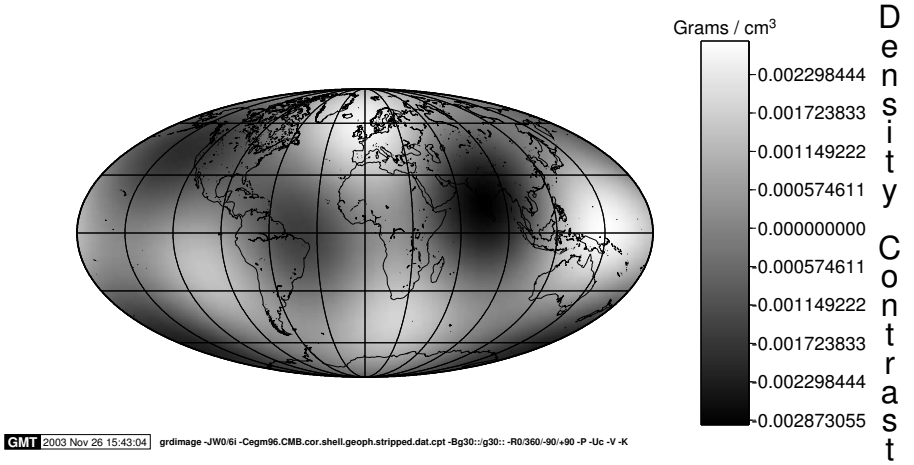

Figure 5-39: *Bowin included 4 deep-seated masses (see* **Table 5-18***) to account for core/mantle boundary potential anomalies. The density contrast due to degrees 2 and 3 of* **EGM96** *is illustrated. The shell thickness was 200 km, centred on the interface. The density contrast was -0.00294708↔0.00279903 gm/cc with an average density of 7.759 gm/cc. The mass variation for the shell was* $-8.9731*10^{22} \leftrightarrow 8.5224*10^{22}$ *grams.*

5.5 Final Comments

This chapter considered an alternative to the wavelet approach for estimating depth to causative bodies. It began by considering how one might estimate body characteristics on the assumption that the bodies in question were at pre-defined depths. These were presumed to be those depths indicated by Bowin, or by the earlier researchers Lithgow-Bertelloni and colleagues. For numerical and geometric reasons this approach was abandoned in favour of a possible alternative.

The alternative identified was the use of the spherical harmonic spectrum as a tool to estimate depth. The examination of the publicly available spectra were not encouraging initially, but recognizing that bodies of different depths (and mass magnitudes) offered a possible means of distinguishing mass depths, the approach was pursued.

Fortunately, an early pioneer (Pollack) had already developed some simple models and a means for computing their spectra on the sphere. One in particular was identified as having a useful property, that being that its spectrum was related to its depth, at least when the spectrum was appropriately normalized.

Investigations of single and multiple point sources and their spectra proved to be very encouraging. Unfortunately, the model and the procedure also proved to have its deficiencies, such as the inability to identify individual sources, and the likelihood that bodies other than those causing the particular spectral response might be hidden. Such problems have to be accepted when using global analysis tools like spherical harmonics. Nevertheless, synthetic testing lead to the examination of recent public geopotential models and for the lower order degrees, the point source depth identification property appeared to hold. From the spectrum, depth to causative bodies could be established, subject to the ambiguities mentioned earlier.

Once some measure of depth had been established, it then became a simple matter of identifying the likely positions of causative bodies, a task that required appropriate search algorithms. Ambiguity was observed here as well, as the choice of search dimension impacted the final geographic positioning of buried masses to a certain extent. Given both depth and location estimates, mass size could then be determined, and these were found to be not unlike the range of values that Bowin had employed in his models.

Point sources were used for modelling simplicity, much as other researchers have done. However, one must accept that this is an unlikely shape, especially after the modelling work of Lithgow-Bertelloni and colleagues. That group had attempted to model the potential field after following the subduction of crustal material over the millennia. They postulated that blocks had been subducted and had sunk to great depth into the mantle. Obviously, these weren't spheres, or point sources.

In an effort to gain increased insight into gradational variations in Earth density, a mathematical equivalence ascribed to George Green (1793-1841), and known as Green's equivalent layer was used. As noted in an earlier chapter, this procedure was extended in [Pail 1999] to allow the consolidation of the mantle in his effort to generate a synthetic potential field for satellite geodesy and other purposes. It was shown in the same chapter that it could be further extended to allow the use of downward continued geopotential spectra to arbitrary depths, including those interpreted as being representative of mantle layers, and which had been used in the point mass model. By making a uniform mean density assumption, it was found possible to determine spatial density contrast variations within shells at those interpreted depths.

Several examples of shell inversions based on the layer interpretation of **EGM96** were

illustrated. The density contrasts observed were within the range of Lithgow-Bertelloni and colleagues assumptions, but on occasion outside of Bowin's models. These results were then qualified by examining the source of possible error in the analysis. Apart from the interpretation of the geopotential field, and the assumptions that were used to justify it, the errors were seen to come primarily from incorrect depth estimates, with a contribution due to incorrect thickness. These error causes were demonstrated graphically. As well, the difference between the presumed 'correct' analysis and various combinations of 'incorrect analysis' were synthesized, displayed and commented upon.

As a follow-on to an attempted analysis of the South American high which was begun in the chapter on wavelet-based depth analysis, the spectral interpretation technique described here was used to gain insight into its cause. Interpretation of the subject area suggested very deep-seated anomalies overlaid by narrow, and much shallower bodies likely induced by subduction along the continental margin were the cause of the anomaly.

For the point mass model, the presumed geologic pictured afforded by the spectral interpretation permitted an approximation of the original geopotential field. While imperfect, it was more like the published field over the degree range used in this research, than that of the geophysical study on subduction. On the other hand, the shell density contrast experiment was performed directly from the published field, thus ensuring a direct link between the field and the densities or masses so determined. For this latter case, the direct link to the observed field ensured that the density contrast (or equivalently the anomalous mass within the shell) derived from the interpretation of the field provided insight into the Earth's structure, thereby realizing the principal goal of this research.

6 Summary, Contributions and Recommendations

6.1 Summary of the Research

This has been an interesting research exercise. The initial objective was to find a way to reproduce the measured geopotential field. By doing so in some reproducible manner, one could perform numerical exercises and other experiments. In principle, reproducing the field is simple enough, and Newton indicated how one might achieve that goal with a deceptively simple expression several hundreds of years ago. Unfortunately, to use his equation, one requires a complete knowledge of the density structure of the Earth, something that is still lacking, although numerous researchers are attempting to determine exactly that and other properties of the Earth using tomographic techniques.

This research tried several different methods to discover the Earth's internal structure. The first, based on proven mathematical and physical principles, employed a relatively new branch of mathematics called 'wavelets'. The technique exploited the similarity of the Poisson kernel to a smoothing function. The method noted that the application of an analyzing wavelet to potential field data, specifically the vertical gradient of the potential (or gravity), could be had by finding the scaled horizontal derivatives of that field. Successive applications of the horizontal gradient to the increasingly smooth upward continued gravity data corresponded to applying the analyzing wavelet with different dilations.

This process is the manifestation of a continuous wavelet transform based on a Poisson kernel. The transform is applicable to potential field data, or any other data which obeys Poisson's equation [Moreau et al. 1997]. It permits one to detect and characterize singularities. This approach to wavelet analysis of a potential field might better be known as the Poisson kernel wavelet transform. It is based in the field of signal processing.

Researchers in fields other than geophysics had determined that the application of analyzing wavelets to pattern recognition problems allowed one to characterize the shape of irregular structures by examining the evolution of wavelet maxima. This was extended for determining the depth to causative bodies in the field of mineral exploration by groups in both France and Australia. It was this technique that was explored for its applicability in mantle-depth Earth structure determination. It was found that while quite appropriate for simple, isolated bodies, very little additional complexity made the method very difficult to use, and so it was abandoned.

Subsequent to the wavelet exercise, it was observed that the spherical harmonic spectrum offered some discrimination with respect to depth, and the opportunity to exploit this was pursued. It was noted that an earlier researcher had described a method of 'normalizing' a spectrum so that it was much more similar to that of a spectrum on the plane. This approach, plus the observation that certain bodies assumed a power law characteristic when their spectra were normalized in the suggested manner, provided the sought-after means for exploitation. A simplifying assumption was required, that being that the causative bodies tend towards a spherical shape, thus making them appear as point sources, as other researchers have assumed.

Using this assumption, it was discovered that there was a convenient relationship between depth and normalized spectrum which resulted from the power law characteristic. Experimentation with synthetic models revealed some limitations related to body depth and mass. Accepting that not all bodies might be recognized, allowed the interpretation of a publicly available geopotential field to be performed, and this indicated that it could be decomposed into several zones or layers as a function of depth. Once depth information was available, it became a simple matter of finding local extrema which resulted from the synthesis of that portion of the spectrum attributable to that depth range. Standard least-squares techniques were then used to determine probable mass magnitudes.

The result of this exercise was a model which could be mapped to a potential field, and which then resembled the measured field to a reasonably high degree; however, there were individual samples of the potential field which were greatly different from the measured field. This point mass model, which might have been used as a starting point for a more detailed model, seemed less than acceptable.

The last attempt to model the Earth's interior was done using a different approach, but which was based on science completed in the nineteenth century. Using a mathematical oddity known as the equivalence layer, a shell extension was deduced, thus allowing one to compute as a continuous function the density contrast at specific depths and for specific shell thicknesses. The depths chosen were those interpreted from **EGM96**, and the thicknesses selected were comparable to those used by other recent researchers. This exercise resulted in density contrasts that were similar or smaller in magnitude than those employed by other workers, and the corresponding anomalous mass range was comparable to within two orders of magnitude to one of several recent researcher's results.

This particular approach to Earth characterization is one which directly links the measured field to the estimated contrast variation. As noted in the last chapter, the interpretation of the field is critical, as errors in thickness and depth can alter the estimated density; nevertheless, one is still left with a 'picture' of the mantle at one or more depths. This can be used as an additional information source for further gravitational inversion, or in tomographic studies, which at present, remains the most direct measuring tool available for geophysical researchers.

6.2 Conclusions and Contributions

6.2.1 Conclusions

This research exercise was both interesting and frustrating. One can conclude several things from the effort:

- The transfer of ideas from one area of geophysics to another is not always fruitful. It seemed perfectly reasonable to identify the characteristics of density anomalies using sound physical principles at the outset of this research. As in the several papers on the subject, initial synthetic studies were very encouraging. The complexities of reality made the wavelet technique far less usable. In mineral exploration, using the Poisson kernel wavelet transform approach may be very appropriate, and indeed very satisfying as it is based on potential theory and well-known characteristics of signal processing; however the writer is skeptical of its general applicability to mantle-depth investigations.
- The interpretation of **EGM96** as a potential field which reflected a layered geology proved to be very useful. It required certain assumptions about the bodies generating the observed field, and also required that one accept that not all bodies would be identified. Accepting these however permitted the modelling of two deeper layers as point sources, much as other researchers had done. That the modelling exercise was 'on the right track' was supported by the magnitudes of the bodies in the model, when compared to others in the literature. Certainly the correlation with the observed field was good, but individual potential values could at time be quite different from the measured field. The conclusion then was that while the exercise was going the right direction, and was superior to the wavelet attempt, it was inadequate for a final model.
- Using the same layered geology interpretation, a much superior model was produced using some old mathematics. The mass variation within the shell model was

similar to that of the point source model, but this approach offered the direct link to the measured field. Furthermore, the model is easily adapted to better defined geopotential fields, and is equally easily modified for improved geological interpretation, possibly resulting from integration with tomographic models. The conclusion is that this continuous description of density contrast is the preferred model owing to its adaptability, and strong dependence on the measured field.

6.2.2 Contributions

The following are the contributions resulting from this research:

- Identified a 'power law' relationship between the depth of a point or spherical mass and its spherical harmonic spectrum.
- Exploited the 'power law' relationship to make a meaningful interpretation of a publicly-available geopotential field. This resulted in the identification of several zones or layers within the mantle that were likely major contributors to the measured spectrum. No attempt was made to correlate these with other geophysically-derived anomalies.
- Developed a model based on point masses attributable to the interpreted field which when converted to surface potential provided a surprisingly good correlation to the measured field.
- Extended Green's surface equivalent layer for potential to a shell-based model which when allied with the field interpretation described earlier allowed one to deduce an approximation of the mantle structure. This technique directly linked the surface field to the density contrast at depth in terms of the spherical harmonic coefficient datasets deduced from satellite and surface gravity analysis. The contributions to error in the analysis were identified and quantified for a modest range of values.
- Identified and characterized a '**polar problem**' and highlighted the use of an alternative spherical pixelization which can reduce the effect of latitude on spherical harmonic analysis, and thereby increase the resolution of high latitude anomalies.
- While doing preparatory work, researching different methods of spherical harmonic analysis revealed some idiosyncrasies about the codes available to the community. These codes, with their advantages and disadvantages have been described in this text, with corrections noted (as appropriate) for their proper use in a geodetic context.

- As an exercise, examined the expansion of orthogonal wavelet coefficients to observe the decay or enhancement of a potential field anomaly to see what insights might be gained. Such an exercise might prove to be useful in an exploration context.
- Explored the use of wavelet techniques for depth analysis of mantle structures. Like the discrete and continuous mass anomaly studies described above, these were developed in a spherical harmonic context, with many calculations being performed in that environment. This wavelet approach was found to be undesirably complicated by moderately complex mass assemblages; nevertheless, the codes developed for this aspect of the study may prove to be relevant for other experimental work.
- Developed an extended set of tools for analyzing, synthesizing and manipulating spherical harmonic fields, for allowing their interpretation and for inverting them in different ways to generate either discrete or continuous models of the subsurface.

6.3 Recommendations for Further Work

[Parker 1974; Parker 1975] and [Parker 1994] describe methods for estimating the best bounds on density and depth. That is to say, it is possible to determine the least upper bound on density contrast, or correspondingly, the greatest lower bound on depth for a deep density anomaly. It would be quite interesting to place the interpretation offered in this research into such a context as it might ensure greater confidence in the proposed density contrasts. Others too have deduced rules to estimate maximum depth for gravity anomalies and these may be worth exploring [Grant and West 1965].

A most interesting exercise would be to marry the results obtained in this research with that of the tomographic community. Their resolution is said to be of the order of hundreds of kilometres, and introducing the results obtained here as control in their studies, might prove to be mutually beneficial. It is equally likely that their models will suggest an adjustment of the interpretation placed on the surface field. Certainly as improved potential field models are developed, a more refined interpretation of depth as a function of the spectrum might be achieved. The two combined (tomography and improved potential models) should help to better align with reality the interpretation offered here.

References

Abdelrahman et al. 2001.

El-Sayed M. Abdelrahman, Tarek M. El-Araby, Hesham M. El-Araby, and Eid R. Abo-Ezz, "A new method for shape and depth determinations from gravity data," *Geophysics,* 66, 6, pp. 1774-1780 (November-December 2001).

Adams and Swarztrauber 1997.

John C. Adams and P.N. Swarztrauber, *SPHEREPACK 2.0: A Model Development Facility,* Preprint from http://www.scd.ucar.edu/softlib/SPHERE.html (September 1997).

Allasia 2001.

G. Allasia, "Approximating potential integrals by cardinal basis interpolants on multivariate scattered data," *Computers and Mathematics with Applications (in press)* (2001).

Arndt 1997.

Jörg Arndt, *hfloat: a C++ library for high precision computations,* Preprint from http://www.jjj.de/hfloat (September 1997).

Barthelmes 1986.

F. Barthelmes, "Untersuchungen zur Approximation des äuBeren Gravitationsfelds der Erde durch Puntkmassen mit optimierten Positionen," Veröff. d. Zentr. Inst. f. Phys. d Erde, Nr. 92, Potsdam (1986).

Bassin et al. 2000.

C. Bassin, G. Laske, and G. Masters, "The Current Limits of Resolution for Surface Wave Tomography in North Americ," *EOS Transactions of the AGU,* 81, F897 (2000).

Beyer 1991.

William H. Beyer, (ed.), *Standard Mathematical Tables and Formulae, 29th Edition,* CRC Press, Boca Raton, USA (1991).

Blais 1988.

J.A.R. Blais, *Estimation and Spectral Analysis,* University of Calgary Press, University of Calgary (1988).

Blais 1995.

J.A.R. Blais, *Gravity Field in Surveying and Geodesy: ENGO527 Lab 2,* Dept. of Geomatics Engineering, University of Calgary (1995).

Blais 1996.

J.A.R. Blais, "Multiresolution Spatial Data Representation and Processing in GISs," Final Report to Dept. of Natural Resources Canada (February 1996).

Blais 1997.

J.A.R. Blais, "Approximation and Estimation Course Notes," ENGO 699.53 (1997).

Blais 1999.

J.A.R. Blais, *Multiresolution Analysis of Geopotential and Related Quantities,* Presentation at the Canadian Geophysical Union annual scientific meeting, Banff, Alberta (June 1999).

Blais 2000.

J.A.R. Blais, *personal communication originally from Erik Grafarend indicating that Theorem 3 os Driscoll and Healy's 1994 paper was used by Wenzel in his analysis to degree 1800.* (August 23, 2000).

Blais 2003.

J.A.R. Blais, personal communication on the subject of separating the calculation of the normalization factor from the Legendre function (July 3, 2003).

Blais and Provins 2000.

J.A.R. Blais and Dean Allen Provins, *Spherical Harmonic Analysis and Synthesis for Multiresolution Applications,* Presented at the Canadian Geophysical Union annual scientific meeting, Banff, Canada (May, 2000).

Blais and Provins 2001.

J.A.R. Blais and Dean Allen Provins, *Multiresolution Analysis of Geopotential and Gravity Data,* Poster presented at the American Geophysical Union meeting, San Francisco, USA (December 2001).

Blais and Provins 2002.

J.A.R. Blais and Dean Allen Provins, "Spherical Harmonic Analysis and Synthesis for Global Multiresolution Applications," *Journal of Geodesy,* 76, 1, pp. 29-35, Springer (January, 2002).

Blais and Provins 2003.

J.A.R. Blais and Dean Allen Provins, "Optimization of Computations in Global Geopotential Field Applications" in *Lecture Notes in Computer Science,* ed. P.M.A. Sloot, D. Abramson, A.V. Bogdanov, J.J. Dongarra, A.Y. Zomaya, and Y.E. Gorbachev, International Conference on Computational Science - ICCS 2003, Part II,

2658, pp. 610-618, Springer-Verlag, St. Petersburg, Russia (June 2-4, 2003).

Blakely 1995.

Richard J. Blakely, *Potential Theory in Gravity and Magnetic Applications,* Cambridge University Press (1995).

Blakely and Simpson 1986.

Richard J. Blakely and Robert W. Simpson, "Approximating edges of source bodies from magnetic or gravity anomalies," *Geophysics,* 51, 7, pp. 1494-1498 (July 1986).

Bond et al. 1999.

J. Richard Bond, Robert G. Crittenden, Andrew H. Jaffe, and Lloyd Knox, "Computing Challenges of the Cosmic Microwave Background," *Computing in Science and Engineering,* pp. 21-35 (March-April 1999).

Boschetti, Hornby, and Horowitz 2000.

F. Boschetti, P. Hornby, and F.G. Horowitz, *Wavelet based inversion of gravity data,* ASEG, Preprint from http://www.ned.dem.csiro.au/unrestricted/people/BoschettiFabio/3054CO/papers/trifurc.pdf (2000).

Boschetti, Horowitz, and Hornby 1999.

F. Boschetti, F.G. Horowitz, and P. Hornby, *Geophysical feature removal by multi-scale edge suppression,* pp. 935-939, ISSPA99, Proceedings of the 5th International Symposium on Signal Processing and its Applications, Brisbane, Australia (1999).

Boschetti, Horowitz, Hornby et al. 2000.

F. Boschetti, F.G. Horowitz, P. Hornby, N. Archibald, D. Holden, and J. Hill, "Improved edge detection in potential field maps and graphical estimation of depth-to-the-top" in *SEG Expanded Abstracts,* Calgary (2000).

Bowin 2000.

Carl Bowin, "Mass Anomaly Structure of the Earth," *Reviews of Geophysics,* 38, 3, pp. 355-387, American Geophysical Union (August 2000).

Butkov 1968.

Eugene Butkov, *Mathematical Physics,* Addison-Wesley Publishing Company, Inc. (1968).

Carslaw 1930.

H.S. Carslaw, *Introduction to the Theory of Fourier's Series and Integrals,* Dover Publications, Inc., New York, USA (1930). 368 pp., third edition.

Chase 1979.

C.G. Chase, "Subduction, the geoid, and lower mantle convection," *Nature,* 282, pp. 464-468 (1979).

Chase 1985.

C.G. Chase, "The Geological Significance of the Geoid," *Annual Review of Earth and Planetary Sciences,* 13, p. 97 (1985).

Christodoulidis and Katsambalos 1977.

D.C. Christodoulidis and K.E. Katsambalos, *An Analysis on the Precision in the Computation of the Integrals of the Fully Normalized Associated Legendre Functions,* Department of Geodetic Science, Ohio State University (1977).

Chui 1992.

Charles K. Chui, *An Introduction to Wavelets,* Academic Press (1992).

Claessens et al. 2001.

S.J. Claessens, W.E. Featherstone, and F. Barthelmes, *Experiences with Point-mass Gravity Field Modelling in the Perth Region, Western Australia,* http://www.cage.curtin.edu.au/~will/pgpubs.htm (December 2001).

Colombo 1981.

O.L. Colombo, "Numerical Methods for Harmonic Analysis on the Sphere," Report No. 310, Department of Geodetic Science, Ohio State University, Columbus (March 1981).

Cook 1963.

A.H. Cook, "Sources of harmonics of low order in the external gravity field of the earth," *Nature,* 198, p. 1186 (1963).

Cooley and Tukey 1965.

James W. Cooley and John W. Tukey, "An Algorithm for the Machine Calculation of Complex Fourier Series," *Mathematics of Computation,* 19, 90, pp. 297-301 (1965).

Crittenden and Turok 1998.

Robert G. Crittenden and Neil G. Turok, *Exactly Azimuthal Pixelizations of the Sky,* Preprint from http://xxx.lanl.gov/list/astro-ph/9806[374] (i.e. article 374 in the 9806 directory) (June 1998).

Crough and Jurdy 1980.

S.T. Crough and D.M. Jurdy, "Subducted lithosphere, hotspots, and the geoid," *Earth and Planetary Science Letters,* 48, 1, pp. 15-22 (June 1980).

Daubechies 1988.

I. Daubechies, "Orthonormal Bases of Wavelets," *Communications on Pure and Applied Mathematics,* 41, pp. 909-996 (1988).

Daubechies 1992.

I. Daubechies, *Ten Lectures on Wavelets,* p. 357, Society for Industrial and Applied Mathematics, Philadelphia, USA (1992).

Dobrin 1960.

M.B. Dobrin, *Introduction to Geophysical Prospecting, Second Edition,* McGraw-Hill Book Company (1960).

Dongarra 2003.

J. Dongarra, "Performance of Various Computers Using Standard Linear Equations Software," University of Tennessee Computer Science Technical Report CS-89-85, http://www.netlib.org/utk/people/JackDongarra/papers.htm (July 24, 2003).

Dongarra et al. 1996.

J. Dongarra, Roldan Pozo, and David Walker, *LAPACK++ V.1.1, High Performance Linear Algebra Users' Guide,* National Institute of Standards ad Technology, University of Tennesee, Knoxville (April, 1996).

Driscoll and Healy 1994.

James R. Driscoll and Dennis M. Healy, Jr., "Computing Fourier Transforms and Convolutions on the 2-Sphere," *Advances in Applied Mathematics,* 15, pp. 202-250 (1994).

Dziewonski and Anderson 1981.

A.M. Dziewonski and D.L. Anderson, "Preliminary Reference Earth Model," *Physics of the Earth and Planetary Interiors,* 25, pp. 297-356 (1981).

Dziewonski, Hager, and O'Connell 1977.

A.M. Dziewonski, B. H. Hager, and R. J. O'Connell, "Large scale heterogeneities in the lower mantle," *Journal of Geophysical Research,* 82 (1977).

Featherstone 1999a.

W.E. Featherstone, "Report of IAG Special Study Group 3.177 Synthetic Modelling of the Earth's Gravity Field (1996-1999)," Report of the IAG 3.177, Preprint from http://www.cage.curtin.edu.au/~will/iuggtrav99.html (1999).

Featherstone 1999b.

W.E. Featherstone, "Tests of two forms of Stoke's integral using a synthetic gravity field based on spherical harmonics" in *Quo vadis geodesia...? Festschrift for Erik*

W. Grafarend on the occasion of his 60th birthday, ed. Friedhelm Krumm / Volker Siegfried Schwarze, 1, pp. 101-112, Universität Stuttgart (1999).

Featherstone 2002.

W.E. Featherstone, "Report of IAG Special Study Group 3.177 Synthetic Modelling of the Earth's Gravity Field (1999-2001)," Report of the IAG 3.177, Preprint from http://www.cage.curtin.edu.au/~will/iagssg3177.html (2002).

Featherstone et al. 2001.

W.E. Featherstone, M.P. Stewart, D.D. Lichti, M. Tsakiri, J.F. Kirby, N.T. Penna, M. Kuhn, T.A. Forward, S.A. Holmes, R.I. Hackney, M. Jia, X. Deng, S.J. Gordon, and M. Dennis, *Recent Research Activities of the Geodesy Group at Curtin University of Technology,* A Spatial Odyssey: 42nd Australian Surveyors Congress (2001).

Gabor 1946.

Dennis Gabor, "Theory of Communication," *Journal of the Institute of Electrical Engineers,* 93, 22, pp. 429-257, IEEE (1946).

Garland 1965.

G.D. Garland, *The Earth's Shape and Gravity,* Pergamon Press (1965).

Gerstl 1980.

M. Gerstl, "On the Recursive Computation of the Integrals of the Associated Legendre Functions," *Manuscripta Geodaetica,* 5, pp. 181-199 (1980).

Gibert and Pessel 2001.

Dominique Gibert and Marc Pessel, "Identification of sources of potential fields with the continuous wavelet transform: Application to self-potential problems," *Geophysical Research Letters,* 28, 9, pp. 1863-1866 (May 2001).

Gonzalez and Wintz 1987.

Rafael C. Gonzalez and Paul Wintz, *Digital Image Processing, second edition,* Addison Wesley, Don Mills, Ontario (1987).

Górski, Hivon, and Wandelt 1998.

Krzysztof M. Górski, Eric Hivon, and Benjamin D. Wandelt, "Analysis Issues for Large CMB Data Sets" in *Proceedings: Evolution of Large Scale Structure,* Garching, Preprint from http://www.tac.dk/~healpix (August 1998).

Górski, Wandelt et al. 1999.

Krzysztof M. Górski, Benjamin D. Wandelt, Eric Hivon, Frode K. Hansen, and Anthony J. Banday, *The HEALPix Primer,* http://arxiv.org/abs/astro-ph/9905275 (May 1999).

Goupillaud et al. 1984.

P. Goupillaud, A. Grossmann, and J. Morlet, "Cycle-octave and Related Transforms in Seismic Signal Analysis," *Geoexploration,* 23, pp. 85-102 (1984-1985).

Granlund 2002.

Torbjörn Granlund, *GNU MP: The GNU Multiple Precision Arithmetic Library, Edition 4.0.1,* The Free Software Foundation, http://swox.com/gmp/ (January 2002).

Grant and West 1965.

F.S. Grant and G.F. West, *Interpretation Theory in Applied Geophysics,* McGRaw-Hill Book Company (1965).

Grebenitcharsky and Sideris 2002.

R.S. Grebenitcharsky and M.G. Sideris, "Effect of compatibility conditions along mountainous coastline region on the numerical solution of altimetry-gravimetry boundary value problems" in *Gravity and Geoid 2002 - GG2002,* ed. I.N. Tziavos, International Association of Geodesy, preprint from http://olimpia.topo.auth.gr/GG2002/SESSION2/session2.html (2002).

Gröbner and Hofreiter 1961.

Wolfgang Gröbner and Nikolaus Hofreiter, *Integraltafel erster teil Unbestimmte Integrale,* Springer-Verlag, Wien (1961).

Gurnis et al. 2000.

Michael Gurnis, Jerry X. Mitrovica, Jeroen Ritsema, and Hendrik-Jan van Heijst, "Constraining mantle density structure using geological evidence of surface uplift rates: The case of the African superplume," *Geochemistry, Geophysics, Geosystems: An Electronic Journal of the Earth Sciences,* 1, p. 5, American Geophysical Union and the Geochemical Society (July 2000).

Haagmans 1999.

Roger Haagmans, "A Synthetic Earth for Use in Geodesy" in *Bulletin: Special Commission #1, Mathematical and Physical Foundations of Geodesy,* International Association of Geodesy, Stuttgart (August 1999).

Hager 1984.

B.H. Hager, "Subducted slabs and the Geoid: Constraints on mantle rheology and flow," *Journal of Geophysical Research,* 89, pp. 6003-6015 (1984).

Healy et al. 1998.

D. Healy, Jr., D. Rockmore, P. Kostelec, and S. Moore, "FFTs for the 2-Sphere -

Improvements and Variations," *To appear in Advances in Applied Mathematics,* Preprint from http://www.cs.dartmouth.edu/~geelong/publications (June 1998).

Heiskanen and Moritz 1966.

Weikko A. Heiskanen and Helmut Moritz, *Physical Geodesy,* Institute of Physical Geodesy, Technical University, Graz, Austria (1966).

Hide and Horai 1968.

R. Hide and K. Horai, "On the topography of the core-mantle interface," *Physics of the Earth and Planetary Interiors,* 1, pp. 305-308 (1968).

Hipkin 2000.

R.G. Hipkin, "Bigger mantle density anomalies at 1300 km than at 670 km," *Proceedings, EGX XXV General Assembly, Nice, France,* Dept. of Geology and Geophysics, University of Edinburgh, http://www.copernicus.org/EGS/egsga/nice00/programme/abstracts/aac5502-1.pdf (April 2000).

Hivon and Górski 1998.

Eric Hivon and Krzysztof M. Górski, *Release Notes on the HEALPIX Tool Kit Version 0.9.0* (January 1998).

Hobson 1931.

E.W. Hobson, *The Theory of Spherical and Ellipsoidal Harmonics,* Chelsea Publishing Company, New York (1931). (reprinted 1955 and 1965).

Holmes and Featherstone 2002a.

S.A. Holmes and W.E. Featherstone, "A unified approach to the Clenshaw summation and the recursive computation of very-high degree and order normalised associated Legendre functions," *Journal of Geodesy,* 76, 5, pp. 279-299 (May, 2002).

Holmes and Featherstone 2002b.

S.A. Holmes and W.E. Featherstone, "SHORT NOTE: Extending simplified high-degree synthesis methods to second latitudinal derivatives of geopotential," *Journal of Geodesy,* 76, 8, pp. 447-450 (November, 2002).

Hornby, Boschetti, and Horowitz 1997.

P. Hornby, F. Boschetti, and F.G. Horowitz, "Potential Field Wavelets; Towards a New Class of Algorithms for Analysing Gravity and Magnetic Surveys," *EOS Transactions AGU Fall Meeting Supplement,* 78, 46, F34 (1997).

Hornby, Boschetti, and Horowitz 1998.

P. Hornby, F. Boschetti, and F.G. Horowitz, "Application of wavelet theory to the analysis of gravity data" in *SEG Expanded Abstracts,* New Orleans (1998).

Hornby, Boschetti, and Horowitz 1999.

P. Hornby, F. Boschetti, and F.G. Horowitz, "Analysis of potential field data in the wavelet domain," *Geophysical Journal International,* 137, pp. 175-196 (1999).

Hornby, Boschetti, Horowitz, and Archibald 1997a.

P. Hornby, F. Boschetti, F.G. Horowitz, and N. Archibald, "Inferring Geology from Geophysics" in *Abstracts, Geodynamics and Ore Deposits Conference, Australian Geodynamics Cooperative Research Centre,* pp. 73-75, Ballarat, Victoria, Australia (see www.agcrc.csiro.au/publications/conferences/Ballarat97/talks/hornby.html) (February 19-21, 1997).

Hornby, Boschetti, Horowitz, and Archibald 1997b.

P. Hornby, F. Boschetti, F.G. Horowitz, and N. Archibald, "Potential Field Wavelets as a Tool in Exploration," *Geological Society of Australia, SG2/SGTSG Meeting, 'Geological Structures and their Geophysical Signatures',* Marysville, Victoria, Australia (December 4-5, 1997).

Ishii and Tromp 1999.

M. Ishii and J. Tromp, "Normal-Mode and Free-Air Gravity Constraints on Lateral Variations in Velocity and Density of Earth's Mantle," *Science,* 285, pp. 1231-1236 (1999).

Jessel 1997.

Mark Jessel, "Three-dimensional geological modelling of potential-field data," *Journal of Australian Geology and Geophysics,* 17, 2, pp. 83-103 (1997).

Kaiser 1994.

G. Kaiser, *A Friendly Guide to Wavelets,* Birkhauser Boston, Cambridge Mass. (1994).

Kampes 1998.

Bert Kampes, "Analysis of Evenly Distributed Data on the Sphere: A Comparison of Least Squares, Quadrature and 2D-Fourier methods," M.Sc. thesis, Faculty of Civil Engineeringand Geosciences, Delft University of Technology, Preprint from http://www.geo.tudelft.ne/fmr/people/kampes (August 1998). 99 pp.

Kanasewich 1981.

E.R. Kanasewich, *Time Sequence Analysis in Geophysics,* University of Alberta Press (1981).

Kaula 1966.

William Kaula, *Theory of Satellite Geodesy: Applications of Satellites to Geodesy,*

Blaisdell Publishing Company, Waltham, Massachusetts (1966).

Kay and Marple 1981.

Steven M. Kay and Stanley Lawrence Marple,0Jr., "Spectrum Analysis - A Modern Perspective," *Proceedings of the IEEE,* 69, 11 (November 1981).

Keller 2000.

Wolfgang Keller, *Lecture Notes on Wavelets,* University of Stuttgart (July, 2000).

Khan 1977.

M.A. Khan, "Depth sources of gravity anomalies," *Geophysical Journal of the Royal Astronomical Society,* 48, pp. 197-209 (1977).

Kotsakis and Sideris 1999.

Christopher Kotsakis and M.G. Sideris, *Application of Multiresolution Filtering in Spectral Geoid Determination,* (preprint) (1999).

Kuhn 2003.

M. Kuhn, "Geoid determination with density hypotheses from isostatic models and geological information," *Journal of Geodesy,* 77, 1-2, pp. 50-65, Springer-Verlag, Heidelberg (May, 2003).

Kuhn and Featherstone 2002a.

M. Kuhn and W.E. Featherstone, "On the Construction of a Synthetic Earth Gravity Model" in *Gravity and Geoid 2002 - GG2002,* ed. I.N. Tziavos, International Association of Geodesy, www.cage.curtin.edu.au/˜will/iagtrav01.pdf (2002).

Kuhn and Featherstone 2002b.

M. Kuhn and W.E. Featherstone, "On the Optimal Spatial Resolution of Crustal Mass Distributions for Forward Gravity Field Modelling" in *Gravity and Geoid 2002 - GG2002,* ed. I.N. Tziavos, International Association of Geodesy, http://olimpia.topo.auth.gr/GG2002/SESSION2/session2.html (2002).

Kumar and Foufoula-Georgiou 1997.

P. Kumar and E. Foufoula-Georgiou, "Wavelet Analysis for Geophysical Applications," *Reviews of Geophysics,* 35, 4, pp. 385-412 (November 1997).

Kuo and Romanowicz 2001.

Chaincy Kuo and Barbara Romanowicz, *On the Resolution of Density Structure in the Mantle,* Berkeley Seismological Laboratory, http://www.seismo.berkeley.edu/seismo/annual_report/ar99_00/node35.html (circa 2001).

Lambeck 1976.

K. Lambeck, "Lateral Density Anomalies in the Upper Mantle," *Journal of Geophysical Research,* 81, B5, pp. 6333-6340 (1976).

Laske, Dziewonski, and Masters 2003.

G. Laske, A. Dziewonski, and G. Masters, *The Reference Earth Model Website,* http://mahi.ucsd.edu/Gabi/rem.html (current as of July, 2003).

Laske and Masters 1997.

G. Laske and G. Masters, "A Global Digital Map of Sediment Thickness," *EOS Transactions of the AGU,* 78, F483 (1997).

Lehmann 1993.

Rüdiger Lehmann, "The method of free-positioned point masses-geoid studies of the Gulf of Bothnia," *BulletinGéodésique,* 67, pp. 31-40, Springer-Verlag (1993).

Lemoine et al. 1998.

F.G. Lemoine, S.C. Kenyon, J.K. Factor, R.G. Trimmer, N.K. Pavlis, D.S. Chinn, C.M. Cox, S.M. Klosko, S.B. Luthcke, M.H. Torrence, Y.M. Wang, R.G. Williamson, E.C. Pavlis, R.H. Rapp, and T.R. Olson, "The Development of the Joint NASA GSFC and NIMA Geopotential Model EGM96," Technical Report NASA/TP-1998-206861:, NASA Goddard Space Flight Center, Greenbelt Maryland, 20771 USA (July, 1998).

Li 1996a.

Zuofa Li, "Multiresolution Approximation of the Gravity Field," *Journal of Geodesy,* 70, pp. 731-739 (1996).

Li 1996b.

Zuofa Li, "Multiresolution Approximation in Gravity Field Modelling," PhD. Dissertation in Geomatics Engineering, UCGE Report No. 20103, University of Calgary (1996).

Lithgow-Bertelloni and Richards 1998.

C. Lithgow-Bertelloni and M.A. Richards, "The Dynamics of Cenozoic and Mesozoic Plate Motions," *Reviews of Geophysics,* 36, 1, pp. 27-78 (February 1998).

Lithgow-Bertelloni, Richards et al. 1993.

C. Lithgow-Bertelloni, M.A. Richards, Y. Ricard, R.J. O'Connell, and D.C. Engebretson, "Toroidal-poloidal partitioning of plate motions since 120 Ma," *Geophysical Research Letters,* 20, pp. 375-378 (1993).

Liu and Sideris 2003a.

Q. Liu and M.G. Sideris, *Wavelet evaluation of some singular geodetic integrals,*

IUGG 2003, poster presentation (July 2003).

Liu and Sideris 2003b.

Q. Liu and M.G. Sideris, *Wavelet evaluation of the Stokes and Vening Meinesz Integrals,* 77, pp. 345 - 356, Springer-Verlag, Heidelberg (August 2003).

MacMillan 1930.

W.D. MacMillan, *Theoretical Machanics, vol. 2: The Theory of Potential,* Dover, New York, USA (1930).

MacRobert 1967.

T.M. MacRobert, *Spherical Harmonics,* International Series of Monographs in Pure and Applied Mathematics, Volume 98, Pergamon Press Ltd., Headington Hill Hall, Oxford (1967).

Mallat 1989a.

S.G. Mallat, "A Theory for Multiresolution Signal Decomposition: The Wavelet Representation," *IEEE Transactions on Pattern Analysis and Machine Intelligence,* 11, 7, pp. 674-693 (July 1989).

Mallat 1989b.

S.G. Mallat, "Multifrequency Channel Decompositions of Images and Wavelet Models," *IEEE Transactions on Acoustics, Speech and Signal Processing,* 37, 12, pp. 2091-2110 (December 1989).

Mallat 1997.

S.G. Mallat, *A Wavelet Tour of Signal Processing,* Academic Press, San Diego, California (1997).

Mallat and Hwang 1992.

S.G. Mallat and Wen Liang Hwang, "Singularity Detection and Processing with Wavelets," *IEEE Transactions on Information Theory,* 38, 2, pp. 617-643 (March 1992).

Mallat and Zhong 1992.

S.G. Mallat and Sifen Zhong, "Characterization of Signals from Multiscale Edges," *IEEE Transactions on Pattern Analysis and Machine Intelligence,* 14, 7, pp. 710-732 (July 1992).

Marple 1987.

S.L. Marple, *Digital Spectral Analysis* (1987).

Marsh et al. 1987.

J.G. Marsh, F.J. Lerch, B.H. Putney, D.C. Christodoulidis, T.L. Felsentreger, B.V. Sanchez, D.E. Smith, S.M. Klosko, T.V. Martin, E.C. Pavlis, J.W. Robbins, R.G. Williamson, O.L. Colombo, N.L. Chandler, K.E. Rachlin, G.B. Patel, S. Bhati, and D.S. Chinn, "An Improved Model of the Earth's Gravitational Field: GEM-T1," Technical Memorandum 4019, NASA Goddard space flight center, Greenbelt, Maryland, USA (1987).

Martelet et al. 2001.

Guillaume Martelet, Pascal Sailhac, Frédérique Moreau, and Michel Diament, *Characterization of geological boundaries using 1-D wavelet transform on gravity data; theory and application to the Himalayas,* Geophysics Online (SEG), http://www.geo-online.org/eman/emanlist.html (June 15, 2001).

McKenzie 1977.

D. McKenzie, "The initiation of trenches: A finite amplitude instability" in *Island Arcs, Deep Sea Trenches, and Back-Arc Basins, Maurice Ewing Series Vol 1,* ed. M. Talwani, W.C. Pitman III, pp. 57-61, AGU, Washington, D.C., USA (1977).

Meju 1994.

Max A. Meju, *Geophysical Data Analysis: Understanding Inverse Problem Theory and Practice, Course Notes Series, Volume 6,* Society of Exploration Geophysicists (1994).

Menke 1989.

William Menke, "Geophysical Data Analysis: Discrete Inverse Theory" in *International Geophysics Series, Volume 45,* Academic Press (1989).

Mohlenkamp 1997.

M.J. Mohlenkamp, "A Fast Transform for Spherical Harmonics," PhD thesis, Yale University (May 1997).

Mohlenkamp 1999.

M.J. Mohlenkamp, "A Fast Transform for Spherical Harmonics," *The Journal of Fourier Analysis and Applications,* 5, 2/3, pp. 159-184, Preprint from http://amath-www.Colorado.edu/appm/faculty/mjm (1999).

Mohlenkamp 2000.

M.J. Mohlenkamp, *Fast spherical harmonic analysis: sample code,* http://amath.colorado.edu/faculty/mjm (2000).

Moore et al. 1998.

Sean Moore, Dennis Healy, Jr., Dan Rockmore, and Peter Kostelec, *Sphar-*

monKit25: Spherical Harmonic Transform Kit 2.5, http://www.cs.dartmouth.edu/~geelong/sphere/ (1998).

Moreau et al. 1997.

Frédérique Moreau, Dominique Gibert, Matthias Holschneider, and Ginette Saracco, "Wavelet analysis of potential fields," *Inverse Problems,* 13, pp. 165-178 (1997).

Moreau et al. 1999.

Frédérique Moreau, Dominique Gibert, Matthias Holschneider, and Ginette Saracco, "Identification of sources of potential fields with the continuous wavelet transform: Basic theory," *Journal of Geophysical Research,* 104, pp. 5003-5013 (1999).

Morgan 1965.

W.J. Morgan, "Gravity Anomalies and Convection Currents, 2, The Puerto Rico Trench and the Mid-Atlantic Rise," *Journal of Geophysical Research,* 70, p. 6189 (1965).

Moritz 1968a.

H. Moritz, "Density distributions for the equipotential ellipsoid," Report 115, Department of Geodetic Science and Surveying, Ohio State University, Columbus, Ohio, USA (1968).

Moritz 1968b.

H. Moritz, "Mass distributions for the equipotential ellipsoid," *Bolletino di Geofisica Teorica ed Applicata,* 10, pp. 59-65 (1968).

Nataf and Ricard 1996.

Henri-Claude Nataf and Yanick Ricard, "3SMAC : an a priori tomographic model of the upper mantle based on geophysical modeling," *Physics of the Earth and Planetary Interiors,* 95, pp. 101-122 (1996).

O'Connor and Robertson 1997.

J J O'Connor and E.F. Robertson, *Jean Baptiste Joseph Fourier,* http://www-groups.dcs.st-and.ac.uk/~history/Mathematicians/Fourier.html (January, 1997).

Oh et al. 1999.

Siang Peng Oh, David N. Spergel, and Gary Hinshaw, "An Efficient Technique to Determine the Power Spectrum from Cosmic Microwave Background Sky Maps," *Astrophysical Journal,* 510, p. 551, available from xxx.lanl.gov/abs/astro-ph/9805339 or www.astro.princeton.edu/~dns (1999).

O'Mullane et al. 2001.

W. O'Mullane, A.J. Banday, K.M. Górski, P. Kunszt, and A. Szalay, *Splitting the Sky - HTM and HEALPix,* preprint: www.mpa-garching.mpg.de/~cosmo/omullane.ps.gz (2001?).

Oppenheim and Schafer 1975.

A.V. Oppenheim and R.W. Schafer, *Digital Signal Processing,* Prentice-Hall, Englewood Cliffs, USA (1975).

Pail 1999.

R. Pail, "Synthetic Global Gravity Model for Planetary Bodies and Applications in Satellite Gravity Gradiometry," Ph.D. Thesis, Technical University of Graz, Austria (1999).

Papoulis 1962.

Athanasios Papoulis, *The Fourier Integral and its Applications,* McGraw-Hill Book Company, Inc., New York, USA (1962). 318 pp.

Papp et al. 1996.

Gábor Papp, János Kalmár, and János Juhász, *Determination and Evaluation of the Lithospheric Geoid in the Pannonian Basin, Hungary,* Preprint from http://www.ggki.hu/a/gravity/geoid1.html (1996 or later).

Parker 1974.

R.L. Parker, "Best Bounds on Density and Depth from Gravity Data," *Geophysics,* 39, pp. 644-649 (1974).

Parker 1975.

R.L. Parker, "The Theory of Ideal Bodies for Gravity Interpretation," *Geophysical Journal International,* pp. 315-224 (1975).

Parker 1994.

R.L. Parker, *Geophysical Inverse Theory,* Princeton University Press, Princeton, U.S.A. (1994).

Parsons and Daly 1983.

B. Parsons and S. Daly, "The relation between surface topography, gravity anomalies and temperature structure of convection," *Journal of Geophysical Research,* 88, B2, pp. 1129-1144 (1983).

Paul 1978.

M.K. Paul, "Recurrence Relations for Integrals of Associated Legendre Functions," *Bulletin Geodesique,* 52, pp. 177-190 (1978).

Pekeris 1935.

C.L. Pekeris, "Thermal Convection in the Interior of the Earth," *Monthly Notices of the Royal Astronomical Society,* Geophysical Supplement, 3, pp. 343-367 (1935).

Pollack 1973.

Henry N. Pollack, "Spherical Harmonic Representations of the Gravitational Potential of a Point Mass, Spherical Cap and a Spherical Rectangle," *Journal of Geophysical Research,* 78, 11, pp. 1760-1768, American Geophysical Union (April 1973).

Press et al. 1992.

W.H. Press, S.A. Teukolsky, W.T. Vetterling, and B.P. Flannery, *Numerical Recipes: The Art of Scientific Computing, Second Edition,* Cambridge Press (1992).

Priestley 1981.

M.B. Priestley, *Spectral Analysis and Time Series,* 1 & 2, Academic Press (1981).

Protter and Morrey 1964.

Murray H. Protter and Charles B. Morrey, Jr., *Modern Mathematical Analysis,* Addison-Wesley Publishing Company, Inc. (1964).

Ramsey 1961.

A.S. Ramsey, *An Introduction to the Theory of Newtonian Attraction,* Cambridge (1961).

Rapp 1982.

Richard H. Rapp, "A FORTRAN Program for the Computation of Gravimetric Quantities from High Degree Spherical Harmonic Expansions," Report 334, Department of Geodetic Science and Surveying, The Ohio State University, Columbus, Ohio (September 1982).

Resovsky and Ritzwoller 1999.

J.S. Resovsky and M.J. Ritzwoller, "Regularization uncertainty in density models estimated from normal mode data," *Geophysical Research Letters,* 26, pp. 2319-22 (1999).

Ricard et al. 1993.

Y. Ricard, M. Richards, C. Lithgow-Bertelloni, and Y. Le Stunff, "A Geodynamic Model of Mantle Density Heterogeneity," *Journal of Geophysical Research,* 98, B12, pp. 21,895-21,909 (December 1993).

Ricardi and Burrows 1972.

L.J. Ricardi and M.L. Burrows, "A Recurrence Technique for Expanding a Func-

tion in Spherical Harmonics," *IEEE Transactions on Computers,* pp. 583-585 (June 1972).

Richards and Hager 1984.

M.A. Richards and B.H. Hager, "Geoid anomalies in a dynamic earth," *Journal of Geophysical Research,* 89, pp. 5987-6002 (1984).

Rioul and Vetterli 1991.

O. Rioul and M. Vetterli, "Wavelets and Signal Processing," *IEEE Signal Processing Magazine,* pp. 14-38 (October 1991).

Robinson 1967.

E.A. Robinson, *Statistical Communication and Detection, with special reference to Digital Data Processing of Radar and Seismic Signals,* Charles Griffin and Co. Ltd., London (1967).

Roland and Denker 2002.

Markus Roland and Heiner Denker, "Evaluation of Terrestrial Gravity Data by New Global Gravity Field Models" in *Gravity and Geoid 2002 - GG2002,* ed. I.N. Tziavos, International Association of Geodesy, http://olimpia.topo.auth.gr/GG2002/SESSION3/session3.html (2002).

Rousset and Romanowicz 2002.

Sébastien Rousset and Barbara Romanowicz, *Investigating Mantle's Density Resolution using the Neighbourhood Algorithm,* http://www.seismo.berkeley.edu/seismo/annual_report/ar01_02/node39.html (circa 2002).

Rummel 1997.

R. Rummel, "Spherical Spectral Properties of the Earth's Gravitational Potential and its First and Second Derivatives" in *Lecture Notes in Earth Sciences 65: Geodetic Boundary Value Problems in View of the One Centimeter Geoid,* pp. 359-404, Springer-Verlag, Berlin Heidelberg (1997).

Salamonowicz 2001.

P.H. Salamonowicz, "A Wavelet Based Gravity Model with an Application to the Evaluation of Stokes Integral" in *International Association of Geodesy Symposia, Volume 123,* ed. M.G. Sideris, pp. 85-90, Gravity, Geoid and Geodynamics 2000 (2001).

Sambridge 1999a.

M. Sambridge, "Geophysical inversion with a neighbourhood algorithm I - Searching a parameter space," *Geophysical Journal International,* 138, pp. 479-494

(1999).

Sambridge 1999b.

M. Sambridge, “Geophysical inversion with a neighbourhood algorithm II - Appraising the ensemble,” *Geophysical Journal International,* 138, pp. 727-746 (1999).

Schiff 1968.

Leonard I. Schiff, *Quantum Mechanics, Third Edition,* McGraw-Hill (1968).

Schroeder 1991.

Manfred Schroeder, *Fractals, Chaos, and Power Laws: Minutes from an Infinite Paradise,* W.H. Freeman and Company, New York, USA (1991).

Selby 1964.

Dr. Samuel M. Selby, (ed.), *Standard Mathematical Tables, Fourteenth Edition,* The Chemical Rubber Co., Cleveland, Ohio, USA (1964).

Sideris 1997.

M.G. Sideris, course notes on the subject of Legendre functions and derivatives (1997).

Singh 1981.

A. Singh, “On Numerical Evaluation of Normalized Associated Legendre Functions,” Ohio State University internal report, Department of Geodetic Science and Surveying (1981).

Smith and Wessel 1998.

W.H.F. Smith and P. Wessel, “New, improved version of Generic Mapping Tools released,” *EOS Transactions of the American Geophysical Union,* 79, 47, p. 579 (1998).

Stacey 1969.

Frank D. Stacey, *Physics of the Earth,* John Wiley & Sons, Inc., Toronto, Canada (1969).

Starck 2002.

J.L. Starck, “Multiscale Transforms and Applications,” Course overheads, http://jstarck.free.fr/cours.htm (November 2002 or earlier).

Suda 2001.

R. Suda, “High performance computation of spherical harmonic transform,” *IPSJ SIGNotes High Performance Computing Abstract No.071 - 002,*

http://www.ipsj.or.jp/members/SIGNotes/Eng/12/1998/071/article002.html (June 2001).

Suda and Takami 2002.

R. Suda and M. Takami, "A Fast Spherical Harmonics Transform Algorithm," *Mathematics of Computation,* 71, 238, pp. 703-715 (April 2002).

Swarztrauber 1979.

P.N. Swarztrauber, "On the Spectral Approximation of Discrete Scalar and Vector Functions on the Sphere," *SIAM Journal of Numerical Analysis,* 16, 6, pp. 934-949 (December 1979).

Swarztrauber 1993.

P.N. Swarztrauber, "The Vector Harmonic Transform Method for Solving Partial Differential Equations in Spherical Geometry," *Monthly Weather Review,* 121, pp. 3415-3437 (December 1993).

Swarztrauber 1996.

P.N. Swarztrauber, "Spectral Transform methods for Solving the Shallow-Water Equations on the Sphere," *Monthly Weather Review,* 124, pp. 730-744 (April 1996).

Szegö 1939.

Gabor Szegö, *Orthogonal Polynomials,* American Mathematical Society, Volume 23, Providence, USA (1939).

Tan and Blais 2000.

C.J. Tan and J.A.R. Blais, "PLFG: A Highly Scalable Parallel Pseudo-Random Number Generator for Monte Carlo Simulations" in *HPCN 2000, LNCS 1823,* pp. 127-135, Springer-Verlag, Berlin Heidelberg (2000).

Tan, Blais, and Provins 1999.

C.J. Tan, J.A.R. Blais, and Dean Allen Provins, "Large Imagery Data Structuring Using Hierarchical Data Format for Parallel Computing and Visualization" in *The Journal of Supercomputing: An International Journal of High-Performance Computer Design, Analysis and Use,* Queen's University, Kingston, Canada (June 13-16, 1999).

Telford et al. 1976.

W.M. Telford, L.P. Geldart, R.E. Sheriff, and D.A. Keys, *Applied Geophysics,* Cambridge University Press, Cambridge (1976).

Teolis 1998.

Anthony Teolis, *Computational Signal Processing,* Birkhäuser (1998).

Tommila 1999.

Mikko Tommila, *apfloat: A C++ High Performance Arbitrary Precision Arithmetic Package,* Preprint from http://www.iki.fi/~mtommila/apfloat/ (June 1999).

Vajda and Vaníček 1999.

P. Vajda and P. Vaníček, "Truncated Geoid and Gravity Inversion for One Point-Mass Anomaly," *Journal of Geodesy,* 73, pp. 58-66 (1999).

Vecsey et al. 2000.

Ludeck Vecsey, David A. Yuen, and Alain P. Vincent, "Detection of Plate Boundaries from Geoid Data using Two-dimensional Wavelets," Report UMSI 2000/121, Supercomputing Institute for Digital Simulation and Advanced Computation, University of Minnesota (June 2000). 17 pp.

Vermeer 1995.

M. Vermeer, "Mass point geopotential modelling using fast spectral techniques; historical overview. toolbox description, numerical experiment," *Manuscripta Geodaetica,* 20, pp. 362-378 (1995).

Wandelt et al. 1998.

Benjamin D. Wandelt, Eric Hivon, and Krzysztof M. Górski, *Topological Analysis of High-Resolution CMB Maps,* Preprint from http://www.tac.dk/~healpix (1998).

Wang et al. 2001.

Bingzhu Wang, Dean Allen Provins, and J.A.R. Blais, *Subsurface Feature Extraction Using Multiresolution Computational Tools,* Presentation at the Canadian Geophysical Union annual scientific meeting, Ottawa, Ontario (May, 2001).

Wenzel 1998a.

Georg Wenzel, "Ultra High Degree Geopotential models GPM98A, B and C to Degree 1800," *Bulletin of International Geoid Service,* preprint from http://www.gik.uni-karlsruhe.de/~wenzel/gpm98abc/gpm98abc.htm (1998).

Wenzel 1998b.

Georg Wenzel, "Ultra High Degree Geopotential Model GPM3E97A to Degree and Order 1800 Tailored to Europe," *Proceedings of the 2nd Continental Workshop on the Geoid in Europe,* Budapest (preprint from http://www.gik.uni-karlsruhe.de/~wenzel/gpm3e/gpm3e97a.htm) (March 10-14, 1998).

Whitten and Brooks 1979.

D.G.A. Whitten and J.R.V. Brooks, *A Dictionary of Geology,* Penguin Books (1979).

Wong et al. 1971.

L. Wong, G. Beuchler, W. Downs, W. Sjogren, P. Muller, and P. Gottlieb, "A surface layer representation of the lunar gravitational field," *Journal of Geophysical Research,* 76, pp. 6220-6236 (1971).

Yakowitz and Szidarovszky 1989.

S. Yakowitz and F. Szidarovszky, *An Introduction to Numerical Computations,* Macmillan Publishing Company, New York, USA (1989).

Young 1970.

R.G.E. Young, "Combining Satellite Altimetry and Surface Gravimetry in Geodetic Determinations," TE-37, Massachusetts Institude of Technology, Measurement System Lab (1970).

Yuen et al. 2001.

D.A. Yuen, A.P. Vincent, M. Kido, and L. Vecsey, "Geophysical application of multidimensional filtering using wavelets," *submitted to Pure and Applied Geophysics,* pp. 1-39, preprint from www.msi.umn.edu/~heather/yuen_pageoph.pdf (Feb 2001).

Zhang 1993.

Changyou Zhang, "Recovery of Gravity Information from Satellite Altimetry Data and Associate Forward Geopotential Models," Report No. 20058, Department of Geomatics Engineering, University of Calgary, Calgary (October 1993).

Index

Z